Low-Mass Stars and Their Companions

Thesis by

Benjamin Tyler Montet

In Partial Fulfillment of the Requirements for the
degree of
Doctor of Philosophy

CALIFORNIA INSTITUTE OF TECHNOLOGY
Pasadena, California

2017
Defended July 18, 2016

Benjamin Tyler Montet
ORCID: 0000-0001-7516-8308

ACKNOWLEDGEMENTS

I am extremely grateful to everyone who has helped me get to Caltech, as well as those who have helped me through these past five years. Of course, this list must begin with my parents: thank you for all your support and encouragement over the past 27 years. I also want to thank my fifth grade teacher, Mrs. Kim Klappauf, for always being so enthusiastic and showing us that being into science was cool.

I want to thank my advisor, John Johnson, and everyone involved in the Exolab during my time. That (long!) list includes Justin Crepp, Phil Muirhead, Leslie Rogers, Brendan Bowler, Jennifer Yee, and Luan Ghezzi for allowing them to regularly bug them with questions in their offices. I especially want to thank Jon Swift for his patience in working through problems on the white board, his pedantry in third order corrections, and his enthusiasm for life both inside and out of Cahill.

I want to thank everyone involved with the Summer 2013 "Modern Statistical and Computational Methods for Analysis of Kepler Data" workshop at the Statistical and Applied Mathematical Sciences Institute in Research Triangle Park, North Carolina. The workshop certainly changed the trajectory of my thesis, and allowed me to meet new friends and collaborators. I thank the organizers, especially Eric Ford and David Hogg (the latter whom, I acknowledge formally, I still owe a bottle of good wine), for allowing me to participate, and the participants for being so amazing, especially Ruth, Dan, Robert, Megan, Ben, Angie, and Gal.

I want to thank the Caltech Astronomy graduate students for being the friendliest, most pleasant classmates and friends one could ask for. I particularly want to thank (in no particular order) Mislav, Antonija, Trevor, Allison, Yi, Matt, Sirio, Gwen, Drew, Ryan and Donal. To my officemates Walter, Shriharsh, Drew, Sirio, and Mislav: thank you for putting up with me. Sorry I took away your couch (if it's any consolation, it looks nice in my apartment.) I also want to thank the faculty for allowing the graduate community to be what it is, especially Wal Sargent. I still miss seeing your face around the department and hearing your opinions on everything from iced tea to camping. And football, especially football.

I will always remember the traditions shared among the Cahill grad students: ski trips to Mammoth (never Big Bear, sorry Trevor), Wednesday night softball with the Big Bangers, Halloween parties, trips to the Athenaeum, wine and cheese, concerts at the Hollywood Bowl, finding space for 15 people to eat lunch together at

Chandler, and so much more.

I would like to thank my committee: Heather Knutson, Gregg Hallinan, Phil Hopkins, and Tony Readhead for reading my thesis (at least this far) and for their support and guidance. I also want to thank Patrick Shopbell, Anu Mahabal, and José Calderon, who must form the best computing staff in all of astronomy.

Finally, I want to thank Laura. Thank you for your support. Thank you for always being there when I need someone. Thank you for always being there when I need someone to put me in my place. I've enjoyed every day of our adventure, and I can't wait to see what happens next.

ABSTRACT

In this thesis, I present seven studies aimed towards better understanding the demographics and physical properties of M dwarfs and their companions. These studies focus in turn on planetary, brown dwarf, and stellar companions to M dwarfs.

I begin with an analysis of radial velocity and transit timing analyses of multi-transiting planetary systems, finding that if both signals are measured to sufficiently high precision the stellar and planetary masses can be measured to a high precision, eliminating a need for stellar models which may have systematic errors. I then combine long-term radial velocity monitoring and a direct imaging campaign to measure the occurrence rate of giant planets around M dwarfs. I find that 6.5% ± 3.0% of M dwarfs host a Jupiter mass or larger planet within 20 AU, with a strong dependence on stellar metallicity.

I then present two papers analyzing the LHS 6343 system, which contains a widely separated M dwarf binary (AB). Star A hosts a transiting brown dwarf (LHS 6343 C) with a 12.7 day period. By combining radial velocity data with transit photometry, I am able to measure the mass and radius of the brown dwarf to 2% precision, the most precise measurement of a brown dwarf to date. I then analyze four secondary eclipses of the LHS 6343 AC system as observed by *Spitzer* in order to measure the luminosity of the brown dwarf in both *Spitzer* bandpasses. I find the brown dwarf is consistent with theoretical models of an 1100 K T dwarf at an age of 5 Gyr and empirical observations of field T5-6 dwarfs with temperatures of 1070 ± 130 K. This is the first non-inflated brown dwarf with a measured mass, radius, and multi-band photometry, making it an ideal test of evolutionary models of field brown dwarfs.

Next, I present the results of an astrometric and radial velocity campaign to measure the orbit and masses of both stars in the GJ 3305 AB system, an M+M binary comoving with 51 Eridani, a more massive star with a directly imaged planetary companion. I compare the masses of both stars to largely untested theoretical models of young M dwarfs, finding that the models are consistent with the measured mass of star A but slightly overpredict the luminosity of star B.

In the final two science chapters I focus on space-based transit surveys, present and future. First, I present the first catalog of statistically validated planets from the *K2* mission, as well as updated stellar and planetary parameters for all systems with candidate planets in the first *K2* field. The catalog includes K2-18b, a "mini-

Neptune" planet that receives a stellar insolation consistent with the level that the Earth receives from the Sun, making it a useful comparison against planets of a similar size that are highly irradiated, such as GJ 1214 b. Finally, I present predictions for the *WFIRST* mission. While designed largely as a microlensing mission, I find it will be able to detect as many as 30,000 transiting planets towards the galactic bulge, providing information about how planet occurrence changes across the galaxy. These planets will be able to be confirmed largely through direct detection of their secondary eclipses. Moreover, I find that more than 50% of the planets it detects smaller than Neptune will be found around M dwarf hosts.

PUBLISHED CONTENT AND CONTRIBUTIONS

This work contains material which was originally published in six articles. They are as follows:

Montet & Johnson (2013): "Model-independent Stellar and Planetary Masses from Multi-transiting Exoplanetary Systems," The Astrophysical Journal, 762, 112. This article has DOI 10.1088/0004-637X/762/2/112. B.T.M. developed the idea behind this project, led the analysis, and wrote the paper.

Montet et al. (2014): "The TRENDS High-contrast Imaging Survey. IV. The Occurrence Rate of Giant Planets around M Dwarfs," The Astrophysical Journal, 781, 28. This article has DOI 10.1088/0004-637X/781/1/28. B.T.M. developed the analysis pipeline used in this project. He also led the statistical analysis and wrote the paper.

Montet et al. (2015a): "Characterizing the Cool KOIs. VII. Refined Physical Properties of the Transiting Brown Dwarf LHS 6343 C," The Astrophysical Journal, 800, 134. This article has DOI 10.1088/0004-637X/800/2/134. B.T.M. reduced the data obtained for this paper, led the analysis, and wrote the paper.

Montet et al. (2015c): "Stellar and Planetary Properties of K2 Campaign 1 Candidates and Validation of 17 Planets, Including a Planet Receiving Earth-like Insolation," The Astrophysical Journal, 809, 25. This article has DOI 10.1088/0004-637X/809/1/25. B.T.M. developed the idea for this paper, coordinated the data collection led by other authors, led the statistical analysis, and wrote the majority of the paper.

Montet et al. (2015b): "Dynamical Masses of Young M Dwarfs: Masses and Orbital Parameters of GJ 3305 AB, the Wide Binary Companion to the Imaged Exoplanet Host 51 Eri," The Astrophysical Journal Letters, 813, 11. This article has DOI 10.1088/2041-8205/813/1/L11. B.T.M. performed the statistical analysis in this work, and led the writing of the paper.

Montet et al. (2016): "Benchmark Transiting Brown Dwarf LHS 6343 C: Spitzer Secondary Eclipse Observations Yield Brightness Temperature and Mid-T Spectral Class," The Astrophysical Journal Letters, 822, 6. This article has DOI 10.3847/2041-8205/822/1/L6. B.T.M. developed the idea for this project, led the efforts to write the proposal to obtain the data, reduced the data, led the analysis of this project, and wrote the paper.

TABLE OF CONTENTS

LIST OF ILLUSTRATIONS

LIST OF TABLES

Chapter 1

INTRODUCTION

1.1 The M Dwarf Spectral Class

For thousands of years, humans have studied stellar astronomy. The ancient Greeks, especially Hipparchos, measured the brightness and position of hundreds of stars. The ancient Egyptians used observations of stars, particularly Sirius and Thuban, to measure time for agricultural purposes. The ancient Chinese observed supernovae for divination purposes. Stars are one of the primary ways we can observe the universe. On large scales, the galaxies we observe at high redshifts are made up of stars; on small scales, the asteroids we observe in our solar system are observable because they are reflecting light from our own sun. In these cases, we can only understand the astrophysical phenomena we observe because we understand the starlight that creates these phenomena.

Different stars are divided into different spectral classes based on their observable spectroscopic features. Type M dwarfs were a part of the original Draper Catalogue of Stellar Spectra (Pickering 1890), classified as having weak but non-zero hydrogen absorption features in their spectra. The system was alphabetical: they were classified between K and O stars, the former having stronger hydrogen absorption and the latter none at all. With the development of the Harvard system, Cannon & Pickering (1901) preserved the M spectral class and placed it at one end of the classification system, next to K stars. We now know that M and O stars have little hydrogen absorption in their atmospheres for very different reasons and the modern classification system maps stellar effective temperature: M dwarfs are the coolest main-sequence stars and the least massive hydrogen burning stars in the galaxy. Today, the boundary between K and M dwarfs is defined by the presence of titanium oxide (TiO) bands in the atmospheres of M dwarfs (Kuiper 1938; Morgan 1938), which can form when a star's effective temperature is below approximately 3500 K.

The single classification for M dwarfs can give the appearance of M dwarfs as a single, monolithic block. Indeed, this is largely true for other spectral types. The Sun has a radiative core, in which nuclear reactions are dominated by the p-p chain, and a convective outer layer, which contributes to the existence of a magnetic field. The same is true for stars from the middle of the F spectral class through early M

dwarfs. M dwarfs, meanwhile, have an incredible diversity. The M dwarf class spans an order of magnitude in mass, an order of magnitude in radius, and a factor of 40 in luminosity (Veeder 1974). There are significant changes in the structure of the stars across this class as well. Below approximately 0.35 $M_{\odot}$, M dwarfs become fully convective, leading to a rapid decrease in the radius and luminosity of stars just below this boundary (Chabrier & Baraffe 1997). At the late edge of the M dwarf class are brown dwarfs, objects without high enough central densities to fuse hydrogen.

In terms of their structure, F7 and K3 dwarfs have more in common than M0 and M9 dwarfs. Some of the stars even vary in time. As a brown dwarf leaves the T Tauri stage of stellar evolution it has a temperature of approximately 3000 K and a spectrum consistent with that of a mid-M dwarf. Brown dwarfs then cool and evolve into "late-type" L, T, and eventually Y dwarfs at a rate which depends on their mass. I will discuss the evolution of brown dwarfs more fully in Section 1.6. If the abundance of M dwarfs and the diversity of their structure had been understood at the time of the development of the Harvard stellar classification system, it is possible that these stars would have been awarded more than a single spectral type.

1.2 M Dwarfs: The Silent Majority

The early work on stellar spectroscopic classification of type M stars is based on spectroscopy of M giants. The Draper catalogue was first published in 1890 and the Harvard stellar classification scheme in 1901, but the first spectrum of an M dwarf was obtained only 100 years ago when Adams (1913) collected an observation of the M+M binary Groombridge 34. This 8th magnitude star was known to be peculiar relative to the M stars with known spectra because of its high proper motion of 3 arcseconds per year; today we know it is within 4 parsec of the Sun.

The oldest known surviving diagram plotting stellar absolute magnitude against spectral type (Russell 1914), now known as a Hertsprung-Russell Diagram, includes hundreds of stars, as shown in Figure 1.1. Today we know that M dwarfs make up approximately 75% of the stars in the galaxy, yet only ~5% of the stars included in Russell's figure are listed as spectral type M. These stars are absent in the original work because they are intrinsically faint.

The faintness of M dwarfs is the result of the physics of their interior, specifically the stellar mass-luminosity relation. To show this, let us begin with the equations

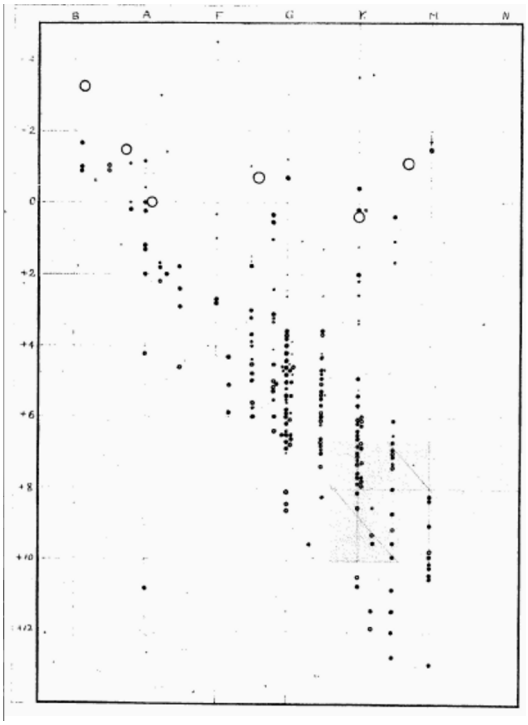

Figure 1.1: The original H-R diagram, as published by Russell (1914). On the y-axis is absolute magnitude, equivalent to the logarithm of the star's luminosity. On the x-axis is stellar spectral type, which we now know maps approximately to stellar effective temperature.

of stellar structure. The first of these declares a star is in hydrostatic equilibrium:

$$\frac{\mathrm{d}P(r)}{\mathrm{d}r} = -\frac{Gm\rho}{r^2}, \tag{1.1}$$

where $P(r)$ is the pressure exerted on a particle at a radius r, G is Newton's constant, m the mass enclosed inside the radius r, and ρ the stellar density, itself a function of radius as well.

The second equation defines mass conservation:

$$\frac{\mathrm{d}m(r)}{\mathrm{d}r} = 4\pi r^2 \rho, \tag{1.2}$$

where π is the ratio of a circle's circumference to its diameter, and all other variables retain their meaning from Equation 1.1.

The third equation defines energy transport:

$$\frac{\mathrm{d}L(r)}{\mathrm{d}r} = 4\pi r^2 \rho \epsilon, \tag{1.3}$$

where L is the energy leaving a spherical shell of radius r, produced by the material in the star interior to r and ϵ is the energy released per unit mass per second inside the star.

The final equation defines the temperature gradient inside a star. The exact form of this equation depends on the method for which energy is transported inside the star. For radiative transport, the temperature gradient is

$$\frac{\mathrm{d}T}{\mathrm{d}r} = -\frac{3}{4ac}\frac{\bar{\kappa}\rho}{T^3}\frac{L}{4\pi r^2}. \tag{1.4}$$

Here, T is the temperature of the star at a radius r, ac is the radiation constant multiplied by the speed of light, also equal to four times the Stefan-Boltzmann constant, and $\bar{\kappa}$ the mean opacity of the material.

Very low-mass stars are fully convective, not radiative, and therefore follow a different limit:

$$\frac{\mathrm{d}T}{\mathrm{d}r} = \left(1 - \frac{1}{\gamma}\right)\frac{T}{P}\frac{\mathrm{d}P(r)}{\mathrm{d}r}, \tag{1.5}$$

where γ is the adiabatic index, and is $5/3$ for a monatomic ideal gas, and all other terms retain their previous meaning.

Let us consider two other proportionalities. First, we assume that the energy generation rate inside a star is a function of its temperature and density:

$$\epsilon = \epsilon_0 \rho T^{\nu}, \tag{1.6}$$

where ν depends on the particular fusion pathway that is dominant in the core of the star. Second, we assume that the ideal gas law holds:

$$P \propto \rho T. \tag{1.7}$$

With these six equations, we can develop a series of homology relations. We can create a series of five linear equations with five unknown parameters: $\log T$, $\log P$, $\log R$, $\log \rho$, and $\log M$. Ignoring constant terms and considering only the adiabatic case (as for fully convective stars),

$$\begin{aligned}
\log P &= 2\log M - 4\log R \\
\log \rho &= \log M - 3\log R \\
\log P &= \gamma \log \rho \\
\log T &= \left(\frac{\gamma - 1}{\gamma}\right)\log P \\
\log L &= \log \rho + \nu \log T + \log M.
\end{aligned} \tag{1.8}$$

We can rearrange these to solve for $\log M$, finding

$$\log R = \left(\frac{2 - \gamma}{4 - 3\gamma}\right)\log M, \tag{1.9}$$

which we can then insert into the final equation in Equation 1.8. This manipulation yields

$$\log L = \left(\frac{2(\nu+1)-\gamma(2\nu+3)}{4-3\gamma}\right)\log M, \tag{1.10}$$

which if we consider the case where we have an ideal, fully ionized gas so that $\gamma = 5/3$ and energy generation dominated by the p-p chain so that $\nu = 4$, we find

$$\log L \approx 8.33 \log M + \text{const}, \tag{1.11}$$

or $L \propto M^{8.33}$! Thus, if we decrease the mass of a fully convective star by a factor of two, we also decrease its luminosity by a factor of 320![1]

We can take a similar approach to understand the relation between the mass and temperature of low-mass stars. We know that

$$L = 4\pi R^2 \sigma T^4, \tag{1.12}$$

so that

$$\log L = 2\log R + 4\log T + \text{const}. \tag{1.13}$$

With equations 1.9 and 1.10, we can find a relation between the log of the star's mass and its temperature:

$$4\log T = \left(\frac{2(\nu+1)-\gamma(2\nu+3)}{4-3\gamma}\right)\log M - 2\left(\frac{2-\gamma}{4-3\gamma}\right)\log M + \text{const}. \tag{1.14}$$

Again we consider the case where we have an ideal, ionized gas and energy generation dominated by the p-p chain, so that $\gamma = 5/3$ and $\nu = 4$. In this case, $\log T \approx 0.44 \log M$, so $T \propto M^{0.44}$. M dwarfs, with effective temperatures around 3,000 Kelvin, have significant molecular absorption in their atmospheres, complicating their analysis even further.

Even worse for optical observing, the peak of the SED of a typical 3,000 K M dwarf peaks at 1 micron, well into the infrared, making them even fainter in the optical. Even though M dwarfs make up 70% of the nearest stars, with 250 of them located within 10 pc of the Sun (e.g. Henry et al. 2006), there are no M dwarfs visible to the naked eye. The brightest, HIP 105090, is only 3.95 ± 0.01 pc from the Sun, yet has an apparent V-band magnitude of 6.76 (van Leeuwen 2007). With so many bright solar-type stars in the solar neighborhood, it is easy to understand why M dwarfs have been and often continue to be overlooked in planet search surveys.

[1] The same manipulation, considering the case of radiative transport, leads to the relation $L \propto M^{5.5}$, similar to what is observed for Sunlike stars.

1.3 Radial Velocity Planet Searches

Stellar Radial Velocities

Planets do not orbit their host stars. Planets and stars, like any pair of bodies orbiting each other, orbit their common center of mass, or barycenter. For circular orbits, the planet and star velocities are constant, and the observed radial component of the velocity is modulated sinusoidally with the period of the planet as the velocity vector changes direction. The magnitude of the RV signal in this case depends only the mass of the planet, m, the mass of the star, M, the orbital period, P, and the unknown inclination i. Specifically, by taking the time derivative of the position of the star in time, the RV can be shown to be

$$v_r = \left(\frac{2\pi G}{P}\right)^{1/3} \frac{m \sin i}{(M+m)^{2/3}} \cos \nu. \tag{1.15}$$

Here, G is Newton's constant and ν the mean anomaly of the planet, which in the circular case increases linearly from 0 to 2π in time over the course of one orbit. For Jupiter, the Sun's reflex RV motion is 13 m s^{-1}; for Earth, 9 cm s^{-1}. We see that the velocity depends on the mass ratio between the planet and star, meaning that we can only characterize the planet as well as we understand the star.

For planets on eccentric orbits, the math is more complicated. Again, the derivation begins with the time derivative of the position of the star, but in the eccentric case neither the linear or angular velocity is constant (Kepler 1609). It can be shown that the radial velocity equation becomes

$$v_r = \left(\frac{2\pi G}{P}\right)^{1/3} \frac{m \sin i}{(M+m)^{2/3}} \frac{1}{\sqrt{1-e^2}} (e \cos \omega + \cos(\omega + \nu)), \tag{1.16}$$

where e is the eccentricity and ω the argument of periapsis, the angle relative to the plane of the sky at which the planet and star make their closest approach. All other terms retain their previous meaning, but from Kepler's second law, the true anomaly no longer increases linearly in time. While we can easily measure the expected RV of the star at any position in its orbit, we do not know the time at which the star will be at that position.

To calculate the expected RV at a given time, we invoke the mean anomaly, which represents the mean angular motion of the two bodies. It is defined to be zero at the time of periapsis, τ, and at all other times t can be calculated such that

$$M = \frac{2\pi}{P}(t - \tau). \tag{1.17}$$

It therefore increases linearly in time from 0 to 2π. The true anomaly can be calculated from the mean anomaly through the eccentric anomaly, E, such that

$$M = E - e \sin E. \tag{1.18}$$

This is a transcendental equation and requires an approximate numerical solution. Once the eccentric anomaly is determined, the true anomaly can be determined as well, such that

$$\tan \frac{\nu}{2} = \sqrt{\frac{1+e}{1-e}} \tan \frac{E}{2}. \tag{1.19}$$

With that, we can solve Equation 1.16 and measure the RV of a star at any time. We note that all three anomalies are identical in the circular case.

Of course, we can only use these equations if we can measure variations in the stellar RV itself. Fortunately, we can leverage stellar atmospheres for this purpose. Stars with masses below ≈ 1.3 $M_\odot$ have convective outer layers, generating magnetic activity which provides a torque as charged particles escape their host star along magnetic field lines (Shu et al. 1994). The spin-down is a predictable function of the star's mass and age, leading to the use of rotation rates as a probe of stellar ages (Barnes 2003). G dwarfs at the age of the Sun rotate at only 1 km s^{-1} at their equators. With a full spectrum of spectral lines to consider, the RV of the star can be measured to 2-5 m s^{-1} depending on the instrument. At this level, systematic effects induced by the instrument can dominate over any planetary signal: in the typical mode used for planet searches, the resolution of Keck/HIRES is 55,000, leading to a pixel scale of 5.5 km s^{-1} $pixel^{-1}$.

To measure precise RVs, both the pixel scale and a precise wavelength calibration must be known, at a level much smaller than a single pixel. During a night, the shape of the instrumental profile of the detector can change, leading to changes in the wavelength calibration considerably larger than the planetary signals targeted. To combat this, one of two approaches are taken. At Keck/HIRES, observers place an iodine cell in the light path before the starlight enters the instrument itself (Butler & Marcy 1996). Iodine has many absorption features in the optical with precisely known wavelengths, so the cell creates a precise, stable wavelength scale to compare against the stellar signal. The iodine also provides information about the shape of the instrumental profile during each observation. At other telescopes, including HARPS, the spectrograph slit is replaced with a fiber, and the instrument is placed in a temperature and pressure controlled enclosure to keep the instrumental profile consistent. Simultaneously with the observations of the stellar spectrum, a

Thorium-Argon lamp is observed which serves the same purposes as the iodine cell, providing a simultaneous wavelength reference.

History of RV Searches

The first radial velocity (RV) planet searches focused almost exclusively on Sunlike (FGK) stars, a reasonable choice as these are the brightest main sequence stars for which magnetic braking occurs, leading to slow rotation (Wright et al. 2004).

The first planet detected around a main sequence star other than the Sun was discovered in 1995 with the detection of 51 Pegasi b, a planet with an orbital period of 4.23 days and a mass of 0.472 ± 0.039 M_{Jup} (Mayor & Queloz 1995). Quickly, dozens of similar "hot Jupiter" planets with masses larger than Saturn but periods around three days were discovered (e.g. Butler et al. 1997; Marcy et al. 1998; Wright et al. 2007).

As more planets were detected around FGK dwarfs, surveys expanded to include other types of stars. As stated previously, A stars do not make ideal RV survey targets due to their rapid rotation. However, when these stars evolve off the main sequence onto the subgiant branch, conservation of angular momentum results in a large increase in the rotation period and thus a decrease in $v \sin i$, making these stars amenable to RV planet searches. These "Retired A stars" were found to have fewer hot Jupiters than their less massive counterparts, but a higher giant planet occurrence rate overall (Johnson et al. 2007a; Bowler et al. 2010; Johnson et al. 2011a).

M dwarfs have many narrow spectral features and make ideal planet search targets as long as they are near enough to be observable. Indeed, the 13th planet discovered via RVs was a 2.3 M_{Jup} planet in a 61-day orbit around GJ 876 (Delfosse et al. 1998; Marcy et al. 1998). Researches detected more giant planets around M dwarfs (Butler et al. 2004, 2006), but the occurrence rate of giant planets around M dwarfs was found to be considerably lower than around higher mass stars. Only $\approx 3\%$ of M dwarfs host a planet at least as massive as Jupiter within 2.5 AU (Johnson et al. 2010a; Bonfils et al. 2013). These surveys also showed a correlation between giant planet occurrence and stellar metallicity (Fischer & Valenti 2005; Johnson & Apps 2009).

To date nearly 600 planets have been discovered via RV variations. These results show hot Jupiters orbit approximately 1% of Sunlike stars (Wright et al. 2012). They also show that 10% of systems have a Saturn-mass or larger planet with or-

bital periods shorter than 2000 days (Cumming et al. 2008). By extrapolating the observed distribution outward, the same authors predict 20% of FGK dwarfs host a gas giant planet within 20 AU.

Despite the large numbers of planets detected so far, RV surveys have substantial limitations. There has been substantial work on improving RV precision, both in instrument development and in understanding stellar activity (Fischer et al. 2016). Yet there is still work to do: even the smallest RV signal claimed as a planetary detection has a Doppler amplitude larger than the Earth's by a factor of six (Dumusque et al. 2012). Worse yet, the planet's very existence has been called into question: the purported signal may be an artifact of the stellar activity modeling techniques applied to the data (Rajpaul et al. 2016).

RV surveys are generally only sensitive to planets which have completed one full orbit. For longer periods, there is a degeneracy between the companion mass and orbital period that cannot be broken without substantial curvature in the orbit, meaning planetary parameters cannot be uniquely determined until the observation baseline exceeds the planet orbital period.

Despite the degeneracy with orbital period, there is still some information to be obtained from planets with periods much longer than the observing baseline. As can be seen in Equation 1.16, the Doppler amplitude only falls off as $P^{-1/3}$, meaning the gravitational pull of a planet is observable even at wide separations. In the case where the planet orbital period is significantly longer than the RV baseline, the planet is observable as a long-term acceleration, or RV "trend." Any constraints on the companion properties are degenerate between the companion mass and separation.

Many of these trends have been shown to be binary systems through direct imaging campaigns, in which case the full three-dimensional orbit of the companion can be ascertained and the companion's mass directly measured (Crepp et al. 2012a, 2013a,b). In cases where imaging can rule out a binary we know the companion is likely a planet, but the exact nature of the companion is unknown. However, statistical analyses of many such systems can provide precise measurements of the overall distribution of planets in wide orbits.

1.4 Transiting Planet Searches

The Importance of Transiting Planets

If a planetary system is aligned in such a way that the planets pass between our viewing position in the solar system and the star itself, they will appear to pass across (or transit) the stellar disk during their orbit. We can not resolve the surface of the star in order to image the transit itself, but we can still detect it. During the transit, a portion of the stellar disk is blocked, decreasing the observed flux from the star. The size of this decrement, δ, corresponds to the fractional area of the star's disk blocked by the planet:

$$\delta = \left(\frac{R_p}{R_*}\right)^2. \tag{1.20}$$

Again, we find that we must understand the star's parameters (in this case, the radius) in order to understand the planetary parameters.

Detecting planets with the transit method is more limited relative to the RV method: only a small fraction of all planets will be directly detectable. Any planets not in nearly edge-on orbits will be missed in a transit search. In addition, transit photometry provides precise information about the location of a planet, but only at one point of its orbit. Even in cases where information about the eccentricity can be inferred from the transit itself (Dawson & Johnson 2012), there is still a degeneracy between the eccentricity and argument of periastron which can not be broken without additional information.

On the other hand, there are a few key advantages in transit searches relative to RV surveys. Transit searches can target many more stars than RV surveys. To a first order approximation, transits are achromatic, with the depth of the transit approximately equal at all wavelengths, so transits can be detected through broadband photometry. As RV surveys require high-resolution spectroscopy, they require comparatively bright stars; transit searches can target much fainter stars, opening up the search for planets to many more M dwarfs. Similarly, as spectral features are no longer required, transit surveys can target rapidly rotating massive stars without convective outer layers and narrow spectral lines.

Transit surveys also allow for a more direct determination of the planetary physical properties. In RV searches, only a minimum mass for the detected planet, $m \sin i$, can be determined. Although the planet mass distribution and geometrical bias both favor large (close to edge-on) inclinations (Ho & Turner 2011), individual objects have unknown inclinations so the absolute masses of the RV planets cannot

be determined. In transit searches, however, the direct observable is the transit depth, which depends directly on the size of the planet: for a sufficiently precise measurement of the stellar radius and transit parameters, any precision on the planet radius can be achieved without a geometric bias.

Perhaps most significantly, transit searches allow us to probe atmospheres of other planets. Planetary atmospheres, Earth's included, are optically thick at some wavelengths and optically thin at others. In the context of the Earth, this makes some wavelengths more amenable for astronomical observations than others, as the atmosphere only interacts with photons of certain wavelengths. The same is true for planets around other stars: at some wavelengths their atmospheres are transparent to radiation from their host stars, while at other wavelengths the atmospheres absorb light. By observing a transit at a wavelength at which the atmosphere is optically thick, the size of the planet inferred is the size of the planet, including its atmosphere. Alternatively, by observing at a wavelength at which the wavelength is optically thin, we measure only the size of the planet itself, not its atmosphere (e.g. Knutson et al. 2011, 2014). Such an analysis, termed *transmission spectroscopy*, is impossible in traditional RV searches for planets.

To fully understand the atmosphere measured during transmission spectroscopy observations, we want to understand the mass (and therefore the density) of the transiting planet as well. If the transiting planet is massive and the star a good RV target (bright and not rapidly-rotating), RVs can be used to measure its mass. Since the planet is known to be transiting, it must have $i \approx \pi/2$, so that $\sin i \approx 1$. Unfortunately, the vast majority of transiting planets are too faint to make ideal RV targets. In these cases, we would like to have an alternative method to measure masses.

When multiple planets orbit the same star, they gravitationally perturb each other during close encounters along their orbit. Transit photometry provides precise information about the location of a planet on its orbit at the moment of transit, especially the times at which the transits begin and end. In *Kepler* data, it is not uncommon to be able to measure individual times of transit to a precision of five minutes or better, with the exact precision a function of the planet size (which affects the size of each individual transit) and orbital period (which affects the speed at which a planet orbits its host star, assuming a circular orbit). Perturbations from other planets can be significantly larger than the transit timing precision, leading to transit timing variations (TTVs). For a hypothetical distant observer detecting transits in our solar system, the presence of Jupiter could be inferred from TTVs on the inner

planets: Jupiter induces TTVs of 10 minutes on Venus and Earth and 100 minutes on Mars (Agol et al. 2005; Holman & Murray 2005).

Kepler enabled the first detections of TTVs. Timing variations have been used to confirm the planetary nature of apparent transiting planet signals in *Kepler* (Holman et al. 2010; Rowe et al. 2014). They have also enabled the detection of non-transiting planets perturbing transiting planets (e.g. Ballard et al. 2011; Nesvorný et al. 2013), as well as measurements of the eccentricity distribution of transiting planets (Hadden & Lithwick 2014). Observations of TTVs enable a direct measurement of the mass ratio between the perturbing planet and the host star (Agol et al. 2005; Lithwick & Wu 2012), again enabling us to understand the mass of the transiting planet at the level at which we understand the mass of the host star.

History of Transit Searches

The first transiting planet detected was a giant planet orbiting HD 209458 (Charbonneau et al. 2000; Henry et al. 2000) This planet, a hot Jupiter, has a radius of 1.14 ± 0.06 $R_\odot$ and an orbital period of 3.52 days. The planet was already known to exist from RV surveys, and had a measured $m \sin i$. Detection of the transit provided a measurement of the inclination, enabling a direct measurement of the mass; the transit detection made it the first planet outside our solar system with a directly measured mass and radius.

Shortly after came the first discovery of a planet via transit, OGLE-TR-56b (Udalski et al. 2002) from the Optical Gravitational Lensing Experiment (OGLE) mission. The primary goal of OGLE is to detect dark matter through microlensing, but it has also discovered many planets via microlensing (Sumi et al. 2011; Cassan et al. 2012). Microlensing surveys require a high photometric precision and a wide field of view so many stars can be observed. These are the same requirements for transit surveys, making them ideal for the discovery of transiting planets, as I discuss in Chapter 8.

Transit surveys discovered 45 more planets between these initial discoveries and 2009, largely through dedicated surveys such as the Super-Wide Angle Search for Planets (SuperWASP, Street et al. 2003), the Hungarian Automated Telescope Network (HATNet, Bakos et al. 2002), and Convection Rotation et Transits planétaires (CoRoT, Auvergne et al. 2009). These surveys continue today, and others, such as MEarth (Nutzman & Charbonneau 2008) are singularly focused on the search for planets around M dwarfs. The planets detected by these surveys have been largely

giant planets in short periods, similar to the early hot Jupiters detected by RV surveys.

In 2009, the *Kepler* mission (Borucki et al. 2010) was launched and began taking data. The precision of *Kepler* was significantly better than any previous mission, allowing 20 parts per million (ppm) photometry over six hours of observation on 12th magnitude stars. It also had a large field of view, staring at 100 square degrees of the northern sky. Every 30 minutes, the telescope recorded photometry of approximately 180,000 stars in a search for periodic transits caused by small planets.

The *Kepler* mission has been a tremendous success. The mission has discovered more than 4,700 planet candidates to date, with more than 2,300 of these being confirmed via other methods or statistically validated as planets at high confidence (Batalha et al. 2013; Burke et al. 2014; Mullally et al. 2015; Rowe et al. 2015; Morton et al. 2016). Most of the stars targeted by the mission are Sunlike FGK dwarfs, so most of the discovered planets transit Sunlike FGK dwarfs. However, there were approximately 5,000 M dwarfs in the original *Kepler* target list, around which more than 100 planets have been discovered. These include planets as small as Mars (Muirhead et al. 2012a) and a planet as large as Jupiter (Johnson et al. 2012a). These planets are located in different environments, with some located in single systems and others tightly packed in resonant chains with low eccentricities and mutual inclinations (Swift et al. 2013; Ballard & Johnson 2016). Morton & Swift (2014) show that these planets are predominantly small, rocky planets in short periods around their host stars.

As *Kepler* is largely a magnitude-limited survey, the majority of the M dwarfs surveyed are early M0 and M1 dwarfs. Only 300 stars had an M2 or later spectral type in the original mission, and only 30 had an M4 or later spectral type. The *K2* mission is providing an opportunity to rectify this oversight. With the failure of two reaction wheels on the *Kepler* spacecraft in 2013, the telescope was left unable to point at its original field, ending the primary mission. The scientific and technical staff behind *Kepler* then designed, with community input, a mission called *K2*. In this mission, the telescope uses the remaining two reaction wheels to point the telescope along the ecliptic plane, while the third axis is approximately balanced by solar radiation pressure. The telescope then rolls about its axis at approximately 1 arcsec hour^{-1}, correcting the roll by periodically firing its thrusters in the opposite direction. In the *K2* mission, the telescope is able to point at fields in the ecliptic plane for approximately 75 days at a time. By the end of the *K2* mission, the

telescope will point at approximately 20 fields covering the ecliptic plane.

K2 is extremely important for the study of M dwarfs. Different fields in the ecliptic point towards or well out of the galactic plane. The typical G dwarf observed in the *Kepler* mission is 300 pc from the Earth, so changes in galactic latitude vastly affect the number of bright FGK dwarfs observable. The typical M dwarf, however, is 50 pc from the Earth, so even pointing directly out of the galactic plane does not affect the stellar density by more than a factor of two, making tens of thousands of M dwarfs observable during the mission. *K2* provides an opportunity to revolutionize our understanding of planets around M dwarfs, if we can confirm planets and characterize their host stars with data from the telescope.

1.5 Understanding M Dwarfs

One of the other downsides of studying companions to M dwarfs is the difficulty in inferring stellar parameters. As can be plainly seen from Equations 1.16 and 1.20, for both RV-detected and transiting planets, the measured quantity of interest (the Doppler amplitude and transit depth) are a function of both planetary and stellar parameters. In both cases, we are only able to understand the planet if we understand its host star: precision planetary astronomy requires precision stellar astronomy.

For solar-type stars, we are able to infer stellar parameters at the few percent level through evolutionary models which motivate well-tested relationships between absolute magnitude and stellar parameters (Andersen 1991; Casagrande et al. 2010). This is largely possible due to an excellent calibration source located 1 AU away from the Earth. For M dwarfs, we do not have a calibration source. The physics of M dwarf atmospheres is more complicated as well. M dwarfs are defined by the presence of titanium oxide (TiO) bands in their atmospheres (Kuiper 1938; Morgan 1938), but also have molecular bands due to vanadium oxide (VO), carbon monoxide (CO), and water (H_2O) (e.g. Mould 1975; Muirhead et al. 2012b). As photons are more scarce, especially in the optical, longer integration times are required to study these stars just to detect the molecular features, much less understand them.

Attempts to understand M dwarf atmospheres and interiors typically depend on empirical relations between photometric or spectroscopic parameters, calibrated to a few stars with known properties. These calibrators tend to be eclipsing binaries with directly measured masses and radii (Birkby et al. 2012) or single, nearby stars with interferometrically measured radii (Boyajian et al. 2012). For example, Delfosse et al. (2000) use observations of 16 M dwarfs with known masses and luminosities

to build a relationship between absolute K-band magnitude and stellar mass that enables mass measurements to approximately 10% precision. However, this observation requires a parallax or other distance measurement, as the required observable is an absolute magnitude.

More recently, Rojas-Ayala et al. (2012) developed a relation between the relative flux of an M dwarf at different wavelengths in the K-band and the star's temperature and metallicity. This method produces uncertainties on stellar parameters of approximately 10% without a direct parallax measurement and has been applied to many of the M dwarfs in *Kepler* to infer stellar parameters (Muirhead et al. 2012b, 2014). Newton et al. (2015) developed a relation between features in the H-band spectra of M dwarfs, finding they can be used to determine a stellar effective temperature with a residual scatter of 73 K and a stellar radius with a residual scatter of 0.027 $R_{\odot}$.

The problem is even worse when we consider young M dwarfs. For very young stars, we can measure their masses by observing the kinematics of the disk of gas and dust surrounding the star (Czekala et al. 2015, 2016). These disks dissipate within the first ten million years of the star's life, decreasing the opportunity to measure directly the masses of stars with ages larger than 10 million years but not yet onto the main sequence. This is especially true for M dwarfs, which are faint, so harder to observe, and also form in binaries less often than their higher mass counterparts (Fischer & Marcy 1992; Shan et al. 2015). Fewer than 20 pre-main sequence (PMS) M dwarfs in binary systems have had dynamical masses measured to a precision of 25% or better through astrometric monitoring (Dupuy et al. 2014). The vast majority of these systems are younger than 10 Myr. In the range 10-100 Myr, for a given luminosity and age, different stellar models predict different stellar masses, some with discrepancies as large as 50% (Hillenbrand & White 2004; Schlieder et al. 2014). Measuring stellar masses of astrometric M+M binaries in young moving groups with known ages provides a first, needed test of these models in order to constrain evolutionary models.

1.6 Brown Dwarfs

The History of Brown Dwarfs

A lower limit on the mass of stars was first proposed by Kumar (1963), who applied models of completely convective stars to determine that stars below a certain mass (which he determined to be between 70 and 90 M_{Jup}) would become com-

pletely degenerate before hydrostatic equilibrium was achieved. He termed these stars "black dwarfs;" a decade later, they were renamed "brown dwarfs" due to the possibility that they may be luminous, especially in the near-IR and at young ages (Tarter 1975).

While these objects were theorized, there was no evidence for their existence for more than two decades. In the late 1980s, the first tentative detections of brown dwarfs appeared. Becklin & Zuckerman (1988) observed an object associated with the white dwarf GD 165 which, from model isochrone fitting, they determined had a mass between 60 and 80 M_{Jup}. From this single detection, although they did not confirm the object as a definitive brown dwarf, they concluded brown dwarfs must be common the galaxy. In 1989, Latham et al. (1989) detected radial velocity variations around HD 114762 which they attributed to a companion with $m \sin i = 11$ M_{Jup}. The authors declared the companion "a probable brown dwarf" but without a direct measurement of the orbital inclination were unable to definitively claim the object as substellar.

The first definitive detections of brown dwarfs came in 1995, the same year as the first definitive exoplanet detection. Rebolo et al. (1995) discovered a young brown dwarf in the Pleiades with a luminosity 0.1% that of the Sun and effective temperature 2350 ± 300 K. The Pleiades is only ~100 Myr old (Basri et al. 1996), but even at that young age the brown dwarf has evolved into a spectral type of M8.5 and is too faint to be burning hydrogen, meaning it must be a brown dwarf. Later that year, Nakajima et al. (1995) imaged an old brown dwarf, Gl 229 B, determining it has a temperature of 1200 K and must have a mass of 20-50 M_{Jup} based on stellar evolution models.

Brown dwarfs appear to be common: there may be as many as 0.02 brown dwarfs per cubic parsec in the solar neighborhood (Reylé et al. 2010), with the nearest only 2 pc from the Sun (Luhman 2014). The physics of star formation do not inhibit their formation. The stellar IMF peaks around 0.2 $M_\odot$, with lower-mass objects increasingly less common below that mass (Chabrier 2003). Objects for which the central density is sufficient for hydrogen burning, with masses larger than approximately 0.069 $M_\odot$ (72 M_{Jup}) are considered stars (Zuckerman 2000), while objects less massive than this boundary are considered brown dwarfs.

On the high-mass end, the boundary between a star and a brown dwarf is clear. On the low-mass end, the separation between brown dwarfs and planets is the subject of debate. Often, especially among observers, the boundary is based on the mass of

the object. Objects larger than 13 M_{Jup}, in which deuterium burning can occur in their core for at least a small fraction of their lifetime, are considered brown dwarfs. This definition is the official definition of a brown dwarf from the International Astronomical Union.

Recent evidence suggests two formation pathways for 13-72 M_{Jup} objects (Bayliss et al. 2016). On the low-mass end, there is a population of transiting brown dwarfs in short orbital periods which may have formed via core accretion, like planets. On the high-mass end, there is a population of transiting brown dwarfs in wider orbital periods which may have formed via gravitational collapse, like other high mass-ratio eclipsing binaries. In the middle, there is a "brown dwarf desert," with a paucity of 30-50 M_{Jup} objects in binary systems. Some, especially theorists, have suggested a definition of brown dwarfs based on their formation, with all objects formed via core accretion called planets and all objects formed via gravitational collapse (but below the hydrogen burning limit) brown dwarfs (e.g. Chabrier et al. 2014). In this thesis, I will follow the IAU definition of a brown dwarf, noting that none of the claims presented within would be significantly affected by following the alternative definition.

Characterizing Brown Dwarfs

Many of the problems for M dwarfs outlined in this introduction are even worse for brown dwarfs. Without active hydrogen burning, they can be significantly fainter than M dwarfs. They cool and collapse in time, meaning their luminosity is continuously decreasing: they can be considered to be effectively PMS objects for longer than the age of the universe (Burrows et al. 2001).

Very young brown dwarfs start their lives as M dwarfs, with effective temperatures between 2500 and 3000 K (Burrows et al. 1997, See also Figure 1.2). Low-mass stars will contract until they reach hydrostatic equilibrium on the main sequence, at which point their effective temperature is approximately constant. Brown dwarfs never reach this point, continuing to contract, cool, and evolve through their life.[2] As brown dwarfs cool below approximately 2500 Kelvin, they enter the L dwarf class, which is defined by the presence of metal hydrides and alkali metals (such as FeH and Na I, respectively) in their atmospheres (Kirkpatrick et al. 1999). Below approximately 1200 Kelvin, brown dwarfs evolve into the T spectral class, which is defined through the presence of methane absorption bands in the near-IR. It is

[2] In this case the "late-type" and "early-type" monikers are—purely by accident—appropriate.

believed that L dwarfs have cloudy, opaque atmospheres while T dwarfs do not. The boundary between these two spectral classes, where the clouds dissipate, features large photometric variability attributed to patchy clouds and a brightening of the brown dwarfs in J-band attributed to a change in the optical depth of the atmosphere (Burgasser et al. 2002a; Metchev et al. 2015) Understanding the physical parameters of an individual brown dwarf requires an assessment of its age as well.

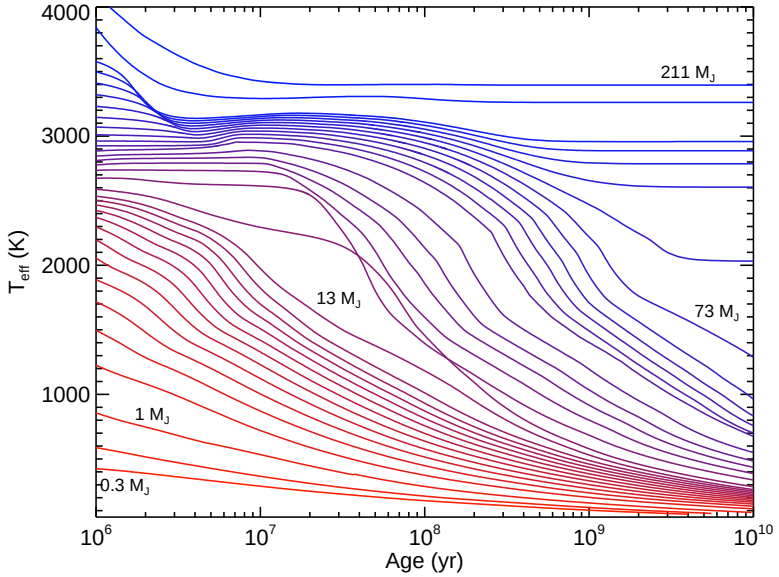

Figure 1.2: Effective temperature vs. age of low-mass stars, brown dwarfs, and planet-mass objects, from Burrows et al. (1997). While all objects cool as they contract at young ages, stars will eventually hit the main sequence. Brown dwarfs continue to evolve throughout their lives, not reaching equilibrium until times significantly longer than the age of the universe.

Broadly speaking, there are two classes of brown dwarfs. Approximately two thousand brown dwarfs have been detected as single objects in the sky, largely through IR surveys like 2MASS and WISE (e.g. Kirkpatrick et al. 1999, 2011). For these objects, we are able to study their atmospheric properties in detail: we can infer the presence of clouds, measure a rotation period, or obtain a spectrum and measure spectroscopic properties like the surface gravity or effective temperature (e.g. Faherty et al. 2014; Filippazzo et al. 2015).

What we are not able to do is measure masses and radii for these single objects. There are only two eclipsing brown dwarf systems known, one in the $\sim$ 1 Myr old Orion Nebula cluster and one in the $\sim$ 10 Myr old Upper Scorpius young moving group (Stassun et al. 2006; David et al. 2016). As both of these are extremely young,

they are not representative of the field brown dwarf population so do not provide useful benchmark comparisons. Among older systems, we know of approximately ten systems with a brown dwarf transiting a main-sequence star, as I will describe in Chapter 5. The vast majority of these systems include a brown dwarf in a short period orbiting close enough so that the energy from stellar irradiation is significantly larger than the emitted heat from the cooling of the brown dwarf, irradiating and possibly inflating the atmosphere of the brown dwarf. In these cases, the brown dwarfs will again appear significantly different from the field brown dwarf population, eliminating the possibility that these could be used as benchmark objects to calibrate brown dwarf masses and radii.

We would ideally want a transiting brown dwarf receiving a low level of irradiation, so we can measure its mass and radius. We would also want this brown dwarf to be nearby so we can measure its atmosphere to compare to the field brown dwarf population, providing a key test of brown dwarf evolutionary models.

If we want a transiting object that is nearby and not highly irradiated by its companion, an ideal place to search is around M dwarfs. As stated previously, M dwarfs in transit searches are typically much closer than higher mass stars, as transit surveys tend to select magnitude-limited samples and M dwarfs are intrinsically faint. Moreover, their low luminosities mean a companion at a given separation will receive significantly less irradiation than the same companion around a higher mass star, so that relatively short periods can allow for non-irradiated companions.

The equilibrium temperature for an object with albedo a at a given separation, r, from a stellar companion with radius $R_\star$, is

$$T_{\rm eq} = T_\star (1-a)^{1/4} \sqrt{\frac{R_\star}{2r}}. \tag{1.21}$$

A 65 $M_{\rm Jup}$ brown dwarf has a temperature of 1100 Kelvin even at the age of the universe (Saumon & Marley 2008). Such a brown dwarf around an M dwarf would be expected to have an albedo of 0.07 (Marley et al. 1999). For this brown dwarf to have an equilibrium temperature of 1100 Kelvin orbiting a 3000 Kelvin M dwarf, it would need to orbit at only 3.7 stellar radii, or approximately 0.01 Astronomical Units (AU), corresponding to an orbital period of approximately one day. Therefore, even M dwarf-brown dwarf binaries with few day periods can provide useful comparisons to the field brown dwarf population. Of course, this brief calculation ignores the possible effects of interactions between the magnetic fields of the two objects. These could play a significant role, as observations of aurorae on brown

dwarfs suggest they can have magnetic fields exceeding 2000 Gauss (Hallinan et al. 2015).

1.7 Goals of this Thesis

M dwarfs provide many opportunities to better understand both their companions and the stars themselves. When the companion is a planet, we can better understand the occurrence and distribution of planets around M dwarfs and focus our attention on planetary atmospheres in low-irradiation environments. In some cases, these can help us better understand the stars themselves. The same is true for brown dwarfs, with the added bonus of collecting additional, badly-needed measurements of the mass and radius relation of brown dwarfs in order to test evolutionary models. When the companion is another M dwarf and the system is young, we can study stellar models in a regime where they are untested, comparing the observed stellar masses to those predicted by theoretical evolutionary models. This thesis aims to probe each of these classes of companions.

In Chapter 2, I develop a new method to measure stellar and planetary parameters without any reliance on stellar models by combining RV and TTV observations of planetary systems. This method could be useful for systems of multiple transiting planets around M dwarfs, where stellar models have relatively large uncertainties in their predictions of stellar masses but multiple-planet systems are common. This work was originally published in Volume 762 of The Astrophysical Journal as Montet & Johnson (2013): "Model-independent Stellar and Planetary Masses from Multi-transiting Exoplanetary Systems" and has DOI 10.1088/0004-637X/762/2/112.

In Chapter 3, I study M dwarfs with long-term RV accelerations. By targeting these systems in a direct imaging campaign, I am able to measure the occurrence rate of giant planets around M dwarfs over the range 0-20 AU, finding that $6.5\% \pm 3.0\%$ of M dwarfs host such a giant planet, with a strong dependence on stellar metallicity. This work was originally published in Volume 781 of The Astrophysical Journal as Montet et al. (2014): "The TRENDS High-contrast Imaging Survey. IV. The Occurrence Rate of Giant Planets around M Dwarfs," and has DOI 10.1088/0004-637X/781/1/28.

In Chapter 4, I focus on LHS 6343 C, a brown dwarf transiting one member of a widely-separated M+M binary. I analyze Keck/HIRES RV data and *Kepler* photometry along with Palomar/TripleSpec spectroscopy of the host star in order to

measure the brown dwarf's mass and radius to 2% precision, making it the most precisely measured brown dwarf radius to date. This work was originally published in Volume 800 of The Astrophysical Journal as Montet et al. (2015a): "Characterizing the Cool KOIs. VII. Refined Physical Properties of the Transiting Brown Dwarf LHS 6343 C," and has DOI 10.1088/0004-637X/800/2/134.

In Chapter 5, I continue the focus on LHS 6343 C, analyzing data from the *Spitzer* Space Telescope to detect and characterize secondary eclipses of the brown dwarf behind its host star. These observations make LHS 6343 C the only non-inflated brown dwarf with a known mass and radius, to have its atmospheric properties directly measured. This work was originally published in Volume 822 of The Astrophysical Journal Letters as Montet et al. (2016): "Benchmark Transiting Brown Dwarf LHS 6343 C: Spitzer Secondary Eclipse Observations Yield Brightness Temperature and Mid-T Spectral Class," and has DOI 10.3847/2041-8205/822/1/L6.

In Chapter 6, I focus on the young M dwarf binary GJ 3305 AB, a young M+M binary in the β Pictoris young moving group. The binary is in orbit around 51 Eridani, a star with a precisely measured parallax and a directly imaged planetary-mass companion. I combine archival astrometric and RV observations with my own recent observations of the system to measure the mass of each component in the system to compare against the newest theoretical models of young M dwarfs. I find that the models reproduce the observed parameters for GJ 3305 A well but underpredict the mass (or overpredict the luminosity) of GJ 3305 B at the age of β Pictoris. This work was originally published in Volume 813 of The Astrophysical Journal Letters as Montet et al. (2015b): "Dynamical Masses of Young M Dwarfs: Masses and Orbital Parameters of GJ 3305 AB, the Wide Binary Companion to the Imaged Exoplanet Host 51 Eri," and has DOI 10.1088/2041-8205/813/1/L11.

In Chapter 7, I analyze data from the *K2* mission. I statistically validate 17 planets from Campaign 1 of the mission, creating the first catalog of confirmed transiting planets from *K2*. One of these planets orbiting an M dwarf is a 2.23 ± 0.25 $R_\oplus$ planet that receives a level of insolation from its host star consistent with what the Earth receives from the Sun. Its equilibrium temperature is 272 ± 15 K, making it a useful comparison against similar size planets around M dwarfs in much shorter orbits, like GJ 1214 b (Charbonneau et al. 2009). This work was originally published in Volume 809 of The Astrophysical Journal as Montet et al. (2015c): "Stellar and Planetary Properties of K2 Campaign 1 Candidates and Validation of 17 Planets, Including a Planet Receiving Earth-like Insolation," and has DOI 10.1088/0004-

637X/809/1/25.

In Chapter 8, I consider the future *WFIRST* mission, designed to target planets via the microlensing technique, as a transit search mission. I show this mission will be able to detect as many as 30,000 transiting planets towards the galactic bulge and will enable a direct test of variations in planet occurrence as a result of different conditions across the galaxy. I also find that the majority of sub-Neptune planets discovered by the mission will orbit M dwarfs. A version of this chapter will be submitted to The Astrophysical Journal in the future.

In Chapter 9, I summarize my results and describe potential future work to improve our understanding of low-mass stars and their companions.

Chapter 2

MODEL-INDEPENDENT STELLAR AND PLANETARY MASSES FROM MULTI-TRANSITING EXOPLANETARY SYSTEMS

In this chapter I develop a method to measure the masses of planets and their host stars without any reliance on stellar models by combining information from RVs and TTVs. This chapter was originally published as "Model-independent Stellar and Planetary Masses from Multi-transiting Exoplanetary Systems," ApJ, 762, 112 (2013) by BTM and John Johnson. This work was inspired by the July, 2012 Sagan Workshop on "Working with Exoplanet Light Curves" held on Caltech's campus. There have been considerable advances in stellar models and empirical relations to characterize low-mass stars over the past five years. Still, the large number of TTV systems that will be discovered by current and future transit missions combined with advances in precision RV spectroscopy leave this method as a viable possibility in order to characterize stars that are not well-explained by stellar models.

2.1 Introduction

With modern radial velocity techniques and the phenomenal success of space-based transit surveys, exoplanetary science has moved from a "stamp-collecting" era of finding individual systems to an era where hundreds of planetary systems are discovered simultaneously (Borucki et al. 2011a). Despite these successes, accurate characterization of planets is still challenging. In general, uncertainties in the radii and masses of planets are dominated by uncertainties in the radii and masses of their host stars (e.g. Muirhead et al. 2012a). Difficulties in characterizing the physical properties of planets are particularly acute for systems discovered by the *Kepler* space telescope. For many systems, the ratio between the radius of the planet and the radius of its host star is known to within 1 part in 1000 (Batalha et al. 2013). Yet the stellar radii are often not known even to within ten percent, meaning much of the precision of *Kepler* is lost when estimating planetary properties (Johnson et al. 2012b; Lissauer et al. 2012).

In general, measuring the masses of exoplanet host stars is a model-dependent procedure. For nearby stars with trigonometric parallaxes, one compares the luminosity, effective temperature, and metallicity of a star to stellar evolution model grids

(Valenti & Fischer 2005; Johnson et al. 2013). For stars without measured parallaxes, the stellar density can be measured from the transit light curve and used in place of the luminosity. However, this relies on either the assumption that the planet's orbit is circular—a poor assumption for periods larger than 10 days—or an RV orbital solution (Sozzetti et al. 2007; Dawson & Johnson 2012). The atmospheres and interior structures of stars are also poorly understood for stars that differ substantially from the Sun, complicating their analyses further. Thus, model-independent methods of measuring stellar masses are extremely valuable.

Agol et al. (2005) suggest that in a system with transiting planets, a precise measurement of the transit duration, which depends on stellar density, coupled with radial velocity information and precise measurements of the scatter in transit times can provide a unique measurement of the stellar mass. Unfortunately, this strategy requires precise knowledge of the inclination of the system, which from a transit light curve is degenerate with limb-darkening coefficients (Jha et al. 2000), especially for low signal-to-noise transit detections.

The method described by Agol et al. (2005) also breaks down for resonant systems, as it assumes the relative positions of the planets change from transit to transit. Moreover, outside of resonance, transit timing effects are small for all but the largest planets, so this method is suboptimal for studying rocky planets. This strategy is successful when the perturbing object is massive, as is the case in circumbinary planets (Doyle et al. 2011; Welsh et al. 2012) but is less promising for studying solar-type systems. It has also been suggested that in a system containing a transiting planet and an exomoon detected through transit timing and duration variations, the stellar mass and radius can be determined directly through dynamical effects (Kipping 2010a). While this technique holds future promise, exomoons to test this procedure have not yet been detected.

Recently, transit timing variations caused by mutual gravitational interactions of bodies in multiple-planet systems have been detected (Holman et al. 2010; Ford et al. 2012a). These deviations from a linear transit ephemeris allow for an estimate of the ratio of the mass of the perturbing planet to the mass of its star. In cases where multiple planets transit, the ratio of the masses of each planet to the mass of the host star can be estimated (Fabrycky et al. 2012; Steffen et al. 2012a).

In this paper, we propose a method to directly measure stellar and planetary masses for multi-transiting systems by combining an analysis of the transit timing signal caused by planet-planet interactions with Doppler radial velocity measurements.

Unlike the technique developed by Agol et al. (2005), our method requires the observed transiting planets to lie near a mean-motion resonance, where transit timing effects are strongest. In §2, we explain how transit timing variations can be combined with radial velocity information to estimate stellar and planetary masses. In §3, we apply our process to the well-studied Kepler-18 planetary system, and compare the result to both numerical integrations of the system and published stellar evolution models. We find the scheme to be viable, but at present there is a lack of radial velocity data to provide meaningful constraints on stellar parameters. In §4, we discuss uncertainties and limitations to our method, as well as its applications to systems discovered by *Kepler* and its eventual successors.

2.2 Unique Masses and Errors

Mass Determination from TTVs

Consider a system of two coplanar planets orbiting near (but not exactly at) a first-order mean motion resonance. The planets have periods P and P' (here and throughout, the unprimed quantity refers to the inner planet and the primed quantity to the outer planet) and orbit their star such that the inner planet completes approximately j orbits in the time the outer planet completes $j - 1$. A nearly edge-on observer will detect both planets transiting their host star. Because of the near-commensurability of their periods, the inner planet will pass its companion at nearly the same location each orbit, driving small gravitational interactions which add coherently, inducing a small forced eccentricity on each object. The two planets will therefore not transit their star in an exactly periodic fashion. Instead, a small, sinusoidal departure from periodicity, termed a transit timing variation (TTV), will be observed (e.g. Nesvorný et al. 2012). TTVs have been used to detect the presence of nontransiting planets (Ballard et al. 2011; Dawson et al. 2012) and to fully characterize systems when multiple planets transit (Holman et al. 2010; Lissauer et al. 2011a). The period of the TTV signal is related to the periods of the planets such that

$$P_{TTV} = \frac{1}{|j/P' - (j-1)/P|}. \tag{2.1}$$

In most cases, the superb photometry provided by the *Kepler* mission allows this quantity to be precisely estimated.

An analytic form for the amplitude of the TTV signal is derived by Lithwick et al. (2012, hereafter L12). The amplitude of the signal depends strongly on the free eccentricity of the system. Here, free eccentricity refers to the component of the eccentricity caused by the initial dynamical conditions of the system, not

the component driven by resonant interactions. Without observing a secondary transit, for small planets the free eccentricity is difficult to constrain precisely via photometry. However, many TTV signals have been detected in systems in which the planets have orbital periods of days to weeks.

In this case, the estimated ages of the planets are larger than the expected tidal circularization timescale at their present locations, so their orbits can be expected to have negligible free eccentricity. This can be verified by analyzing the phase of the TTV signal. If the zeropoints of the TTV signal occur when the longitude of conjunction is parallel to the line of sight, L12 suggest the free eccentricity can be neglected. In this case, the amplitudes of the TTV signals, V and V', are

$$V = \frac{m'}{M}\left|\frac{f}{\Delta}\right|\frac{P}{\pi j^{2/3}(j-1)^{1/3}} \tag{2.2}$$

$$V' = \frac{m}{M}\left|\frac{g}{\Delta}\right|\frac{P'}{\pi j}, \tag{2.3}$$

where m and M are the planet and stellar mass, Δ is the fractional distance from commensurability, typically of order 0.01, and f and g the appropriate coefficient of the disturbing function, which characterizes the interactions between the planets. These sums of Laplace coefficients can be calculated by using the information found in Appendix B of Murray & Dermott (2000). Additionally, the values of f and g for common resonances have been conveniently listed in L12. To first order, these coefficients are of order unity and depend only weakly on Δ. For systems with TTVs, Equations 2.2 and 2.3 enable a unique determination of the planet-star mass ratio, but normally one must rely on stellar models to further constrain stellar and planetary properties. However, if radial velocity measurements are available, the amplitude of the Doppler signal can be used in conjunction with the TTV information to estimate the masses of the planets and the star.

Including Radial Velocities

The semiamplitude of a radial velocity Doppler signal is

$$K = \left(\frac{2\pi G}{P}\right)^{1/3}\frac{m}{(M+m)^{2/3}}\frac{\sin i}{\sqrt{1-e^2}}, \tag{2.4}$$

with i and e the inclination and eccentricity, respectively (Paddock 1913). Despite the lack of free eccentricity, we may expect a small forced eccentricity as a result of 3-body interactions. The magnitude of this forced eccentricity is $\lesssim 0.05$, so neglecting it will induce an error of $\lesssim 0.1\%$ in our semiamplitude calculation. An

error of the same magnitude but in the opposite direction is induced by assuming $i = 90°$, since a strong constraint is provided by our requirement of a transit.

Thus, neglecting eccentricity and assuming an edge-on orbit, in the limit where $m \ll M$ the radial velocity semiamplitude can be approximated as

$$K = \left(\frac{2\pi G}{P}\right)^{1/3} \frac{m}{M^{2/3}}, \tag{2.5}$$

and the radial velocity can be modeled as

$$v(t) = -K \sin\left(\frac{2\pi(t - t_c)}{P}\right), \tag{2.6}$$

with t_c the time of transit center. Again, a degeneracy exists between the planet and stellar mass, so stellar models must be invoked. However, the degeneracy is different from the one recovered from transit timing variations, so these two expressions taken together can be used to solve for the planet and stellar masses individually. This allows for two independent measurements of the mass of the star and one unique measurement of the mass of each planet. The mass of the star is

$$M = \left[\frac{PP'^3 g^3}{2\pi^4 G\Delta^3 j^3}\right]\frac{K^3}{V'^3} \tag{2.7}$$

$$= \left[\frac{P'P^3 f^3}{2\pi^4 G\Delta^3 j^2(j-1)}\right]\frac{K'^3}{V^3}, \tag{2.8}$$

and the mass of each planet is

$$m = \frac{P^3}{2\pi G}\left(\frac{P'g}{\Delta\pi j}\right)^2 \frac{K^3}{V'^2} \tag{2.9}$$

$$m' = \frac{P'^3}{2\pi G}\left(\frac{Pf}{\Delta\pi j^{2/3}(j-1)^{1/3}}\right)^2 \frac{K'^3}{V^2}. \tag{2.10}$$

Simply put, for a given system containing two planets with precisely known periods, the quantities $M^{1/3}V'K^{-1}$ and $M^{1/3}VK'^{-1}$ are constants. Thus, by precisely measuring the RV semiamplitude and comparing it to the magnitude of the TTV signal, the stellar mass can be directly estimated. Because of *Kepler*'s exceptional photometry, the periods of each planet and terms derived from these (such as Δ) are well known. Thus we expect the errors in the mass estimates to be dominated by the errors in V and K, and neglect the errors caused by other terms. In this case,

$$\left(\frac{\delta M}{M}\right)^2 = \left(3\frac{\delta K}{K}\right)^2 + \left(3\frac{\delta V'}{V'}\right)^2$$
$$= \left(3\frac{\delta K'}{K'}\right)^2 + \left(3\frac{\delta V}{V}\right)^2 \quad (2.11)$$
$$\left(\frac{\delta m}{m}\right)^2 = \left(3\frac{\delta K}{K}\right)^2 + \left(2\frac{\delta V'}{V'}\right)^2 \quad (2.12)$$
$$\left(\frac{\delta m'}{m'}\right)^2 = \left(3\frac{\delta K'}{K'}\right)^2 + \left(2\frac{\delta V}{V}\right)^2, \quad (2.13)$$

where we expect the covariant terms to be zero since K and V are independently measured quantities. Here, the fractional uncertainties depend quite sensitively on the ability to measure K and V. Typically for systems of multi-transiting planets, only one of these quantities is well measured. Therefore, we would expect to only weakly constrain the stellar masses at present; with more observations the constraints will tighten considerably. In the limit where $m \gg m'$, K and V' are much larger than their counterparts and can be more easily constrained. Thus when one planet is substantially more massive than its companion, one stellar mass measurement will be considerably more precise than the other and the mass of the more massive planet will be better constrained than the less massive planet. In the case where $m \approx m'$, both measurements are expected to have similar uncertainties.

2.3 Example

Kepler-18 (KOI 137, KIC 8644288) is a planetary system containing three nearly coplanar planets with 3.5, 7.6, and 14.9 day periods orbiting a $0.97 M_\odot$ star (Cochran et al. 2011, henceforth C11). These planets (137.03, 137.01, and 137.02, or Kepler-18 b, c, and d, respectively) were confirmed by a combination of transit timing and radial velocity measurements. The star has been observed using the *Kepler* short cadence mode nearly continuously for two years, allowing for precise measurements of transit times over dozens of transits. Moreover, 18 radial velocity measurements of this $K_p = 13.5$ star, where K_p is the apparent magnitude in the *Kepler* bandpass, have been collected over the past three years by the California Planet Search team with the Keck 1 High Resolution Echelle Spectrometer (HIRES). Thus, enough data exist to attempt to determine the mass of each member of this system dynamically.

We first fit a limb-darkened light curve to a series of phase-folded transits to estimate the observable transit parameters, such as the impact parameter and limb-darkening coefficients, following the OCCULTQUAD routine developed by Mandel & Agol (2002). Because of the high signal to noise ratio of these observations and

the one-minute integration times, transit parameters can be easily measured from individual transits: we find no significant difference in these parameters or their uncertainties when fitting one individual transit instead of fitting a phase-folded transit.

Once the shape of the light curve is modeled, we fit a curve of this shape to each individual transit, allowing only the time of transit center to vary. Each individual transit light curve consists of over 200 in-transit data points, allowing for measurements of the transit center time to sub-minute precision. We remove from our dataset transits that occur simultaneously with the transit of another planet. As expected, the transits follow a sinusoidal deviation from a linear ephemeris; these deviations, shown in Table 2.4, appear to be anti-correlated between the two planets.

For our method to provide meaningful mass estimates, the primordial (free) eccentricity of the system must be damped on a timescale shorter than the age of the system. As explained in L12, if the zeropoints of the transit timing variations occur at the times at which the longitude of conjunction of the planets is equal to 0 or 180 degrees, then the system is likely to have negligible free eccentricity. We check the phase of these transit timing variations by fitting each TTV curve independently to a sinusoid. We determine parameters of this sinusoid and their uncertainties by minimizing the χ^2 statistic through a Levenberg-Marquardt algorithm. Additionally, we allow for a vertical offset to the sine function in the fit (indicative of a miscalculated time of transit center t_c), and also a linear trend (indicative of a miscalculated orbital period). The results of this minimization can be found in Table 2.1. Both planets are consistent with having zero free eccentricity and anticorrelated TTV signals. From these parameters, we measure a fractional distance from commensurability $\Delta = -2.776 \times 10^{-2}$ and find the coefficients of the disturbing function to be $f = -1.251$ and $g = 0.5308$. The amplitude of the TTV signals for Kepler-18 c and d can be measured to within 3.3 and 6.8 percent, respectively.

Planet	Phase (deg)	Amplitude (min)	Period (day)	T_c (BJD - 2454900.0)	TTV Period (day)
18-c	184.5 ± 4.1	5.54 ± 0.18	7.6415716(5)	68.4071(2)	265.1 ± 2.5
18-d	3.2 ± 8.8	4.46 ± 0.30	14.858941(1)	61.1531(1)	265.9 ± 5.3

Table 2.1: TTV fitting results for Kepler-18

These results can then be combined with radial velocity measurements in order to uniquely constrain the stellar and planetary masses. C11 used 14 radial velocity measurements to confirm this system; we used these data plus four additional

observations collected between 1 July 2012 and 1 August 2012, all of which are provided in Table 2.2.

BJD-2440000	RV ($m\,s^{-1}$)	σ $m\,s^{-1}$
15076.009	7.750	2.539
15076.927	6.950	2.487
15081.024	8.617	4.214
15082.007	-1.007	2.381
15084.984	-7.320	2.977
15318.066	3.388	2.625
15322.029	-10.093	2.303
15373.004	12.189	2.150
15403.019	24.983	2.915
15405.909	-11.692	2.350
15406.881	0.340	2.195
15413.011	-10.788	2.498
15432.970	0.205	2.233
15436.782	-6.675	2.256
16109.905	-14.919	2.261
16111.845	4.123	2.642
16115.973	-0.326	2.434
16140.839	-8.153	2.730

Table 2.2: Keck/HIRES relative RV measurements of Kepler-18

The large uncertainties in each individual observation, coupled with the small number of observations relative to the number of observed transits, suggest our mass uncertainties will be dominated by uncertainties in the radial velocity semiamplitude. In fact, many different solutions fit the RV data equally well. As an example, C11 fit a larger RV semiamplitude for planet d than c, despite the fact that they find planet c to be both more massive and nearer the star than planet d. The analysis is complicated by the existence of the much smaller planet b, orbiting inside the other two. In this case, we invoke one additional piece of information. Equations 2.2 and 2.3 can be combined to solve for the mass ratio of the resonant planets,

$$\frac{m'}{m} = \frac{P}{P'}\frac{f}{g}\frac{V'}{V}\left(\frac{j}{j-1}\right)^{1/3}, \tag{2.14}$$

which in this case implies $m'/m = 1.22 \pm 0.09$, where m' refers to planet c and m to planet d. This can be applied as an additional constraint in the radial velocity fit. In the case where $\sigma_{RV} \ll \sigma_{TTV}$, an equivalent mass ratio constraint, derived from the radial velocity semiamplitude ratio, can be applied to the TTV fit.

With this additional constraint, we model the RVs as the sum of three sinusoids of the form of Equation 2.6, with three free parameters: the semiamplitude of one of the resonant planets (c or d; here, we fit c), the semiamplitude of the innermost planet b, and an offset term, γ. We find the best fitting parameters to be $K_c = 6.89 \pm 1.40$ m/s, $K_b = 4.18 \pm 2.14$ m/s, and $\gamma = 1.30 \pm 1.45$ m/s. From the mass ratio above, this implies a semiamplitude for planet d of $K_d = 4.52 \pm 0.97$ m/s. We now have enough information to estimate the stellar and planetary masses; these results are shown in Table 2.3.

Object	C11	L12	Analytic Result[1]	Dynamical Estimate[2]
Star ($M_\odot$)	0.972 ± 0.042	Assumed C11	0.83 ± 0.51	$0.92^{+0.61}_{-0.40}$
Planet c ($M_\oplus$)	17.3 ± 1.8	20.2 ± 1.9	18.6 ± 11.6	$14.8^{+9.4}_{-6.0}$
Planet d ($M_\oplus$)	16.4 ± 1.4	17.4 ± 1.2	15.4 ± 9.5	$15.4^{+11.0}_{-7.0}$

Table 2.3: Mass estimates for the Kepler-18 system.
(1) Result derived by applying Equations 11-13.
(2) Result determined from numerical integrations.

When both the RV and TTV amplitudes are measured without invoking the extra constraint of Equation 2.14, two independent measurements of the stellar mass can be calculated, one through K and V', and one through K' and V. However, since our value for K' is found by assuming a value for K, we only calculate one independent measure of the stellar mass. We find a stellar mass of $0.83 \pm 0.51 M_\odot$, consistent with that found by C11. We find the masses of planets c and d to be 18.6 ± 11.6 and $15.4 \pm 9.5 M_\oplus$, respectively.

It is somewhat disappointing that the uncertainties in the stellar mass are so large in this example, but this should be considered a shortcoming in the available data, not in the potential of our technique. Because most Kepler Objects of Interest (KOIs) are considerably fainter than typical stars probed by radial velocity surveys, follow-up radial velocity measurements are often carried out only to a level necessary to confirm the planetary nature of a transiting system. Thus for most systems that exhibit transit timing variations, radial velocity measurements alone are rarely precise to within even 20%. Better constraints on K are regularly achieved for stars targeted in radial velocity surveys, and with more follow-up observations these mass estimates will be greatly improved. This is discussed more fully in §2.4.

We can confirm the validity of our method by comparing our analytic result to results obtained through numerical integrations of this system. To accomplish this task, we make use of the Systemic Console developed by Meschiari et al. (2009).

This program is designed to simultaneously fit Doppler and transit timing measurements. The Console contains several built-in integrators, including an eighth-order Runge-Kutta scheme employed in this work. The Console is not designed to enable the user to solve for the stellar mass as a free parameter. We circumvent this problem by first assuming a stellar mass. We fix the period and mean anomaly at BJD = 2455128.0 so that they are consistent with values found in Table 7 of C11; we then allow the planet masses, inclinations, and eccentricities to vary and minimize the χ^2 of the system. Once χ^2 is calculated, we vary the stellar mass slightly and repeat this procedure. With this technique, we can map the likelihood space in both M and m. As shown in Table 2.3, both the best fitting parameters and their uncertainties are consistent with the analytic result, suggesting that our method is viable and that dynamical techniques can be used in conjunction with our analytic result to further constrain the stellar and planetary parameters.

In all cases, our uncertainties are dominated by our 20% errors in the radial velocity semiamplitudes. The uncertainty in the radial velocity semiamplitude will decrease considerably with more radial velocity observations. We prove this claim by simulating observations placed randomly between the months of June and October, when the *Kepler* field is visible at night. We first find the true radial velocity of the system at that time, assuming K_c = 7.0 m/s. An statistical uncertainty σ is randomly drawn from the observed errors in previous HIRES measurements, and a Gaussian random number is drawn from a distribution $\mathcal{N}(0,\sigma)$. The radial velocity measurement is shifted by an amount equal to this random number, and the statistical uncertainty is recorded as σ. Finally, to simulate the effects of radial velocity "jitter" caused by stellar pulsations, a random number is drawn from $\mathcal{N}(0,3$ m/s); this value is also added to the radial velocity measurement. The observations are fitted to a combination of sinusoids as described above, and the stellar and planetary masses are estimated. The fractional error in the semiamplitudes for the largest planet as a function of the number of observations is shown in Figure 2.1 (solid line).

We find that, with 30 more radial velocity observations, the uncertainty in our calculation drops by nearly a factor of two, from the current 61 percent to 33 percent. To provide substantially better than 33 percent uncertainties without obtaining 50 radial velocity measurements, we can target a less massive star. As stated in §2.1, this method will be optimal for stars for which evolutionary models are less able to constrain stellar parameters precisely, such as F-type stars, subgiants,

and M-dwarfs. Since M-dwarfs are less massive than their G-type counterparts, a given mass planet around an M-dwarf produces a comparatively larger RV signal. Since the mass uncertainties will generally be dominated by the Doppler uncertainty, focusing on low-mass stars will enhance the observed signal, allowing for more meaningful mass constraints to be set. As proof, we again simulate observations of orbiting planets, but with larger values for K, corresponding to a less massive star or more massive planets. By sampling at the same times and assuming the same statistical errors and jitter levels, the fractional error in K decreases significantly for a fixed number of observations. These results are also shown in Figure 2.1 (dashed lines). For example, a planet identical to Kepler-18 c orbiting a star of mass $M = 0.33 M_{\odot}$ would produce a semiamplitude $K = 15$ m/s; with only 20 observations the RV semiamplitude could be constrained to within 8 percent and the stellar mass to within 30 percent. It is worth noting that these observations are all simulated assuming similar levels of statistical noise as the Kepler-18 observations. This is a reasonable approximation for the stars hosting Kepler Objects of Interest, but these stars are considerably fainter than the average Doppler planet search target. If transit timing variations are detected around a considerably brighter star, as one would expect from next-generation space-based planet finding missions, radial velocity observations could be carried out to considerably higher precision, decreasing the number of observations required to precisely measure the stellar radial velocity semiamplitude.

2.4 Summary and Discussion

We present a method of measuring stellar and planetary masses dynamically by combining TTVs measured from transit light curves and follow-up radial velocity measurements. Our method can be used as an alternative to relying on stellar evolutionary models, which can be poorly constrained for non-solar type stars like M-dwarfs, subgiants, and F stars. By analyzing the Kepler-18 system and confirming our expressions with dynamical simulations of this system, we show the potential of our method.

While we show our method to be viable, especially for low-mass stars, using our method requires a somewhat specific set of circumstances. The system must contain two planets with masses large enough to force a detectable Doppler signal and observable transit timing variations on circular orbits near a first-order commensurability. *Kepler* data suggests planets near resonance are common: more than 12 percent of planet systems show evidence for detectable transit timing variations

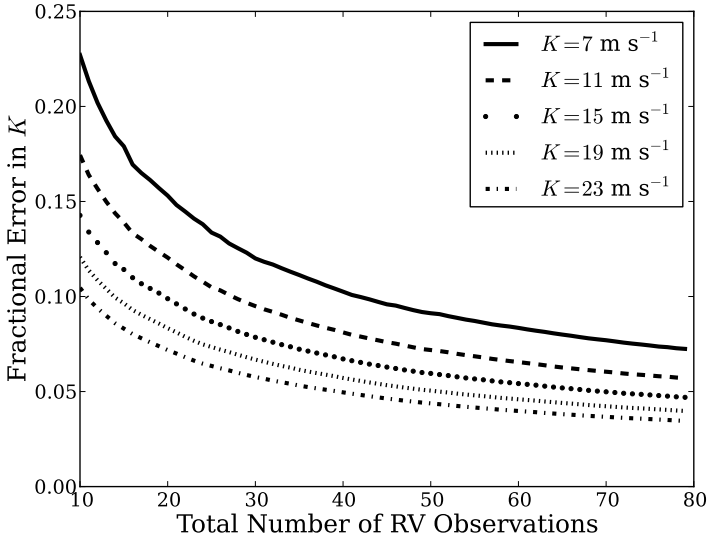

Figure 2.1: Derived fractional errors in the Doppler semiamplitude measurement as a function of number of radial velocity observations taken, for various values of K, the Doppler semiamplitude. For all observations, the same statistical uncertainties and RV jitter levels are assumed. The jitter level is 3 m/s, a reasonable estimate for all but the youngest dwarf stars. From top to bottom, these curves represent semiamplitudes of $[7, 11, 15, 19, 23]$ m/s. For a system like Kepler-18, where $K \approx 7$ m/s, many more measurements would be required to constrain K to five percent (and thus the stellar mass to 15 percent). However, for a system with either larger planets or a smaller star, this level of precision could be reached with fewer observations.

(Ford et al. 2012b), and dozens of planets near resonance have been confirmed through TTVs (Steffen et al. 2013). Both the TTV and Doppler signals can be measured for super-Earth planets with periods less than 30 days; short-period systems such as these are extremely common (Howard et al. 2012). Thus, it is likely that despite the specific requirements needed to use our system, it can be applied to a considerable number of *Kepler* planetary systems.

As shown in Equations 14 and 15 of L12, the amplitude of the TTV signal is given such that

$$|V| \sim |V_{\rm damped}|\left(1 + \frac{|Z_{\rm free}|}{|\Delta|}\right), \tag{2.15}$$

with $|V_{\rm damped}|$ the amplitude of the TTV signal if the system were damped of its free eccentricity. The quantity $Z_{\rm free}$ is defined such that $Z_{\rm free} = f z_{\rm free} + g z'_{\rm free}$, where z is the complex eccentricity of the planet, $z = e \exp^{i\omega}$. Thus, our method as described will break down unless $|Z_{\rm free}| \ll |\Delta|$. This is a reasonable assumption for planets with periods under ten days. In theory, even if a non-negligible amount of free

eccentricity remains in the system, a detailed radial velocity orbital solution could be used to calculate $Z_{\rm free}$ and determine the system dynamical masses.

As a projection of the utility of this method, consider KOI 1241, a system containing two planets with periods of 10.5 and 21.4 days orbiting a giant star ($R = 3.14 R_\odot$, Steffen et al. 2013). There is evidence that this system has not dissipated all its free eccentricity, meaning it is not optimal for our study. However, with nine quarters of public *Kepler* data, we can constrain the TTV signal caused by the larger planet in this system to 8.2 percent. Moreover, with only nine radial velocity observations, we can determine the radial velocity semiamplitude of the larger planet to 5.3 percent. Thus, from our method alone, if a system existed that was nearly identical to KOI 1241 but damped of free eccentricity, by Equations 11-13, we expect we could determine the stellar mass to 29 percent and the mass of the larger planet to within 22 percent. Our method could also be applied to KOI 1241 in the future if enough radial velocity data is collected to determine the magnitude of $Z_{\rm free}$ for the system. The uncertainties in the TTV signal of KOI 1241 are larger than the uncertainty in the RV semiamplitude. The transit timing errors will decrease as more *Kepler* data are released: decreasing the TTV error to five percent without including any additional radial velocity observations will reduce the uncertainty in the stellar mass to 20 percent. Thus our method could provide significant constraints on stellar masses in regimes where stellar atmospheres are less well-understood, such as subgiants and cool stars. For these cases, our method will be able to compliment asteroseismology results as an independent measure on the mass of the star. Moreover, our method can be used to find systems where the analytic stellar mass is substantially different than the Kepler Input Catalog values, which can then be followed up with dynamical modeling, asteroseismology, or high resolution spectroscopy to better characterize the star and orbiting planets.

With present data our technique is only viable as an alternative to stellar modeling in the most exceptional cases. Transit timing variations have been detected to remarkable precision by *Kepler*, but very few KOIs have been followed up with radial velocity measurements. In the cases where RV data exists, only enough measurements were collected to confirm the planetary nature of the system, not to independently measure the planetary masses (Holman et al. 2010). Our routine will become more useful for systems in which the RV semiamplitude can be better constrained. Additionally, the constraints provided by our technique can be applied as priors for model-grid interpolations of stellar masses. Thus these model-independent mass

measurements can be used to guide and improve model-based stellar mass estimates.

Despite the faintness of the *Kepler* planet candidate host stars, there are a few stars that would be ideal candidates for applications of our method. From the collection of Kepler Objects of Interest, we searched for stars hosting at least two transiting planets each with $P < 25$ days. We required at least one planet to be larger than 2 $R_\oplus$ and the planet periods to lie within five percent of a first-order mean-motion resonance. To ensure that all targets were optimized for radial velocity follow-up, we eliminated all targets fainter than $m_{\rm Kp} = 13.0$. After making these cuts, we find 8 candidate systems to which this technique can be applied: KOI 85, 111, 115, 117, 244, 304, 1241, and 1930. As stated earlier in this section, KOI 1241 is not an ideal target because it has not been fully damped of its primordial eccentricity and there is not enough radial velocity information to uniquely determine the eccentricity of both planets. Of the remaining 7 systems, the CPS team has collected more than 10 radial velocity measurements only on one, KOI 244. Additional radial velocity measurements of any or all of the above systems would enable further validation of our procedure as well as additional constraints on the masses of each of the stars and their planets. Moreover, next-generation planet finding missions, such as TESS (Brown & Latham 2008) and PLATO (Catala et al. 2010) will target bright stars, making detailed radial velocity follow-up observations of systems exhibiting transit timing variations a much more practical possibility.

KOI	n	t_n (BJD-2454900)	TTV$_n$ (d)	σ_n (d)
137.01	0	198.3142	-0.0006	0.0012
137.01	1	205.9557	0.0002	0.0013
137.01	2	213.5973	0.0019	0.0018
137.01	3	221.2389	0.0017	0.0010
137.01	4	228.8804	0.0021	0.0017
137.01	5	236.5220	0.0014	0.0015
137.01	6	244.1636	0.0031	0.0011
137.01	7	251.8052	0.0030	0.0011
137.01	8	259.4467	0.0037	0.0012
137.01	9	267.0883	0.0050	0.0012
137.01	10	274.7299	0.0041	0.0012
137.01	11	282.3714	0.0037	0.0018
137.01	12	290.0130	0.0035	0.0018
137.01	13	297.6546	0.0028	0.0012
137.01	14	305.2961	0.0034	0.0011

137.01	15	312.9377	0.0026	0.0011
137.01	16	320.5793	0.0013	0.0011
137.01	17	328.2209	0.0018	0.0012
137.01	18	335.8624	0.0008	0.0015
137.01	20	351.1456	0.0001	0.0011
137.01	21	358.7871	-0.0005	0.0012
137.01	22	366.4287	-0.0027	0.0014
137.01	23	374.0703	-0.0033	0.0014
137.01	24	381.7119	-0.0024	0.0011
137.01	25	389.3534	-0.0025	0.0011
137.01	26	396.9950	-0.0033	0.0011
137.01	27	404.6366	-0.0036	0.0013
137.01	28	412.2781	-0.0046	0.0012
137.01	29	419.9197	-0.0037	0.0011
137.01	30	427.5613	-0.0038	0.0015
137.01	31	435.2028	-0.0039	0.0013
137.01	32	442.8444	-0.0019	0.0012
137.01	33	450.4860	-0.0013	0.0011
137.01	34	458.1276	-0.0017	0.0010
137.01	35	465.7691	-0.0008	0.0015
137.01	36	473.4107	0.0005	0.0013
137.01	37	481.0523	0.0016	0.0011
137.01	38	488.6938	0.0026	0.0014
137.01	39	496.3354	0.0027	0.0015
137.01	40	503.9770	0.0030	0.0014
137.01	41	511.6186	0.0038	0.0011
137.01	42	519.2601	0.0032	0.0013
137.01	43	526.9017	0.0052	0.0013
137.01	44	534.5433	0.0055	0.0013
137.01	45	542.1848	0.0034	0.0010
137.01	46	549.8264	0.0025	0.0014
137.01	47	557.4680	0.0049	0.0021
137.01	48	565.1095	0.0035	0.0011
137.01	49	572.7511	0.0030	0.0012
137.01	50	580.3927	0.0017	0.0010
137.01	51	588.0343	0.0034	0.0016
137.01	52	595.6758	0.0013	0.0011
137.01	54	610.9590	-0.0006	0.0012
137.01	55	618.6005	-0.0019	0.0012
137.01	56	626.2421	-0.0015	0.0016
137.01	57	633.8837	-0.0026	0.0012
137.01	58	641.5253	-0.0016	0.0012
137.01	61	664.4500	-0.0046	0.0014

137.01	62	672.0915	-0.0028	0.0012
137.01	63	679.7331	-0.0042	0.0012
137.01	65	695.0162	-0.0032	0.0011
137.01	66	702.6578	-0.0025	0.0013
137.01	67	710.2994	-0.0029	0.0012
137.01	68	717.9410	-0.0029	0.0011
137.01	69	725.5825	-0.0004	0.0013
137.01	71	740.8657	0.0006	0.0013
137.01	72	748.5072	0.0006	0.0014
137.01	73	756.1488	0.0014	0.0011
137.01	74	763.7904	0.0049	0.0017
137.01	75	771.4320	0.0011	0.0016
137.01	76	779.0735	0.0033	0.0012
137.01	77	786.7151	0.0021	0.0011
137.01	78	794.3567	0.0031	0.0012
137.01	79	801.9982	0.0039	0.0012
137.01	80	809.6398	0.0029	0.0014
137.01	81	817.2814	0.0038	0.0011
137.01	82	824.9229	0.0016	0.0012
137.02	0	194.8832	0.0000	0.0010
137.02	1	209.7421	-0.0012	0.0011
137.02	2	224.6011	-0.0025	0.0010
137.02	3	239.4600	-0.0037	0.0010
137.02	4	254.3189	-0.0029	0.0010
137.02	6	284.0368	-0.0032	0.0011
137.02	7	298.8958	-0.0040	0.0011
137.02	8	313.7547	-0.0013	0.0010
137.02	9	328.6136	-0.0023	0.0023
137.02	10	343.4726	-0.0005	0.0011
137.02	11	358.3315	0.0008	0.0009
137.02	12	373.1905	0.0017	0.0012
137.02	13	388.0494	0.0036	0.0010
137.02	14	402.9083	0.0029	0.0011
137.02	15	417.7673	0.0020	0.0010
137.02	16	432.6262	0.0008	0.0012
137.02	17	447.4852	0.0008	0.0011
137.02	18	462.3441	0.0008	0.0011
137.02	19	477.2030	-0.0001	0.0011
137.02	20	492.0620	0.0002	0.0010
137.02	21	506.9209	-0.0023	0.0011
137.02	22	521.7799	-0.0024	0.0010
137.02	23	536.6388	-0.0038	0.0010
137.02	24	551.4977	-0.0035	0.0010

137.02	25	566.3567	-0.0033	0.0011
137.02	26	581.2156	-0.0033	0.0010
137.02	27	596.0746	-0.0013	0.0015
137.02	29	625.7924	0.0020	0.0010
137.02	31	655.5103	0.0032	0.0014
137.02	32	670.3693	0.0015	0.0011
137.02	33	685.2282	0.0026	0.0009
137.02	34	700.0871	-0.0011	0.0011
137.02	35	714.9461	0.0008	0.0010
137.02	36	729.8050	-0.0019	0.0010
137.02	37	744.6640	-0.0012	0.0011
137.02	38	759.5229	-0.0027	0.0011
137.02	39	774.3818	-0.0030	0.0012
137.02	40	789.2408	-0.0034	0.0010
137.02	41	804.0997	-0.0052	0.0010
137.02	42	818.9587	0.0003	0.0013

Table 2.4: Transit times for *Kepler* transiting planet candidates in the KOI-137 system

Chapter 3

THE OCCURRENCE RATE OF GIANT PLANETS AROUND M DWARFS

In this chapter I develop a method to determine the occurrence rate of giant planets in wide orbits around their host stars. These planets are large enough to cause a slow drift, or trend, in the RV of their host star, but too distant from their star to observe the full orbit on a reasonable timescale. Such a trend could be caused by a planet, or a star on a much wider orbit. As stars would be easily observable with high-contrast direct imaging, the existence of a trend combined with an AO non-detection suggests the presence of a planet is likely. The definitive presence of any single planet can not be determined, but by analyzing a population of these systems their bulk occurrence can be measured. This chapter was originally published as "The TRENDS High-contrast Imaging Survey. IV. The Occurrence Rate of Giant Planets around M Dwarfs," ApJ, 781, 28 (2014) by BTM, Justin Crepp, John Johnson, Andrew Howard, and Geoff Marcy.

3.1 Introduction

Over the past twenty years, numerous planets have been detected by several different techniques, permitting the first estimates of the occurrence rate of planets orbiting stars in the solar neighborhood (e.g. Gould et al. 2010; Howard et al. 2010a; Johnson et al. 2010b; Vigan et al. 2012). As successful as these detection methods have been, each is sensitive only to a relatively narrow range of parameter space. For example, radial velocity (RV) studies are most sensitive to massive planets with orbital periods shorter than the time baseline of observations. Johnson et al. (2010b) find that $3.4^{+2.2}_{-0.9}$% of M dwarfs have a Saturn-mass or larger planet within 2.5 AU. Beyond a few AU, RV searches are incomplete as the time required for a planet to complete one orbit is longer than the typical observing baseline. Some studies have attempted to extrapolate beyond this boundary. For instance, Cumming et al. (2008) fit the observed RV planet population to a power law in planet mass and period and find that 18% ± 1% of FGK stars host a Saturn-mass or larger planet within 20 AU. Recently, targeted RV surveys of M-dwarfs have suggested the giant planet occurrence rate is significantly smaller for these diminutive stars. Bonfils et al. (2013) suggest fewer than 1% of M-dwarfs host a Saturn-mass or larger planet

with an orbital period $1 < P < 10$ days, and 2^{+3}_{-1}% host giant planets with orbital periods between 10 and 100 days.

Transit studies suffer from similar detection biases. Since a planet transits only once each orbit, several orbits must be observed to definitively confirm a planet, so characterization is limited to planets with periods shorter than a fraction of the observing baseline (Gaudi et al. 2005). Additionally, the probability of a planet transiting its host star decreases with increasing orbital period (Winn 2011), such that hundreds of thousands of stars must be monitored in order to study the planet population at $a \approx 1$ AU (Borucki & Summers 1984). Nevertheless, the success of the *Kepler* mission (Borucki et al. 2010; Koch et al. 2010) has allowed for statistical analyses of transiting planets to be undertaken. For example, Morton & Swift (2014) analyze M dwarfs included in the 2012 list of announced Kepler Objects of Interest (KOIs, Batalha et al. 2013). By correcting for false positives (detections when no transiting planet exists), false negatives (nondetections when a transiting planet is present) and geometric effects (nondetections of nontransiting planets), they estimate an occurrence rate of 1.5 planets with periods less than 90 days and radii larger than $0.5R_\oplus$ per M dwarf star. The occurrence rate found by these authors is slightly higher than previous analyses which measure rates of approximately one planet per star (Youdin 2011; Mann et al. 2012; Dressing & Charbonneau 2013; Swift et al. 2013).

Neither RV nor transit searches are yet conducive to the discovery and characterization of planets well beyond the "snow line," where water exists as ice. Instead, high contrast direct imaging techniques can be a powerful tool for detecting young planetary companions in this domain. The first direct imaging planet discoveries are securely in hand, including four companions to HR 8799 (Marois et al. 2008, 2010) and one each around β Pictoris (Lagrange et al. 2009), and Gl 504 (Kuzuhara et al. 2013)[1]. Recent studies using these techniques have calculated an occurrence rate around A stars of $8.7^{+10.1}_{-2.8}$% at 1σ confidence for planets larger than $3M_J$ and separations between 5 and 320 AU (Vigan et al. 2012). Imaging studies have been most effective around high mass stars. (Crepp & Johnson 2011; Carson et al. 2013). Nondetections around lower-mass stars have been used to place upper limits on the frequency of giant planets. For example, Nielsen & Close (2010) rule out the presence of giant planets orbiting FGKM stars beyond 65 AU with 95% confidence.

[1]Companions detected around Fomalhaut (Kalas et al. 2008; Currie et al. 2012), HD 95086 (Rameau et al. 2013), and LaCa15 (Kraus & Ireland 2012) are also good candidates to be directly imaged planets, but their true nature is somewhat ambiguous.

High contrast imaging, while powerful, only provides a measure of the relative brightness of a companion. To estimate the companion's mass, the age of the star must be known and planetary thermal evolution models must be applied to estimate the temperature (and brightness) of the companion (Chabrier et al. 2000; Baraffe et al. 2003). Moreover, direct imaging is currently only sensitive to massive planets; the HR8799 planets and β Pic b are believed to have masses $m > 5M_J$. RV and transit studies suggest such "super-Jupiters" are rare compared to Jovian-mass and smaller objects at smaller separations (Howard et al. 2010a, 2012).

The gravitational microlensing technique is also effective for finding giant planets in wide orbits and does not rely on planetary evolution models. Using this technique, planets can be detected by observing perturbations to the photometric gravitational microlensing signal when a planet and its host pass in front of a more distant star. Since $70 - 75\%$ of stars in the galaxy are M-dwarfs, most lenses have mass $M < 0.5M_\odot$. Microlensing searches thus provide a measure of planet occurrence around low mass stars. Microlensing studies are sensitive to planets near the Einstein ring, $R_E \sim 3.5\mathrm{AU}(M/M_\odot)^{1/2}$, a much wider separation than RV and transit searches Gould et al. (2010). Cassan et al. (2012) find microlensing searches are most sensitive to planets at a projected separation in the range $[s_{\rm max}^{-1}R_E, s_{\rm max}R_E]$, where $s_{\rm max} \sim (q/10^{-4.3})^{1/3}$ and q is the mass ratio between a companion and the host star. These authors find a planet occurrence rate that can be parameterized by a double power-law function, in mass ratio q and separation s, such that

$$\frac{d^2N}{d\log q d\log s} = 10^{-0.62\pm0.22}\left(\frac{q}{5\times10^{-4}}\right)^{-0.73\pm0.17}\mathrm{dex}^{-2}. \tag{3.1}$$

The normalization constant is equivalent to $0.24^{+0.16}_{-0.10}$. These results are calculated under the assumption that planets are distributed uniformly in $\log s$, as is the case for binary stars (Öpik 1924). Additionally, Sumi et al. (2010) find a power-law slope in mass such that $dN/d\log q \propto q^{-0.68\pm0.20}$ for Neptune-sized planets, but do not attempt to quantify a normalization factor.

As microlensing studies focus on distant M-dwarfs ($d > 1$ kpc) in the direction of the galactic bulge (Gaudi et al. 2002), these stars can be difficult to characterize accurately due to crowding. Stellar masses and metallicities are often estimated without being measured spectroscopically. If these host stars have different masses than assumed, it would affect the results of planet occurrence rate studies by microlensing groups as microlensing results do not account for correlations between stellar and planet properties. Additionally, as microlensing searches are most sen-

sitive near $r = R_E$, beyond approximately 10 AU the lensing signal becomes very weak, and differentiating distant planets from unbound, "free-floating" planets becomes difficult (Sumi et al. 2011).

RV and microlensing studies probe different regions around a star, and extrapolations between the two domains suggest a possible discrepancy. Cassan et al. (2012) estimate a total giant planet occurrence rate significantly lower than the Cumming et al. (2008) RV result. Derived power-law distributions in mass may also be different for planets found by each method: Cumming et al. (2008) find a distribution such that $dN/d\log m \propto m^{-0.31\pm0.20}$ from RV-detected planets, while Cassan et al. (2012) find a distribution such that $dN/d\log q \propto q^{-0.73\pm0.17}$. Since microlensing studies target M-dwarfs, which are confined to a narrow mass range, we can approximate $q = m/M$ as m. In this case, the microlensing result and RV result differ by 1.6σ. Since giant planet occurrence decreases with decreasing stellar mass and metallicity (Johnson et al. 2010a), the expected giant planet occurrence rate around M dwarfs would be smaller than that for FGK stars. Therefore, it is necessary to compare the microlensing planet population not to a population of FGK stars, but instead to a study of RV detected planets around M-dwarfs.

Historically, RV observations have been used to detect and characterize planets once they complete a full orbit, limiting studies to planets with periods shorter than the observing time baseline. In this paradigm, potentially useful information is overlooked. Wide companions are not completely undetectable: instead they can be identified by the presence of long-term RV accelerations (linear "trends") which can be used to infer the existence of a companion in a more distant orbit (Liu et al. 2002; Crepp et al. 2012b). However, a linear acceleration does not provide unique information about the mass and period of the companion: the same trend could be caused by a Jupiter-mass planet at 5 AU or a $100M_J$ M-dwarf at 25 AU. This degeneracy can be broken by adaptive optics (AO) imaging. Low-mass binary companions to nearby M-dwarfs can be easily imaged by modern AO systems (Lloyd 2002; Siegler et al. 2003). Such detections form the basis for the TRENDS High-Contrast Imaging Survey, which to date has detected four M-dwarfs and one white dwarf companion to higher mass stars(Crepp et al. 2012a, 2013a,b).

In this work, we combine RV and AO observations of nearby cool stars to estimate the frequency of giant planets in wide orbits around M-dwarfs. From a sample of 111 M-dwarfs observed with a median Doppler RV baseline of 11.8 years, we identify 4 systems with long-term RV accelerations but no known companions and

target these stars with AO imaging in an attempt to detect stellar-mass companions. We discuss these observations and our methodology in Section 3.2. Given an observed RV trend or lack thereof, we determine with high statistical confidence if a giant planet exists around each star. We analyze the effects of false positive and false negative detections of RV accelerations in our sample in Section 3.3. In Section3.4 we estimate the occurrence rate of giant planets around M-dwarfs and compare the measure to results from other techniques. We summarize and conclude in Section 3.5, and provide notes about individual targets in Section 3.6. In Section 3.7, we include a brief note about magnetic activity.

This study represents the first measurement of the planet population in the range 0–20 AU. While we rely on brown dwarf cooling models, our study does not make use of theoretical planetary evolution models, unlike other AO studies of planetary systems.

3.2 Sample and Observations

Target Selection

Since 1997, the California Planet Search (CPS) collaboration has undertaken a comprehensive Doppler search for extrasolar planets at the Keck Observatory (e.g. Howard et al. 2010b). Using Keck/HIRES (Vogt et al. 1994), the CPS program monitors over 2000 stars, most selected to be chromospherically quiet, single, and bright. Included in this sample is a collection of M-dwarfs from the Gliese and Hipparcos catalogs brighter than $V = 11.5$ and lacking known stellar companions within 2 arcseconds (Rauscher & Marcy 2006). This sample was later extended to $V = 13.5$ and currently includes 131 M-dwarfs within 16 pc of the Sun, where we define the M spectral class as targets with $B - V > 1.44$.

To develop the sample used here, we first remove from this set 16 stars with a known, nearby stellar binary companion. We define "nearby" as a separation small enough that a test particle orbit with semimajor axis $\geq$ 30 AU would be unstable, following the instability criterion of Holman & Wiegert (1999). This criterion depends on the unknown eccentricity of the binary pair, as perturbative effects are maximized at periapsis. We take $e = 0.5$ as a typical value and find the onset of instability occurs for binary stars with $a \sim 250$ AU. Planets can still form in these more compact binary systems (e.g. Gl667C; Anglada-Escudé et al. 2012a) but at such small separations protoplanetary disk formation and planet evolution would be affected significantly by the presence of stellar companions. This selection thus

allows us to study a class of planets that likely followed similar evolutionary processes. Moreover, the detection of an acceleration around these stars is ambiguous, as it could be caused by the binary star, a planetary-mass companion, or both together.

After making the above selection we are left with 111 RV targets, all of which have at least 8 radial velocity observations and a time baseline longer than 2.9 years. The median number of observations is 29 over a median time baseline of 11.8 years. The stars have spectral types from M0 to M5.5 and masses in the range $0.64M_{\odot} - 0.10M_{\odot}$. Stellar masses are estimated using the empirical relation between mass and absolute K-band magnitude, M_K, described by Delfosse et al. (2000). We take 10% as a typical uncertainty in the stellar mass, in line with previous estimates (Bean et al. 2006). K-band apparent magnitudes are measured using apparent magnitudes from the 2MASS point-source catalog (Cutri et al. 2003). The majority of our parallaxes are taken from an analysis of *Hipparcos* data (van Leeuwen 2007). Some of our stars were not observed by Hipparcos, while others have had their distances updated more recently. In these cases, we apply the distances listed in the SIMBAD astronomical database (Table 3.1). For example, for Gl 317 we use the parallax found by Anglada-Escudé et al. (2012b); their derived mass and metallicity are consistent with our estimated values. In all cases, stellar metallicities are estimated by measuring the offset between the star's position in the $\{V - K_s, M_{K_S}\}$ plane from a calibrated main sequence following the method of Neves et al. (2012). We take 0.17 dex as a typical uncertainty in the stellar metallicity, representative of the scatter between this photometric method and spectroscopic measures of stellar metallicity. Stellar parameters for these targets are listed in Table 3.1 and observational parameters are listed in Table 3.2. The distribution of RV observational parameters are shown in Figure 3.1. Spectral types are estimated by comparing the spectrum collected with HIRES to other spectra collected with this same instrument. RV observations for a representative sample of six "typical" stars are shown in Figure 3.2.

Detecting Accelerations from Radial Velocities

The detection of a long-term RV acceleration is facilitated by having many observations over a long time baseline to increase signal, but complicated by astrophysical "jitter" caused by rotational modulation of surface inhomogeneities. To determine the masses and semimajor axes to which we are sensitive to planetary companions, we inject a series of artificial companions into orbit around the stars in our sample.

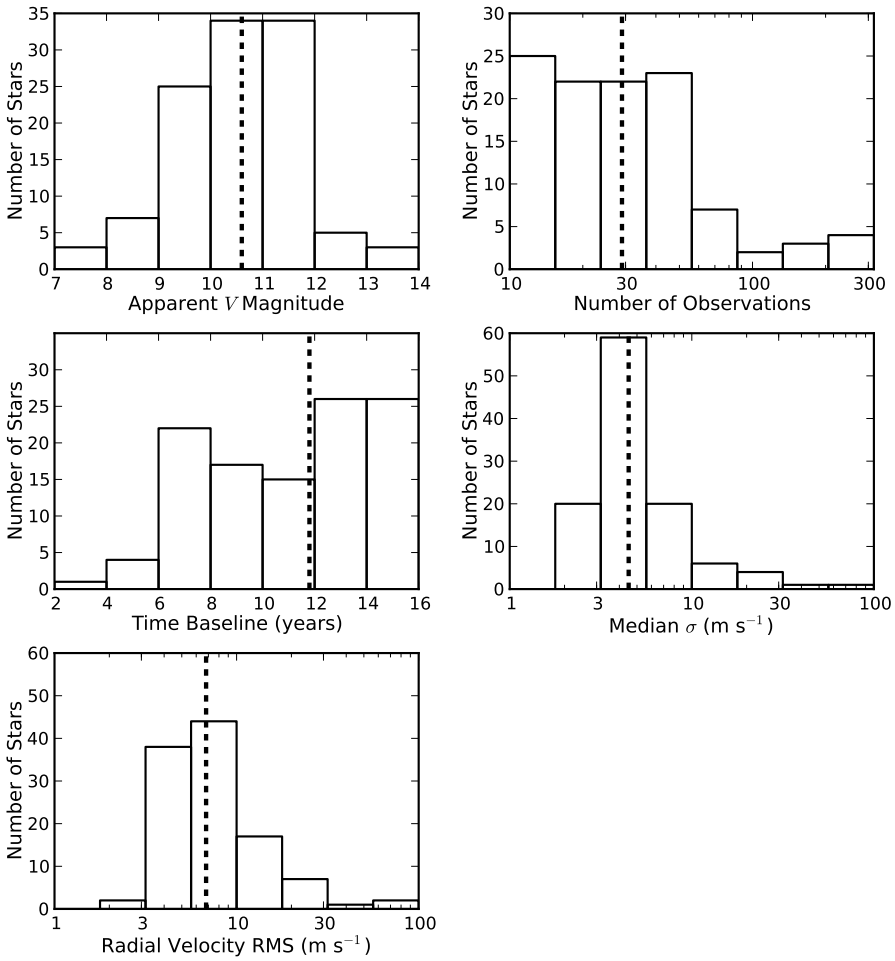

Figure 3.1: Distributions of the RV observational parameters. Dashed lines represent the median values for each parameter. The median target brightness is $V = 10.6$, and the median target has been observed 29 times over 11.8 years. The median measurement uncertainty σ, defined as the sum in quadrature of rotational jitter and statistical uncertainty (Eq. 3.2) is 4.5 m s^{-1}. Specific parameters for each individual system are shown in Table 3.1.

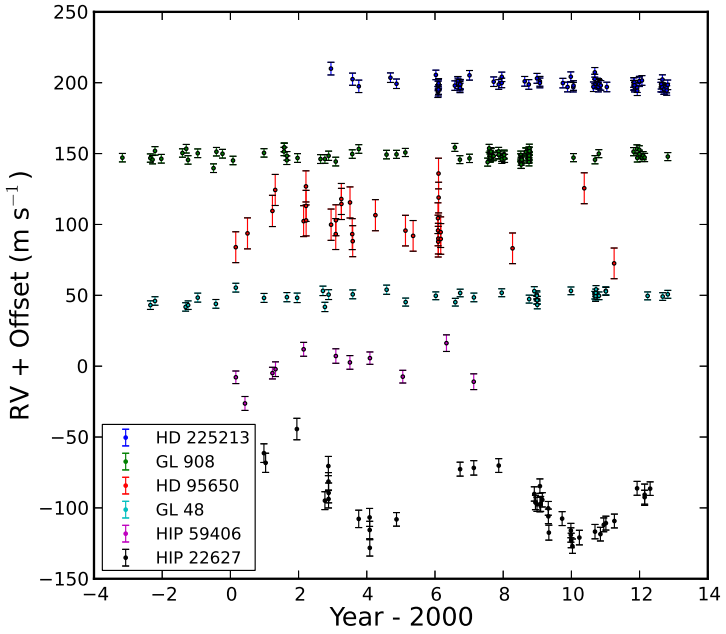

Figure 3.2: RV measurements for a representative sample of six example stars. The stars are arranged such that the brightest star is at the top of the plot. The individual stars vary considerably with respect to observing baselines, measurement uncertainty, and number of observations. Of these stars, HIP 59406 has a wide binary companion, while HIP 22627 has both a known inner planet and long-term RV acceleration.

We define a logarithmically spaced grid of companion masses and semimajor axes spanning the range $0.75M_J < m < 100M_J$ and 3AU $< a <$ 30AU, such as the one shown in Figure 3.3. At each point, we inject 500 planets and randomly assign each of the remaining orbital elements. The longitude of ascending node Ω, time of periapsis t_p, and argument of periapsis ω are drawn from a uniform distribution, while the inclination is drawn from a distribution $dn/di = \sin i$ and the eccentricity from a distribution such that dn/de follows a beta distribution with $a = 1.12$ and $b = 3.09$, which well-replicates the distribution of observed eccentricities for RV planets with orbits longer than 382 days (Kipping 2013). We then numerically integrate these orbits forward in time over our true observing baseline.

At the epochs each star was observed by CPS, we calculate the expected radial velocity signal caused by our injected planet. Each velocity is perturbed from the true expected Keplerian velocity by a normal variate with zero mean and standard

deviation σ representative of the total expected noise:

$$\sigma = \sqrt{\sigma_\gamma^2 + \sigma_{\rm jitter}^2}. \tag{3.2}$$

Here, σ_γ is the photon noise, estimated for each individual observation by randomly selecting a single measurement of the measured Poisson photon noise from a true observation of the star. To account for the effects of jitter, we follow the method of Isaacson & Fischer (2010), who develop an empirical relation between the level of stellar jitter, a star's $S_{\rm HK}$ value, and its $B - V$ color. $S_{\rm HK}$ is defined as the ratio of the flux in the Ca II line cores to flux in the surrounding continuum. We compare the S_{HK} value observed by CPS to that expected from the star's $B - V$ color, which provides an estimate of $\sigma_{\rm jitter}$. This value is added in quadrature to the photon noise to estimate a total observational uncertainty, σ. Typical observations carry a photon noise of $2 - 4$ m s^{-1} and jitter values are typically $3 - 5$ m s^{-1} for a total σ value of $3 - 6$ m s^{-1} for the majority of stars. Median σ values for each star are listed in Table 3.2.

Once all observations are accounted for, we search for evidence of our injected planetary companion, manifested as an acceleration in the RV data. Here, we define the existence of a trend using the Bayesian Information Criterion (BIC; Schwarz 1978; Bowler et al. 2010; Campo et al. 2011; Stevenson et al. 2012), which prefers simple, well-fitting models subject to

$$\mathrm{BIC} \equiv -2 \ln \mathcal{L} + k \ln N, \tag{3.3}$$

where $\mathcal{L}$ is the maximum likelihood for a model with k free parameters and N observations. The BIC thus favors models that fit the underlying data well, but penalizes increasingly complex models. For a more complex model to be preferred by the BIC, it must improve the fit by an amount greater than $k \ln N$ to overcome the penalty term.

Kass & Raftery (1995) claim a difference between BIC values provides a bounded approximation of twice the logarithm of the Bayes factor. A change in BIC value of ten or more (corresponding to a Bayes factor of approximately 0.01) suggests strong evidence for an association between two parameters. If the BIC value decreases by more than 10 when considering a model with a linear acceleration over a model with only an offset, a planet is considered to be detected. Otherwise, the system is considered a non-detection. We find that the ΔBIC value chosen here is consistent with by-eye inspection of our data in a visual search for RV accelerations. In both

cases, we allow for a linear offset in the RV data in August, 2004, corresponding to an upgrade of the HIRES CCD detector (Wright et al. 2011). Effectively, we treat the data from before and after the upgrade as coming from two distinct instruments, which serves to slightly decrease our sensitivity to small RV accelerations.

By repeating this process for many simulated planets over our mass-semimajor axis grid, we can map out the relative probability of detecting a linear trend caused by a planet as a function of companion mass and semimajor axis. As an example, Figure 3.3 shows RVs for HIP 70975 and the likelihood of detecting a planet at a given mass and period given these observations. Figure 3.4 shows the mean likelihood of detecting a planet around a given star across our sample. Throughout this work, we report the occurrence rate of planets with masses in the range $1M_J < m < 13M_J$. We can detect accelerations caused by planets smaller than $1M_J$ in certain instances, but would miss the majority of these planets. As Figure 3.4 shows, we can only detect a $0.75M_J$ planet at 6 AU 50% of the time; planets at smaller separations would exhibit significant curvature over a 12 year time baseline and could be detected through an RV survey alone. We are more efficient at detecting planets larger than $1M_J$, although we would still not expect to detect all planets in this range. We account for false negative "missed" planets in our analysis, as described in Section 3.3.

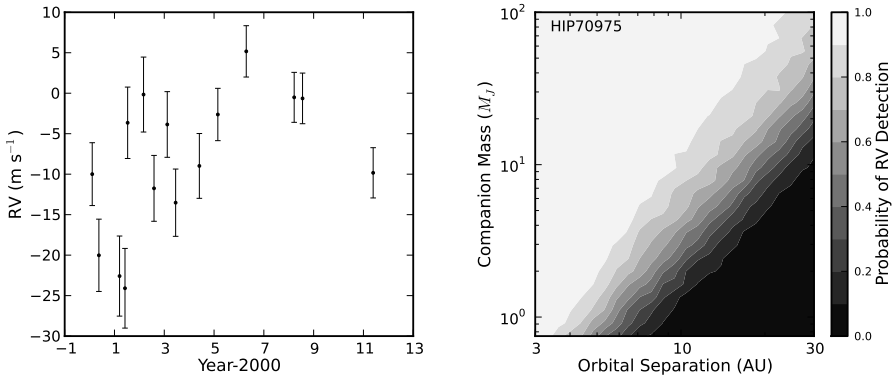

Figure 3.3: (left) RVs for HIP 70975, a typical star in our survey. This $0.32M_\odot$ M-dwarf has a total of 15 radial velocity observations over a baseline of 15.5 years, with an average RV precision (including photon noise and jitter) of 4 m/s. (right) Detectability plot showing the likelihood of an RV detection for a companion orbiting HIP 70975 as a function of companion mass and semimajor axis from its host star.

Eight of the stars in our sample host known planets with closed orbits. All of the

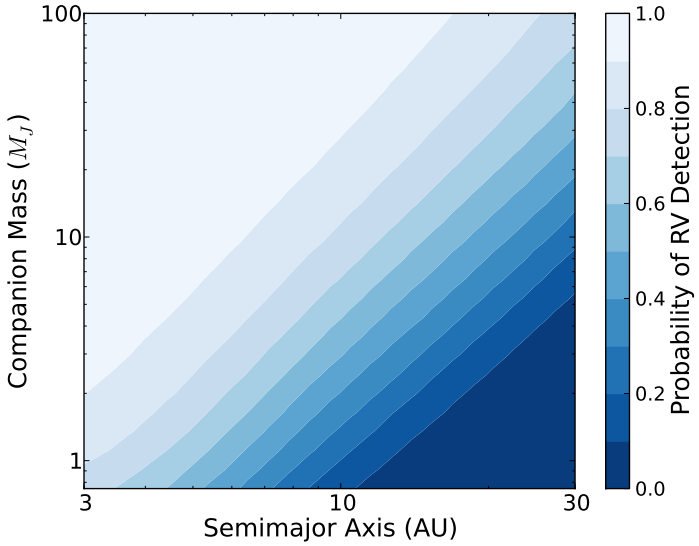

Figure 3.4: The ensemble average likelihood over all 111 stars of an RV detection for a companion to a star in our sample as a function of companion mass and orbital semimajor axis. We can detect accelerations induced by planets as small as $1 M_J$ in short orbits, but a planet distribution function is required to determine the number of $1 M_J$ planets in wide orbits and calculate the overall giant planet occurrence rate.

planets have $m \sin i < 2.5 M_J$ and are listed in Table 3.3. To identify radial velocity accelerations caused by outer planets, we include the signal from these planets by comparing a model which contains the known planet and an acceleration to a model which contains only the known planet. Two known planets in our sample, Gl 876b and Gl 317b, are larger than $1 M_J$, so in addition to searching these systems for long-term RV accelerations, we also include these known planets in our giant planet occurrence calculations.

One additional planet, Gl 649b, has a best-fitting mass $m \sin i = 0.90 \pm 0.05 M_J$; if the inclination is smaller than 64 degrees this planet has mass $m > 1 M_J$. We follow the method of Ho & Turner (2011) to determine the probability of this event. That is, we define the probability that the true mass m is greater than some value X given an observed mass, $m_O = m \sin i$ such that

$$P(m > X | m_O) = 1 - \frac{\int_{m_O}^{X} \frac{(m_O/m^2)}{\sqrt{1-(m_O/m)^2}} P(m) dm}{\int_{m_O}^{m_{\max}} \frac{(m_O/m^2)}{\sqrt{1-(m_O/m)^2}} P(m) dm}. \quad (3.4)$$

Here, $P(m)$ is the true planet mass distribution function and $m_{\max}$ is the physical upper mass limit for a planet. Since the true distribution function is strongly biased

towards small planets, the number selected here does not significantly affect our results. By simply assuming the star is aligned randomly along our line of sight so that the inclination distribution is flat in $\cos i$, the result of a flat planet mass distribution function, we expect a observed mass $m \sin i = 0.90 M_J$ to be produced by a Jupiter-mass or larger planet 56% of the time; all reasonable assumptions of an underlying mass distribution affect this value by less than 10%. We repeat this procedure for all confirmed planets in our sample with masses $m \sin i < 1 M_J$ to quantify the likelihood that other known planets are $m > 1 M_J$ planets with low inclinations. We find, in addition to Gl 849b, HIP 22627b ($m \sin i = 0.64 M_J$) has approximately a 25% probability of having a mass $m > 1 M_J$. This probability is vanishingly small for all other known planets.

Of our sample of 111 stars, 2 have confirmed planets larger than $1 M_J$, 6 systems have confirmed RV planets with masses $m \sin i < 1 M_J$ only, two exhibit RV acceleration caused by known brown dwarfs, and four show unexplained long-term RV accelerations, such that $\Delta\mathrm{BIC} > 10$ when we include an acceleration term in our fit to the RV data. In the case of Gl 849b, the long-term acceleration exhibits significant curvature, so we are able to place constraints on this object's mass and orbital semimajor axis. In all other cases, the magnitude of the observed acceleration is different from zero by 3σ. Additionally, the magnitude of the acceleration is such that over the observing baseline, the expected ΔRV induced by the putative outer planet is larger than the uncertainties of each individual data point. The distribution of these systems in the stellar mass-metallicity plane is shown in Figure 3.5.

For the four targets with an observable RV drift, we create a grid of logarithmically-spaced companion masses and semimajor axes over the range $0.75 < m/M_J < 100$ and $3\mathrm{AU} < a < 30\mathrm{AU}$. For a given grid point, we determine the best-fitting Keplerian orbit for a given eccentricity and inclination. We assume the inclination and eccentricity distributions are the same as assumed previously. The eccentricity distribution is well-characterized for solar-type stars, but may not hold for planets around lower-mass stars. We find the exact choice of eccentricity distribution does not significantly affect our results.

We determine the likelihood of the best-fitting orbit for each mass, period, eccentricity, and inclination. We then convert these likelihoods into relative probabilities, assuming our errors are uncorrelated so that $P \propto (-\exp(\chi^2/2)))$. We then marginalize over eccentricity and inclination and normalize our probabilities so that

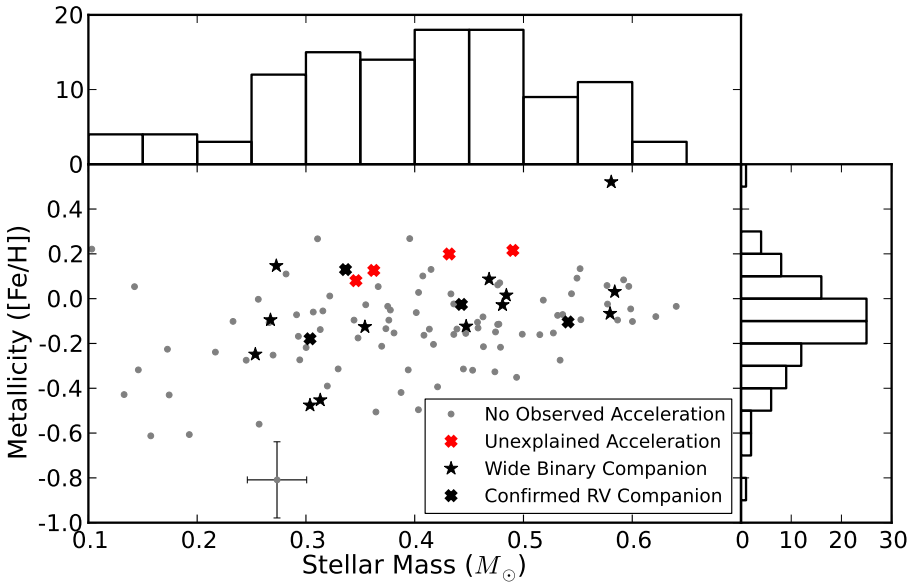

Figure 3.5: Observed M-dwarf sample in the stellar mass-metallicity plane. Systems with observed RV accelerations are shown in red while those without a detected acceleration are in black. Systems with a wide binary companion are labeled with stars, while diamonds represent systems with confirmed planets of any mass. The error bars displayed for HD 33793 are representative of the uncertainties for all stars in our sample.

$\sum_{M,a} P = 1$. In these cases, we assume the inclination is random on the sky, so that the inclination follows the distribution $f(i) = \sin i$. Assuming a different planet mass distribution function affects this result by less than 10%. The result is a contour in the mass-semimajor axis plane for the likelihood that a given object could cause the observed stellar radial velocity variation (Wright et al. 2007). An example is shown in Figure 3.6. Implicit in this analysis is the assumption the radial velocity variation is dominated by the motion of a single, massive companion rather than the constructive interference of the RV signal of two or more smaller objects. We discuss false positive probabilities in Section 3.3 and conclude the assumption that one signal dominates the observed RVs is reasonable.

The magnitude of an acceleration depends on both the semimajor axis and mass of the companion. For a planet in a circular orbit, the magnitude of the change in radial velocity, $\dot{\gamma} = dv/dt$, is given by

$$\dot{\gamma} = (6.57 \text{ m s}^{-1}\text{yr}^{-1})\left(\frac{m_p}{M_J}\right)\left(\frac{a}{5\text{AU}}\right)^{-2} \hat{v}_p \cdot \hat{r}_{los}, \tag{3.5}$$

with M_J the mass of Jupiter and a the orbital semimajor axis. $\hat{v}_p$ and $\hat{r}_{los}$ are

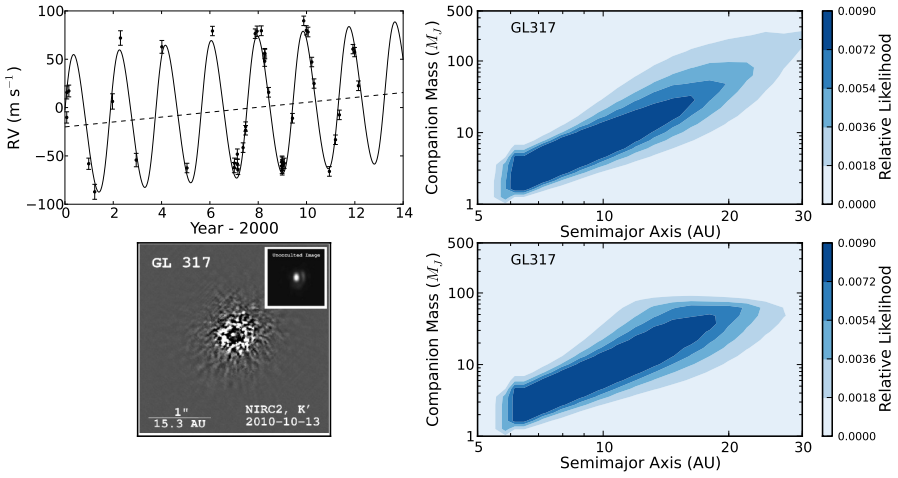

Figure 3.6: (top left) RV observations for Gl 317 over our 12.1 year baseline. The best-fitting RV acceleration is -2.51 ± 0.62 m s^{-1} yr^{-1} (dashed line); the best-fitting model which includes both the planet and the acceleration is shown as a solid line. (top right) Probability contours marginalized over eccentricity and inclination, displaying the location of a giant companion orbiting Gl 317 from RVs alone. The likelihood values are normalized such that the sum of the likelihood over our 26x25 grid of companion masses and separations sums to unity. (bottom left) AO image of Gl 317, showing no companion is visible in the AO imagery, either in the unocculted image (inset) or when a coronagraph is inserted. This eliminates the possibility of a stellar-mass companion at a projected separation smaller than 48 AU. (bottom right) Probability contours displaying the location of a giant companion to Gl 317 when the RV data is combined with AO data. We find the RV acceleration is likely induced by a substellar companion.

unit vectors along the direction of the planet's velocity vector and the line of sight, respectively. When the companion has longitude of periapsis $\varpi = 90$ or 270, the magnitude of this trend is maximized: $\hat{v}_p \cdot \hat{r}_{los} = \sin i$. To determine if our observed accelerations are caused by planets or more massive companions, we obtained AO imaging observations of each star.

Adaptive Optics Observations

The detectability diagnostics developed in Section 3.2 are based strictly on the information encoded in the RV data. Since we are looking at accelerations caused by objects in wide orbits around the primary star, we must break the degeneracy between companion mass and orbital semimajor axis for a given observed acceleration. AO imaging allows us to immediately detect the presence or nonexistence of nearly all stellar-mass companions and most brown dwarf companions to our

primary stars, so we can readily separate stellar-induced accelerations from those caused by planets.

All four targets with an observable RV acceleration were observed with NIRC2 (instrument PI: Keith Matthews) at the W.M. Keck Observatory using the AO system (Wizinowich et al. 2000) (Table 3.4). In most cases, images were obtained in the K' filter ($\lambda_c = 2.12\mu$m). We nominally execute a three-point dither pattern to facilitate removal of instrument and sky background noise. Images were processed by flat-fielding, correcting for hot pixels with interpolation, subtracting the sky background, and rotating the frames to standard north-east orientation. In three cases, we applied the angular differential imaging (ADI) point spread function subtraction technique, allowing the observed field to rotate around the target star during the observation, while instrumental artifacts remain fixed. In all cases, we use the large hexagonal pupil mask and the narrow camera. For all four systems exhibiting long-term RV accelerations, we did not image a massive companion. In the cases where our field of view is not large enough to eliminate the possibility of massive stars in very wide orbits ($> 4''$), we supplement our AO data with publicly available 2MASS images.

The luminosity ratio between our M-dwarfs and their companions depends on the mass of the companion and the age of the system. Stars observed by the CPS team are selected to avoid excessive chromospheric activity, and are thus likely older than 1 Gyr (Wright 2005). We assume all targets have fully contracted and assert an age of 5 Gyr for each system. For systems with nondetections, we estimate the flux (and thus the mass) a companion would need to have to be observed at a given projected separation in our observations. From that value, we can then determine the region of parameter space excluded by the observations (Figure 3.7). In general, AO imaging eliminates nearly all stellar companions, while ADI can also probe the brown dwarf mass regime.

For each of our targets with unexplained accelerations, a contrast curve showing the mass to which we are sensitive to companions at the 5σ level as a function of projected separation is shown in Figure 3.7. This choice provides similar results to the detection limits found by visual inspection, as tested by injecting artificial companions into AO images (Metchev & Hillenbrand 2009). We convert relative brightness to mass using the theoretical evolutionary tracks of Baraffe et al. (2003) for substellar companions and Girardi et al. (2002) for more massive companions. Interpolation between the two sets of models provides reasonable results in the in-

termediate domain near $125 M_J$. The resultant parameter space where a companion could reside to cause the observed stellar acceleration is shown in Figure 3.6.

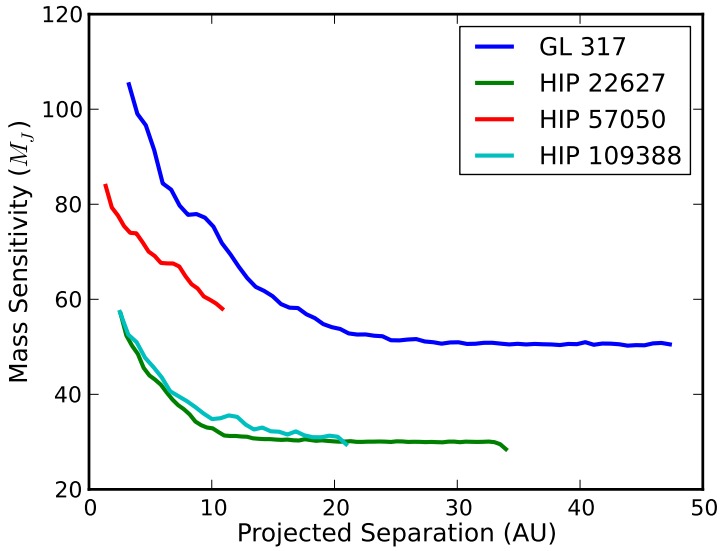

Figure 3.7: Mass sensitivity for a 5σ detection of a companion object as a function of projected angular separation for each of our four stars with long-term RV drifts. The maximum projected separation eliminated corresponds to the field of view of the AO system and thus varies for each star as a function of the distance to each star. For all stars except HIP 57050, we rule out stellar mass companions beyond 1 arcsecond through our adaptive optics imaging. When our field of view is small, we supplement our AO data with 2MASS seeing-limited images. Stellar companions at small projected separations would have RV accelerations larger than those observed in our sample.

The assumption of a 5 Gyr age for each star does not significantly affect our results. For all plausible system ages, stellar mass companions would be easily detectable by AO. Our sensitivity to stars is independent of assumed age, as luminosities of M-dwarfs are constant over the age of the universe. At no ages $>$ 1 Gyr are we sensitive to any planetary mass companions. As shown in Figure 3.8, assuming a different age for each star would only change the efficiency of detecting brown dwarfs. Since the occurrence rate of brown dwarfs is only a few percent, much smaller than the occurrence rate of planets or low-mass stars (Metchev & Hillenbrand 2009; Dieterich et al. 2012), errors induced by assuming an incorrect stellar age from missed brown dwarfs are small. "False negatives" such as these will be discussed in Section 3.3.

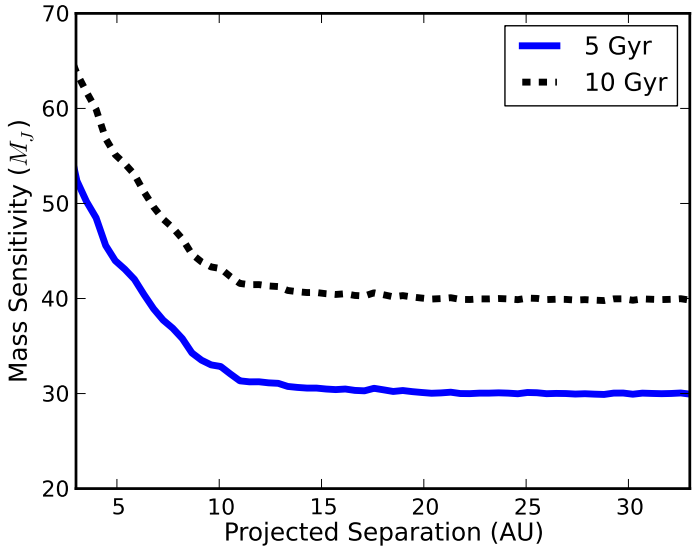

Figure 3.8: Adaptive optics mass exclusion plot for the star HIP 22627 showing the relative insensitivity of our results to the assumed age of M-star planet hosts. Adaptive optics observations rule out essentially all stellar mass companions. Sensitivity to substellar objects is a function of age, but brown dwarfs are scarce at close separations (Marcy & Butler 2000), and wide separations (Metchev & Hillenbrand 2009). Thus, our estimate of the planet frequency around M-stars is only weakly dependent on our assumed age of the host stars.

3.3 Measuring the Giant Planet Occurrence Rate

We estimate the occurrence rate of giant planets orbiting M-dwarfs using statistical inference. The fraction of stars which host giant planets, given some number of observed accelerations $N_{\rm trends}$ and some number of nondetections $N_{\rm ND}$ from a sample of targets, is given such that

$$f_{pl} = \frac{N_{\rm trends} P(\text{planet}|\text{trend}) + N_{\rm ND} P(\text{planet}|\text{ND})}{N_{\rm targets}}. \quad (3.6)$$

To calculate the posterior probability that a given star hosts a gas giant planet, we must estimate the *a priori* likelihood that a planet exists given the presence of an RV acceleration (a true positive), the likelihood a planet would not be detected in an RV survey (a false negative) and the likelihood that an observed acceleration is caused by some effect other than the movement of a planet (a false positive).

False Negatives

There are multiple ways for a giant planet to be missed in our survey. For each planet in a wide orbit, we observe only a fraction of a revolution. A planet near its maximal sky-projected separation from its host star has acceleration primarily

in the tangential, not radial, direction. In cases such as this the change in radial velocity over our observing baseline may not be noticeable. Thus we may expect to have a lower RV detection efficiency for planets near their maximal sky-projected separation.

Similarly, we may expect to have a lower imaging detection efficiency for stars near their minimal sky-projected separation, when the RV acceleration is the largest. However, in these cases we would still expect to detect the binary companion. If the companion is located directly along the line of sight to the star, then it will also appear in the 0.85 arcsecond wide spectrograph slit used with HIRES. Therefore, we would expect such systems to appear as SB2s. We explore this fully, and show that we would detect all such systems, in Section 3.4.

To determine the likelihood that such a planet would be missed by our search, we use our detectability matrices developed in Section 3.2. We assume the distribution of planets follows a double power-law, such that

$$\frac{d^2N}{d\log m d\log a} \propto m^{\alpha} a^{\beta}, \tag{3.7}$$

similar to that assumed by Cumming et al. (2008) and Bowler et al. (2010), and comparable to the power-law distributions applied in the analyses of microlensing surveys. At a given companion mass and semimajor axis, we can then determine the relative likelihood that a planet exists at this position. We multiply this by the likelihood of detecting such a planet to determine the fraction of planets we would find orbiting each star and the fraction we would miss. These numbers are determined through our analysis of observations of simulated injected planets, as developed in Section 3.2.

We can test our detectability calculation by analyzing the known wide-separation companions in our sample. Of our 111 stars, four are known to host directly imaged brown dwarf companions. Of these, two (HD 71898B and HIP 63510B) were detected as accelerations in our sample, while two (Gl 569B and Gl 229B) are at very large separations and were not detected. The detection or nondetection of each system is consistent with what would be expected from our analysis of injected planets.

We detect the two brown dwarfs with high expected RV detection efficiency, and do not detect the two with expected detection efficiencies near zero, both of which have $a > 40$ AU. We would like a larger sample to test this method, but the limited

number of brown dwarfs suggests our ability to detect giant planets is consistent with expectations. This sample also suggests f_{BD} is only a few percent, consistent with complementary studies (Dieterich et al. 2012).

A giant planet could also be missed if it was in a system with multiple giant planets. We observe only the sum of all radial velocity signals from all planets orbiting a star. For example, if a star hosts two giant long-period planets with one on each side of the star, the two signals would destructively interfere. Even if the acceleration was still detectable, this interference would cause us to measure an incorrect magnitude of the acceleration, so our probability contours would be incorrect. Giant planet multiplicity around M-dwarfs is not well understood, but since giant planet occurrence is believed to be small (Bonfils et al. 2013) the multiplicity rate of giant planets around M-dwarfs is likely also small. Presently, there are no known systems with two planets larger than Jupiter orbiting one M-dwarf. Even in cases with two large planets, one planet will dominate the RV signal. For example, OGLE-2006-BLG-109L contains a $0.73 \pm 0.06 M_J$ planet at 2.3 ± 0.5 AU and a $0.27 \pm 0.02 M_J$ planet (slightly less massive than Saturn) at $4.5^{+2.1}_{-1.0}$ AU (Gaudi et al. 2008; Bennett et al. 2010). In this case the Doppler amplitude of the inner planet would be a factor of 3.3 larger than the Doppler amplitude of the outer planet. Similarly, an external observer of the solar system would observe an RV signal from Jupiter 4.5 times larger than that of Saturn. Thus we neglect this possible source of error.

We then claim that the likelihood of the existence of a giant planet given the non-detection of an RV acceleration is

$$P(\text{planet}|\text{ND}) = f_{pl}(1 - \eta_{pl,\star}), \tag{3.8}$$

where $\eta_{pl,\star}$ is the probability of detecting a giant planet around a given star as a function of planet mass and orbital semimajor axis, estimated by simulating observations of injected planets. The true probability of missing a planet depends on the true giant planet occurrence rate and the planet distribution function. We can determine this value directly if the underlying planet distribution function (Equation 3.7) is assumed. By counting the observed trends and analyzing our RV detection efficiencies for each star as a function of mass and separation, we can determine the number of missed planets. We find our final result is not a strong function of mass index α or semimajor axis index β (see Section 3.4).

False Positives

Multiple Planets

In some cases, observed accelerations may not be induced by the orbit of a giant planet. If two smaller planets are orbiting one star, when they are both on the same side of the star their RV signals would constructively interfere, giving the appearance of a giant planet where none exists. Again, multiplicity rates of large planets are unknown for these small stars but are likely small; we again neglect this effect as a possible source of error. This is a reasonable assumption even if the multiplicity rate of gas giant planets around M-dwarfs was much larger than currently expected. Both the orientation of the system and the relative positioning of the planets during our observations is random. Therefore, it is equally likely that multiple planets would be in the "constructive" or "destructive" phase of their orbits. Thus, similar numbers of false additional planets would be added to our sample as missed true planets.

Secular Acceleration

A false positive can also be caused by secular acceleration. When a high proper motion star moves quickly relative to the Sun, its peculiar velocity vector changes direction in time, causing the star's systemic radial velocity to increase. For a star with proper motion μ at a distance d the magnitude of this effect is, to first order,

$$\dot{\gamma} = 23.0 \text{ cm s}^{-1} \text{ yr}^{-1} \left(\frac{d}{10 \text{ pc}} \right) \left(\frac{\mu}{1 \text{ arcsec yr}^{-1}} \right)^2 . \tag{3.9}$$

The secular acceleration $\dot{\gamma}$ is always positive, so that the star's radial velocity only increases because of this effect. For several nearby stars secular acceleration is large enough to create an apparent acceleration or cause an astrophysical RV acceleration to be incorrectly measured. For example, Barnard's star has a secular acceleration of 4.515 ± 0.002 m s^{-1} yr^{-1} (Choi et al. 2013), larger than all of our observed accelerations. Fortunately, the magnitude of the secular acceleration can be precisely quantified if the star's distance and proper motion are known. All of our stars have measured proper motions and parallaxes, so we can determine the expected secular contribution. This acceleration is subtracted from the observed radial velocity automatically by the CPS RV pipeline (Howard et al. 2010b), so this potential source of error is automatically accounted for in our data. Moreover, none of our observed accelerations are consistent with what would be expected from secular acceleration alone.

Magnetic Activity

Magnetic activity on a star can cause a false positive: rotating active regions can affect the shape of the observed spectral lines and thus the apparent RV (Gray 1988). A magnetic cycle can occur over years and hide or mimic a radial velocity signal. We denote the fraction of stars with a magnetically-induced acceleration as f_A. Gomes da Silva et al. (2012) claim six stars from their sample of 27 M-dwarfs with variability ($22\% \pm 9\%$) have RVs induced by magnetic activity. We are interested in the converse (how many trends are induced by variability?) but their result suggests f_A may be significant. To determine f_A, we review all 165 M-dwarfs observed by the CPS team, both as part of this survey and as part of the M2K survey (Apps et al. 2010; Fischer et al. 2012). Between these two programs, there are a total of 34 systems with RV trends. We analyze the S_{HK} values for these stars and find the RV correlates with S_{HK} with a correlation coefficient $|r| > 0.5$ in 7 cases, suggesting $20.6\% \pm 7.8\%$ of long-term RV trends may be magnetically induced. We adopt this value as f_A. Even if the true value for f_A is a factor of two larger, it would decrease our planet occurrence rate from $f_{pl} = 6.5\%$ to only $f_{pl} = 4.9\%$, still within our uncertainties.

Brown Dwarfs

Our adaptive optics search is sensitive to all stellar-mass companions, but only to the most massive brown dwarfs. We can detect brown dwarfs larger than approximately $50 M_J$, although this number varies from target to target. For each target, we can determine the fraction of brown dwarfs we would expect to detect by our adaptive optics imaging, given the assumption that a trend was caused by a brown dwarf. We call this efficiency η_{BD}. Here, we assume a form for the brown dwarf mass function where $dn/d\log(m) \propto m^{0.4\pm0.2}$ (Peña-Ramírez et al. 2012). Thus we can estimate the likelihood of detecting a brown dwarf around a star in our sample, given that a brown dwarf exists. To estimate the probability a brown dwarf exists, we use the result of Dieterich et al. (2012), who, through an HST/NICMOS snapshot program, estimate that $f_{BD} = 2.3^{+5.0}_{-0.7}\%$ (at 1σ) of M-dwarfs have an L or T companion between 10 and 70 AU. This is consistent with the result of Metchev & Hillenbrand (2009), who estimate a brown dwarf companion frequency of $f_{BD} = 3.2^{+3.1}_{-2.7}\%$ (at 2σ) around solar-type (FGK) stars.

White Dwarfs

Compact stellar remnants are often faint and such binary companions can evade direct detection, especially when the compact object is cool ($T < 4000K$) so that the infrared light is dominated by the primary star (Crepp et al. 2013b). Since our targets are all M-dwarfs, it is not unreasonable to expect that some may have formed as lower mass companions in binary systems with the higher mass object having evolved off the main sequence to become a white dwarf. Napiwotzki (2009) combine observations of local white dwarfs with galactic structure models and find that in the thin disk there is a white dwarf number density of $n_{WD} = 2.9 \times 10^{-3}$ pc^{-3}. From an analysis of PanSTAARS data, Wheeler (2012) estimate 20% of all white dwarfs have an M-dwarf companion ($f_{M|WD}$), somewhat larger than the 12% found by Napiwotzki (2009). Considering the measurement by Chang et al. (2011) of $n_\star = 0.030 \pm 0.002$ stars per cubic parsec, and that approximately 70% of all stars are M-dwarfs ($f_{M|\star}$, Henry et al. 2006), we can determine the fraction of M-dwarfs in the thin disk with a white dwarf companion, a number we define as f_{WD}. If we take $f_{M|WD} = 0.16 \pm 0.04$, we find that

$$f_{WD} = \frac{n_{WD} f_{M|WD}}{n_\star f_{M|\star}} = 2.2\% \pm 0.5\%, \tag{3.10}$$

where the error is dominated by the uncertainty in $f_{M|WD}$.

By combining the false positive events from Section 3.3, Section 3.3, and Section 3.3, we conclude that given the existence of a trend in our data, the likelihood it is caused by a giant planet is

$$P(\text{planet}|\text{trend}) = (1 - f_A)[1 - f_{BD}(1 - \eta_{BD,\star})](1 - f_{WD}). \tag{3.11}$$

Determining f_{pl}

We determine the giant planet occurrence rate, f_{pl}, by combining our estimate of the number of false positives and false negatives with the number of observed accelerations. Specifically, the occurrence of giant planets is given by Eq. 3.6 if the number of observed accelerations is known, along with the probability of a false negative or false positive in our sample. These probabilities are defined by Equations 3.8 and 3.11, respectively.

For each star in our sample, we use our map of giant companion detectability (e.g. Figure 3.6) to estimate our efficiencies, η_{BD} and η_{pl}. We measure the total planet fraction, f_{pl} and its uncertainty through a Monte Carlo experiment. For each trial,

we establish an expected number of observed accelerations, drawing from a binomial distribution with $n = 111$ and $p = 4/111$, representing the most likely underlying distribution behind our observed sample. In practice, we draw from our star list 111 times, with replacement, to determine a stellar sample. We then draw randomly from our previously defined distributions to estimate f_A, f_{BD}, and f_{WD}. These values are sufficient to calculate the probability an observed acceleration is caused by a false positive astrophysical event. In cases where known planets with masses $m > 1 M_J$ exist in our sample, we include their presence in our calculation of f_{pl}.

The derivative of the RV acceleration (the "jerk") for Gl 849 is nonzero, so we can use the RV information to fit a two-planet model to this system, instead of a planet plus a linear acceleration. We find the inner planet to have a mass $m \sin i = 0.90 \pm 0.05 M_J$ with a period of 5.24 ± 0.07 years, and the outer planet to have a mass $m \sin i = 0.70 \pm 0.31 M_J$ with a period of $19.3^{+17.1}_{-5.9}$ years. More data is needed to determine the exact parameters of the orbit of Gl 849c, but from the existing RV information we can determine the probability each planet has a mass $m > 1 M_J$. The exact value depends on the planet mass distribution function; assuming each orientation has equal probability (so that $\alpha = -1$) we find probabilities of 0.577 and 0.419, respectively. Following the method of Ho & Turner (2011), we find changing the distribution function changes these values by less than 10%.

Since we know the region of mass-separation parameter space to which we are sensitive to planets for each star, we can self consistently estimate the planet frequency in this parameter space. We then assume the result from Cumming et al. (2008), who find the power-law indices (Eq. 3.7) of $\alpha = -0.31 \pm 0.20$ and $\beta = 0.39 \pm 0.15$. We randomly select values for α and β from these distributions and use our detection efficiencies to determine the number of false negative missed planets in our sample. Through Equation 3.6, we then have enough information to estimate the planet fraction as a function of each parameter. By repeating this process many times, varying each of our assumed parameters, we can measure the overall planet fraction and its uncertainty.

3.4 Results and Discussion

The Frequency of Giant Planets

Given an observed trend, we can estimate the likelihood the signal is caused by a massive planet. By analyzing our 111 targets as described in Section 3.3, we recover

a distribution in giant planet occurrence as shown in Figure 3.9. We find from this analysis that $6.5\% \pm 3.0\%$ of all M-dwarfs host a giant planet with a semimajor axis smaller than 20 AU. This number is lower than previous studies of higher-mass stars. Bowler et al. (2010) find $24^{+8}_{-7}\%$ of "retired" A stars host Jupiter-mass planets within 3 AU, while Cumming et al. (2008) find that $f_{pl} = 10\% \pm 1\%$ of FGK stars host Jupiter-mass planets within 20 AU.

If we consider multiplicity in situations where we have a giant planet and an RV acceleration (or in the case of Gl 849, two giant planets), then we measure a giant planet occurrence rate of 0.083 ± 0.019 giant planets per star. To estimate this, we repeat the calculations of the previous section, but count known giant planets separate from observed accelerations in the cases when we observe both a planet and a "trend." This number does implicitly assume that observed accelerations are caused by the motion of one giant planet, not a combination of multiple planets in motion. The multiplicity rate of giant planets around M-dwarfs appears to be lower than the multiplicity rate of small planets, such as those detected by *Kepler* (Youdin 2011).

Our result is consistent with the result of microlensing surveys of M-dwarfs, which suggest a total occurrence rate of $0.09^{+0.03}_{-0.05}$ giant planets per star in the range $1 M_J < m < 10 M_J$ and 0.5 AU $< a <$20 AU Cassan et al. (2012). However, the power-law distribution determined by the microlensing studies is considerably different than the Cumming et al. (2008) distribution assumed here. We discuss this further and constrain α and β in Section 3.4.

This is the first study using observed RV accelerations to estimate the giant planet occurrence rate. However, previous RV studies have discussed the presence or non-detection of RV accelerations in their analysis. For example, Endl et al. (2003) mentioned all RV accelerations in their sample are likely the cause of stellar binaries. Our observations are generally more precise than theirs, as we detect some planets that they miss (such as Gl 436 and Gl 849).

Bonfils et al. (2013) detect 15 long-term accelerations in their sample of 102 southern M-dwarfs. Some of these can be attributed to long period binary companions (such as Gl 250B and Gl 618A). Of the stars where we detect an RV acceleration, only one (Gl 849) is in the HARPS sample; these authors also detect an acceleration. Bonfils et al. (2013) also detect an acceleration around Gl 699 (Barnard's star) that we do not detect. Such an acceleration has also not been found by other studies: Choi et al. (2013) claim the RV of Barnard's star is increasing at 4.515 ± 0.002

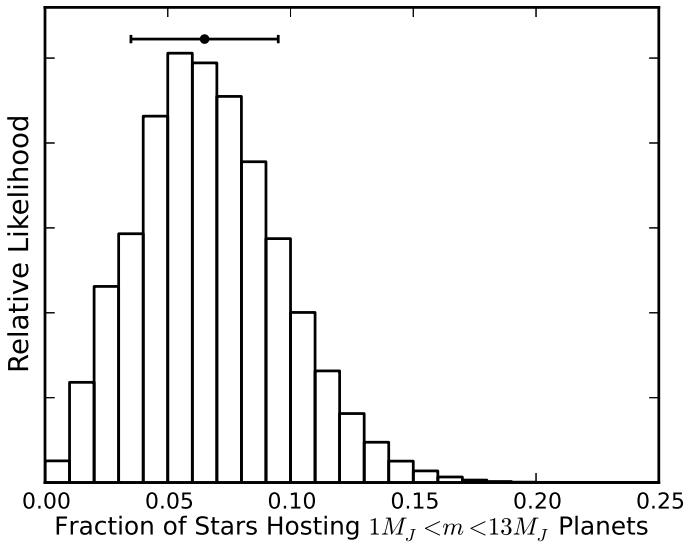

Figure 3.9: Giant planet occurrence for our sample of 111 nearby M-dwarfs. We find 6.5% ± 3.0% of M-dwarfs host a planet with mass $1M_J < m < 13M_J$ and $0 < a < 20$ AU.

m s^{-1} yr^{-1}, consistent with the expected secular acceleration but inconsistent with the -3.043 ± 0.646 m s^{-1} yr^{-1} acceleration observed by Bonfils et al. (2013). With more observations over a longer time baseline, this discrepancy will be resolved.

Potential Missed Binary Stars

We only collect AO images for systems with long term RV accelerations. For these accelerations to be observable, the orbiting companion must have a component of its movement along our line of sight so that the radial velocity changes during an orbit. A giant planet would be missed if it was in a near face-on orbit, such that the star's reflex motion was primarily in the plane of the sky. Such systems are accounted for in our detectability calculations (Figure 3.3), as we have determined the probability of detecting a planet's RV acceleration as a function of its mass and separation, marginalized over all other orbital parameters. These calculations do not, however, account for the possible presence of close stellar binary companions in face-on orbits. Although less common than edge-on systems, any missed binary systems that we have not rejected from our sample would cause our planet occurrence rate to be artificially low (assuming these systems could not form dynamically stable planets). Close binaries would be observable as double-lined spectroscopic systems (SB2s) in the CPS data, while wider binary pairs would be easily imaged by AO systems.

The RV sample was originally selected to reject systems with known binary companions within 2 arcseconds. We would expect companions with a flux ratio larger than 0.01 ($\Delta V = 5$) to be detected as binaries (Robinson et al. 2007). For our brightest targets, this would correspond to M6 dwarfs and brighter. As the cutoff for hydrogen burning is the M6 spectral class (Luhman 2012), we would expect all close stellar-mass binaries to be removed from our HIRES observations.

To determine how many missed binaries are in our sample, we simulate a population of binary companions to M-dwarfs. We create binary companions such that their semimajor axes are assigned following the observed distribution found by Fischer & Marcy (1992). We randomly assign the other orbital parameters and determine there is a 41.8% ± 0.3% chance a binary companion in our sample around a random star would have a projected separation smaller than two arcseconds. Thus, considering Fischer & Marcy (1992) find 42% ± 9% of local M-dwarfs are in binary or multiple systems, we would expect to have a total of 24 ± 6 binary systems in our sample, which originally contained 137 stars before the removal of known binaries. As we actually observe 22 binary systems (containing 26 stars), this result is consistent with our expectation.

We then determine the radial velocity each simulated binary star would induce on our host companion. For each binary that induces a measurable acceleration on the host star, we simulate imaging observations to determine the probability this binary companion would be detected in either our AO survey or, for very wide separation binaries, a seeing-limited ground based survey such as 2MASS. By applying our joint AO/seeing-limited contrast curves, we find that if a binary star system in our survey induces an RV acceleration, we would have a 96.0% ± 0.4% chance of imaging this binary companion. Therefore the probability that one or more of our observed accelerations is caused by a "missed" binary companion is negligible and this possibility does not significantly affect our results.

Dependence on Stellar Mass

Previous RV studies have found a correlation between stellar mass and giant planet occurrence at $a < 2.5$ AU, with more massive stars more likely to host giant planets (Johnson et al. 2010a). To test this relation inside the M-dwarf spectral class, we analyzed the high mass stars separately from the low mass stars in our sample. From our best fit masses, half of our sample is more massive than $M = 0.41 M_{\odot}$. We thus use this value as a dividing line to separate our sample into two groups.

Our masses have typical uncertainties of 10%, so for each star, given its mass and uncertainty, we determine the probability it is larger or smaller than $0.41 M_{\odot}$ assuming normally distributed errors. We then use that value as a weighting factor to assign a probability for each individual star to reside in our high mass or low mass bin, and then repeat our analysis for each individual subsample.

We find an occurrence rate for the high mass subsample of $4.8 \pm 3.3\%$ and for the low mass subsample of $7.9 \pm 4.2\%$ (Figure 3.10). Johnson et al. (2010a) find planet occurrence is correlated with stellar mass such that $f_{pl} \propto 10^{(1.2\pm0.2)[\mathrm{Fe/H}]} M_{\star}^{(1.0\pm0.3)}$. The average star in our high-mass sample has a mass of 0.5 $M_{\odot}$ while the average star in our low-mass sample has a mass of 0.3 $M_{\odot}$, so we would expect the high-mass subsample to have an occurrence rate larger than the low-mass sample by a factor of 1.67. We find the true occurrence rate to change by a factor of 0.61 ± 0.87 in moving from the lower-mass to higher-mass bin. This is inconsistent with the expected result from Johnson et al. (2010a), but the difference between the two bins is not significantly different from zero. A larger sample is required to determine if the small difference between these two populations of M-dwarfs is real or the result of a statistical anomaly. However, our result is lower than the Cumming et al. (2008) result for FGK stars, that $f_{pl} = 10\% \pm 1\%$ of FGK stars host Jupiter-mass planets within 20 AU. This difference is consistent with the Johnson et al. (2010a) correlation between stellar mass and planet occurrence.

Dependence on Metallicity

Previous RV studies of giant planets have also found evidence for a correlation between planet occurrence and metallicity (Fischer & Valenti 2005; Johnson et al. 2010a). To test if this correlation holds for more distant planets, we again split our sample into two, using the same method from the previous section. In this case, we use [Fe/H] $= -0.10$, the sample median metallicity, as the dividing line for our subsamples. We assume all stars have metallicity uncertainties of 0.17 dex, consistent with the scatter expected from the Neves et al. (2012) empirical relation. Again, we assume Gaussian errors to determine the probability each star is in a specific subsample. We then repeat our analysis on both groups.

In the high-metallicity subsample, we find an occurrence rate such that $12.4 \pm 5.4\%$ of M-dwarfs host giant planets. In the low metallicity sample the occurrence rate drops to $0.96 \pm 0.51\%$. In Figure 3.11 we plot a histogram of our posterior distribution of planet occurrence for our high-metallicity subsample. Vertical lines

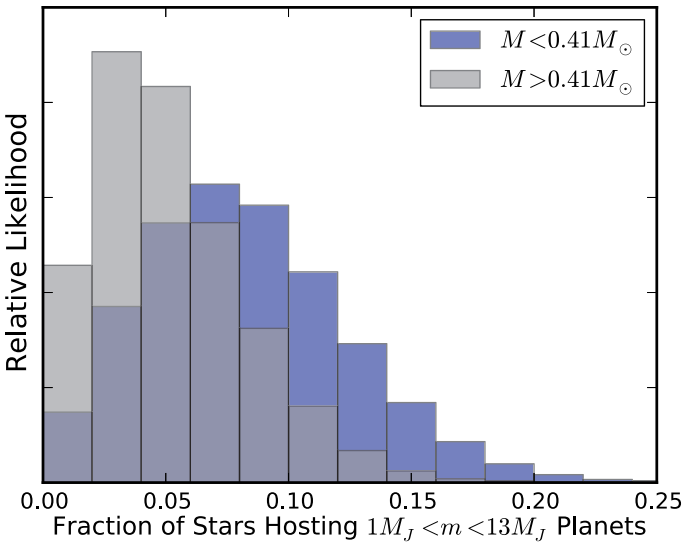

Figure 3.10: Planet occurrence for a low mass subsample (blue) and a high mass subsample (gray) of M dwarfs. Both subsets have nearly similar giant planet occurrence rates, suggesting planet occurrence may not depend strongly on stellar mass within the M spectral class. A larger sample is required to determine if the lack of difference in occurrence rates is astrophysical or statistical variance.

represent (from left to right) 1σ and 3σ upper limits on the planet occurrence rate for the low-metallicity subsample. From these distributions, the giant planet occurrence rate for metal-rich stars has only a 2.4% probability of being lower than the 3σ upper limit on the planet occurrence rate for metal-poor stars. The difference between these subsamples may be suggestive of the same effect seen for RV-confirmed planets within 2.5 AU (Johnson & Apps 2009; Johnson et al. 2012b).

An increase in the planet occurrence rate with metallicity for planets beyond a few AU may suggest giant planets in wide orbits are commonly formed by the same processes as the RV giant planet population. This study will be facilitated by the development of reliable spectroscopic metallicity measurements (Rojas-Ayala et al. 2010).

The Stellar Mass-Metallicity Plane

We can quantify our giant planet occurrence rate with respect to stellar mass and metallicity. Such an approach has been undertaken for planets with $a < 2.5$ AU orbiting stars of all spectral types previously (Johnson et al. 2010a); we follow the techniques of these authors but confine ourselves to strictly giant planets in the range $0 < a < 20$ AU orbiting stars of the M-dwarf spectral class.

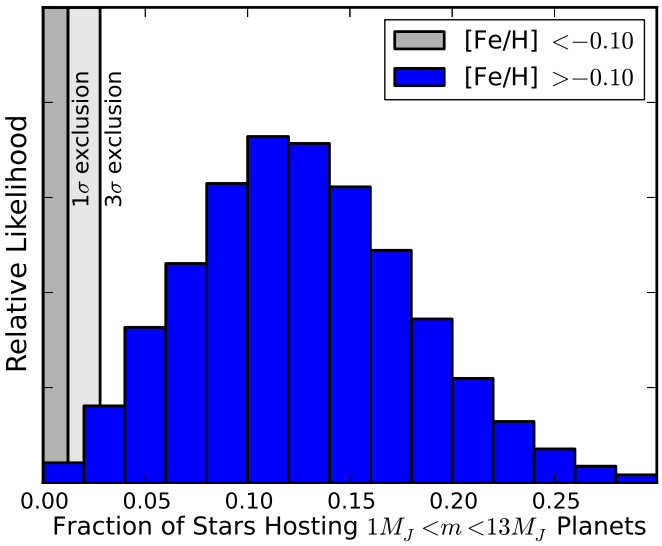

Figure 3.11: Planet occurrence for a high metallicity subsample (blue) and 1σ and 3σ exclusion regions for a low metallicity subsample (gray) of M dwarfs. In the low metallicity subsample, we are able to rule out planet occurrence rates larger than 1.2% at 1σ and 2.8% at 3σ, represented by the labeled vertical lines. The high metallicity sample has a significantly higher occurrence rate than the low metallicity sample, similar to the phenomenon observed for RV-detected planets at smaller separations.

We assume that stellar mass and metallicity produce separate effects on the giant planet occurrence rate, so that the fraction of stars with planets as a function of mass and metallicity can be written as a double power-law,

$$f(M,F) = CM^a 10^{bF}, \tag{3.12}$$

where C, a, and b are constants, $M \equiv M/M\odot$, and $F \equiv$ [Fe/H].

In this analysis, we have a binary result: a star either has a giant planet, detectable as an RV acceleration or closed orbit, or it does not. Therefore, each of the N stars in our sample represents a Bernoulli trial. Given T total observed giant planets, if we assume the probability of a Doppler detection of a giant planet around any given star i is $f(M_i,F_i)$, then by Bayes' theorem, the probability of a given model X given our data d is

$$P(X|d) \propto P(X) \prod_i^T f(M_i,F_i) \times \prod_j^{N-T} [1 - f(M_j,F_j)]. \tag{3.13}$$

Our measurements of stellar masses and metallicities are imperfect. Therefore, we treat the masses and metallicities of these stars as probability distributions. We con-

sider each star's mass and metallicity distribution to be a two-dimensional Gaussian with mean M_i, F_i and standard deviation $\sigma_{M,i}, \sigma_{F,i}$ and call this term p. In this case, the predicted planet fraction for a star with mass M_i and metallicity F_i is

$$f(M_i, F_i) = \int \int p(M_i, F_i) f(M, F) dM\, dF. \tag{3.14}$$

We can thus apply Eq. 3.13 with varying parameters, $X = C, a, b$, to maximize $\mathcal{L}$ conditioned on the data. We elect to use uniform priors, instead of applying the results of previous studies as a prior. Johnson et al. (2010a) and Mortier et al. (2013) study a sample of stars including all stellar types F to M, so their results may not represent our population well. More recent studies, such as Neves et al. (2013), are restricted to M-dwarfs. However, while their techniques are similar, they only attempt to constrain metallicity, implicitly assuming $a = 0$. Additionally on of the three detected planets in their sample is a planet smaller than Jupiter around a metal-poor star. As our sample is limited to planets larger than Jupiter, the resultant distribution found by these authors may not be representative of the population of giant planets ($m > 1 M_J$).

We find our giant planet fraction is described by the distribution function

$$f(M, F) = 0.039^{+0.056}_{-0.028} M^{0.8^{+1.1}_{-0.9}} 10^{(3.8 \pm 1.2) F}. \tag{3.15}$$

The 1σ confidence interval for C is highly skewed, while the other two parameters are approximately normally distributed. In Figure 3.12, we plot the marginal posterior probability distribution functions for each pair of parameters. Perhaps not surprisingly, we find a covariance between C and b. Because our metallicity parameter b is so steep, small changes in b must cause changes in C to keep the giant planet fraction consistent at a given metallicity.

Our results are steeper in b than Neves et al. (2013), although the giant planet occurrence rates at [Fe/H] ~ 0.1 are consistent between the two studies. This is likely due to the inclusion of a planet with a minimum mass of 0.7 Jupiter masses in the "Jovian" sample of these authors. This planet orbits a star with a metallicity [Fe/H] $= -0.19 \pm 0.08$, flattening the distribution with metallicity. The fact remains that, while the metallicity distribution of field stars is centered near [Fe/H] $= 0.0$ with a standard deviation of 0.13 dex, there are presently no giant planets orbiting M-dwarfs with measured metallicities smaller than +0.08 in either the HARPS or HIRES sample. The giant planet distribution function must therefore be a strong

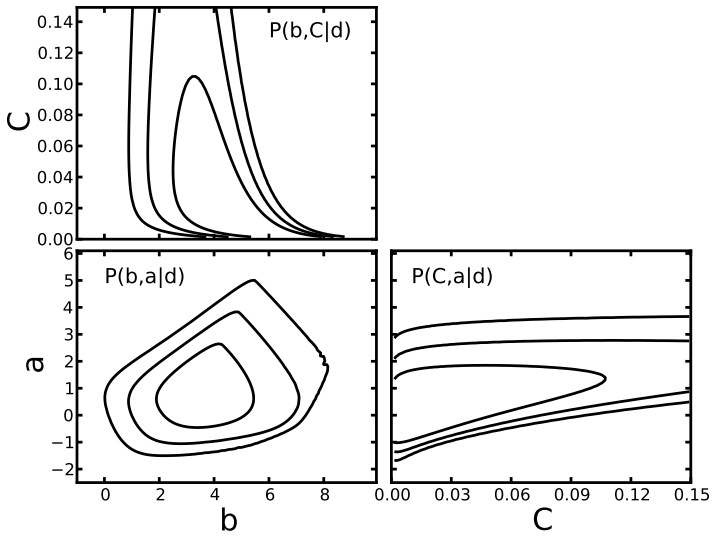

Figure 3.12: Marginal posterior pdfs for the planet population model conditioned on our M-dwarf data. We find, as by other methods in previous sections, that giant planet occurrence is a strong function of stellar metallicity, but may not depend strongly on stellar mass inside of the M spectral class.

function of stellar metallicity. Moreover, it is essential to develop improved methods to measure metallicities of low-mass stars, such as the techniques developed by Rojas-Ayala et al. (2012) and Mann et al. (2013a).

The Effect of Distant Binary Companions

In the above analysis, we neglect binary stars where a test particle at 30 AU would be in an unstable orbit, but include 14 binaries at wider separations. Although these systems formally allow stable orbits, Kaib et al. (2013) suggest these orbits can change significantly over time. Because the binary pair is weakly bound, interactions with the galactic tidal field or nearby passing stars can vary the binary orbit. The binary can then strongly perturb formerly stable planetary companions, potentially resulting in the ejection of planets from the system within 5 Gyr, our estimated age for the M-dwarfs in our sample. None of our 10 wide binary systems show evidence for an RV acceleration, providing weak but tantalizing evidence in favor of this theory. If we repeat our analysis but neglect these stars as potential hosting systems, we find that 7.4% ± 3.3% of single stars host giant planets, compared to 6.5% ± 3.0% of our full sample. With zero detections in a sample of 14 wide binaries, we can only place an upper limit of $f_{pl} \leq 0.20$ at 95% confidence on the occurrence rate of giant planets in wide binary systems. With more observations

of stars with wide binary companions, the occurrence rate of planets orbiting true field stars can be compared to the rate for wide binaries.

Sensitivity to Power-Law Parameters

The result for f_{pl} is dependent on the exact parameters of the planetary distribution function, as that function determines the number of missed (false negative) planets in our sample. To quantify the dependence of the planetary occurrence rate on our choice of α and β we repeat our analysis over a grid of values for α and β. The giant planet occurrence rate as a function of these two parameters is shown in Figure 3.13. We find that there is only a weak relation between α and f_{pl} in the range $-2.0 < \alpha < 0.5$, where we might reasonably expect α to reside. f_{pl} depends more strongly on β, but our overall result does not change by more than 1σ by selecting any β in the range $-1.0 < \beta < 1.0$ for a given α. Selecting any α or β over this range affects our final result by less than a factor of two.

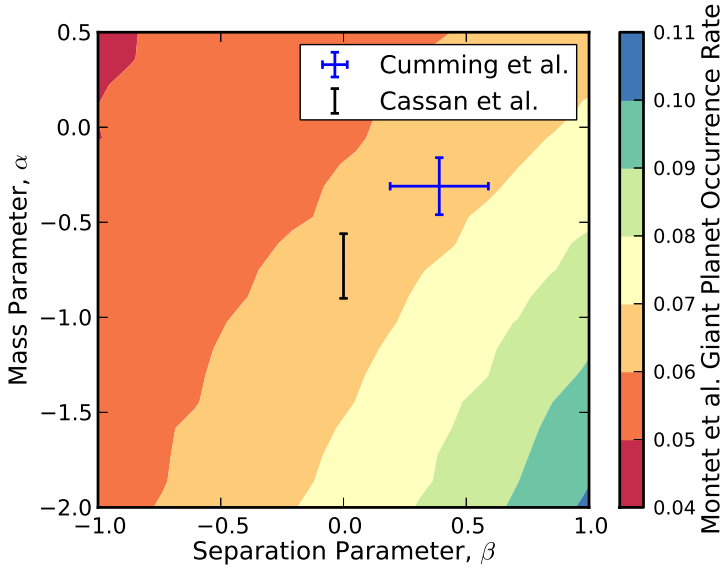

Figure 3.13: Calculated giant planet occurrence rate, f_{pl}, as a function of the mass parameter index α and separation parameter index β. There is not a strong dependence on α or β; selecting $\alpha < -1.0$ and $\beta > 0.5$ is required to affect our result at more than the 1σ level. Labeled points include the Cumming et al. (2008) result for FGK stars, with $\alpha = -0.31 \pm 0.15$ and $\beta = 0.39 \pm 0.15$, and the microlensing result of Cassan et al. (2012), who find $\alpha = -0.73 \pm 0.17$ and assume $\beta \equiv 0$.

From our sample of targets alone, we are unable to place constraints on acceptable values of α and β. To constrain α and β, the occurrence rate of giant planets at a given mass or separation is required. We have determined the bulk occurrence

rate of planets, but cannot uniquely determine their properties. With continued observations, as our RV accelerations "turn over" and become closed orbits, we will be able to determine the exact locations of giant planets around M-dwarfs and constrain the power-law parameters. Alternatively, we can constrain α and β by combining our results with those from microlensing observations.

Comparison with Microlensing Results

In Section 3.4, we showed that our bulk occurrence rate is not a strong function of α and β. However, the types and locations of our planets is a function of these parameters: if α is large, then most of our observed trends must be caused by large planets in wide orbits. Since microlensing results are most sensitive at projected separations corresponding to the Einstein radius, where $R_E \sim 3.5\mathrm{AU}(M_\star/M_\odot)^{1/2}$, we can compare our results to microlensing planet occurrence studies. As our results will only be consistent with microlensing estimates of the planet occurrence rate at the Einstein radius for specific values of α and β, comparisons between the two methods will enable us to constrain α and β.

To compare the two sets of results, we assume the population of M-dwarfs observed by microlensing studies is similar to that targeted by RV surveys in the local neighborhood. We find evidence for a correlation between giant planet frequency and metallicity in our sample, similar to that found by previous RV analyses of planets with $a < 2.5$ AU (Fischer & Valenti 2005; Johnson & Apps 2009). M-dwarfs studied by microlensing are at distances larger than 1 kpc and in the direction of the galactic bulge, along the galactic metallicity gradient (Rolleston et al. 2000). Measurements of the metallicity of Cepheids suggest the iron content in the disk varies such that $d[\mathrm{Fe/H}]/dr = -0.051 \pm 0.004$ dex kpc^{-1} between 5 and 17 kpc from the galactic center (Pedicelli et al. 2009). Thus, the microlensing M-dwarfs may be more metal-rich than stars in the local neighborhood, so f_{pl} may be larger for the microlensing population than the RV population. Without spectra of galactic stellar planet-hosting lenses their true stellar properties are unknown. Programs dedicated to collecting spectra of galactic stellar planet-hosting lenses would greatly inform our knowledge of these stars and their planets.

If we assume the planet mass distribution function of Cumming et al. (2008), then from our analysis we would expect microlensing studies to measure a planet occurrence rate $f_{pl} = 0.056 \pm 0.023$ bound Jupiter-mass planets per star by analyzing signals from planets near the Einstein radius. Cassan et al. (2012) claim an occur-

rence rate of $10^{-0.62\pm0.22}$ ($0.24^{+0.16}_{-0.10}$) Saturn-mass planets at this separation. If we scale this occurrence rate to Jupiter-mass planets following the mass index observed in microlensing studies, $\alpha = -0.73 \pm 0.17$, then the observed microlensing density of Jupiter mass planets would be 0.101 ± 0.016 planets per star, different from our expectation at 1.6σ. If (and only if) the two populations have intrinsically similar occurrence rates of giant planets, then the difference between the number of planets found must be due to a planet distribution different from the one used by Cumming et al. (2008). As the RV planet distribution was developed from an analysis of FGK stars, while the microlensing population generally consists of M dwarfs that may be preferentially metal-rich compared to stars in the local neighborhood, it may not be surprising if the RV planet population is intrinsically different from the microlensing planet population.

Joint Constraints on α

We depart from our previously assumed values of α and β to determine what values of α and β satisfy both our observed RV accelerations and the results of Cassan et al. (2012). We assume the planet occurrence rate presented by Cassan et al. (2012) is representative of the planet population at the Einstein radius. Moreover, we assume planet orbital semimajor axes are distributed uniformly in logarithmic space following Öpik's Law ($\beta = 0$), as microlensing studies assume. This is slightly shallower than what is observed in the RV planet population ($\beta = 0.39 \pm 0.15$), but since the RV population of giant planets likely underwent considerable migration this may be a reasonable assumption. We then vary α, and for each value determine the space density of planets at 2.5 AU. We then compare our expected result to the result from Cassan et al. (2012), which we scale to Jupiter-mass planets according to our α parameter. We finally require $\alpha < 0$: despite the uncertainties in this mass parameter, previous studies agree that around M dwarfs, small planets are more common than massive planets (Swift et al. 2013; Morton & Swift 2014).

We find microlensing results agree with our result for f_{pl} when $\alpha = -0.94 \pm 0.56$ (Figure 3.14). This result is consistent with the best-fitting values for α found by Gould et al. (2010) and Cassan et al. (2012). If we include the Cassan et al. (2012) result as a prior in our analysis, we find $\alpha = -0.77 \pm 0.22$. However, while our result agree with microlensing studies, our result for α is different from the Cumming et al. (2008) result for FGK stars at 1.1σ and significantly different from the Bowler et al. (2010) constraints for A stars, which rule out all $\alpha < 0.25$ with 90% confidence

and all $\alpha < 1.75$ with 50% confidence. Since microlensing predicts a larger number of planets found at the Einstein radius relative to that expected by RV extrapolations, it is not surprising that we find a smaller value for α is required for our result to be consistent with the microlensing results: if the two populations are the same, there must be many low-mass giant planets below the simultaneous RV and imaging detectability limits than high-mass planets above the limits.

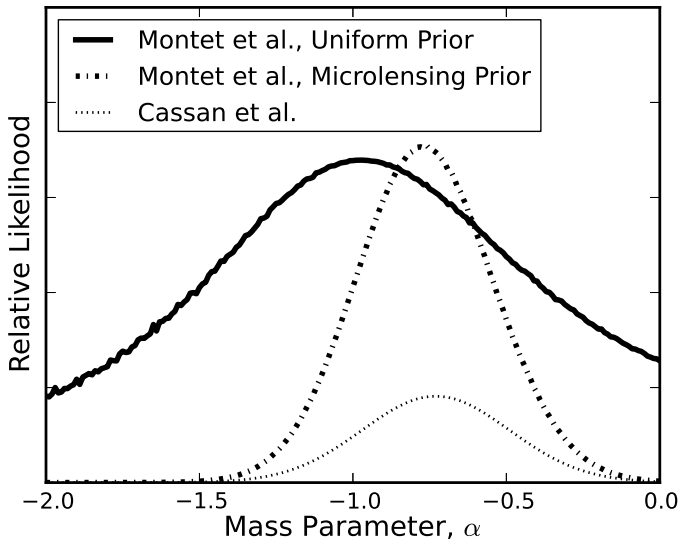

Figure 3.14: Relative likelihood values for the mass parameter α, assuming the planets in our sample and microlensing systems are members of the same population. We find a maximum likelihood value of $\alpha = -0.94 \pm 0.56$, consistent with values of α found from analyses of microlensing planets but steeper than previous RV results for FGK stars at 1.1σ. This result may suggest the planet distribution function is different for M stars as compared to higher mass stars. When we include the Cassan et al. (2012) result as a prior on our measurement, we find $\alpha = -0.77 \pm 0.22$.

Simultaneous Constraints on α and β

We are not restricted to Öpik's Law. We can allow both α and β to vary, and compare the normalization of Cassan et al. (2012) for Saturn-mass objects at 2.5 AU to our projected planet density at that mass and separation (Figure 3.15). Performing this exercise, we find the most acceptable values of α and β are correlated approximately along the line $\alpha - \beta = -1$. That is, for every 1 dex increase in α, β must decrease by 1 dex to maintain a reasonable fit to both our result and the microlensing results.

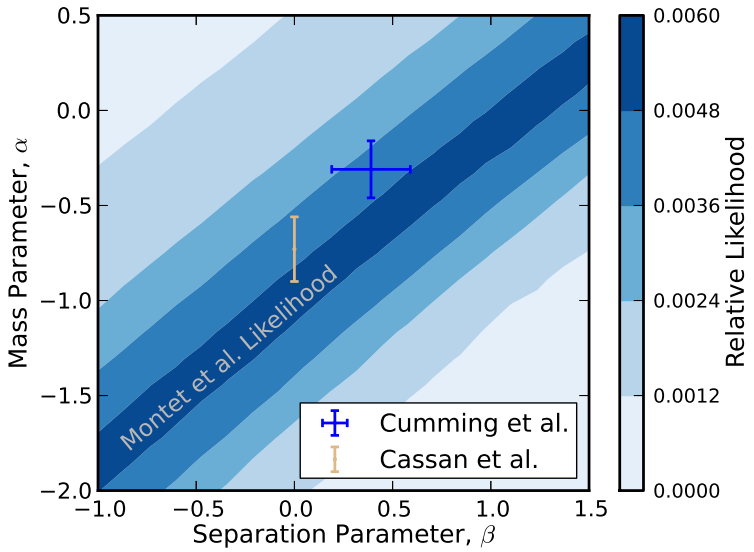

Figure 3.15: Relative likelihood values for the mass parameter α and separation parameter β. There is a maximum likelihood contour approximately along the line $\alpha - \beta = -1$, suggesting a relationship between the two parameters required to fit both our result and the microlensing results, assuming the local planets in our sample and microlensing systems are members of the same population. Points included in the plot are the Cumming et al. (2008) RV result (blue) and the Cassan et al. (2012) microlensing result (cyan), the latter of which assumes an Öpik's Law value of $\beta = 0$. The small discrepancy between our result and the Cumming et al. (2008) result may suggest the planet distribution function may differ between M-dwarfs and FGK stars.

A Model-Independent f_{pl}

We can apply these relative likelihood values as priors to the occurrence rate as a function of α and β shown in Figure 3.13 to determine an occurrence rate independent of our choices of α and β, but dependent on the RV and microlensing stars both being representative of similar populations. We assume our separation parameter must be in the range $-1.0 < \beta < 1.0$, consistent with the assumptions from previous microlensing studies, and allow our mass parameter to be any value subject to the constraints of Figure 3.15. By weighting our occurrence rates found in Section 3.4 in this manner, we find a most likely occurrence rate of $7.2 \pm 3.1\%$, consistent with that found by assuming the power-law distribution of Cumming et al. (2008). As the measured planet frequency depends on the distribution function parameters, an improved value of the planet occurrence rate, either by this method, microlensing, or through astrometry measured by *Gaia* (Casertano et al. 2008), will

provide immediate constraints on the distribution function of giant planets. Similarly, improved constraints on the distribution parameters will enable an immediate improvement of the determination of the giant planet occurrence rate.

The Cumming et al. (2008) power-law parameters α and β are less consistent with our results. This may suggest the planet distribution function around FGK stars is systematically different from the planet distribution function around M-dwarfs. As Bowler et al. (2010) find an even larger value for α in their study of retired A stars (excluding all $\alpha < 0$), which matches comparison studies between RV surveys and high-contrast imaging searches (Crepp & Johnson 2011), this possibility is certainly plausible. With additional M-dwarfs targeted by a combination of RV observations with longer time baselines and high-contrast imaging to improve the estimate of the occurrence rate, we will be able to directly probe this possibility.

3.5 Summary and Conclusion

We have analyzed a collection of 111 nearby M-dwarfs observed in RV surveys with a median time baseline of 11.8 years in a search for long-term RV accelerations. We have developed a new technique to determine the incidence of giant planets in which we target systems with such accelerations using adaptive optics imaging to "peer beyond the horizon" set by Doppler time baselines. With a relatively short exposure image using the Keck AO system, we can eliminate the possibility of binary stellar companions and massive brown dwarfs. We conclude with high statistical confidence that accelerations without a directly imaged companion are likely caused by a planet in a wide orbit.

Accounting for false positive and false negative rates, we find that 6.5 ± 3.0% of M-dwarfs host a giant planet with mass $1 < m/M_J < 13$ and semimajor axis $0 < a < 20$ AU, assuming such planets are distributed following the power-law parameters estimated by Cumming et al. (2008). The exact integrated planet occurrence rate does not depend strongly on the distribution function parameters chosen. We find evidence for a correlation between giant planet frequency and stellar metallicity, similar to that observed in the RV-detected planet population. Additional follow-up work confirming this result would suggest giant planets in wide orbits may form in the same way as the RV-detected giant planets. Observations of more stars are needed to determine if a correlation exists between planet occurrence at wide separations and stellar mass inside of the M-dwarf spectral class.

Our overall occurrence rate is consistent with what might be expected based on the

results of microlensing planet search surveys. However, if the giant planet distribution is given as a double power law similar to that found by Cumming et al. (2008), such that $d^2N \propto M^{\alpha} a^{\beta} d\ln M d\ln a$, with $\alpha = -0.31 \pm 0.20$ and $\beta = 0.39 \pm 0.15$, where α and β are planet distribution power-law indices defined in Eq. 3.7, then microlensing studies overestimate the giant planet occurrence rate. From our bulk occurrence rate, we determine an expected planet detection rate for microlensing studies which depends on our chosen planet distribution function. By assuming an Öpik's Law distribution (i.e., flat in $\log a$), the microlensing planet occurrence rate is consistent with our result if the planet population is represented by the power-law $dN \propto m^{-0.94\pm0.56} d\log m$. This value for α is consistent with previous M-dwarf studies conducted by microlensing planet search teams (Gould et al. 2010; Cassan et al. 2012). We also find other non-Öpik distributions can be chosen to simultaneously explain our results and the microlensing results; these fall approximately on the line $\alpha - \beta = -1$. Moreover, an improved estimate of the giant planet occurrence rate, as measured by *Gaia*, can be combined with our results to provide enhanced constraints on α and β.

Our knowledge of planets around M-dwarfs has significantly improved in the last few years thanks to both targeted RV searches and high contrast imaging campaigns (Apps et al. 2010; Bowler et al. 2012). As such surveys continue, they will begin to confirm and characterize planets in wider orbits, pushing into the domain currently only studied by microlensing studies. To directly compare these populations, understanding the properties of host stars to planets found by microlensing will be extremely important; when possible, every effort should be made to collect spectroscopic followup data on microlensing events to determine the physical properties of lens host stars to better understand both the planet population around M-dwarfs and how it changes across the galaxy.

The method developed in this paper can be extended to higher-mass stars with little difficulty. For example, a large sample of K-dwarfs has been observed by the CPS collaboration. This sample is larger, has more observations, and exhibits less astrophysical jitter than our M-dwarf sample; all of these factors improve our ability to detect RV accelerations. However, the stars are more luminous and on average more distant, complicating adaptive optics searches. Care must be taken to ensure low-mass stellar companions are accounted for, as adaptive optics imaging may not be sensitive to all M-dwarf companions to K-dwarfs without longer observations or the use of ADI. In the future, we intend to apply this technique to the CPS K-dwarfs

to determine the planet occurrence rate around higher mass stars and compare to the M-dwarfs.

Star	RA	Dec	Mass ($M_\odot$)	[Fe/H]	Spectral Type	V	V Source	d (pc)
Hip 428	00:05:10.9	+45:47:11.6	0.53	-0.07	M1	9.93	Gliese & Jahreiß (1991)	11.25
HD 225213	00:05:24.4	-37:21:26.5	0.39	-0.42	M1.5	8.57	Koen et al. (2010)	4.34
Hip 1734	00:21:56.0	-31:24:21.8	0.55	0.09	M1.5	11.1	Koen et al. (2010)	17.98
Gl 26	00:38:59.0	+30:36:58.5	0.43	0.02	M2.5	11.2	Høg et al. (2000)	12.6
Hip 3143	00:39:58.8	-44:15:11.6	0.55	-0.09	M0.5	11.4	Koen et al. (2010)	23.99
Gl 48	01:02:32.2	+71:40:47.3	0.48	0.06	M3	10.0	Høg et al. (2000)	8.24
Gl 49	01:02:38.9	+62:20:42.2	0.58	0.06	M1.5	9.56	Høg et al. (2000)	9.96
Hip 5643	01:12:30.6	-16.59.56.3	0.13	-0.43	M4.5	12.1	Koen et al. (2010)	3.69
Hip 8051	01:43:20.2	+04:19:18.0	0.41	-0.16	M2	10.9	Koen et al. (2010)	11.41
Gl 83.1	02:00:13.0	+13:03:07.0	0.15	-0.31	M4.5	12.3	Landolt (1992)	4.50
G244-047	02:01:35.3	+63:46:12.1	0.48	0.07	M3	11.0	Høg et al. (2000)	12.76
Gl 87	02:01:35.3	+63:46:12.1	0.45	-0.32	M1.5	10.0	Koen et al. (2010)	10.41
Hip 11048	02:22:14.6	+47:52:48.1	0.62	-0.08	M0.5	9.41	Gliese & Jahreiß (1991)	11.94
Gl 105B	02:36:15.3	+06:52:19.1	0.27	-0.10	M4	11.6	Jenkins et al. (2009)	7.73
Gl 109	02:44:15.6	+25:31:24.1	0.35	-0.18	M3	10.6	Koen et al. (2010)	7.51
Hip 21556	04:37:42.9	-11:02:19.9	0.48	-0.11	M1.5	10.3	Koen et al. (2010)	11.10
Gl 179	04:52:05.7	+06:28:35.6	0.36	0.13	M3.5	12.0	Koen et al. (2010)	12.29
Hip 22762	04:59:50.0	-17:46:24.3	0.42	-0.20	M2	10.9	Koen et al. (2010)	12.12
Hip 23512	05:03:20.1	-17:22:24.7	0.27	-0.25	M3	11.7	Koen et al. (2010)	9.21
HD 33793	05:11:40.6	-45:01:06.3	0.27	-0.81	M1	8.85	Koen et al. (2010)	3.91
Hip 24284	05:12:42.2	+19.39.56.4	0.45	-0.16	M2	10.7	Koen et al. (2010)	12.29
HD 36395	05:31:27.4	-03:40:38.0	0.60	-0.05	M1.5	7.92	Koen et al. (2010)	5.66
G097-054	05:34:52.1	+13:52:47.2	0.37	0.05	M3.5	11.9	Kharchenko (2001)	12.39
HD 233153	05:41:30.7	+53:29:23.3	0.60	0.05	M0.5	9.75	Gliese & Jahreiß (1991)	12.44
Hip 26857	05:42:09.3	+12.29:21.6	0.22	-0.24	M4	11.5	Landolt (1992)	5.83

G192-13	06:01:11.1	+59:35:50.8	0.27	-0.11	M3.5	11.7	van Altena et al. (1995)	7.93
Hip 29052	06:07:43.7	-25:44:41.5	0.30	-0.22	M4	11.9	Koen et al. (2010)	11.35
Gl 226	06:10:19.8	+82.06:24.3	0.41	-0.14	M2	10.5	Gliese & Jahreiß (1991)	9.37
Gl 229B	06:10:34.6	-21:51:52.7	0.58	-0.07	M1	8.13	Koen et al. (2010)	5.75
Gl 250B	06:52:18.1	-05:11:24.2	0.45	-0.12	M2	10.1	Gliese & Jahreiß (1991)	8.71
HD 265866	06:54:49.0	+33:16:05.4	0.35	-0.03	M3	10.11	Høg et al. (2000)	5.59
Gl 273	07:27:24.5	+05:13:32.8	0.29	-0.07	M3.5	9.87	Koen et al. (2010)	3.80
Hip 36338	07:28:45.4	-03:17:53.4	0.40	0.03	M3	11.4	Koen et al. (2010)	12.29
Hip 36834	07:34:27.4	+62:56:29.4	0.40	-0.50	M0.5	10.4	Høg et al. (2000)	11.47
Hip 37217	07:38:41.0	-21:13:28.5	0.29	-0.27	M3	11.7	Koen et al. (2010)	10.60
Hip 37766	07:44:40.2	+03:33:08.8	0.31	0.27	M4.5	11.2	Koen et al. (2010)	5.96
GJ 2066	08:16:08.0	+01:18:09.3	0.46	-0.10	M2	10.1	Koen et al. (2010)	9.12
Gl 317	08:40:59.2	-23:27:23.3	0.43	0.20	M3.5	12.0	van Altena et al. (1995)	15.31
HD 75732B	08:52:40.8	+28:18:59.0	0.27	0.15	M4	13.1	Gliese & Jahreiß (1991)	13.02
Hip 46655	09:30:44.6	+00:19:21.6	0.29	-0.17	M3.5	11.7	Koen et al. (2010)	9.67
Hip 46769	09:31:56.3	+36.19:12.8	0.53	-0.27	M0	10.1	Høg et al. (2000)	13.91
Gl 357	09:36:01.6	-21:39:38.9	0.33	-0.31	M2.5	10.9	Koen et al. (2010)	9.02
Hip 47513	09:41:10.4	+13:12:34.4	0.48	-0.12	M1.5	10.4	Koen et al. (2010)	11.26
Hip 47650	09:42:51.7	+70:02:21.9	0.41	0.13	M3	11.4	Høg et al. (2000)	11.35
Hip 48714	09:56:08.7	+62:47:18.5	0.64	-0.03	M0	9.00	Gliese & Jahreiß (1991)	10.56
Gl 382	10:12:17.7	-03:44:44.4	0.54	0.02	M1.5	9.26	Koen et al. (2010)	7.87
Gl 388	10:19:36.3	+19:52:10.1	0.41	0.10	M3.5	9.46	Høg et al. (2000)	4.69
Hip 51007	10:25:10.8	-10:13:43.3	0.54	-0.07	M1	10.1	Koen et al. (2010)	12.35
Gl 393	10:28:55.6	+00:50:27.6	0.44	-0.14	M2	9.65	Landolt (2009)	7.07
Hip 53020	10:50:52.0	+06:48:29.2	0.26	0.00	M4	11.7	Landolt (1992)	6.76
Gl 406	10:56:28.9	+07:00:52.8	0.10	0.22	M5.5	13.5	Landolt (1992)	2.39

Gl 408	11:00:04.3	+22:49:58.6	0.38	-0.15	M2.5	10.0	Koen et al. (2010)	6.66
HD 95650	11:02:38.3	+21:58:01.7	0.59	-0.10	M0	9.57	Koen et al. (2010)	11.77
HD 95735	11:03:20.2	+35.58:11.6	0.39	-0.32	M2	7.52	Oja (1985)	2.55
Hip 54532	11:09:31:3	-24:35:55.1	0.46	-0.08	M2	10.4	Koen et al. (2010)	10.75
HD 97101B	11:11:01.9	+30:26:44.4	0.58	0.52	M1.5	10.7	Høg et al. (2000)	11.87
Hip 55360	11:20:04.8	+65:50:47.3	0.49	-0.35	M0	9.30	Høg et al. (2000)	8.92
Gl 433	11:35:26.9	-32:32:23.9	0.47	-0.15	M1.5	9.81	Koen et al. (2010)	8.88
Hip 57050	11:41:44.6	+42:45:07.1	0.35	0.08	M4	11.9	Kharchenko (2001)	11.10
Gl 436	11:42:11.2	+26:42:22.6	0.44	-0.03	M2.5	10.6	Høg et al. (2000)	10.14
Gl 445	11:47:41.4	+78:41:28.2	0.25	-0.27	M3.5	10.8	Høg et al. (2000)	5.35
Hip 57548	11:47:44.4	+00:48:16.4	0.17	-0.23	M4	11.1	Landolt (1992)	3.36
Gl 450	11:51:07.3	+35:16:19.3	0.46	-0.21	M1	9.72	Høg et al. (2000)	8.59
Hip 59406	12:11:11.8	-19:57:38.1	0.35	-0.13	M3	11.7	Koen et al. (2010)	12.59
Hip 59406b	12:11:17.0	-19:58:21.4	0.25	-0.25	M4	12.6	Gliese & Jahreiß (1991)	12.59
Hip 60559	12:24:52.5	-18:14:32.2	0.26	-0.56	M4	11.3	Koen et al. (2010)	8.85
Gl 486	12:47:56.6	+09:45:05.0	0.32	0.01	M3.5	11.4	Koen et al. (2010)	8.37
Hip 63510	13:00:46.6	+12:22:36.6	0.594	0.04	M0.5	9.76	Koen et al. (2010)	11.4
Gl 514	13:29:59.8	+10:22:37.8	0.53	-0.15	M0.5	9.03	Koen et al. (2010)	7.66
HD 119850	13:45:43.8	+14:53:29.5	0.50	-0.16	M1.5	8.50	van Belle & von Braun (2009)	5.39
Hip 67164	13:45:50:7	-17:58:05.6	0.31	-0.06	M3.5	11.9	Koen et al. (2010)	10.24
HD 122303	14:01:03.2	-02:39:17.5	0.52	-0.16	M1	9.71	Koen et al. (2010)	10.03
Hip 70865	14:29:29.7	+15:31:57.5	0.52	0.00	M2	10.7	Koen et al. (2010)	14.00
Hip 70975	14:31:01.2	-12:17:45.9	0.32	-0.05	M3.5	11.9	Koen et al. (2010)	10.82
Hip 71253	14:34:16.8	-12:31:10.4	0.28	0.11	M4	11.3	Koen et al. (2010)	6.06
Hip 71898	14:42:21.6	+66:03:20.9	0.361	-0.35	M3	10.8	Høg et al. (2000)	9.87
Gl 569A	14:54:29.2	+16:06:03.8	0.48	-0.03	M2.5	10.2	Koen et al. (2010)	9.65

Gl 581	15:19:27.5	-07:43:19.4	0.30	-0.18	M3	10.6	Høg et al. (2000)	6.21
HD 147379B	16:16:45.3	+67:15:22.5	0.47	0.09	M3	10.7	Gliese & Jahreiß (1991)	10.74
Gl 625	16:25:24.6	+54:18:14.7	0.32	-0.39	M1.5	10.2	Høg et al. (2000)	6.52
Gl 649	16:58:08.9	+25:44:39.0	0.54	-0.10	M1	9.66	Høg et al. (2000)	10.34
Hip 83762	17:07:07.5	+21:33:14.5	0.38	-0.10	M3	11.7	Koen et al. (2010)	13.4
Hip 84099	17:11:34.7	+38:26:33.9	0.38	-0.05	M3.5	11.5	Høg et al. (2000)	12.00
Hip 84790	17:19:52.7	+41:42:49.7	0.37	-0.21	M2.5	11.4	Gliese & Jahreiß (1991)	12.38
Gl 687	17:36:25.9	+68:20:20.9	0.40	-0.06	M3	9.15	Høg et al. (2000)	4.53
Gl 686	17:37:53.3	+18:35:30.2	0.44	-0.31	M1	9.58	Koen et al. (2010)	8.09
Gl 694	17:43:56.0	+43:22:43.0	0.44	-0.02	M2.5	10.5	Høg et al. (2000)	9.48
Gl 699	17:57:48.5	+04:41:36.2	0.16	-0.61	M4	9.51	Koen et al. (2010)	1.82
HD 165222	18:05:07.6	-03:01:52.8	0.48	-0.22	M1	9.36	Koen et al. (2010)	7.76
G205-028	18:31:58.4	+40:41:10.4	0.31	-0.14	M3.5	12.0	Gliese & Jahreiß (1991)	11.9
GJ 4063	18:34:36.6	+40:07:26.4	0.19	-0.61	M3.5	11.8	Høg et al. (2000)	7.25
Hip 91699	18:41:59.0	+31:49:49.8	0.37	-0.13	M3	11.3	Kharchenko (2001)	11.45
Hip 92403	18:49:49.4	-23:50:10.4	0.17	-0.43	M3.5	10.5	Koen et al. (2010)	2.97
Gl 745A	19:07:05.6	+20:53:17.0	0.30	-0.48	M1.5	10.8	Koen et al. (2010)	8.51
Gl 745B	19:07:13.2	+20:52:37.2	0.31	-0.45	M1.5	10.7	Koen et al. (2010)	8.75
G207-019	19:08:30.0	+32:16:52.0	0.34	-0.10	M3	11.8	Kharchenko (2001)	12.39
HD 180617	19:16:55.3	+05:10:08.1	0.48	0.02	M2.5	9.12	Koen et al. (2010)	5.87
Gl 793	20:30:32.0	+65:26:58.4	0.38	-0.03	M2.5	10.7	Høg et al. (2000)	8.00
Gl 806	20:45:04.1	+44:29.56.7	0.44	-0.16	M1.5	10.8	Høg et al. (2000)	12.32
Hip 103039	20:52:33.0	-16:58:29.0	0.23	-0.10	M4	11.4	Koen et al. (2010)	5.71
HD 199305	20:53:19.8	+62:09:15.8	0.58	-0.02	M0.5	8.60	Høg et al. (2000)	7.05
Hip 104432	21:09:17.4	-13:18:09.0	0.36	-0.51	M1	10.9	Landolt (2009)	12.17
HD 209290	22:02:10.3	+01:24:00.8	0.60	-0.10	M0	9.15	Koen et al. (2010)	10.24

Gl 849	22:09:40.3	-04:38:26.6	0.49	0.22	M3.5	10.4	Koen et al. (2010)	9.10
Hip 109555	22:11:30.1	+18:25:34.3	0.55	0.13	M2	10.2	Koen et al. (2010)	11.62
Gl 876	22:53:16.7	-14:15:49.3	0.34	0.13	M4	10.2	Landolt (2009)	4.69
HD 216899	22:56:34.8	+16:33:12.4	0.58	0.03	M1.5	8.64	Koen et al. (2010)	6.84
HD 217987	23:05:52.0	-35:51:11.0	0.47	-0.33	M0.5	7.34	Gliese & Jahreiß (1991)	3.28
Hip 114411	23:10:15.7	-25:55:52.7	0.46	-0.13	M2	11.3	Koen et al. (2010)	16.08
Hip 115332	23:21:37.4	+17:17:25.4	0.40	0.27	M4	11.7	Koen et al. (2010)	10.99
Hip 115562	23:24:30.5	+57:51:15.5	0.59	0.08	M1	10.0	Gliese & Jahreiß (1991)	12.96
Gl 905	23:41:55.0	+44:10:40.8	0.14	0.05	M5	12.3	Jenkins et al. (2009)	3.16
Gl 908	23:49:12.5	+02:24:04.4	0.42	-0.39	M1	8.99	Landolt (2009)	5.98

Table 3.1: M-dwarf stars analyzed in this study. Metallicity uncertainties are taken to be 0.17 dex, while mass uncertainties are taken as 10%, following the method of Delfosse et al. (2000)

Star	N_{obs}	Baseline (yr)	Med. σ_γ (m s^{-1})	Jitter (m s^{-1})	RMS (m s^{-1})	RV Planets	Binary Companion
Hip 428	41	12.2	1.6	4.2	4.8	0	K6 (Bidelman 1954)
HD 225213	67	9.9	1.1	3.2	3.1	0	-
Hip 1734	8	8.1	2.6	4.7	7.6	0	-
Gl 26	40	11.6	2.8	2.9	7.7	0	-
Hip 3143	8	9.8	5.6	2.6	11.6	0	-
Gl 48	41	15.2	1.3	2.5	3.5	0	-
Gl 49	22	14.2	1.4	7.9	5.0	0	-
Hip 5643	15	7.1	3.4	13.2	7.8	0	-
Hip 8051	33	12.7	1.5	3.0	5.0	0	-
Gl 83.1	21	8.2	3.3	12.5	20.2	0	-
G244-047	10	7.5	2.8	3.6	4.0	0	-
Gl 87	62	13.0	1.3	2.5	7.4	0	-
Hip 11048	44	12.6	1.1	4.8	5.4	0	-
Gl 105B	12	9.1	2.7	3.7	13.0	0	K3 (Gray et al. 2006)
Gl 109	32	13.1	1.4	2.8	4.4	0	-
Hip 21556	31	12.7	1.3	2.5	4.3	0	-
Gl 179	42	12.2	2.5	4.4	19.7	1	-
Hip 22762	39	12.6	1.6	2.7	4.6	0	-
Hip 23512	11	6.7	4.1	5.0	6.7	0	-
HD 33793	36	13.8	1.4	2.9	3.2	0	-
Hip 24284	30	9.1	1.4	2.3	5.4	0	-
HD 36395	33	15.8	1.7	5.7	7.8	0	-
G097-054	11	6.6	3.6	3.4	8.7	0	-
HD 233153	11	6.7	2.3	5.8	6.6	0	K1 (Montes et al. 2001)
Hip 26857	10	6.7	4.7	4.6	11.8	0	-

G192-13	16	7.8	4.3	4.1	11.4	0	-
Hip 29052	16	7.7	4.6	3.5	10.5	0	-
Gl 226	35	14.7	1.6	2.3	8.7	0	-
Gl 229B	33	15.9	1.2	4.5	5.1	0	T7 (Faherty et al. 2009)
Gl 250B	29	8.0	1.3	3.7	3.4	0	K3 (Gliese & Jahreiß 1991)
HD 265866	61	14.8	1.3	2.6	4.6	0	-
Gl 273	41	14.8	2.1	2.3	5.0	0	-
Hip 36338	10	10.7	2.9	2.3	5.8	0	-
Hip 36834	22	6.4	2.7	5.8	14.6	0	-
Hip 37217	11	11.8	3.4	25.7	5.3	0	-
Hip 37766	22	11.1	3.1	87.9	95.2	0	-
GJ 2066	37	14.8	1.5	2.5	5.3	0	-
Gl 317	45	12.1	2.2	4.5	56.9	1	-
HD 75732B	21	9.1	5.2	4.9	17.1	0	G8 (Montes et al. 2001)
Hip 46655	11	6.0	3.9	2.9	18.6	0	-
Hip 46769	23	8.0	1.4	3.5	6.3	0	-
Gl 357	36	14.2	1.8	2.1	6.1	0	-
Hip 47513	29	12.1	1.4	3.8	6.1	0	-
Hip 47650	10	6.2	3.2	16.2	11.0	0	-
Hip 48714	16	11.2	1.4	6.3	9.6	0	-
Gl 382	29	12.9	1.5	5.3	6.4	0	-
Gl 388	39	5.7	1.8	24.0	17.9	0	-
Hip 51007	19	11.1	2.2	4.2	6.1	0	-
Gl 393	42	14.4	1.2	3.3	3.9	0	-
Hip 53020	12	6.3	3.4	6.5	13.0	0	-
Gl 406	21	13.0	6.8	20.1	15.0	0	-

Gl 408	39	14.8	1.4	3.1	4.2	0	-
HD 95650	30	11.1	1.8	10.8	14.8	0	-
HD 95735	211	15.2	1.0	2.7	3.9	0	-
Hip 54532	26	12.2	2.6	2.9	12.9	0	-
HD 97101B	25	10.5	1.4	4.7	4.7	0	K8 (Gliese & Jahreiß 1991)
Hip 55360	30	11.9	2.4	2.2	8.2	0	-
Gl 433	27	13.1	2.4	2.4	6.8	0	-
Hip 57050	40	11.8	3.1	3.4	25.9	1	-
Gl 436	257	12.0	1.7	2.2	12.0	1	-
Gl 445	48	13.3	1.7	2.4	7.0	0	-
Hip 57548	17	12.8	2.8	9.2	5.9	0	-
Gl 450	31	14.1	2.0	4.7	7.0	0	-
Hip 59406	11	7.0	4.4	2.2	11.4	0	M4 (Table 3.1)
Hip 59406b	12	6.2	6.1	3.2	13.2	0	M3 (Table 3.1)
Hip 60559	14	6.3	3.4	3.1	8.9	0	-
Gl 486	20	8.2	3.0	2.5	11.3	0	-
Hip 63510	41	11.3	3.4	6.0	1011.0	0	M7 (Beuzit et al. 2004)
Gl 514	50	13.9	1.4	3.5	6.0	0	-
HD 119850	42	13.9	1.3	2.2	3.2	0	-
Hip 67164	14	6.2	4.0	2.2	8.3	0	-
HD 122303	37	11.8	1.3	3.4	6.9	0	-
Hip 70865	21	8.5	1.8	2.7	7.5	0	-
Hip 70975	15	11.3	2.9	2.8	8.5	0	-
Hip 71253	21	7.9	2.7	4.2	8.1	0	-
Hip 71898	30	14.1	2.4	2.9	41.0	0	L0 (Faherty et al. 2009)
Gl 569A	13	5.1	2.5	14.7	6.6	0	M8.5+M9 (Mason et al. 2001)

Gl 581	197	12.5	1.3	2.8	9.9	4	-
HD 147379B	14	5.9	2.2	4.1	4.8	0	M1 (Herbig 2007)
Gl 625	48	14.0	1.7	2.7	3.6	0	-
Gl 649	50	12.6	1.4	5.6	9.4	1	-
Hip 83762	8	2.9	1.3	2.8	7.1	0	-
Hip 84099	16	6.2	2.8	2.6	6.6	0	-
Hip 84790	17	4.9	3.0	2.2	5.6	0	-
Gl 687	100	13.8	1.2	2.3	5.9	0	M3.5 (Jenkins et al. 2009)
Gl 686	60	14.4	1.1	2.4	3.4	0	-
Gl 694	38	14.4	2.2	3.1	4.6	0	-
Gl 699	230	15.3	1.3	7.0	4.1	0	-
HD 165222	142	14.4	1.2	3.1	3.4	0	-
G205-028	12	6.2	3.8	27.6	8.1	0	-
GJ 4063	14	6.9	2.7	2.5	6.1	0	-
Hip 91699	17	12.0	2.9	3.4	11.6	0	-
Hip 92403	27	8.1	2.8	7.7	18.8	0	-
Gl 745A	26	13.3	1.5	2.9	3.9	0	M1.5 (Table 3.1)
Gl 745B	21	10.4	2.5	2.9	5.5	0	M1.5 (Table 3.1)
G207-019	12	6.2	3.3	9.7	7.9	0	-
HD 180617	143	9.8	1.3	3.3	4.7	0	M8 (Jenkins et al. 2009)
Gl 793	30	14.2	1.6	4.9	5.0	0	-
Gl 806	63	15.3	1.6	3.1	6.5	0	-
Hip 103039	19	8.2	3.4	5.5	6.7	0	-
HD 199305	45	15.3	1.1	4.5	3.3	0	-
Hip 104432	34	12.3	1.7	3.1	5.0	0	-
HD 209290	56	11.0	1.0	4.6	3.7	0	-

Gl 849	84	14.4	1.6	3.1	21.5	1	-
Hip 109555	16	11.1	2.5	12.5	8.4	0	-
Gl 876	207	14.4	2.1	4.0	150.4	4	-
HD 216899	50	15.1	1.1	4.2	4.6	0	M2 (Zakhozhaj 2002)
HD 217987	69	14.3	1.2	3.3	4.9	0	-
Hip 114411	11	8.9	2.7	3.3	7.2	0	-
Hip 115332	14	6.7	3.4	3.2	9.2	0	-
Hip 115562	10	8.8	1.6	6.2	9.0	0	-
Gl 905	17	8.0	3.8	8.6	8.8	0	-
Gl 908	89	16.0	1.2	2.6	2.9	0	-

Table 3.2: RV observations for all stars in the sample

Star	Planet $m \sin i$ (M_J)	Period (days)	Discovery	Updated Parameters
Gl 179	0.82 ± 0.07	2288 ± 59	Howard et al. (2010b)	Howard et al. (2010b)
Gl 317	1.80 ± 0.05	691.8 ± 4.7	Johnson et al. (2007b)	Anglada-Escudé et al. (2012b)
Hip 57050	0.298 ± 0.025	41.397 ± 0.016	Haghighipour et al. (2010)	Haghighipour et al. (2010)
Gl 436	0.0737 ± 0.0052	2.643899 ± 0.000001	Butler et al. (2004)	Southworth (2010)
Gl 581	0.049 ± 0.001	5.369 ± 0.002	Bonfils et al. (2005)	Tadeu dos Santos et al. (2012)
	0.017 ± 0.001	12.931 ± 0.002	Udry et al. (2007)	Tadeu dos Santos et al. (2012)
	0.006 ± 0.003	1.0124 ± 0.0001	Udry et al. (2007)	Tadeu dos Santos et al. (2012)
	0.006 ± 0.003	2.149 ± 0.002	Mayor et al. (2009)	Tadeu dos Santos et al. (2012)
Gl 649	0.328 ± 0.032	598.3 ± 4.2	Johnson et al. (2010b)	Johnson et al. (2010b)
Gl 849	0.82 ± 0.07	1890 ± 130	Butler et al. (2006)	Butler et al. (2006)
Gl 876	1.9506 ± 0.0039	61.1166 ± 0.0086	Marcy et al. (1998)	Rivera et al. (2010)
	0.612 ± 0.003	30.0881 ± 0.0082	Marcy et al. (2001)	Rivera et al. (2010)
	0.018 ± 0.001	1.93778 ± 0.00002	Rivera et al. (2005)	Rivera et al. (2010)
	0.039 ± 0.005	124.26 ± 0.70	Rivera et al. (2010)	Rivera et al. (2010)

Table 3.3: Previously published RV planets

Star	RV Slope (m s^{-1} yr^{-1})	AO Observation Date	Instrument	Filter	ADI	Cause of Acceleration
Gl 317	2.51 ± 0.62	2010 October 13	NIRC2	K'	Yes	Presumed Companion
Gl 179	−1.17 ± 0.29	2012 February 2	NIRC2	K'	Yes	Presumed Companion
Hip 57050	1.39 ± 0.39	2012 December 27	NIRC2	Ks	No	Presumed Companion
Gl 849	N/A[1]	2011 June 24	NIRC2	L	Yes	Identified Companion
Hip 63510	N/A[1]	N/A	N/A	N/A	N/A	Brown Dwarf[2]
Hip 71898	8.6 ± 0.4	N/A	N/A	N/A	N/A	Brown Dwarf[3]

[1]Curvature in RV
[2]Beuzit et al. (2004)
[3]Golimowski et al. (2004)

Table 3.4: Stars with measured RV accelerations and imaging nondetections

3.6 Notes on Individual Targets

Gl 849

The RV data for Gl 849 exhibits a clear planetary signal from the known companion Gl 849b. The residuals to the best-fitting orbit for this planet exhibit strong curvature, motivating our two-planet fit. Moreover, there is no correlation between this long period signal and stellar magnetic activity, suggesting the planet is not the result of an apparent velocity change during the star's magnetic cycle. To determine the orbital parameters of both planets, we utilize emcee, an affine invariant MCMC ensemble sampler (Foreman-Mackey et al. 2013). For both planets, we fit five orbital parameters: the eccentricity e, argument of periapsis ω, time at which a transit would occur $t_{\varpi=90}$, Doppler semiamplitude K (or the product of the planet mass and the inclination $m \sin i$), and planet orbital period P. We also include the systemic radial velocity γ as a free parameter, as well as a velocity offset between observations taken before August 18, 2004 and after that date, corresponding to an upgrade of the HIRES CCD detector (Wright et al. 2011).

Due to the curvature in the outer planet's orbit, we are able to constrain the mass and period of both companions. As shown in Figure 3.16, the orbit of the outer planet is only weakly constrained. Nevertheless, the data can rule out orbits with $m \sin i > 2.5 M_J$. Moreover, we refine the inner planet's parameters: we find the "b" component's best-fitting mass and period increase slightly, but the distributions for each are consistent with those found by Butler et al. (2006). Our parameters for each planet are included in Table 3.5.

Parameter	Mean	50%	15.8%[2]	84.2%[2]
Planet b				
Orbital period P (yr)	5.241	5.243	-0.067	+0.064
Planet mass[1] $m \sin i$ (M_J)	.899	0.900	-0.045	+0.043
Time of potential transit $t_{\varpi=90}$ (JD-2440000)	537.3	536.9	-161.3	+164.7
$e^{1/2} \cos \omega$	-0.048	-0.059	-0.105	+0.122
$e^{1/2} \sin \omega$	0.099	0.116	-0.161	+0.114
Planet c				
Orbital period P (yr)	24.04	19.35	-5.93	+17.20
Planet mass[1] $m \sin i$ (M_J)	0.773	0.702	-0.203	+0.344
Time of potential transit $t_{\varpi=90}$ (JD-2440000)	3586.3	5660.3	-7356.0	+2387.6
$e^{1/2} \cos \omega$	-0.311	-0.346	-0.185	+0.260
$e^{1/2} \sin \omega$	-0.348	-0.361	-0.234	+0.253
System Parameters				
HIRES detector upgrade offset (m s^{-1})	17.07	17.18	-5.25	+5.01

[1]Assuming a stellar mass of 0.49 $M_\odot$

[2]Values given relative to the 50% data point

Table 3.5: Orbital Parameters for Gl 849

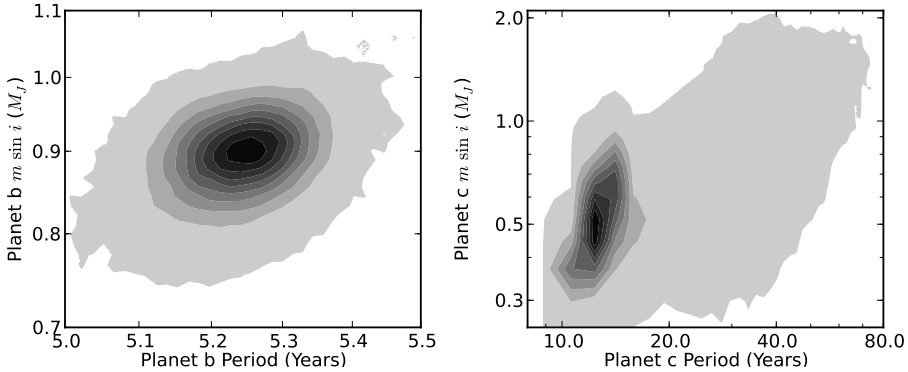

Figure 3.16: Position of (left) Gl 849b and (right) Gl 849c in the mass-period plane. The orbital parameters for the inner planet are much more tightly constrained than the outer planet. Depending on the exact shape of the planet distribution function, the inner planet may have more than a 50% probability of being more massive than Jupiter when orientation uncertainties are taken into account.

HIP 109555

When observing HIP 109555 we detected a possible faint companion object located tens of arcseconds away. To prove this companion is not associated with the primary but is instead unrelated, we compare the proper motion of both objects by identifying them in the 2MASS catalog (Skrutskie et al. 2006) and the Palomar Observatory Sky Survey (Abell 1959). Comparing the POSS data collected 16 July 1950 to the 2MASS observation, we detect a proper motion for HIP 109555 of 0.36 arcsec/yr, consistent with previously published results (van Leeuwen 2007). The hypothetical companion motion, however, is only 5 miliarcseconds per year. Additionally, the companion is bluer in colors derived using the 2MASS J, H, and K filters than HIP 109555. These are both consistent with the companion being a distant background object, and we neglect its presence in our analysis.

HIP 57050

We observed HIP 57050 (=GJ1148) on December 27, 2012 using the K_s filter on NIRC2. Our imaging is only complete at separations smaller than 1 arcsecond, corresponding to a projected separation of 11 AU. This does not enable us to rule out most stellar companions that could cause our observed RV trends, as shown in Figure 3.17. If the observed trend is caused by a stellar-mass companion, the companion is likely beyond 10 AU, which corresponds to a separation of 0.9 arcseconds. Thus any stellar companions at their maximum separation that could cause this trend would be expected to be found in a seeing-limited survey. We find no ev-

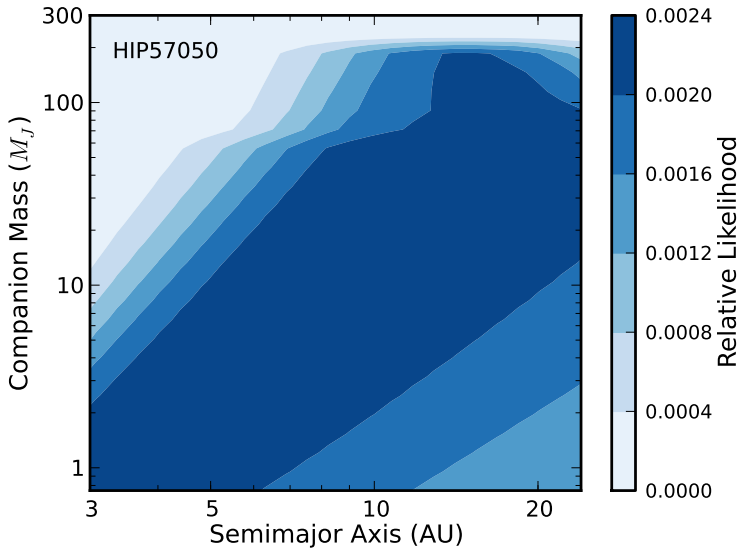

Figure 3.17: Probability contours displaying the location of a giant companion orbiting HIP 57050, given that exactly one such planet exists, when the RV data is combined with adaptive optics imaging and 2MASS data. Because the AO imagery only extends to 11 AU, there is a small region of parameter space where a low-mass M-dwarf companion could reside. Additional AO observations with a wider field of view would be required to rule out this possibility. Lower-mass companions are allowed in shorter orbital periods due to possible curvature in the radial velocity data.

idence for such a companion. While unlikely, additional AO observations with a wider field of view are required to fully eliminate the possibility that a low-mass star exists.

HIP 63510

HIP 63510B (Ross 458) is an M7 brown dwarf orbiting an M0.5 dwarf at approximately 3 AU (Beuzit et al. 2004). Twelve years of RV observations suggest an orbit with a period of 13.9 years, an eccentricity of 0.32, and a minimum mass $m \sin i = 67.9 M_J$, suggesting a nearly edge-on orbit. We estimate a detection efficiency of 1.000 in an RV survey, which is not surprising considering the stellar RV semiamplitude is $K = 1.24$ km s^{-1}. This system contains a second companion which is separated from the host star by 1100 AU (Goldman et al. 2010; Scholz 2010)

HIP 71898

HIP 71898B is an L0 dwarf in a wide orbit around an M3.5 dwarf. Golimowski et al. (2004) report a projected separation of 30.01 ± 3.78 AU. This target has an RV baseline of 14 years, over which 30 observations were collected. From these observations we measure an acceleration of 8.6 ± 0.4 m s^{-1} yr^{-1}. At 30 AU, this would suggest a minimum dynamical mass $m \sin i > 45 M_J$, consistent with an L0 dwarf. A detectability plot for companions to HIP 71898 is shown in Figure 3.18. The observed acceleration lies near a contour representing a 0.9 probability of RV detection, so it is not surprising this companion was detected by CPS.

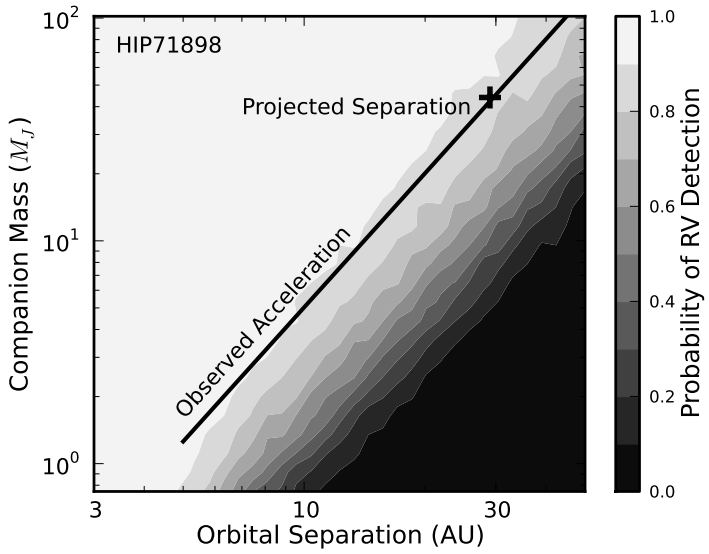

Figure 3.18: Probability contours displaying the likelihood that a planet of a given mass and semimajor axis would be detected around HIP 71898 in the CPS RV survey. The diagonal line represents companions that would produce an acceleration of 8.6±0.4 m s^{-1} yr^{-1} in an edge on system when the companion was moving along the observer's line of sight. The + marks the spot at which a $45 M_J$ companion at 30 AU would reside; this is the minimum mass and semimajor axis expected from this companion.

Gl569

Gl 569B is a brown dwarf binary, with an M8.5+M9 pair orbiting each other every 870 ± 9 days. The system has a combined mass of $0.140^{+0.009}_{-0.008} M_\odot$ (Dupuy et al. 2010) and is separated from the primary, an M3.5 dwarf, by a projected separation of 5 arcsec, or 47 AU (Femenía et al. 2011). The maximum RV acceleration from such a companion is 3.7 m s^{-1} yr^{-1}. For this star, we have a 5.1 year baseline and the median σ is 15 m s^{-1}. By injecting simulated companions, we estimate an RV

detection efficiency near zero for these companions. Thus it is not surprising that it is missed in our sample.

Gl 229B

Gl 229B (HD 42581) is a T7 dwarf at a projected separation of 44 AU (Faherty et al. 2009). This companion has been directly imaged (Nakajima et al. 1995) but not detected as a strong acceleration through RV variations. As with Gl 569, this object is beyond our range for efficient brown dwarf detection through RV observations. If we assume a mass of 40 M_J, we would expect a maximal RV acceleration of 1.1 m s^{-1} yr^{-1}. Thus, again we should not be surprised it is not detected.

3.7 A Brief Note on Radial Velocities and Magnetic Activity

We account for the possibility that any apparent RV accelerations may be induced by magnetic activity statistically, as described in Section 3.3. Often, the $S_{\rm HK}$ value, a measure of the ratio of flux in the Ca II line cores to flux in nearby continuum regions, is taken as a proxy for chromospheric activity (Wilson 1968; Henry et al. 1996). While not a perfect measure, it is comforting to note that the observed radial velocities do not correlate with $S_{\rm HK}$ in any of our stars with long-term RV accelerations. The RVs for our systems with detected accelerations as well as $S_{\rm HK}$ for observations after the HIRES detector upgrade are included in Figure 3.19 and Table 3.6.

JD-2440000	RV (m s^{-1})	$\sigma_{\rm RV}$ (m s^{-1})	$S_{\rm HK}$	JD-2440000	RV (m s^{-1})	$\sigma_{\rm RV}$ (m s^{-1}	$S_{\rm HK}$
Gl 317							
11550.993	369.80	5.83	N/A	14544.905	456.22	4.92	0.97
11552.990	395.68	6.74	N/A	14545.894	455.37	4.96	1.11
11582.891	397.16	6.08	N/A	14603.777	415.82	5.00	0.97
11883.101	321.88	5.83	N/A	14806.029	344.83	5.02	1.13
11973.795	292.84	7.74	N/A	14807.069	337.39	5.70	1.01
12243.073	386.34	7.95	N/A	14808.138	343.93	4.94	1.11
12362.949	451.96	7.50	N/A	14809.059	335.15	4.95	1.22
12601.045	325.69	6.93	N/A	14810.161	339.65	4.87	1.20
12989.125	442.81	6.64	N/A	14811.128	341.51	4.93	1.21
13369.016	337.48	4.90	1.26	14839.107	342.36	5.26	1.09
13753.983	479.22	4.85	1.13	14963.795	388.95	4.98	1.46
14084.001	337.88	5.29	1.22	15134.090	489.75	4.90	1.24
14086.141	342.52	5.21	1.20	15173.079	479.92	4.79	1.09
14130.082	351.80	5.37	1.21	15199.017	478.18	4.98	1.16
14131.014	341.73	5.11	1.07	15255.869	447.15	4.89	1.19
14138.932	335.57	4.86	1.12	15289.857	424.86	4.82	1.16
14216.733	358.57	4.95	1.04	15522.057	333.93	4.97	0.85
14255.743	376.54	4.92	1.45	15613.960	366.70	4.92	1.24
14255.749	380.38	4.79	1.20	15672.848	392.45	4.92	1.14
14400.110	476.46	4.91	0.98	15878.127	460.49	4.81	1.03

14428.062	479.05	5.29	1.02	15903.017	457.41	4.79	1.02
14492.901	479.46	5.05	1.13	15960.986	422.57	4.98	1.01
14543.948	448.01	5.34	0.97				
Gl 849							
10606.068	190.31	4.78	N/A	14455.744	165.29	3.45	1.06
10666.001	205.60	4.69	N/A	14456.733	163.51	3.48	1.11
10715.957	205.19	4.99	N/A	14460.742	173.41	3.53	1.00
10983.038	217.69	4.67	N/A	14634.083	176.64	3.34	1.10
10984.084	224.23	4.55	N/A	14635.042	173.89	3.32	1.00
11410.021	254.67	4.08	N/A	14636.051	176.71	3.33	1.01
11439.865	245.85	4.30	N/A	14637.116	176.23	3.31	1.00
12095.081	225.97	4.52	N/A	14638.059	177.42	3.41	0.96
12096.046	219.06	4.38	N/A	14639.067	174.78	3.42	1.00
12133.013	221.49	4.39	N/A	14640.115	171.70	3.36	1.08
12160.909	211.60	4.10	N/A	14641.117	173.84	3.38	1.07
12161.846	207.39	4.19	N/A	14644.113	177.39	3.40	1.01
12162.887	209.34	4.22	N/A	14674.936	176.17	3.40	1.02
12486.968	194.80	4.66	N/A	14688.952	177.11	3.40	1.06
12535.852	194.96	4.43	N/A	14690.005	183.22	3.51	1.06
12807.011	209.44	4.30	N/A	14721.949	183.11	3.52	1.03
12834.013	208.07	4.39	N/A	14790.752	184.27	3.43	1.04
12989.720	217.41	4.08	N/A	14807.793	183.33	3.47	1.00
13014.710	222.75	4.27	N/A	14989.063	213.37	4.17	0.98
13015.711	221.97	4.60	N/A	15015.047	199.35	3.42	1.04
13016.706	222.33	4.07	N/A	15016.074	202.71	3.36	0.98
13154.080	228.16	4.76	N/A	15029.019	201.72	3.52	0.98
13180.108	231.43	4.45	N/A	15043.042	212.32	3.40	1.02
13196.931	228.82	4.63	N/A	15048.996	209.45	3.39	0.98
13238.929	230.55	3.44	1.01	15075.082	205.14	3.55	1.00
13301.838	228.44	3.39	1.00	15080.084	215.78	3.50	0.90
13302.742	228.98	3.32	1.05	15082.073	213.97	3.44	0.99
13303.798	228.40	3.27	1.02	15134.922	210.04	3.41	1.02
13603.939	221.04	3.43	0.93	15135.876	210.90	3.37	1.03
13724.712	207.52	3.39	0.98	15169.797	210.64	3.55	1.01
13746.715	205.70	3.60	1.01	15188.725	223.58	3.42	1.07
13746.721	203.74	3.72	1.03	15352.082	238.03	4.18	0.98
13749.698	194.88	3.51	0.87	15376.032	226.26	3.36	1.01
13927.015	187.71	3.42	0.93	15395.958	229.16	3.32	0.98
13959.087	191.03	3.34	1.90	15397.048	227.85	3.36	1.00
13960.955	188.72	3.31	0.95	15436.111	227.10	3.40	0.99
13960.962	191.05	3.32	0.95	15521.801	216.77	3.53	0.99
13983.000	191.46	3.36	1.11	15555.792	228.55	3.38	1.04
14083.750	174.45	3.67	1.05	15736.122	221.64	3.86	1.10
14337.074	164.82	3.45	1.00	15770.878	212.94	3.41	1.09
14343.872	165.90	3.35	1.03	15807.063	210.62	3.40	1.04
14429.742	166.12	3.44	1.05	15851.759	205.57	3.33	1.00
Hip 22627							
11580.831	139.11	6.00	N/A	14838.995	115.36	5.10	1.15
11882.888	138.64	6.58	N/A	14846.957	102.80	5.28	2.81
11901.002	131.80	6.77	N/A	14864.957	105.69	5.05	1.97
12235.849	155.64	7.57	N/A	14928.732	99.68	4.86	1.25
12536.088	105.11	6.31	N/A	14929.726	94.02	5.14	1.00

12572.991	129.52	6.78	N/A	14934.731	82.53	5.28	1.53
12573.950	118.58	6.32	N/A	15077.110	92.45	4.91	1.23
12575.047	106.25	6.29	N/A	15170.784	80.88	5.08	1.23
12575.991	110.57	7.00	N/A	15170.791	84.01	5.07	1.27
12898.116	92.25	6.13	N/A	15174.093	77.01	5.12	1.26
13014.818	93.28	6.34	N/A	15187.837	72.99	5.07	1.07
13015.832	84.39	6.15	N/A	15261.771	79.05	5.15	1.20
13016.832	71.79	5.78	N/A	15429.120	83.25	5.07	1.17
13302.975	91.91	4.79	1.34	15487.096	81.47	4.81	1.17
13984.089	127.34	4.92	1.09	15522.938	88.05	4.89	0.95
14130.853	128.24	5.10	1.22	15545.819	89.25	4.89	1.35
14397.938	129.88	4.87	1.04	15636.775	90.74	4.87	1.24
14778.991	109.83	5.06	1.11	15879.984	113.81	4.90	1.09
14790.995	103.81	5.07	1.05	15960.761	109.29	7.51	1.28
14807.917	102.51	4.97	1.02	15960.765	107.53	4.93	1.08
14838.988	102.33	5.11	0.98	16019.733	113.58	4.78	1.29
Hip 57050							
11581.046	-63.25	4.53	N/A	15172.138	-9.58	4.64	0.81
11705.827	-67.09	4.79	N/A	15174.138	-14.72	4.67	0.80
11983.009	-9.42	5.27	N/A	15188.151	-14.99	4.64	0.82
12064.864	-0.39	5.34	N/A	15189.155	6.60	4.25	0.86
12308.077	4.98	5.01	N/A	15190.153	25.56	4.11	0.93
12391.034	6.53	5.63	N/A	15191.133	28.40	4.36	0.83
12681.050	-1.92	5.15	N/A	15197.136	42.23	4.28	0.79
12804.885	10.26	5.05	N/A	15198.054	35.70	4.59	0.81
13077.104	-38.83	5.83	N/A	15199.170	36.95	4.42	0.87
13398.975	-33.44	4.33	1.02	15229.114	-28.84	4.45	0.74
13753.068	12.88	4.64	0.96	15229.958	-10.72	4.71	0.72
14131.092	1.32	4.96	0.90	15232.054	4.35	4.63	0.78
14545.002	15.61	4.55	0.79	15251.997	0.76	4.38	0.81
14546.007	22.29	4.29	0.80	15284.858	9.29	4.64	0.73
14671.811	-3.54	5.13	5.32	15636.023	-32.36	4.31	0.90
14955.894	9.12	4.47	0.83	15671.915	-13.93	4.34	0.92
14963.930	-13.66	4.43	0.80	15698.820	16.56	5.97	7.95
15014.782	-46.65	4.50	0.70	15707.812	-12.89	4.66	0.88
15015.804	-47.40	4.41	0.72	15723.769	-34.04	4.41	0.92
15041.758	11.31	5.04	0.83	15903.064	12.42	4.40	0.83

Table 3.6: RVs and $S_{\rm HK}$ values for systems with long-term RV accelerations

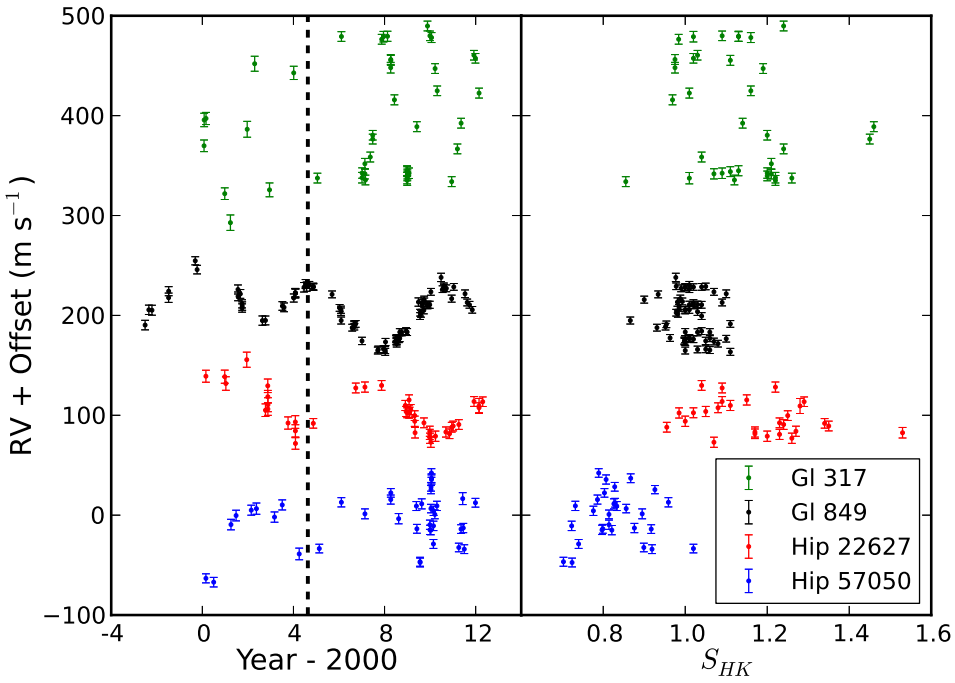

Figure 3.19: (left) RV time series for our four systems exhibiting long-term RV accelerations. The vertical line in 2004 represents the HIRES detector upgrade in August of that year. (right) RVs as a function of $S_{\rm HK}$. All four RV accelerations are visible, but none of the RV data appear to correlate with $S_{\rm HK}$, commonly used as a proxy for stellar chromospheric activity.

Chapter 4

PHYSICAL PROPERTIES OF THE TRANSITING BROWN DWARF LHS 6343 C

In this chapter I focus on LHS 6343 C, a brown dwarf transiting one member of an M+M binary in the *Kepler* field. Given the relative brightness of the host star and the high signal-to-noise ratio on the individual transits themselves, analyzing this system was a test of the limits of *Kepler* data: given a sufficiently high signal transit, what limits our precision? Are there any assumptions we often make, such as details of limb darkening, that will eventually break down? Are there any robust methods to characterize the star without relying on the fine details of any particular set of stellar models? This chapter was originally published as "Characterizing the Cool KOIs. VII. Refined Physical Properties of the Transiting Brown Dwarf LHS 6343 C," ApJ, 800, 134 (2015) by BTM, John Johnson, Phil Moorhead, Ashley Villar, Corinne Vassallo, Cristoph Baranec, Nick Law, Reed Riddle, Geoff Marcy, Andrew Howard, and Howard Isaacson.

4.1 Introduction

The growth of brown dwarf astronomy has closely mirrored that of exoplanetary astronomy. Although Latham et al. (1989) discovered a likely brown dwarf candidate, the first confirmed detection of a brown dwarf was announced two months before the announcement of the first exoplanet orbiting a main sequence star (Mayor & Queloz 1995; Rebolo et al. 1995). That same year also saw the discovery of the first brown dwarf orbiting a stellar-mass companion (Nakajima et al. 1995). Today, more than 2,000 brown dwarfs have been discovered. The majority of these substellar objects have no detected companions, so characterization is often limited to spectroscopic observations. In these cases, the atmosphere of the brown dwarf can be extensively studied (e.g. Burgasser et al. 2014; Faherty et al. 2014), but its physical parameters, including mass and radius, cannot be measured directly.

When a brown dwarf with a gravitationally bound companion is detected, detailed characterization of its physical properties is possible. Radial velocity (RV) surveys have produced a significant number of brown dwarf candidates with minimum mass determinations (e.g. Patel et al. 2007). Astrometric monitoring of directly imaged brown dwarf companions to stars has led to dynamical mass measurements of

brown dwarfs (Liu et al. 2002; Dupuy et al. 2009; Crepp et al. 2012b). While there are many brown dwarfs with measured masses, radii can only be directly measured in transiting or eclipsing systems. The first eclipsing brown dwarf system, discovered by Stassun et al. (2006) in the Orion Nebula, produced the first measurement of a brown dwarf's radius and the first test of theoretical mass-radius relations. Today, there are eleven brown dwarfs with measured masses and radii (Díaz et al. 2014a). Of this sample, eight transit a stellar-mass companion and only four are not inflated due to youth or irradiation. If the brown dwarf is assumed to be coeval with its host star, the brown dwarf's age and metallicity can be estimated. Both properties are expected to affect the brown dwarf mass-radius relation, making observations of transiting brown dwarfs especially valuable (Burrows et al. 2011).

Recently, four brown dwarfs have been detected by the *Kepler* mission (Bouchy et al. 2011a; Johnson et al. 2011b; Díaz et al. 2013; Moutou et al. 2013). Launched in 2009, the *Kepler* telescope collected wide-field photometric observations of approximately 200,000 stars in Cygnus and Lyra every 30 minutes for 4 years (Borucki et al. 2010). The mission was designed as a search for transiting planets. As brown dwarfs have radii similar to Jupiter, brown dwarfs were also easily detected; only a few RV observations are necessary to distinguish between a giant planet and brown dwarf companion (e.g. Moutou et al. 2013).

The first unambiguous brown dwarf detected from *Kepler* data was found in the LHS 6343 system and announced by Johnson et al. (2011b, hereafter J11). The authors analyzed five transits of the primary star observed in the first six weeks of *Kepler* data, combined with one transit observed in the Z-band with the Nickel telescope at Lick observatory and 14 RV observations with Keck/HIRES. The authors also obtained PHARO adaptive optics imaging data from the Palomar 200 inch telescope, imaging a companion 0.5 magnitudes fainter than the primary at a separation of 0.7 arcsec. From these observations, the authors were able to measure a mass for the brown dwarf of 62.7 ± 2.4 M_{Jup}, a radius of 0.833 ± 0.021 R_{Jup}, and a period of 12.71 days, corresponding to a semimajor axis of 0.0804 ± 0.0006 AU. The authors define LHS 6343 A as the primary star, LHS 6343 B as the widely-separated binary M dwarf, and LHS 6343 C as the brown dwarf orbiting the A component, and note the architecture of this system is very similar to the NLTT 41135 system discovered by Irwin et al. (2010).

Additional papers have expanded our knowledge of LHS 6343. Southworth (2011) re-fit the *Kepler* light curve, using data through Quarter 2 from the mission. By

fitting the observations using five different sets of stellar models, he attempted to reduce biases caused by any one individual stellar model. He found different models provide a consistent brown dwarf radius at the 0.08 R_{Jup} level, but found a higher mass than J11: his best fitting mass for LHS 6343 C was 70 ± 6 M_{Jup}. Oshagh et al. (2012) analyzed the lack of transit timing variations in the system, finding that any additional companions to LHS 6343 A with an orbital period smaller than 100 days must have a mass smaller than that of Jupiter. With 6 quarters of *Kepler* data, Herrero et al. (2013) measured a photometric rotation period of 13.13 ± 0.02 days for LHS 6343 A. The authors also claimed to observe spot-crossing events during the transits of LHS 6343 A, as well as out-of-transit photometric modulation with a period consistent with the orbital period of LHS 6343 C. Herrero et al. (2014) updated this work, concluding that the out-of-transit variations are dominated by relativistic Doppler beaming.

In many of the papers about the LHS 6343 system after the discovery paper, the authors assumed the physical parameters of J11. This is not necessarily an ideal assumption to make. J11 used a limited dataset during their analysis. Their photometry consisted of only six transits and 14 RVs, and they estimated the third light contribution of LHS 6343 B by extrapolating from near-IR observations to the *Kepler* bandpass. Moreover, the derived stellar parameters in that paper were based only on photometric observations and depend strongly on the accuracy of the Padova model grids (Girardi et al. 2002) upon which they are based.

The conclusion of the primary *Kepler* mission affords us an opportunity to reanalyze the LHS 6343 system using the complete *Kepler* dataset. Such a reanalysis enables us to better measure the brown dwarf's mass and radius. There are only three non-inflated brown dwarfs with both a mass and radius measured to 5% or better: LHS 6343 C, KOI-205 b (Díaz et al. 2013), and KOI-415 b (Moutou et al. 2013). To test theoretical brown dwarf evolutionary models, we would like to measure the masses, radii, and metallicities of these objects as precisely as possible. In this work, we analyze the full *Kepler* dataset for this object to measure the transit profile. We combine this light curve with additional RV observations, near-infrared spectroscopy of LHS 6343 AB, and Robo-AO visible-light adaptive optics. Without any reliance on stellar models beyond an empirical main sequence mass-radius relation, we are able to measure the mass of LHS 6343 C to a precision of 3% and the radius to a precision of 2%. Beyond the empirical main-sequence relation, the mass and radius measurements depend only on the following parameters, all measured

directly from the data: the orbital period, stellar density $\rho_\star$, reduced semimajor axis $a/R_\star$, Doppler semiamplitude K, eccentricity, and inclination. Our technique allows one to calculate the mass and radius for both members of a transiting system. We also combine our data with the predictions for the mass of LHS 6343 A from the Dartmouth stellar evolutionary models of Dotter et al. (2008). These combined data enable us to measure a model-dependent mass and radius of LHS 6343 C to better than 2% each; we also measure a metallicity of the system of 0.02 ± 0.19 dex.

In Section 4.2 we describe the observations used in this paper. In Section 4.3 we outline our data analysis pipeline. In Section 4.4 we present our results. In Section 4.5 we summarize our present efforts and outline our future plans to measure the brown dwarf's luminosity.

This study presents, to date, the most precise mass and radius measurements of a non-inflated brown dwarf. Observations such as these are essential for future detailed characterization of field brown dwarfs.

4.2 Observations

Kepler Photometry

The LHS 6343 system (KIC 10002261, KOI-959) was part of the initial *Kepler* target selection and was observed during all observing quarters in long cadence mode. Between 22 February 2011 and 14 March 2011, the system was also observed using *Kepler*'s short cadence mode, with observations collected every 58.84876 seconds in the reference frame of the spacecraft. We downloaded the entire dataset from the NASA Multimission Archive at STScI (MAST).

For both long and short cadence observations, *Kepler* data consist of a postage stamp containing tens of pixels, a small number of which are combined to form an effective aperture. The flux from all pixels in the aperture are combined to create a light curve. The *Kepler* team defines an aperture for all targets and performs aperture photometry as a part of their Photometric Analysis (PA) pipeline, which produces a light curve from the pixel-level data (Jenkins et al. 2010). This pipeline also removes the photometric background and cosmic rays.

In analyzing the pipeline-generated light curve, we detected occasional anomalies during transit events, with the recorded flux systematically larger than expected. These anomalies were also detected by Herrero et al. (2013), who attribute them to occultations of spots on LHS 6343 A by LHS 6343 C. The anomalies occur only in the long cadence data, and only when the transit is symmetric around one data point

in the *Kepler* time series, so that the central in-transit flux measurement would be expected to be significantly lower than the surrounding data points. By investigating the pixel-level data, we find that each anomaly has been registered as a cosmic ray by the PA pipeline, and "corrected" to an artificially large value.

Using the pixel-level data, recorded before the cosmic ray correction in the pipeline, we removed these artificial corrections. We find the anomalies can be completely explained as false cosmic ray detections: there is no evidence for transit-to-transit variability in the *Kepler* data.

We expect stellar granulation to induce correlated photometric variability only at a level significantly below the precision of our observations. Correlated noise attributed to stellar granulation has been previously observed when modeling transits of companions to higher mass stars (e.g. Huber et al. 2013) and used to derive fundamental parameters of the stars themselves (Bastien et al. 2013). Both the timescale and magnitude of the correlated noise are inversely proportional to the stellar density (Gilliland et al. 2010). For an M dwarf with a mass around $0.3 M_{\odot}$, we expect granulation to induce correlated noise with a period of approximately 10 seconds and an amplitude of 50 ppm (Winget et al. 1991). Therefore, given the precision and cadence of the *Kepler* observations we do not expect to observe correlated noise due to granulation in the LHS 6343 system.

We tested for correlated noise on transit timescales by calculating the autocorrelation matrix for out-of-transit sections of the data. For both long cadence and short cadence data, all off-diagonal elements have absolute values less than 0.03; we found no periodic structure to the autocorrelation matrix. Therefore, on transit timescales the noise can be treated as white.

We converted all times recorded by *Kepler* to Barycentric Dynamical Time (TDB), not UTC, which was mistakenly recorded during the first three years of the mission. As a result, our times differ from those reported in the analysis of J11 by 66.184 seconds.

We then detrended the light curve to remove the effects of stellar and instrumental variability. For all transit events with at least four data points recorded continuously before and after the transit, we selected a region bounded by a maximum of three transit durations on either side of the nominal transit center. If there is any spacecraft motion, such as a thruster fire or data downlink, we clipped the fitting region to not include these data. We then fit a second-order polynomial to the out of transit

flux. We normalized the light curve by dividing the observed flux values by the calculated polynomial. We repeated this procedure near the midpoint between successive transits in order to search for evidence of a secondary eclipse. We estimated the noise level in the data by measuring the variance observed in the out of transit segments of the data.

Keck/HIRES Radial Velocities

We obtained spectroscopic observations of LHS 6343 using the HIgh Resolution Echelle Spectrometer (HIRES, $R \approx 48{,}000$) at the W. M. Keck Observatory. All observations were taken using the C2 decker. With a projected length of 14.0 arcsec, the decker enables accurate sky subtraction. The first four observations were obtained using a 45 minute exposure time and the standard iodine-cell setup described by Howard et al. (2010b). Once LHS 6343 C was identified as an transiting brown dwarf, the remaining observations were obtained with 3 minute exposure times and without the iodine cell. For all observations, the slit was aligned along the binary axis so that light from both stars fell upon the detector.

To measure the RV of LHS 6343 A, we used LHS 6343 B as a wavelength reference. We began with an iodine-free spectrum of HIP 428, oversampled onto a grid with resolution 15 m s^{-1}. For each observation, we restricted our analysis to the 16 orders covered by the "green" CCD chip, which covers the region typically used in iodine cell analyses, as well as the first two orders covered by the "red" chip where telluric contamination is negligible. From these 18 orders, we first estimated and divided out the continuum flux level following the method of Pineda et al. (2013). We then removed the regions of the spectrum contaminated by telluric lines. We added to this template a shifted, scaled version of itself to represent LHS 6343 B. We varied the positions of both stars and compared to the observed spectrum of LHS 6343 in order to find the maximum likelihood velocity separation between the two stars. By assuming the relative RV of LHS 6343 B does not change over our observing baseline, our method enables us to measure the RV of LHS 6343 A relative to that of a stationary wavelength calibration source observed simultaneously.

There is no evidence of orbital motion of LHS 6343 B at the level of our RV precision. From an observed projected separation and mass estimate we can estimate the maximum expected RV acceleration induced by a companion. Following Torres (1999) and Knutson et al. (2014), the maximum RV acceleration is defined such

that

$$|\dot{v}| < 68.8\text{m } s^{-1} \ yr^{-1}\left(\frac{M_{comp}}{M_{Jup}}\right)\left(\frac{d}{\text{pc}}\frac{\rho}{arcsec}\right)^{-2}, \quad (4.1)$$

for a system at a distance d, with a companion with mass M_{comp} at an angular separation ρ. For a companion with a mass approximately 30% of the Sun's and a projected separation ($d\rho$) of approximately 20 AU, we expect a maximum RV acceleration of 40 m s^{-1} yr^{-1}. We would only observe this RV acceleration if we happened to observe the two stars at the time of their maximum orbital separation and if their orbit was edge-on to our line of sight. Our RV signal is considerably larger than any effects induced by LHS 6343 B; any RV acceleration over our three-year baseline is similar in size to our measurement uncertainties.

The median RV precision of our observations is 85 m s^{-1}. Our RV precision is much lower ($\approx$ 400 m s^{-1}) for the first four observations when the spectra are contaminated by the iodine cell. Our RV precision is also impeded when the difference between the RV of LHS 6343 A and LHS 6343 B is smaller than one-half of a pixel, about 500 m s^{-1}.

A table of our RVs is included as Table 4.1.

Visible-light Adaptive Optics Imaging

J11 estimated the third-light contribution of LHS 6343 B in the *Kepler* bandpass by extrapolating from JHK adaptive optics observations using the Padova model atmospheres of Girardi et al. (2002). To minimize any potential biases that may be induced by their reliance on stellar models, we obtained adaptive optics imaging of LHS 6343 with the Robo-AO laster adaptive optics and imaging system on the Palomar Observatory 60-inch telescope (Baranec et al. 2014). Robo-AO successfully observed thousands of KOIs; we used their standard setup (Law et al. 2014). With SDSS g, r, and i filters (York et al. 2000), we imaged the system on UT 2013 21 July; we observed the system again in g band on UT 2013 27 July. Each observation consisted of full-frame-detector readouts at 8.6 Hz for 90 seconds. We use 100% of the frames during each integration. The images were then combined using a shift-and-add processing scheme, using LHS 6343 A as the tip-tilt star. At all wavelengths, we detected both LHS 6343 A and LHS 6343 B, as shown in Figure 4.1. While we would be sensitive to a change in the position angle between the two M dwarfs of two degrees, we do not detect any orbital motion of LHS 6343 B relative to LHS 6343 A between the original Palomar/PHARO data in 2010 and these observations in 2013.

JD −2440000	RV (km s^{-1})	Uncertainty (km s^{-1})
15373.095	12.993	0.498
15373.998	13.878	0.429
15377.078	3.041	0.425
15377.098	2.825	0.423
15378.030	-2.470	0.562
15379.052	-4.599	0.076
15380.127	-5.967	0.082
15380.827	-5.412	0.089
15380.831	-5.015	0.166
15395.984	3.726	0.084
15396.970	8.522	0.068
15404.974	-5.447	0.092
15405.821	-5.618	0.074
15406.865	-3.860	0.086
15407.853	-0.495	0.666
15413.032	11.540	0.072
15414.009	7.951	0.089
15668.120	8.714	0.161
15669.083	4.243	0.174
15673.982	-3.661	0.083
15705.917	10.005	0.093
15843.859	13.444	0.084
16116.017	-3.562	0.077
16164.014	8.408	0.064
16172.915	10.070	0.078
16192.886	-4.885	0.073
16498.042	-5.035	0.079
16506.891	9.963	0.073
16513.001	-3.995	0.081
16513.988	0.033	0.733
16522.939	-3.889	0.078
16524.890	-5.555	0.113
16524.892	-5.473	0.081
16530.943	13.348	0.092

Table 4.1: Radial Velocities for LHS 6343 A

To calculate the relative flux ratio of the two stars in each bandpass, we sky-subtract our observations and measure the flux inside a 0.5 arcsec aperture centered on each star. The point spread functions of each star are larger than the apertures, so each aperture contains light from both stars. We subtract out the contamination from each star by measuring the flux in a similar aperture on the opposite side of each

star.

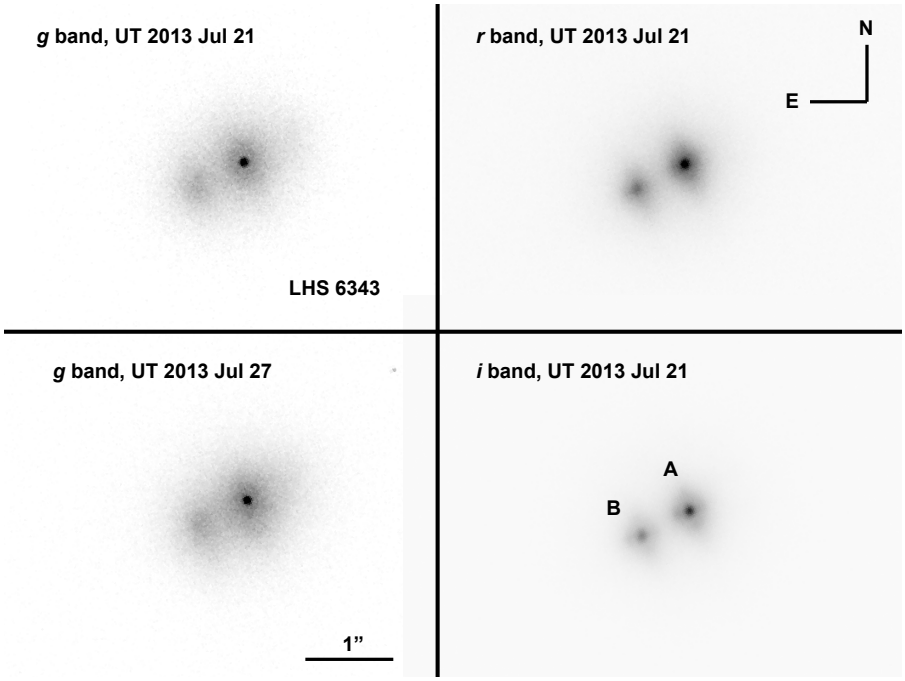

Figure 4.1: Robo-AO adaptive optics imaging of the LHS 6343 system taken with three different bandpasses. Both the scale and orientation are held constant across all images. We obtained two images of the system in the g-band, six days apart. We obtained a single image of the system in both the r- and i-bands.

In our g-band data we observed tripling, induced when the shift-and-add processing algorithm temporarily locks on LHS 6343 B instead of LHS 6343 A. Tripling causes the appearance of an artificial third object coaxial with the two real objects. The third object is observed to have the same projected separation between the primary as the true secondary, at a position angle offset of 180 degrees, as discussed by Law et al. (2006). By measuring the flux ratios between the primary star and the two imaged companions, and defining $I_{jk} \equiv F_j/F_k$, then the true binary flux ratio F_R is

$$F_R = \frac{2I_{13}}{I_{12}I_{13} + \sqrt{I_{12}^2 I_{13}^2 - 4I_{12}I_{13}}}, \tag{4.2}$$

where F_1 is the observed flux from the primary component, F_2 the observed flux from the secondary component, and F_3 the observed light from the tertiary, “tripled” component. When $F_3 = 0$ this equation is undefined, but the asymptotic behavior is correct.

We find the third light contributions in each bandpass are given such that $\Delta g = 0.93 \pm 0.07$, $\Delta r = 0.74 \pm 0.06$, and $\Delta i = 0.57 \pm 0.05$. From these, we interpolate

using the Dartmouth stellar models to calculate a value for the third light in the *Kepler* bandpass, which encompasses roughly the g, r, and i filters. We find $\Delta K_p = 0.71 \pm 0.07$ magnitudes. This is consistent with the extrapolation of J11, who predict a third-light in the *Kepler* bandpass of $\Delta K_p = 0.74 \pm 0.10$.

NIR Spectroscopy

The transit light curve itself can be used to measure some properties of LHS 6343 A, such as the stellar density. Other parameters such as the stellar temperature, as well as all physical properties of LHS 6343 B, can only be estimated by relying on stellar models. To inform the models, on UT 2012 July 05 we obtained simultaneous JHK spectroscopy with the TripleSpec Spectrograph on the 200" Hale Telescope at Palomar Observatory. TripleSpec is a near-infrared slit spectrograph with a resolving power ($\lambda/\Delta\lambda$) of 2700 (Wilson et al. 2004; Herter et al. 2008).

Observations were collected on four positions along the slit, ABCD, to minimize the effects of hot and dead pixels on the spectrograph detector. Each exposure was 30 seconds long in order to achieve a signal-to-noise ratio of 60. We then observed a nearby, rapidly rotating A0V star to calibrate absorption lines caused by the Earth's atmosphere.

To reduce the data, we followed the methodology of Muirhead et al. (2014), using the SpexTool reduction package of Cushing et al. (2004). We differenced the A and B observations and the C and D observations separately, then extracted the combined-light spectrum and combined the separate observations with SpexTool. To remove the system's absolute radial velocity of -46 km s^{-1}, we cross-correlated the spectrum with data from the IRTF spectral library (Cushing et al. 2005; Rayner et al. 2009), then applied an offset to the wavelength solution corresponding to the peak of the cross-correlation function. The result is a single spectrum displaying the combined light from LHS 6343 A and LHS 6343 B, as shown in Figure 4.2

4.3 Data Analysis

Temperature and Metallicity of LHS6343 A and B

We measured the temperature of each star following the method of Rojas-Ayala et al. (2012), who built on the efforts of Covey et al. (2010) to determine a relation between K-band spectroscopic features and the temperature and metallicity of M dwarfs. Specifically, Rojas-Ayala et al. define a temperature-sensitive "H_2O–K2

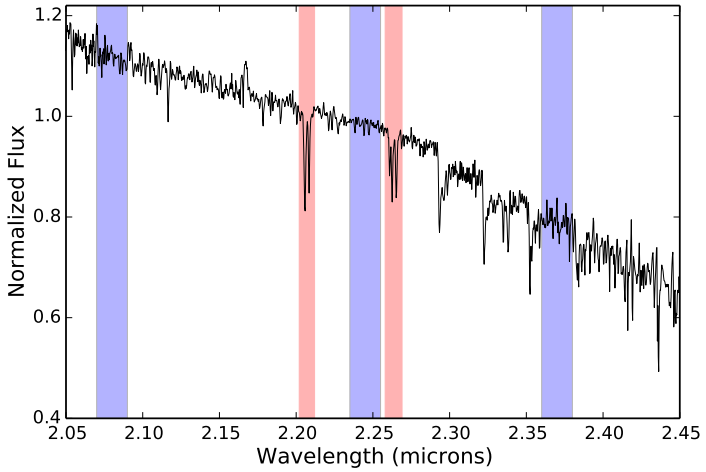

Figure 4.2: Combined-light K-band spectrum for the LHS 6343 system. The broad, blue shaded regions are used to derive the "H_2O–K2 water index," as described in Section 4.3. The narrow, red shaded regions encompass the sodium doublet and calcium triplet. Together, these regions have been used to develop empirical relations for the temperature and metallicity of M dwarfs (Rojas-Ayala et al. 2012).

water index," representing the water opacity between 2.07 μm and 2.38μm:

$$H_2O\text{–K2} = \frac{\langle \mathcal{F}\,(2.070 - 2.090)\rangle / \langle \mathcal{F}\,(2.235 - 2.255)\rangle}{\langle \mathcal{F}\,(2.235 - 2.255)\rangle / \langle \mathcal{F}\,(2.360 - 2.380)\rangle}. \tag{4.3}$$

Here, $\langle \mathcal{F}\,(a - b)\rangle$ represents the median flux level in the region $[a, b]$, with both a and b in μm. They also defined a relation between a star's metallicity, the H_2O–K2 index, and the equivalent width of the 2.21 μm sodium doublet and 2.26 μm calcium triplet. We calculated H_2O–K2 and the two equivalent widths, as well as their uncertainties, by creating a sequence of simulated spectra in which random noise is added to the observed flux consistent with the flux uncertainty at each wavelength. We found the calculated H_2O–K2 values to be normally distributed such that $H_2O\text{–K2} = 0.919 \pm 0.002$. The equivalent width of the sodium doublet is 5.533 ± 0.101 Å and the equivalent width of the calcium triplet is 3.863 ± 0.089 Å.

If our spectrum consisted of the flux from only one star, we could convert our value directly into a stellar effective temperature and metallicity. In this case, each value is really the combination of two separate values, one for each M dwarf. However, if we assume the two stars have the same metallicity, useful information can still be extricated. We first drew from the posterior of ΔK values from our PHARO near-infrared adaptive optics observations and our posteriors for H_2O–K2 and the equivalent widths. From these, we used the relations of Rojas-Ayala et al. (2012) to

calculate the system metallicity. We then interpolated the table provided in that paper to find a relation between H_2O–K2 and effective temperature for a given metallicity. Using the Dartmouth stellar evolution models, we then determined which two modeled stars best fit both the observed flux ratio and combined H_2O–K2 index value. By repeating this process many times, continuously drawing from the posteriors for each measured value we determined a posterior on the temperature, and by extension the mass, of each star. The joint posterior on the temperature of the two stars is shown as Figure 4.3.

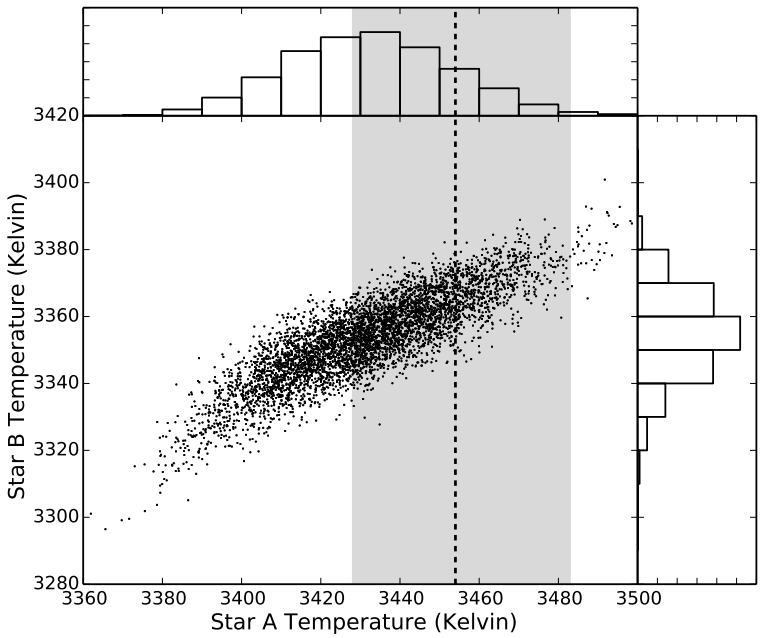

Figure 4.3: Joint posterior on the effective temperature of LHS 6343 A and LHS 6343 B. Marginalizing over the temperature of each star separately, we find the A component has a temperature of 3431 ± 21 K and the B component has a temperature of 3354 ± 17 K. The dashed line and shaded region correspond to the temperature of LHS 6343 A expected based on our model-independent mass measurement from the combined transit and RV fit.

Transit Parameters

To measure the parameters of LHS 6343 C, we forward modeled the LHS 6343 A-C system over the timespan from the launch of *Kepler* to the date of the final RV observation in 2013. At each time corresponding to an RV observation, we calculated the expected radial velocity relative to a stationary LHS 6343 B assuming a Keplerian orbit. At each *Kepler* timestamp during a transit or near the expected time of

secondary eclipse, we calculated the expected relative flux assuming a Mandel & Agol (2002) light curve model. We fit four limb darkening parameters using the prescription of Claret & Bloemen (2011), allowing the value for each limb darkening coefficient to float as a free parameter. In calculating the light curves, we used an adapted version of the PyAstronomy package[1], modified to allow eccentric orbits.

In all, we fit for 16 parameters: $\sqrt{e}\cos\omega$, $\sqrt{e}\sin\omega$, time of central transit, orbital period, brown dwarf mass, orbital inclination, LHS 6343 A-C radius ratio, four limb darkening parameters, the third light from LHS 6343 B, log(g) of LHS 6343 A, the secondary eclipse depth, the stellar mass, and the RV zeropoint (relative to LHS 6343 B). We did not use an RV jitter term, as our RV uncertainties of $\sim$ 100 m s^{-1} are significantly larger than the jitter expected for a main-sequence M dwarf. We used `emcee`, an affine-invariant ensemble sampler described by Goodman & Weare (2010) and implemented by Foreman-Mackey et al. (2013), to maximize the likelihood function

$$\begin{aligned}\mathcal{L} &= 0.5\Big[\sum_i \left(\frac{\mathrm{RV}_{\mathrm{model},\,i} - \mathrm{RV}_{\mathrm{observed},\,i}}{\sigma_{\mathrm{RV},i}}\right)^2 \\ &+ \sum_i \left(\frac{f_{\mathrm{model\ SC},\,i} - f_{\mathrm{observed\ SC},\,i}}{\sigma_{f_{\mathrm{SC}},i}}\right)^2 \\ &+ \sum_i \left(\frac{f_{\mathrm{model\ LC},\,i} - f_{\mathrm{observed\ LC},\,i}}{\sigma_{f_{\mathrm{LC}},i}}\right)^2\Big]. \end{aligned} \tag{4.4}$$

Here, f_{LC} corresponds to the observed flux in the *Kepler* long cadence data and f_{SC} corresponds to the short cadence data. The period we fit and report here is the period observed in the frame of an observer at the barycenter of the solar system, not in the frame of the LHS 6343 system. That is, we do not correct for relativistic effects induced by the star system's systemic velocity.

We imposed two different priors on the stellar mass, reflecting various levels of trust in theoretical stellar evolutionary models. First we apply the stellar empirical mass-radius relation of Boyajian et al. (2012), which encodes no direct model-dependent information, as a prior We use their relation for "single stars." While our star has a wide binary companion at tens of AU, the single collection is more representative of LHS 6343 A than the short-period eclipsing binaries used to build the eclipsing binary main sequence of Boyajian et al. (2012). Given a precise measurement of the stellar density $\rho_\star$, semimajor axis $a/R_\star$, Doppler semiamplitude K, eccentricity,

[1] https://github.com/sczesla/PyAstronomy

and inclination, the mass and radius of both the primary and secondary star can then be calculated.

We next repeated this analysis, applying a prior on the stellar mass using the spectroscopic parameters from our TripleSpec analysis, as described in Section 4.3.

In each of these cases, we can calculate the mass and radius of LHS 6343 B through the Dartmouth models by comparing the relative brightness of LHS 6343 A and LHS 6343 B in conjunction with the (now known) mass of LHS 6343 A. We can also measure a model-dependent distance to the system, which depends both on our measured mass and the mass-luminosity relation encoded in the stellar models.

The best fit model to the light curve data and RVs are plotted in Figures 4.4 and 4.5, respectively.

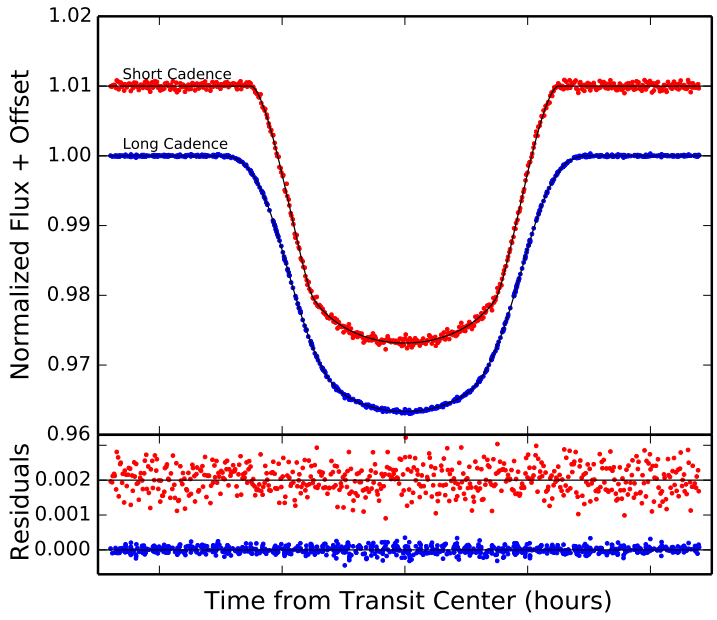

Figure 4.4: Phase-folded transit light curve, fit to the maximum likelihood model. Blue points represent long cadence data and red points represent short cadence data. The scale of the residuals is a factor of five larger than the scale of the light curve.

4.4 Results

The orbital parameters for LHS 6343 C are listed in Table 4.2. The physical properties of the LHS 6343 system are listed in Table 4.3. In the latter table, we include two columns of values. The first set of values represents the values we find using our data-driven model, using only the empirical mass-radius relation of Boyajian

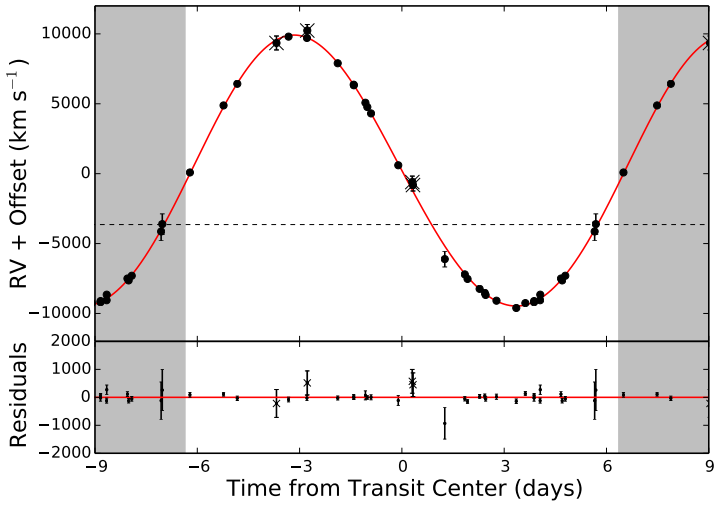

Figure 4.5: Phase-folded RV curve, fit to the maximum likelihood model. For the majority of observations, the data points are larger than the size of the error bars. The gray shaded regions represent an extension of the RV data beyond one phase to provide clarity for the reader. Observations marked with an cross represent data collected while using the iodine cell. The dashed line represents the RV of LHS 6343 B, which does not change at the level of our precision over the 3-year RV baseline.

et al. (2012) without any direct use of stellar models. The second set of values corresponds to the inclusion of a model-dependent prior on the stellar mass. In this case, we impose as a prior our mass derived from the near-IR spectroscopy, found in Section 4.3.

We find that we are able to measure the observed transit depth, uncorrected for the third light contributions of LHS 6343 B, to a precision of 0.5%. We are additionally able to measure the Doppler semiamplitude K to 0.3%. Therefore, our uncertainties in the brown dwarf's physical parameters are dominated by the uncertainties on the absolute physical parameters of the two M dwarfs in the system.

We can measure the stellar mass directly from the light curve and RV observations without any direct reliance on theoretical stellar models, as shown in the Discussion. In this case, we measure a mass for LHS 6343 A of 0.381 ± 0.019 $M_\odot$ and a radius of 0.380 ± 0.007 $R_\odot$. We then find a mass and radius of LHS 6343 C of 64.6 ± 2.1 M_{Jup} and 0.798 ± 0.014 R_{Jup}, respectively. Thus, in this case we can measure the mass of the brown dwarf to a precision of 3.2% and the radius to 1.8%.

From our near-IR spectroscopic analysis of the system, we measure a temperature

for LHS 6343 A of 3431 ± 21 K, which gives us a mass of 0.339 ± 0.016 $M_\odot$. We repeat our analysis, using this value as a prior on our stellar mass. In this case, we find a value for the stellar mass between our empirical value and that imposed by our model prior: 0.358 ± 0.011 $M_\odot$. We then find a mass for the brown dwarf of 62.1 ± 1.2 M_{Jup} and a radius of 0.782 ± 0.013 R_{Jup}. This is a model-dependent mass measured to a precision of 1.9% and a model-dependent radius to 1.4%.

Our brown dwarf mass is consistent with that found by J11, while our radius is smaller at the 1.4σ level. Part of this discrepancy may be due to the choice of models used: these authors used the Padova model grids of Girardi et al. (2002). These models predict a larger mass than both the Dartmouth models we use and the BT-Settl models (Allard & Freytag 2010). Using the Padova models, the authors of the discovery paper adopted a slightly smaller log(g), which for a given mass implies a larger star, and therefore a larger planet. The discrepancy may also be affected by our choices of limb darkening models: the authors of the discovery paper use a quadratic limb darkening model. With only five transits observed, this is a reasonable choice. Given the signal to noise obtained from fitting four years of *Kepler* data simultaneously, we require a four-parameter limb darkening solution to develop an appropriate model fit.

Our mean density for LHS 6343 C is 40% larger than that reported in the discovery paper. This appears to be because the authors of that paper misreported their density, as it is inconsistent with their reported mass and radius. These authors may have reported the density relative to Jupiter, not in units of g cc^{-1} as listed in their Table 5. Even with this correction, the density we report is larger than the density of J11 due to the difference in the radius of the brown dwarf described in the previous paragraph.

We measure a period of 12.7137941 ± 0.0000002 days in the frame of the solar system. The uncertainty in the period is 17 milliseconds, and the period is measured to a precision of 15 parts per billion.

We measure the total mass in the LHS 6343 AC system to a precision of 4.8 percent. Neglecting our uncertainty in the measured period, from differentiating Kepler's Third Law we expect our measurement of the semimajor axis to be three times more precise than that of the total mass. In fact, we measure a semimajor axis of 0.0812 ± 0.0013 AU, a precision of 1.6 percent.

Secondary Eclipse Observation

J11 do not detect a secondary eclipse and can only place an upper limit of 65 parts per million on the potential eclipse depth. With a full four years of *Kepler* data, we are considerably more sensitive to eclipses. From the RVs and shape of the primary eclipse alone, we know the A-C system has a nonzero eccentricity: we find $e\cos\omega = 0.024 \pm 0.003$. As a result, we expect the secondary eclipse to occur approximately 4.5 hours after the midpoint between consecutive primary transits.

When we include a secondary eclipse in our system model, we detect a signal at 3.5σ, as shown in Figure 4.6. This eclipse has a depth of 25 ± 7 parts per million and occurs 4.44 ± 0.16 hours after the midpoint between primary transits. From these data, we measure $e\cos\omega = 0.0228 \pm 0.0008$.

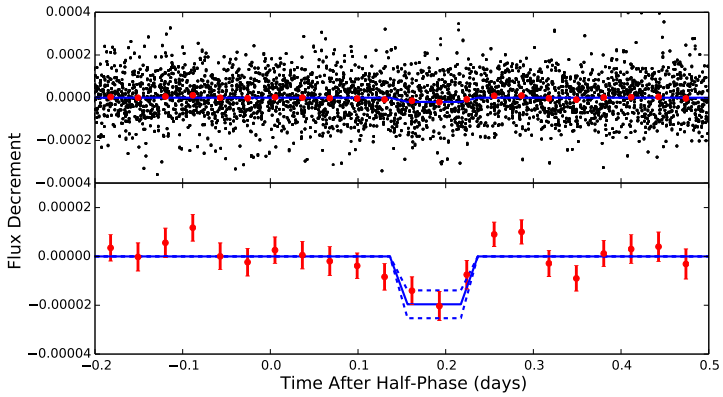

Figure 4.6: Secondary eclipse of LHS 6343 C as observed by *Kepler*. (top) In black, the *Kepler* data are phase-folded and plotted; we bin every 0.03 days of observations together to reduce the apparent scatter, as shown in red. As the noise is nearly completely white, this is justified for plotting purposes. In blue is our best-fitting secondary eclipse model. We treat the brown dwarf as a uniform sphere in our modeling efforts. (bottom) Same as the above, excluding the raw data. We detect an eclipse depth of 25 ± 7 ppm after accounting for the correction for the third light contribution from LHS 6343 B. The dashed blue lines represent the 1σ deviation in eclipse depth from the best-fitting model.

Distance to the LHS 6343 System

There is, at present, no measured parallax to the LHS 6343 C system. We must therefore rely on stellar models to convert the measured apparent magnitudes to distance estimates. J11, using the Padova model atmospheres, announced a distance to the system of 36.6 ± 1.1 pc. The Dartmouth models predict a lower mass, and therefore a lower luminosity for LHS 6343 A, so to maintain the observed brightness of

the system from g to K_s-band, these models require a smaller distance modulus. We find a model-dependent distance to the system of 32.7 ± 1.3 pc. A measured parallax to this system, either from the ground or from Gaia, will be useful for resolving the 2σ discrepancy between these distances, informing the upcoming next generation of stellar evolution models.

Parameter	Value		1σ Confidence Interval
Orbital Period, P [days]	12.7137941	±	0.0000002
Transit Center (TDB −2440000)	15008.07259	±	0.00001
Radius Ratio, $(R_P/R_\star)$	0.216	±	0.004
Observed Transit Depth (percent)	3.198	±	0.015
Scaled Semimajor axis, $a/R_\star$	46.0	±	0.4
Orbital Inclination, i [deg]	90.45	±	0.03
Transit Impact Parameter, b	0.36	±	0.02
Argument of Periastron ω [degrees]	-40	±	4
Eccentricity	0.030	±	0.002
Secondary Phase $(e \cos \omega)$	0.0228	±	0.0008
Secondary Depth (ppm)	25	±	7
Velocity semiamplitude K_A [km s^{-1}]	9.69	±	0.02
Star A-B RV Offset [km s^{-1}]	3.64	±	0.02

Table 4.2: Orbital Parameters for the LHS 6343 AC System. All parameters calculated by simultaneously fitting to the RV data and *Kepler* data near the times of transit and secondary eclipse.

Parameter	Value (Empirical Prior)		1σ Confidence Interval	Value (Model Prior)	1σ Confidence	Comment Interval	
Stellar Parameters							
M_A [$M_\odot$]	0.381	±	0.019	0.358	±	0.011	A
M_B [$M_\odot$]				0.292	±	0.013	A
R_A [$R_\odot$]	0.380	±	0.007	0.373	±	0.005	A
R_B [$R_\odot$]				0.394	±	0.012	A
ρ_A [$\rho_\odot$]	6.96	±	0.19	6.93	±	0.19	A
$\log g_A$ [cgs]	4.86	±	0.01	4.85	±	0.01	A
Metallicity [Fe/H]				0.03	±	0.26	B
Metal Content [a/H]				0.02	±	0.19	B
Distance [pc]				32.7	±	1.3	C
Flux Ratio $F_B/F_A, K_p$	0.461	±	0.055	0.518	±	0.032	A
ΔK_p [magnitudes]	0.84	±	0.12	0.71	±	0.07	A
$T_{eff,A}$ [K]				3431	±	21	B
$T_{eff,B}$ [K]				3354	±	17	B
Brown Dwarf Parameters							
M_C [M_{Jup}]	64.6	±	2.1	62.1	±	1.2	A
R_C [R_{Jup}]	0.798	±	0.014	0.783	±	0.011	A
Semimajor Axis, A-C System (AU)	0.0812	±	0.0013	0.0797	±	0.0008	A
Mean Planet Density, ρ_C [g cm^{-3}]	170	±	5.	173	±	5	A
$\log g_C$ [cgs]	5.419	±	0.008	5.420	±	0.008	A
T_{eq} ($T_{eff}(\frac{R_\star}{2a})^{1/2}$) [K]				358	±	3	A,B

Table 4.3: Physical Parameters for LHS 6343 ABC.
(A) Calculated by simultaneously fitting to the RV data and *Kepler* data near the times of transit and secondary eclipse.
(B) Measured from near-IR spectroscopy following the method of Rojas-Ayala et al. (2012).
(C) Calculated by fitting the observed apparent magnitudes to model-predicted absolute magnitudes.

4.5 Discussion

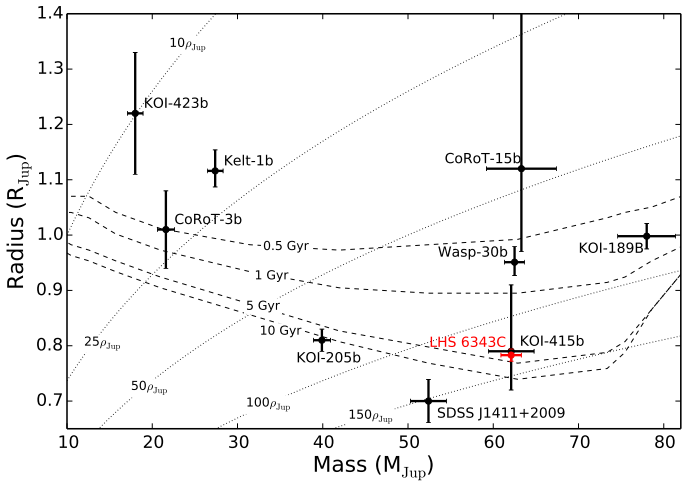

Figure 4.7: Mass-radius diagram for known transiting brown dwarfs. The dashed lines represent the Baraffe et al. (2003) isochrones for (top to bottom) ages of 0.5, 1.0, 5.0, and 1.0 billion years. The dotted lines are isodensity contours for (top left to bottom right) densities corresponding to 10, 25, 50, 100, and 150 times the density of Jupiter. LHS 6343 C has a density of 130 ± 4$\rho_{\rm Jup}$ and appears to have an age of 3-5 Gyr. Data taken from Deleuil et al. (2008), Bouchy et al. (2011b,a), Siverd et al. (2012), Díaz et al. (2013), Moutou et al. (2013), Triaud et al. (2013), Díaz et al. (2014a), and Littlefair et al. (2014). Not shown are the components of the young binary brown dwarf system 2MASS 2053-05 (Stassun et al. 2006), which have radii well above the plot range.

There are now nine brown dwarfs with measured masses and radii (Moutou et al. 2013). Of this sample, there are only four that are not inflated due to youth or irradiation. LHS 6343 C is effectively a field brown dwarf: the equilibrium temperature for an object at its orbital separation is 360 K while a 65 $M_{\rm Jup}$ brown dwarf is expected to cool to only 700 K over a Hubble time (Burrows et al. 2001). Thus, the irradiation from the primary star on the brown dwarf is negligible. Additionally, since the system has a nonzero eccentricity, the system is not tidally locked, minimizing any effects the primary star may have on any one point on the brown dwarf's surface. LHS 6343 C can be used as a laboratory to study the physics of solitary brown dwarfs, as it is effectively a field brown dwarf with a known mass, radius, and metallicity. The sample of transiting brown dwarfs that can be used to probe the physics of field brown dwarfs is highly limited, making each individual system extremely valuable.

There is some evidence that our current best understanding of the physics of brown

dwarfs is incomplete. Dupuy et al. (2009) find evidence for a "substellar luminosity problem," in which the brown dwarf binary HD 130948 BC is twice as luminous as predicted by evolutionary models. A similar result is found in the Gl 417 BC system (Dupuy et al. 2014). As these are the only two brown dwarf systems with reliable measurements of both mass and age, this result is suggestive of a fundamental issue with substellar models.

We have only a lower limit on the age of the system: J11 find no youth indicators present in the LHS 6343 system so it is likely not less than 1-2 Gyr old. Therefore, a measured luminosity would be most useful as a probe of this specific plane if the luminosity were consistent with extreme youth ($<$ 1 Gyr) or extreme age ($>$ 14 Gyr). A measured luminosity is still useful, as it allows us to locate the brown dwarf's position in the mass-radius-luminosity plane. While there is a collection of non-inflated brown dwarfs with masses and luminosities measured, there are only three with mass and radius and none with both radius and luminosity. Moreover, we also know the metallicity of the brown dwarf, assuming it has the same composition as LHS 6343 AB.

There is a degeneracy between the inferred age of the system and the atmosphere of the brown dwarf. Specifically, a brown dwarf with the mass and radius of LHS 6343 C would be expected to be significantly older if it were covered with optically-thick clouds, as the clouds would keep the brown dwarf at a hotter internal adiabat. The models of Baraffe et al. (2003), which do not include clouds, suggest an age of approximately 5 Gyr, consistent with the cloudless models of Saumon & Marley (2008). However, Saumon & Marley (2008) predict a cloudy brown dwarf with a mass of LHS 6343 C and an age equal to the age of the universe would have a radius 2σ larger than that observed for this object. This is consistent with the models of Burrows et al. (2011), who find the system must be very old if LHS 6343 C has a thick layer of clouds. These authors claim thinner clouds or no clouds may be preferred by the data. Therefore, any additional observations which suggest the presence of clouds on LHS 6343 C would be at odds with the predictions from theoretical brown dwarf model atmospheres.

The luminosity of LHS 6343 C can be measured by observing its secondary eclipses as it passes behind LHS 6343 A. In the *Kepler* bandpass, we find the eclipse depth is 25 ± 7 parts per million. Between 1 and 3 microns, the depth is expected to be 0.1%, observable with ground-based telescopes. In the 4.6 μm Spitzer bandpass, the eclipse depth may be as large as 0.5% if the brown dwarf's atmosphere is cloud-

free. We will observe this system during four secondary eclipse events in Spitzer Cycle 10, observing two eclipses in each available IRAC bandpass. In addition to probing for extreme variability caused by patchy clouds in the atmosphere of LHS 6343 C, combining these observations with the *Kepler* secondary and ground-based JHK photometry will enable us to measure a luminosity of this brown dwarf from the visible to the mid-infrared. These observations will allow us to place the first data point on the brown dwarf mass-radius-metallicity-luminosity plane, testing the underconstrained brown dwarf atmospheric models in this parameter space for the first time.

Derivation of Direct Mass and Radius Measurement

Seager & Mallén-Ornelas (2003) derive four directly observable parameters in an exoplanet light curve under a specific set of assumptions. Namely, they assume circular orbits, $M_2 \ll M_1$, and that the third light contribution from a blended star is zero. None of these are true for the LHS 6343 system. As a result, the derivation which follows provides an analytic result which is exactly true when written in terms of physical parameters, but when common approximations for these parameters in terms of observables such as the transit duration, impact parameter, and relative flux decrement during transit are substituted for these parameters, the results below only approximate the truth. When calculating physical parameters using this method, care should be taken to avoid using these oversimplified expressions.

Following Seager & Mallén-Ornelas (2003), the transit light curve enables a direct measurement of the stellar density $\rho_\star$ and the reduced semimajor axis and the stellar radius, $a/R_\star$. From these, if the stellar mass-radius relation is known, then the stellar mass can be measured directly from the light curve.

We know from Kepler's Third Law that, for two orbiting bodies with masses $M_\star$ and m_p (by convention, $M_\star > m_p$) and orbital period P, that

$$a = \left(\frac{GP^2(M_\star + m_p)}{4\pi^2}\right)^{1/3}, \tag{4.5}$$

where G is Newton's constant. The mean stellar density is defined for a star of mass $M_\star$ and radius $R_\star$ to be

$$\rho_\star = \frac{3M_\star}{4\pi R_\star^3}. \tag{4.6}$$

We can combine these two in such a way that we recover an expression for the mass

ratio that depends only on observable parameters. We find

$$1 + \frac{m_p}{M_\star} = \left(\frac{3\pi}{GP^2}\right)\left(\frac{1}{\rho_\star}\right)\left(\frac{a}{R_\star}\right)^3 \equiv c_1. \tag{4.7}$$

Famously, the Doppler semiamplitude K observed in a radial velocity survey is

$$K = \left(\frac{2\pi G}{P}\right)^{1/3} \frac{m_p \sin i}{(M_\star + m_p)^{2/3}} \frac{1}{\sqrt{1-e^2}}. \tag{4.8}$$

Here, i is the orbital inclination and e the eccentricity, while all other variables retain their previous meaning. Rearranging this equation, we can once again write the mass ratio in terms of observable parameters only. In this case,

$$\frac{m_p^3}{(M_\star + m_p)^2} = \frac{K^3 P}{2\pi G}\left(\frac{\sqrt{1-e^2}}{\sin i}\right)^3 \equiv c_2. \tag{4.9}$$

With two equations and two unknown masses, we can solve for the primary and secondary mass individually. We find

$$\begin{aligned} M_\star &= \frac{c_1^2 c_2}{(c_1 - 1)^3} \\ &= \frac{\left(\frac{9\pi}{2}\right)\left(\frac{1}{\rho_\star}\right)^2\left(\frac{a}{R_\star}\right)^6\left(\frac{K}{GP}\right)^3\left(\frac{\sqrt{1-e^2}}{\sin i}\right)^3}{\left[\left(\frac{3\pi}{GP^2}\right)\left(\frac{1}{\rho_\star}\right)\left(\frac{a}{R_\star}\right)^3 - 1\right]^3} \end{aligned} \tag{4.10}$$

$$\tag{4.11}$$

and

$$\begin{aligned} m_p &= \frac{c_1^2 c_2}{(c_1 - 1)^2} \\ &= \frac{\left(\frac{9\pi}{2}\right)\left(\frac{1}{\rho_\star}\right)^2\left(\frac{a}{R_\star}\right)^6\left(\frac{K}{GP}\right)^3\left(\frac{\sqrt{1-e^2}}{\sin i}\right)^3}{\left[\left(\frac{3\pi}{GP^2}\right)\left(\frac{1}{\rho_\star}\right)\left(\frac{a}{R_\star}\right)^3 - 1\right]^2}. \end{aligned} \tag{4.12}$$

$$\tag{4.13}$$

From the stellar density, the calculated mass can be used to measure the stellar radius. Plugging this equality in to Equation 4.6 above, we find that

$$R_\star = \frac{\left(\frac{3}{2}\right)\left(\frac{1}{\rho_\star}\right)\left(\frac{a}{R_\star}\right)^2\left(\frac{K}{GP}\right)\left(\frac{\sqrt{1-e^2}}{\sin i}\right)}{\left[\left(\frac{3\pi}{GP^2}\right)\left(\frac{1}{\rho_\star}\right)\left(\frac{a}{R_\star}\right)^3 - 1\right]}. \tag{4.14}$$

From a known stellar radius, the transit depth can be used to measure the planet radius directly. For a flux decrement ΔF,

$$R_p = R_\star \sqrt{\Delta F}. \tag{4.15}$$

Therefore, by measuring the stellar density, reduced semimajor axis, orbital period, transit depth, inclination, eccentricity, and Doppler semiamplitude, we can measure the stellar and planetary mass and radius. Moreover, since the companion is transiting, we know $\sin i \approx 1$.

Dawson & Johnson (2012) present equations for the physical parameters above in terms of parameters directly observable from the light curve. Specifically, they find, in the limit of $m_p << M_\star$,

$$\frac{a}{R_\star} = \frac{2\delta^{1/4} P}{\pi \sqrt{T_{14}^2 - T_{23}^2}} \frac{\sqrt{1-e^2}}{1 + e \sin w} \tag{4.16}$$

and

$$\rho_\star = \Big[\frac{2\delta^{1/4}}{\sqrt{T_{14}^2 - T_{23}^2}}\Big]^3 \Big(\frac{3P}{G\pi^2}\Big)\Big(\frac{\sqrt{1-e^2}}{(1 + e \sin w)}\Big)^3. \tag{4.17}$$

Here, $\delta = (R_p/R_\star)^2$ is the fractional transit depth, or the relative areas of the transiting companion and the host star. T_{14} is the transit duration from first to fourth contact (including ingress and egress), and T_{23} is the transit duration from second to third contact (excluding ingress and egress).

If we substitute these into our above equations for the stellar mass and radius, we find our expressions for the mass and radius are undefined. Specifically, our denominator, $c_1 - 1$ is undefined at $m = 0$. Our equations above work specifically in the case where the mass of the companion is not negligible. This is because the stellar density cannot be measured exactly from the light curve alone. While often neglected in exoplanet studies, the true observable is $(M_\star + m_p)/R_\star^3$. In cases where the mass ratio is large, this value approaches $M_\star/R_\star^3$, enabling the stellar density to be approximated well. For the case of a Jupiter-sized planet transiting a sun-like star, such an approximation is reasonable. However, this approximation breaks down for small mass ratios. In this case, an additional constraint is required.

An additional constraint can be provided by using the mass ratio, which can be measured by observing ellipsoidal variations in the full phase curve (Loeb & Gaudi

2003). Ellipsoidal variations have been used both to confirm transiting planets (e.g. Mislis et al. 2012) and to measure the mass ratios of already-confirmed planets (e.g. Welsh et al. 2010; Jackson et al. 2012). By including such an observation, the degeneracy between the stellar density and mass ratio can be broken and the stellar mass measured directly.

When both the mass ratio is small and ellipsoidal variations cannot be observed from the light curve, the masses can still be measured directly if the star can be assumed to fall on the main sequence, as outlined by Seager & Mallén-Ornelas (2003). For a fixed transit depth, reduced semimajor axis, and Doppler semi-amplitude, a star's inferred mass is related to the star's predicted radius such that $M \propto R^{>3}$, with the exact coefficient depending on the host-companion mass ratio (and approaching 3 as the mass ratio becomes infinite). Since the stellar main-sequence has a significantly different mass-radius relation, this information can be used to rule out many unphysical transit models. An example of this is shown as Figure 4.8.

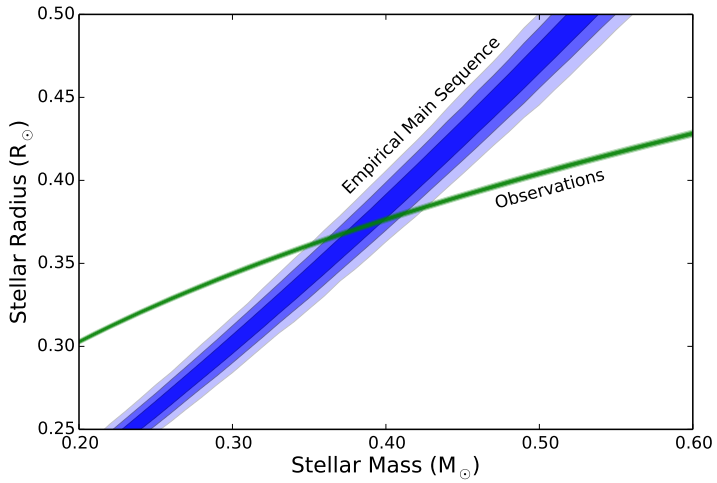

Figure 4.8: (green) Mass-radius relation for LHS 6343 A from the observed transit light curve and RV observations, plotted with (blue) the mass-radius relation for K and M dwarfs of Boyajian et al. (2012). There are many possible stellar masses and radii which are formally allowed, but are unphysical. By combining weak constraints from empirical observations of the main sequence, a robust direct measurement on the mass and radius of both LHS 6343 A and LHS 6343 C can be made.

Because a nonzero mass ratio is required, this method is likely only applicable when the companion is a hot Jupiter, transiting brown dwarf, or low-mass stellar compan-

ion. Moreover, it requires precise knowledge of both the Doppler semiamplitude and transit parameters. Therefore, the potential of this method is likely limited at present to hot transiting companions orbiting bright host stars. Yet for these cases this technique may be very useful, especially when stellar evolutionary models may have systematic errors, such as when the host is an M dwarf or subgiant star.

Chapter 5

SPITZER SECONDARY ECLIPSE OBSERVATIONS OF LHS 6343 C YIELD BRIGHTNESS TEMPERATURE AND MID-T SPECTRAL CLASS

In this chapter I continue the discussion of LHS 6343 C. Given the precise mass and radius measured in the previous chapter, we considered what observations would be necessary to compare this object to the field brown dwarfs with well-characterized atmospheres but no direct measurements of their masses and radii. We concluded the best opportunity to measure the atmosphere of the brown dwarf would be through secondary eclipses observations of the system as observed with *Spitzer*, leading to a successful Cycle-10 proposal to observe four eclipses, two in each *Spitzer* bandpass. In this chapter I analyze these data and compare them to both theoretical models of brown dwarfs and empirical observations of field brown dwarfs. This chapter was originally published as "Benchmark Transiting Brown Dwarf LHS 6343 C: Spitzer Secondary Eclipse Observations Yield Brightness Temperature and mid-T Spectral Class," ApJL, 822, 6 (2016) by BTM, John Johnson, Jonathan Fortney, and Jean-Michel Desert.

5.1 Introduction

There are only eleven brown dwarfs with measured masses and radii (Montet et al. 2015a, hereafter M15, and references therein). These objects serve as useful benchmark stars to compare theoretical predictions of physical parameters for the thousands of known brown dwarfs with measured luminosities, colors, or other atmospheric parameters (Faherty et al. 2013; Mace et al. 2013; Helling & Casewell 2014). Such comparisons are not currently possible as the only brown dwarfs with measured masses and radii and inferred atmospheric parameters are larger than field objects due to youth or irradiation and therefore not representative of their old, isolated counterparts (Stassun et al. 2006; Siverd et al. 2012).

Recently, M15 announced refined physical properties of the transiting brown dwarf LHS 6343 C (Johnson et al. 2011b), measuring a mass of 62.1 ± 1.2 M_{Jup} and a radius of 0.783 ± 0.011 R_{Jup}. These authors also detected a secondary eclipse in the *Kepler* dataset with a depth of 25 ± 7 ppm. This 3.6σ detection is insufficient for atmospheric characterization, but it allows for the possibility of observations

at other wavelengths to probe the temperature, age, and atmospheric properties of the brown dwarf. LHS 6343 C presents the first opportunity to robustly measure the atmospheric properties of an old, non-inflated brown dwarf with a known mass and radius, enabling a key connection between the field and transiting brown dwarf populations.

Spitzer (Werner et al. 2004) enables us to obtain observations of the secondary eclipse of LHS 6343 C behind LHS 6343 A, providing an opportunity to measure the emitted near-IR radiation from the brown dwarf. Given the low level of irradiation from the host star, LHS 6343 C should behave like a field brown dwarf for which direct mass and radius measurements are generally unobtainable (Section 5.5.1)

In this paper, we present detections of the secondary eclipse of LHS 6343 C in both *Spitzer* IRAC bandpasses. We measure the eclipse depths by jointly fitting a Gaussian process (GP) model to the instrumental systematics and a physical model of the astrophysical signal. We use these data to infer a temperature and age of the system through theoretical models of brown dwarf evolution, making LHS 6343 C the first non-inflated brown dwarf with a known mass, radius, and direct measurement of its atmospheric properties.

5.2 Data Collection and Analysis

We collected data during four separate eclipses with *Spitzer*, two each in the 3.6 and 4.5 μm IRAC bands (Fazio et al. 2004). These data were collected on 2014 July 06, July 19, September 21, and October 16 as a part of *Spitzer* Cycle 10 program 10122 (PI Montet). Data in both bandpasses were collected in subarray mode with 2.0 second exposures. In all observations, a 30-minute peak-up preceded the science observations to place the star on the detector "sweet-spot" to minimize pixel-phase effects (e.g. Ballard et al. 2010). Each set of science observations contains a total of 8768 frames spread over 4.9 hours approximately centered on the time of eclipse. For computational feasibility, we binned the observations by a factor of eight, giving a cadence of $\approx$16 seconds per binned data point, shorter than any astrophysical quantity of interest.

We measure the observed flux in each binned frame by performing aperture photometry, repeating this procedure 11 times with circular apertures between 1.6 and 3.5 pixels. By fitting a two-dimensional Gaussian to the 5x5 region of the detector directly surrounding the brightest pixel, we measure the position of the star on the

detector in each frame (Agol et al. 2010). We find a scatter of ~0.1 pixels during each observation. A background estimate is calculated by fitting a Gaussian to the histogram of flux values obtained over each full frame.

Noise Model

The *Spitzer* light curves are dominated by instrumental systematics largely caused by intrapixel variability in the sensitivity of the InSb detector (Charbonneau et al. 2005; Knutson et al. 2008). To account for these systematics, we fit an instrumental model simultaneously with our secondary eclipse model. Our instrumental model is the GP model of Evans et al. (2015), who employ a covariance kernel which is a function of the centroid xy coordinates of the star and the time t of the observation. For any two points i and j, their covariance is defined such that

$$K_{ij} = k_{xy} + k_t, \tag{5.1}$$

where

$$k_{xy} = A_{xy}^2 \exp\left[-\left(\frac{x_i - x_j}{L_x}\right)^2 - \left(\frac{y_i - y_j}{L_y}\right)^2 \right] \tag{5.2}$$

and

$$k_t = A_t^2 \left[1 + \frac{t_i - t_j}{L_t}\sqrt{3}\right] \exp\left[-\left(\frac{t_i - t_j}{L_t}\right)\sqrt{3}\right]. \tag{5.3}$$

Here, x_i and y_i are the centroid positions of the star during the ith observation, taken at time t_i. A_{xy} and A_t define the magnitude of the correlation between data points and L_x, L_y, and L_t define the length scales of said correlation. A larger value of K_{ij}, when the temporal or spatial separation between two points is small relative to L_t, L_x, or L_y, implies a stronger correlation.

Our noise model then has 19 free parameters. As each observation falls on a different region of the detector, A_{xy}, A_t, L_x, and L_y are not shared between observations. L_t is shared between observations. We also fit for two white noise parameters, one for each bandpass, added in quadrature to our covariance kernels.

Physical Model

Simultaneously we fit a physical model of the secondary eclipses of LHS 6343 C behind LHS 6343 A. We use the transit model of Mandel & Agol (2002) with no limb darkening, as the primary star is not being occulted: the observed flux should be unchanging between second and third contact. We fit for four separate eclipse depths, allowing for the possibility of variability similar to that observed in *Spitzer* surveys of field brown dwarfs (Buenzli et al. 2012; Metchev et al. 2015). We also

fit the orbital period, radius ratio between LHS 6343 A and LHS 6343 C, time of transit, eccentricity vectors $\sqrt{e}\cos\omega$ and $\sqrt{e}\sin\omega$, reduced semimajor axis $a/R_\star$, and impact parameter. For each of these, we apply a prior following the results of the simultaneous RV and transit fit of M15. With 11 parameters defining the astrophysical model, we have 30 parameters total. Our model is shown in Figure 5.1.

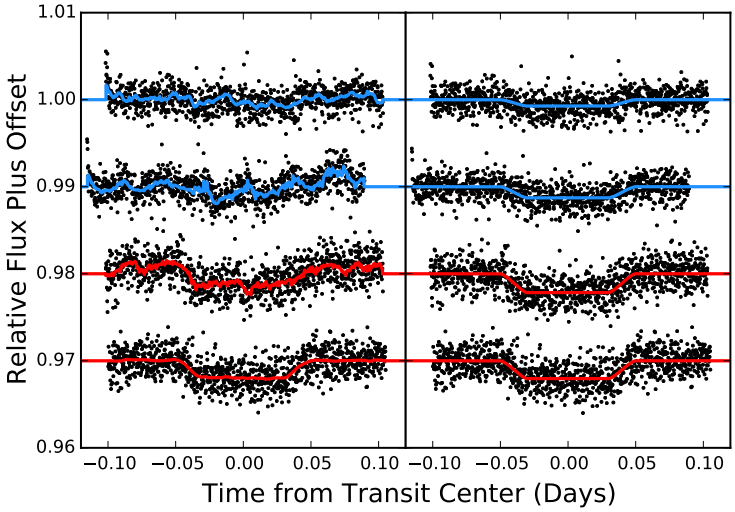

Figure 5.1: (Left) Observed secondary eclipses of LHS 6343 C. The solid line represents the maximum likelihood joint fit of the instrumental and astrophysical models. The observations are arranged chronologically from top to bottom. The top two, in blue, are eclipses in the IRAC 1 3.6μm bandpass. The bottom two, in red, are taken in the IRAC 2 4.5μm bandpass. (Right) The same eclipses, with the maximum likelihood instrumental model divided out for illustration.

Parameter Estimation

We first calculate a maximum likelihood solution for each eclipse with each of our eleven apertures. We then choose the single aperture which maximizes our likelihood function and restrict ourselves to that aperture. For the first 3.6μm eclipse and both 4.5μm eclipses, we find the likelihood function is maximized with a 2.0 pixel aperture; for the other 3.6μm eclipse, we use a 2.3 pixel aperture. In all cases, these apertures include both M dwarfs in the system. To compute the covariance matrix and likelihood function for each model, we use `george`[1], an implementation of the hierarchically off-diagonal low-rank matrix solver of Ambikasaran et al. (2016).

To infer the eclipse depths, we then explore the parameter space using `emcee`

[1] http://dan.iel.fm/george

(Foreman-Mackey et al. 2013), an implementation of the affine-invariant ensemble sampler of Goodman & Weare (2010). We initialize 200 walkers clustered around the maximum likelihood values for each eclipse. We then allow these walkers to evolve for 1,500 steps, limiting each noise parameter to values within a factor of e^{10} of the maximum likelihood value. We remove the first 600 steps as burn-in and verify our system has converged through the test of Geweke (1992) and visual inspection.

5.3 Results

Our results are shown in Table 5.1. We find less correlated noise in the 4.5μm bandpass, in line with previous *Spitzer* analyses (Hora et al. 2008). We do not find significant evidence for variability between eclipses. In the 3.6μm bandpass the two depths are consistent at 1.4σ; at 4.5μm, 0.8σ. We consider these observations to represent the system in similar states and combine the likelihoods on the eclipse depth through a kernel density estimation of each individual depth. From this, we measure an eclipse depth of 1.06 ± 0.21 parts per thousand (ppt) at 3.6μm and 2.09 ± 0.08 ppt at 4.5μm, as shown in Figure 5.2. We also calculate brightness temperatures for each bandpass using the BT-Settl model spectra of Allard et al. (2012) to infer the expected blackbody flux from the brown dwarf, finding T_b = 1026 ± 57 K at 3.6μm and T_b = 1249 ± 36 K at 4.5μm.

To test the robustness of our GP model, we calculate the maximum likelihood solutions with two different instrumental models. Following Knutson et al. (2008), we fit a second-order polynomial to the inferred centroid positions of the star to decorrelate the telescope motion from the astrophysical signal. We also apply the pixel-level decorrelation method of Deming et al. (2015), which decorates the observed fluxes against the pixel counts inside a subarray centered on the PSF of the star. In both cases, we find no statistical difference on the inferred eclipse depths.

5.4 Temperature and Age of LHS 6343 C

Given the *Spitzer* eclipse depths and the known mass and radius of LHS 6343 C, we can infer the temperature of LHS 6343 C and the age of the system. The eclipse depths only provide a ratio between the flux from the brown dwarf and the two M dwarfs:

$$\delta = \frac{F_C}{F_A + F_B + F_C}. \tag{5.4}$$

We have no direct measurement of the brightness of the two M dwarfs in the IRAC bandpasses so we must infer them. M15 use the Dartmouth stellar evolutionary

Parameter	Median		Uncertainty (1σ)
IRAC 1 Parameters			
Transit Depth, 2014 July 06 (ppt)	0.74	±	0.27
Transit Depth, 2014 July 19 (ppt)	1.26	±	0.24
Transit Depth, Combined (ppt)	1.06	±	0.21
M_A (Vega)[1]	6.56	±	0.08
M_B (Vega)[1]	6.97	±	0.10
M_C (Vega)	13.43	±	0.23
T_b (K)	1026	±	57
IRAC 2 Parameters			
Transit Depth, 2014 September 21 (ppt)	2.16	±	0.12
Transit Depth, 2014 October 16 (ppt)	2.03	±	0.12
Transit Depth, Combined (ppt)	2.09	±	0.08
M_A (Vega)[1]	6.45	±	0.07
M_B (Vega)[1]	6.86	±	0.09
M_C (Vega)	12.58	±	0.07
T_b (K)	1249	±	36
System Parameters			
Time of Secondary Eclipse (BJD - 2400000)	56845.401	±	0.001
Orbital Period (days)[2]	12.7137941	±	0.0000002
Eccentricity Vector $e \cos \omega$	0.0229	±	0.0001
Star C Surface Gravity (m s^{-2})[2]	2630	±	50
Star C Luminosity ($\log(L_\star/L_\odot)$)[3]	-5.16	±	0.04
Star C Temperature[3] (K)	1130	±	50
Star C Age (Gyr)[3]	5	±	1

Table 5.1: Measured parameters for the LHS 6343 ABC system.
(1) Inferred through $VRJHK$ photometry and the Dartmouth models of Dotter et al. (2008)
(2) From M15
(3) Dependent on the BT-Settl evolutionary models of Allard et al. (2012)

models of Dotter et al. (2008) to infer a mass and radius for each star given available $VRJHK$ photometry. Here, we use the posterior distributions on the stellar masses and the Dartmouth models to predict the absolute magnitudes of the stars at 3.6 and 4.5μm(Table 5.1). This technique also reproduces the expected brightness of the M dwarfs to within the photometric uncertainties in all bandpasses where we do have data. We then use these predictions and the observed eclipse depths to calculate the absolute magnitude of LHS 6343 C in both IRAC bandpasses: we determine $M_{C,3.6} = 13.43 \pm 0.23$ and $M_{C,4.5} = 12.58 \pm 0.07$ so that $[3.6 - 4.5] = 0.85 \pm 0.24$.

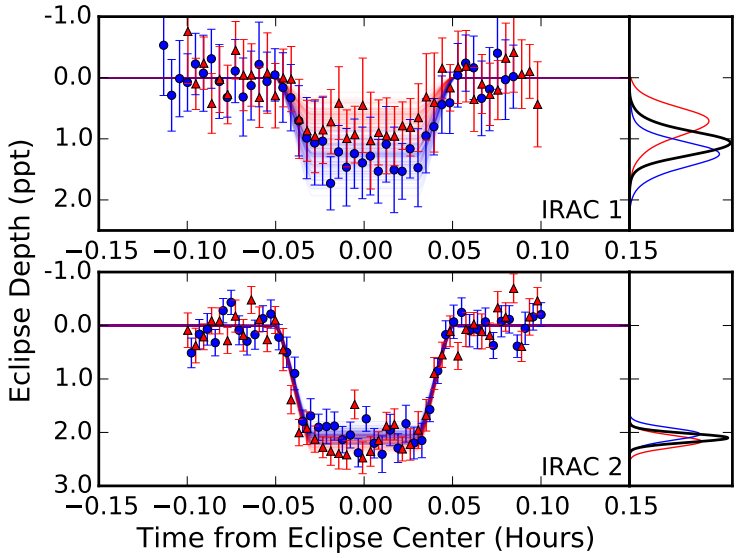

Figure 5.2: (Left) Observed secondary eclipses in each bandpass, with different transits in each bandpass labeled with red triangles and blue circles. A representative instrumental model has been removed for clarity. Red and blue lines represent draws from the transit model posterior distributions. (Right) Marginalized posterior distributions of the eclipse depth for each individual transit (red, blue) and combined (black). The observed eclipse depths are consistent at 1.4σ in the 3.6μm IRAC 1 bandpass and 0.8σ in the 4.5μm IRAC 2 bandpass. We find depths of 1.06 ± 0.21 ppt at 3.6μm and 2.09 ± 0.08 ppt at 4.5μm.

We repeat this procedure with the resolved flux measurements and the BT-Settl evolutionary models of Allard et al. (2012), finding no difference in the extrapolated IRAC absolute magnitudes of the M dwarfs at the 1σ level.

Brown dwarf evolutionary models can be used to determine a temperature and age of LHS 6343 C. We investigate the predictions of several models.

The BT-Settl models provide the best fit to the available data. We use the isochrones calculated for the CIFIST 2011 abundances and opacities (Caffau et al. 2010; Allard et al. 2012), the most recent for which magnitudes have been tabulated at these masses and ages. With this model grid, we infer a brown dwarf with $t = 5 \pm 1$ Gyr, $T = 1130 \pm 50$ K, and $\log(L_\star/L_\odot = -5.16 \pm 0.04$ by evaluating the likelihood of the model fit to our calculated absolute magnitudes in each bandpass and marginalizing over all other parameters. This strategy provides an estimate of the statistical error, but not the systematic error caused by uncertainty or errors in the models. We note that of field brown dwarfs with measured temperatures and colors, this model set predicts the correct temperatures with a scatter of $\sim$ 50K, consistent with the

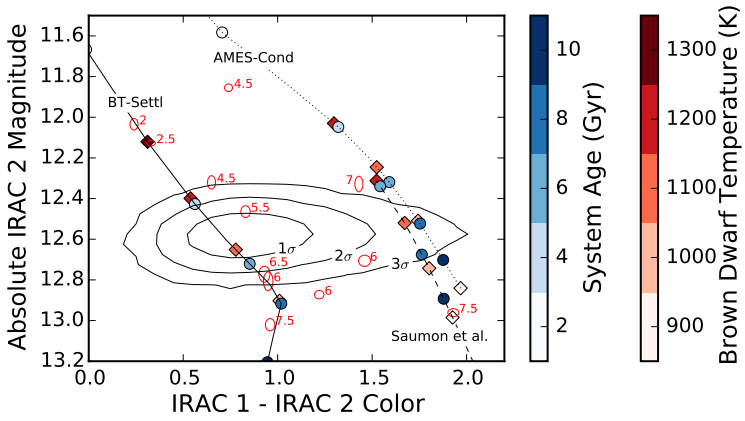

Figure 5.3: Color-magnitude diagram showing the absolute magnitude in the IRAC 2 4.5μm bandpass against the IRAC 1 - IRAC 2 color. Contours represent the allowed parameter space in which LHS 6343 C could reside. The labeled lines represent the theoretical evolutionary tracks of a brown dwarf with the mass of LHS 6343 C from (left to right) the BT-Settl, Saumon et al. (2012), and AMES-Cond models. Dots correspond to model predictions at (white to dark blue) 2, 4, 6, 8, and 10 Gyr; diamonds correspond to model predictions for temperatures of (white to dark red) 900, 1000, 1100, 1200, and 1300 K.The BT-Settl model provides a good fit at 5 ± 1 Gyr; the AMES-Cond and Saumon models fit the data at lower significance at 8 ± 1 Gyr. Red ellipses represent field brown dwarfs from Dupuy & Liu (2012) and Filippazzo et al. (2015); labels represent the spectral subtype inside the T class.

published uncertainties in temperature.

The AMES-Cond models of Allard et al. (2001) provide a fit to the *Spitzer* photometry, mass, and radius of LHS 6343 C such that $t = 8 \pm 1$ Gyr and $T = 1000 \pm 50$ K. However, this model grid underpredicts the 3.6μm luminosity, leading to an overestimation of the [3.6 - 4.5] color at all ages (Figure 5.3). The AMES-Dusty models, meanwhile, do not provide a good fit, overpredicting the luminosity even if the system were the age of the universe, as is common with brown dwarf models (Rice et al. 2010; Dupuy et al. 2015).

The isochrones of Saumon & Marley (2008) combined with synthetic photometry from Saumon et al. (2012) predict IRAC photometry as a function of temperature and system age. These models provide a slightly better fit to the data than the AMES-Cond models for an 1100 ± 50 K brown dwarf, but still overpredict the [3.6 - 4.5] color. Their hybrid models, meant to model the L/T transition, suggest an older brown dwarf with an age of 8 ± 1 Gyr. Their cloudy L dwarf models do not provide a good fit at any age. Given the inability of the cloudy models to

explain the observations, as well as the consistency between models in predicting temperatures below the L/T transition (Burgasser et al. 2002b; Golimowski et al. 2004), we confirm LHS 6343 C as a T dwarf.

Objects near the L/T transition with temperatures 1000-1400 K are particularly challenging for brown dwarf evolutionary models. The uncertainties in all models are dominated by systematics, so we cannot develop one statistical posterior on the temperature or age. We note the BT-Settl models provide the best fit to these data and to the population of similar mid-T dwarfs in color-magnitude space. This system compares favorably to other known T5-6 dwarfs (Dupuy & Liu 2012, Figure 5.3). Of the field brown dwarfs with measured luminosities and temperatures, it is consistent with being between T4.5 dwarf 2MASS 0000+2554 (1227 ± 95 K) and T6 dwarfs 2MASS 0243-2453 (973 ± 83 K) and 2MASS 1346-0031 (1011 ± 86 K, Filippazzo et al. 2015) in its evolution. This age measurement, while model dependent, is the first measurement of the age of the system: previously, Johnson et al. (2011b) were able to only place a lower limit of 1-2 Gyr on the system age.

5.5 Discussion

Irradiation from LHS 6343 A

We ignore irradiation from LHS 6343 A. Given the (Dartmouth model-dependent) temperature of the host of 3430 ± 20 K and semi major axis $a/R_\star = 46.0 \pm 0.4$, the equilibrium temperature of the brown dwarf is $T_{eq} = 365 \pm 3$ K, assuming a Bond albedo of 0.07, expected for a massive brown dwarf around an M2V dwarf (Marley et al. 1999). Therefore, the emitted flux as a result of the absorption and reemission of stellar radiation from LHS 6343 A is $\approx 1\%$ the total flux. While irradiation may affect the thermal profile of the brown dwarf, it should be negligible considering the ≈ 0.1 mag uncertainties on the brown dwarf's magnitude.

Moreover, given the advanced age of the system, we expect high energy irradiation from the host star to be negligible. West et al. (2008) find a rapid decay in M dwarf magnetic activity over stellar age; Shkolnik & Barman (2014) find the same to be true for UV emission, with a steep drop in UV emission at ages above 1 Gyr. Stelzer et al. (2013) study nearby M dwarfs to find X-ray emission decays even more quickly for M dwarfs than UV emission, with a difference of three orders of magnitude between young M dwarfs in TW Hydra and old, field M dwarfs. Any high energy radiation that may have once influenced the atmosphere of LHS 6343 C has been at a low level for billions of years, allowing the brown dwarf to achieve an

equilibrium representative of field brown dwarfs.

Metallicity of LHS 6343 C

M15 infer a metallicity for the two M dwarfs in the system [a/H] = 0.02 ± 0.19. If the brown dwarf formed through core accretion, it may be expected to have a higher metallicity than its host stars (Pollack et al. 1986; Podolak et al. 1988), as is the case for the planet orbiting GJ 504 (Skemer et al. 2016). Because of the low mass of the host star and likely low mass of its protoplanetary disk (Andrews et al. 2013), it is considerably more likely this brown dwarf formed like a binary star system so that the metallicity of LHS 6343 C is likely not significantly different from its host star (Desidera et al. 2004). Additional observations that infer a spectrum of LHS 6343 C can provide tests of theoretical brown dwarf spectra given the known metallicity of the system. These tests are especially important for mid/late T dwarfs, where metallicity effects can affect near-IR colors by as much as 0.3 dex (Burningham et al. 2013).

Dynamical History of LHS 6343

The secondary eclipses are centered at phase 0.5146 ± 0.0001, corresponding to times of transit 0.185 ± 0.001 days after half-phase between successive primary transits, or an eccentricity vector $e \cos \omega = 0.0229 \pm 0.0001$. This value is consistent with that inferred from RV observations and *Kepler* photometry (0.0228 ± 0.0008, M15)

The eccentricity in the LHS 6343 A-C subsystem may be primordial or the result of dynamical perturbations from star B. LHS 6343 B is presently at a sky-projected separation of ~20 AU from the A-C subsystem. Depending on the orbit of LHS 6343 B, the system may be susceptible to Kozai-Lidov oscillations (Kozai 1962; Lidov 1962). Kozai-Lidov cycles would lead to oscillations in the orbital inclination and eccentricity of the A-C subsystem on a timescale

$$\tau \approx P_C \frac{M_{AC}}{M_B} \left(\frac{a_{AC-B}}{a_{AC}} \right)^3 (1 - e_{AC-B})^{3/2}, \tag{5.5}$$

where P_C is the orbital period of the brown dwarf, M_{AC} the A-C subsystem mass, M_B the perturber mass, a_{AC-B} and e_{AC-B} the orbital semimajor axis and eccentricity of star B around the AC subsystem, and a_{AC} the orbital semimajor axis of C around A. The two M dwarfs have similar masses. The semimajor axis $a_{AC} = 0.08$ AU is known, but we only know the instantaneous sky-projected separation between AC and B is ≈20 AU. Taking this value as a proxy for the true semimajor axis,

we find $\tau \sim 10^6(1 - e_{AC-B})^{3/2}$ years. Even for significantly larger orbits of star B and high eccentricities, the timescales for Kozai-Lidov cycles would be shorter than the $\sim 10^{10}$ year age of the system, suggesting the system may be susceptible to Kozai-Lidov oscillations given appropriate initial conditions.

The current orbit can provide clues about the dynamical history of this system. Measurement of an inclined orbit of LHS 6343 B through astrometric monitoring could provide evidence for Kozai-Lidov cycles, as would a misalignment between the spin axis of LHS 6343 A and the orbit of LHS 6343 C. While close binaries are not always neatly aligned (Albrecht et al. 2014), they often are, especially for low-mass binaries (Harding et al. 2013; Triaud et al. 2013).

Chapter 6

MASSES AND ORBITAL PARAMETERS OF GJ 3305 AB, THE WIDE BINARY COMPANION TO THE IMAGED EXOPLANET HOST 51 ERI

In this chapter I continue comparing observations of low-mass stars to predictions from theoretical models. Throughout my graduate studies I have led a long-term program to measure masses of M dwarfs in young moving groups through astrometric and RV observations of their orbits using the Differential Speckle Survey Instrument (DSSI) at the Discovery Channel Telescope and Gemini Observatory and the Tillinghast Reflector Echelle Spectrograph at Mt. Hopkins. As we must observe a substantial fraction of the orbit before we can determine a unique mass, this is a long-term project not intended to be completed during this thesis. As a part of this thesis, we published the first results from this survey, outlining our methods and presenting the first binary system with a closed orbit, the GJ 3305 AB binary. This chapter was originally published as "Dynamical Masses of Young M Dwarfs: Masses and Orbital Parameters of GJ 3305 AB, the Wide Binary Companion to the Imaged Exoplanet Host 51 Eri," ApJL, 813, 11 (2015) by BTM, Brendan Bowler, Evgenya Shkolnik, Katherine Deck, Ji Wang, Elliott Horch, Michael Liu, Lynne Hillenbrand, Adam Kraus, and Dave Charbonneau.

6.1 Introduction

Loose associations of young, nearby (<70 pc) stars with common ages, kinematics, and origins have been a subject of increasing interest (Zuckerman et al. 2004; Shkolnik et al. 2012; Malo et al. 2013). Because of their proximity to Earth, these young moving groups (YMGs) are excellent targets to study pre-main sequence (PMS) stellar and substellar evolution, protoplanetary and debris disk structure, and giant planet formation at ages between distant star-forming regions and old field stars (e.g. Close et al. 2005; Nielsen & Close 2010). About 10 YMGs containing hundreds of objects between 8 and 120 million years old are known (e.g. Torres et al. 2008).

As these moving groups are amenable to numerous age dating methods, including kinematic techniques, they provide the opportunity to measure dynamical masses of PMS low-mass binary objects and test stellar evolution models (Stassun et al. 2014).

Generally, PMS stellar masses are inferred by comparing a star's temperature, luminosity and metallicity to model predictions (e.g. Schaefer et al. 2014). These models are poorly constrained by observations and may induce systematic offsets (Dupuy et al. 2009, 2014). Worse yet, different models predict disparate masses, primarily due to uncertainties in the treatment of convection in low-gravity atmospheres (Baraffe et al. 2002), stellar accretion history (Baraffe & Chabrier 2010), and molecular line lists (Baraffe et al. 2015). In some cases, model-predicted masses can differ by a factor of two or more (Hillenbrand & White 2004; Schlieder et al. 2014). Dynamical mass measurements of binary stars with known ages are essential to test models.

Recently, Macintosh et al. (2015) presented 51 Eri b, the first exoplanet discovery from the Gemini Planet Imager. The planet has a mass of ≈ 2 M_{Jup} (assuming a hot start model), a projected separation of 13 AU, a temperature of 600-750 K, and a T4.5-T6 spectral type. GJ 3305 is known to be a binary with combined spectral type M0 (Kasper et al. 2007). Feigelson et al. (2006) identified GJ 3305 and 51 Eri as an F0-M0 common proper motion pair, separated by 66 arcsec or ~2000 AU.

As a binary system, a dynamical mass can be measured for both stars in GJ 3305 AB. As both stars are members of the β Pictoris moving group, an approximate age of the system is known (24 ± 3 Myr; Binks & Jeffries 2014; Mamajek & Bell 2014; Bell et al. 2015). While most dynamical masses of M dwarfs are limited by distance uncertainties, 51 Eri has a parallax from *Hipparcos* measured to a precision of 1%. Combining this parallax with 15 years of imaging and RV data enables us to determine the system orbital parameters, elucidating the architecture of this 4—or more—body system.

In this paper, we combine RV and astrometric observations of GJ 3305 AB to measure orbital parameters and masses for each star. We compare these masses to model predictions and discuss the possible implications of this binary pair on the long-term evolution of the orbit of 51 Eri b.

6.2 Data Collection and Reduction

GJ 3305 AB has been imaged and resolved many times (Kasper et al. 2007; Bergfors et al. 2010; Delorme et al. 2012; Janson et al. 2012, 2014). The system was also imaged with NIRC2 (Wizinowich et al. 2000) in one unpublished epoch in 2001 available in the Keck Observatory Archives (KOA, PI Zuckerman). In this work, we combine these data with five observations from 2002 to 2015, three us-

ing Keck/NIRC2 and one with the Differential Speckle Survey Instrument (DSSI, Horch et al. 2009) at the Discovery Channel Telescope at Lowell Observatory.

All NIRC2 data were obtained with the narrow camera mode, which has a field of view of 10.2 arcsec × 10.2 arcsec and a plate scale of 9.952 mas pixel^{-1} (Yelda et al. 2010). All images were flat fielded and cleaned of bad pixels and cosmic rays. Astrometry and relative photometry of GJ 3305 was derived by simultaneously fitting three bivariate Gaussians to each component following Liu et al. (2010).

DSSI allows for simultaneous observations in two filters. We use the DSSI R and I filters, with central wavelengths 692 and 880 nm and FWHMs of 40 and 50 nm. We obtained 1000 40-ms exposures in each channel simultaneously. The data were then reduced following Horch et al. (2015). Specifically, the autocorrelation of each frame was calculated and summed over all exposures, and the near-axis subplanes of the image bispectrum were calculated. To create a reconstructed image, the Fourier transform of the autocorrelation of the binary was divided by that of a nearby point source (HR 1415). The square root of this value is taken, and the result combined with a phase function derived from the bispectral subplanes. The pixel scale (19 mas pixel^{-1} in R and 20 mas pixel^{-1} in I) and orientation of the detector were found by observing several widely separated binaries with known astrometry. Our astrometry is listed in Table 6.1.

Epoch (Year)	Bandpass	RV (km s^{-1})	Contrast (Δ mag)	Separation (mas)	Position Angle (deg)	Source
2001.910	$H_2(\nu$=1–0)		1.00 ± 0.02	286 ± 1	198.1 ± 0.1	This Work
2002.162	H		1.02 ± 0.02	275.4 ± 1.5	197.9 ± 0.2	This Work
2003.05	K		0.94 ± 0.05	225 ± 5[1]	195.0 ± 1.5[1]	Kasper et al. (2007)
2003.195	H		0.99 ± 0.01	217 ± 1	196.8 ± 0.1	This Work
2004.02	L'			159 ± 2	194 ± 1	Delorme et al. (2012)
2004.95	L'		0.88 ± 0.28	93 ± 2	189.5 ± 0.4	Kasper et al. (2007)
2008.88	SDSS z'		1.39 ± 0.16	218 ± 2	20.3 ± 0.3	Bergfors et al. (2010)
2008.88	SDSS i'		2.57 ± 0.05	218 ± 2	20.3 ± 0.3	Bergfors et al. (2010)
2009.13	SDSS i'+z'			231 ± 2	19.2 ± 0.3	Janson et al. (2012)
2009.90	L'			269 ± 3	18.6 ± 1.0	Delorme et al. (2012)
2009.98	L'			272 ± 3	19.2 ± 1.0	Delorme et al. (2012)
2010.10	SDSS z'		1.34 ± 0.01	284 ± 3	18.5 ± 0.6	Janson et al. (2012)
2010.10	SDSS i'		3.73 ± 0.01			Janson et al. (2012)
2010.81	SDSS z'			297 ± 3	19.4 ± 0.3	Janson et al. (2014)
2011.67	L'			303 ± 3	18.1 ± 1.0	Delorme et al. (2012)
2011.87	SDSS z'			295 ± 4	18.5 ± 0.3	Janson et al. (2014)
2012.01	SDSS z'			307 ± 3	18.2 ± 0.3	Janson et al. (2014)
2014.629	Brγ		0.92 ± 0.01	244 ± 1	16.8 ± 0.1	This Work
2014.746	DSSI R		1.89 ± 0.04	239 ± 1	16.4 ± 0.2	This Work
2014.746	DSSI I		1.17 ± 0.03	240 ± 1	16.1 ± 0.2	This Work
2015.653	K		0.93 ± 0.01	199 ± 1	15.6 ± 0.1	This Work
2015.653	H		0.99 ± 0.01	198 ± 1	15.6 ± 0.1	This Work
2015.653	J		0.97 ± 0.01	199 ± 1	15.6 ± 0.2	This Work
2015.653	Y		1.06 ± 0.03	200 ± 1	15.6 ± 0.1	This Work
2003.796	HIRES V	19.41 ± 0.38				This work
2004.884	NIRSPEC K	19.86 ± 0.05				Bailey et al. (2012)
2005.862	NIRSPEC K	20.55 ± 0.06				Bailey et al. (2012)
2005.971	HIRES V	21.70 ± 0.30				Shkolnik et al. (2012)
2006.014	NIRSPEC K	20.82 ± 0.05				Bailey et al. (2012)
2006.016	NIRSPEC K	20.95 ± 0.05				Bailey et al. (2012)
2006.019	NIRSPEC K	20.95 ± 0.05				Bailey et al. (2012)
2011.778	UVES Blue	24.40 ± 0.04				Elliott et al. (2014)
2001.994	UVES Blue	23.30 ± 0.02				Elliott et al. (2014)
2012.022	UVES Blue	23.80 ± 0.02				Elliott et al. (2014)

Table 6.1: Data for GJ 3305 AB. In some previous analyses, contrast ratios were not listed for specific epochs. Observations without listed separations correspond to simultaneous multiband photometry.
(1) Observations published without uncertainty estimates; we choose conservative values.

The GJ 3305 binary system has also been monitored spectroscopically with a 12-year observational baseline. One Keck/HIRES spectrum from 2003 exists in the KOA (PI Zuckerman); we measure the RV following Kraus et al. (2015). We combine this spectrum with nine additional spectra from Bailey et al. (2012), Shkolnik et al. (2012), and Elliott et al. (2014). In all cases, the RVs were calculated treating the system as an SB1. We take the reported RV and uncertainty for each observation, but assume the flux from the secondary is non-negligible, as explained in Section 6.3.

6.3 Analysis

We infer the orbital parameters of GJ 3305 AB by comparing the astrometric and RV data to a Keplerian orbit model at each of the observation times. A parallax, astrometric orbit, and SB1 RV data can be combined to measure individual masses of each star (e.g. Bean et al. 2007). There is no measured parallax for GJ 3305, so we adopt the Hipparcos distance to 51 Eri/HIP 21547: 29.43±0.30 pc (van Leeuwen 2007). These two comoving systems have a projected separation of 1940±20 AU, or 0.01 pc. It is unlikely that the radial distance between the two could be significantly larger while remaining bound; we apply this parallax as a prior on the distance to GJ 3305.

We then fit for nine additional parameters that define the orbits of the two stars as viewed from Earth. Of these, seven can be obtained from astrometry. These parameters are the eccentricity vectors $\sqrt{e}\cos\omega$ and $\sqrt{e}\sin\omega$, the time of periapsis t_P, the period P, the total mass $M_1 + M_2$, the inclination i, and the longitude of the ascending node Ω. We parameterize the eccentricity vector in this manner following Eastman et al. (2013). The RV data can provide additional information about several of these (not $M_1 + M_2$ or Ω directly), also allowing us to fit the systemic RV γ and the secondary mass M_2.

We include ten additional terms to account for possible systematics in the datas. This star has been imaged, resolved, and published by four different groups. We account for the possibility each group may have underestimated their uncertainties on the orbital separation and position angle by a multiplicative factor by including a systematic error term on the measured positions from each group, allowing outlier points to be downweighted without manually choosing specific points to downweight. We do the same with our reductions of both archival and new data, allowing for separate systematic error terms on our data from Keck/NIRC2 and DCT/DSSI,

providing a total of six systematic error terms. We allow the uncertainties on each dataset to be inflated up to a factor of five.

Similarly, we allow for the possibility that the uncertainties in the RVs may be underestimated, possibly due to stellar variability (Moulds et al. 2013), errors in systemic RVs of standard stars, or drifts in the stability of the spectrographs. As our RV data originate from four sources, we allow each to have its own systematic error term, analogous to the jitter term commonly applied in RV orbit fits of exoplanets (e.g. Johnson et al. 2011a):

$$\log \mathcal{L} \propto -\sum_i \left[\log \sqrt{\sigma_{o,i}^2 + \sigma_s^2} + 0.5\left(\frac{(f_i(t) - v_i(t))^2}{\sigma_{o,i}^2 + \sigma_s^2} \right) \right]. \tag{6.1}$$

Here, $\mathcal{L}$ is the likelihood of the data given some underlying physical model, $\sigma_{o,i}$ is the observed uncertainty on the ith data point, σ_s the systematic error associated with each particular set of observations, $f_i(t)$ the RV model evaluated at time t, and $v_i(t)$ the observed RV at each t. Maximum likelihood jitter values range from 0.13 km s^{-1} for the 2003 HIRES data to 0.57 km s^{-1} for the UVES data, suggesting stellar jitter is significant in the RV data, as expected for young stars.

In all cases, one set of lines are observed because the RV separation is smaller than the line width. We expect each RV measurement to be the flux-weighted sum of the two individual RVs. At each step, we calculate the RVs for each star, weighting them according to their expected flux contribution in each bandpass, using the observed flux ratios in the visible and near-IR as priors and assuming an additional 0.1 mag of variability in the optical and 0.05 mag in the near-IR.

We neglect the possibility that 51 Eri could contribute significantly to the observed RV signal. Following Equation 1 of Montet et al. (2015a), the maximum RV acceleration expected from 51 Eri is 3 cm s^{-1} yr^{-1}, well below our sensitivity.

We calculate posterior distributions for all parameters using the `emcee` package (Foreman-Mackey et al. 2013), an implementation of the affine-invariant Markov Chain Monte Carlo ensemble sampler of Goodman & Weare (2010). After performing a local optimization to determine a maximum-likelihood fit, we move 3000 walkers each 4000 steps. We discard the first 2000 steps of each walker as burn-in, and use the test of Geweke (1992) and visual inspection to verify the system has converged. The data and allowed orbits are shown in Figure 6.1. Summary statistics for the orbital parameters are given in Table 6.2. We note the fitted systemic RV of 20.76 ± 0.18 km s^{-1} is consistent with the measured RV for 51 Eri, 21.0 ± 1.2 km

s^{-1} (Bobylev 2006) and the UVW velocities are consistent with Mamajek & Bell (2014). Our samples are available online.[1]

Parameter	Median		Uncertainty (1σ)
$\sqrt{e}\cos\omega$	0.160	±	0.019
$\sqrt{e}\sin\omega$	-0.406	±	0.015
Eccentricity	0.19	±	0.02
Argument of Periastron ω [deg]	-69	±	3
Time of Periastron [Year]	2007.14	±	0.16
Orbital Period [Year]	29.03	±	0.50
GJ 3305 A Mass [$M_\odot$]	0.67	±	0.05
GJ 3305 B Mass [$M_\odot$]	0.44	±	0.05
Total System Mass [$M_\odot$]	1.11	±	0.04
Mass Ratio M_B/M_A	0.65	±	0.10
Orbital Inclination, i [deg]	92.1	±	0.2
Orbital Semimajor Axis, a [AU]	9.78	±	0.14
Long. of Ascending Node, Ω [deg]	18.8	±	0.2
Systemic RV Velocity, γ [km s^{-1}]	20.76	±	0.18
RV semiamplitude K_A [km s^{-1}]	4.01	±	0.38
U [km s^{-1}]	-13.76	±	0.24
V [km s^{-1}]	-16.40	±	0.40
W [km s^{-1}]	-9.71	±	0.36
GJ 3305 A Luminosity [$L_\odot$]	0.112	±	0.007
GJ 3305 B Luminosity [$L_\odot$]	0.043	±	0.005

Table 6.2: Measured orbital parameters for GJ 3305 AB

We estimate bolometric luminosities for both of the stars in the system by integrating the CFHIST2011_2015 model spectra of Baraffe et al. (2015). We use the 3700 and 3500 K models with $\log g = 4.5$ (cgs) as spectral templates, scaling them until they match the observed combined and differential magnitudes in each available bandpass. We add in quadrature 0.10 mag of uncertainty in our visible-light magnitudes and 0.05 mag in the near-IR to account for stellar variability.

6.4 Comparison with BHAC15 Evolutionary Models

Given the known distance to the system from *Hipparcos* we can test if theoretical stellar evolution models accurately predict the inferred stellar masses and age of the β Pic moving group. Combined-light photometry spanning from B (0.4 μm) to Ks (2.3 μm) was measured by the APASS, 2MASS, and *WISE* surveys (Table 6.3). We add an uncertainty of 0.03 mag in quadrature to the listed APASS uncertainties due

[1] http://www.astro.caltech.edu/~btm/research/gj3305.html

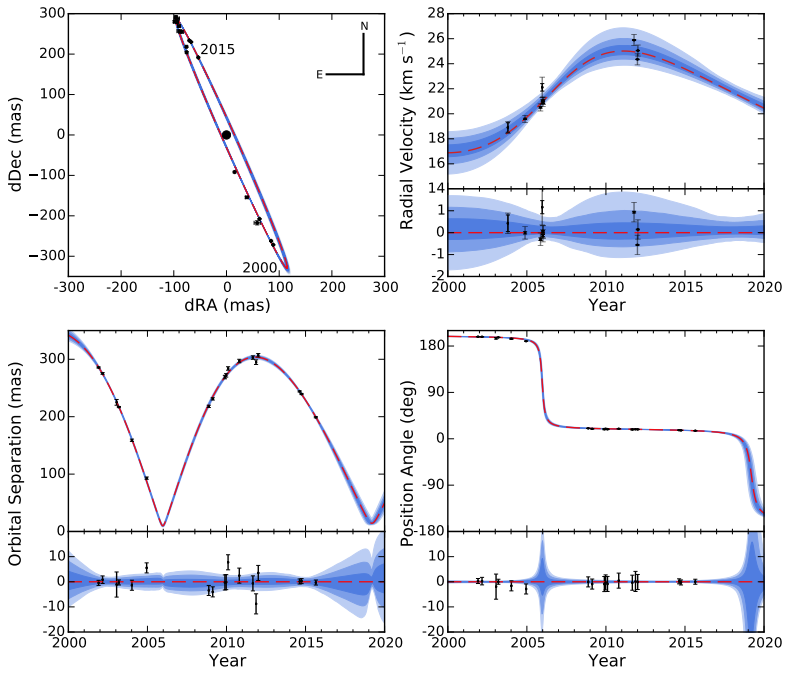

Figure 6.1: (Top Left) Astrometry for GJ 3305 AB. Data points correspond to the observations listed in Table 6.1. Blue lines correspond to random draws from the posterior distributions of orbital elements. The red, dashed line corresponds to the maximum likelihood orbit. (Top Right) RV data for GJ 3305 A from the literature. The published uncertainties are in black; in gray are the best-fitting uncertainties, incorporating an RV jitter model. The red, dashed line corresponds to the maximum likelihood orbit. The blue shaded regions correspond to the 1−, 2−, and 3σ uncertainties in the RV of GJ 3305 A. (Bottom Left) Measured separations for GJ 3305 AB and residuals from the maximum likelihood model. Each feature on the plot retains its meaning from the previous subplot. (Bottom Right) Measured position angles for GJ 3305 AB and residuals from the maximum likelihood model.

to the presence of systematics in APASS DR9 at that level (Henden et al. 2012). We also have obtained one epoch of differential photometry in two visible-light bandpasses with DSSI and two near-IR bandpasses (H and Brγ) with Keck/NIRC2.

Bandpass	Source	Magnitude	Uncertainty
Combined			
B	APASS DR9	11.94	0.03
V	APASS DR9	10.56	0.05
g'	APASS DR9	11.27	0.03
r'	APASS DR9	10.03	0.07
J	2MASS	7.30	0.02
H	2MASS	6.64	0.05
K	2MASS	6.41	0.02
$W1$	WISE	6.34	0.03
$W2$	WISE	6.21	0.02
$W3$	WISE	6.16	0.02
$W4$	WISE	6.00	0.04
Resolved			
Δ692	DSSI	1.89	0.04
Δ880	DSSI	1.17	0.03
ΔH_2	Keck/NIRC2	1.00	0.02
ΔBrγ	Keck/NIRC2	0.92	0.01
ΔH	Keck/NIRC2	1.00	0.02

Table 6.3: Photometry for GJ 3305 AB

We compare the observed brightness of GJ 3305 AB to that predicted by the newest evolutionary models of Baraffe et al. (2015) for two stars of masses consistent with those inferred during our analysis as a function of age. We find models of 25 Myr old stars accurately predict the combined-light near-IR flux for these stars, although the models predict brighter V magnitudes than those observed (Figure 6.2). However, star B is brighter than these same models predict: a 25 Myr old GJ 3305 B would be significantly brighter than what is observed. Assuming the stars are coeval, the models then predict a mass for GJ 3305 B that is 20% lower than the observed mass.

We create a simulated spectral energy distribution for each star, given the measured masses and the average age of β Pic as measured from higher-mass stars. We interpolate absolute magnitudes predicted by the updated BHAC15 models of Baraffe et al. (2015) along isochrones and isomass contours to predict apparent magnitudes for these stars in each bandpass. We find that the total received flux is lower than

predicted by the BHAC15 models in each bandpass. While the flux for GJ 3305 A is consistent with the model predictions, GJ 3305 B is fainter than predicted.

Given the observed masses, we then vary the age of the system, assuming both stars are coeval, to determine which system age would be predicted by these models given the observed combined and differential magnitudes. We apply a flat prior on the age of the system, finding the BHAC15 models predict an age of 37 ± 9 Myr, consistent with the overall age of the moving group (24 ± 3 Myr, Bell et al. 2015). As the system is unambiguously young, we can also confirm 51 Eri b as a planetary mass object.

6.5 Discussion

We have measured the masses and orbits of GJ 3305 AB, finding both to be consistent with the BHAC15 models at the 1.5σ level. In the future GJ 3305 AB and the gravitationally bound 51 Eri Ab will be able to act as an isochronal test as a coeval, co-metallicity quadruple system spanning stellar to planetary mass regimes.

The derived period of GJ 3305 (29.03 ± 0.50 year) is longer than the 21 year found by Delorme et al. (2012). The authors of that paper did not have sufficient data to fit all orbital parameters, so they fixed the total system mass to 1.3 $M_{\odot}$. Given our lower mass measurement, it is not surprising that our measured orbital period is longer.

Current Limitations

It is possible that an unseen very low-mass star or brown dwarf orbiting GJ 3305 B could cause us to overestimate its mass, causing the observed 20% discrepancy. For the system to be stable over 20 Myr, such a companion would have to be in a close ($P < 50$ day) orbit. The companion would then have to be in a nearly face-on ($i < 10°$) orbit to evade RV detection. Such companions could be found through continued astrometric monitoring of GJ 3305. Such a companion would not affect our astrometry due to its small separation from GJ 3305 B and would likely not affect our photometry due to its low luminosity relative to the other stars in the system.

Most PMS M dwarfs have distance measurements to a precision no better than 5%, meaning the total mass cannot be measured to better than 15% (e.g. Shkolnik et al. 2012). The uncertainty in the mass of GJ 3305 AB is only 4%: the dominant source of uncertainty in this value is the 1% *Hipparcos* parallax to 51 Eri, making this

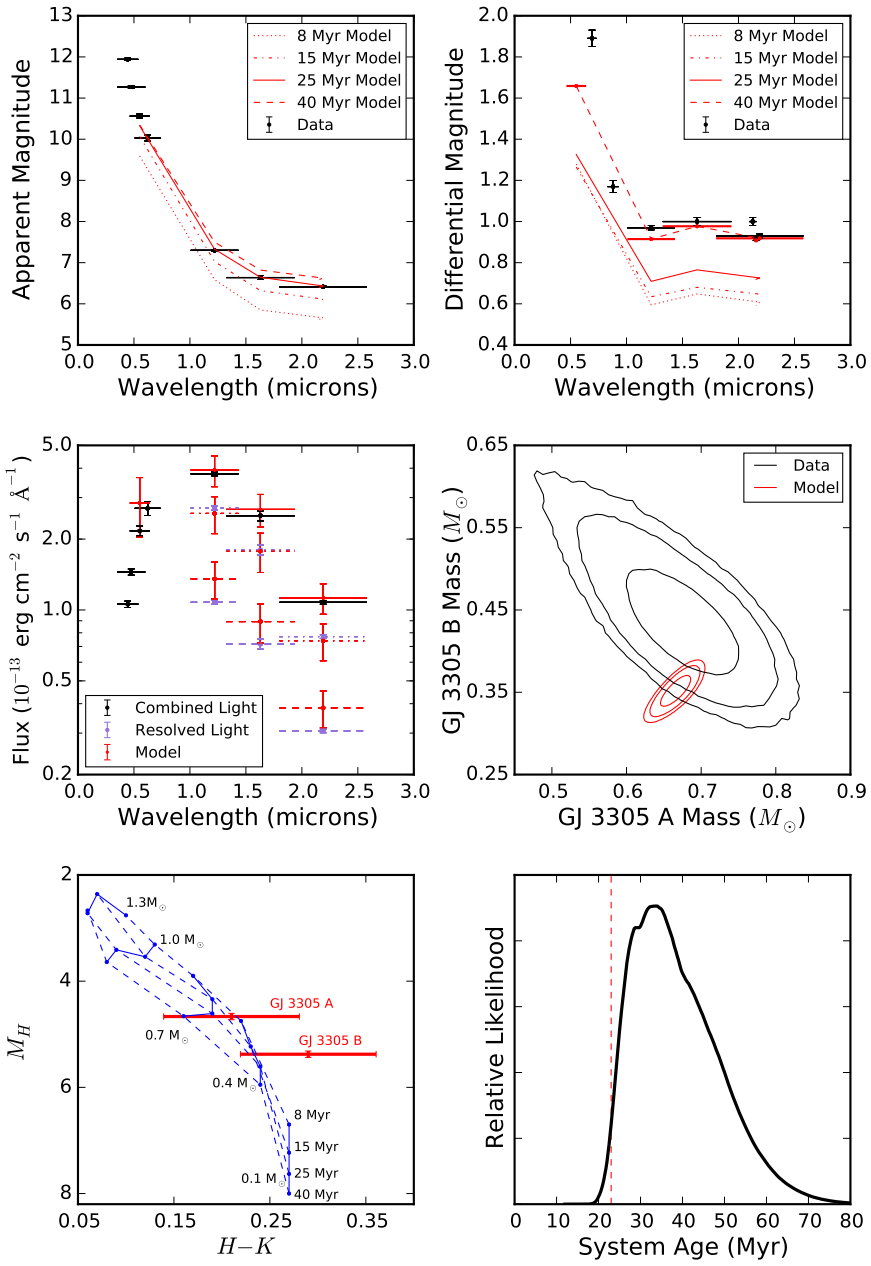
Apparent Magnitude
Wavelength (microns)
8 Myr Model
15 Myr Model
25 Myr Model
40 Myr Model
Data
Differential Magnitude
Wavelength (microns)
Flux (10^{-13} erg cm^{-2} s^{-1} Å^{-1})
Wavelength (microns)
Combined Light
Resolved Light
Model
GJ 3305 B Mass ($M_\odot$)
GJ 3305 A Mass ($M_\odot$)
Data
Model
M_H
$H-K$
1.3M$_\odot$
1.0 M$_\odot$
0.7 M$_\odot$
0.4 M$_\odot$
0.1 M$_\odot$
GJ 3305 A
GJ 3305 B
8 Myr
15 Myr
25 Myr
40 Myr
Relative Likelihood
System Age (Myr)

system an ideal low-mass benchmark. With a Gaia parallax forthcoming in the next few years, parallaxes for low-mass PMS stars will be improved substantially. Long-term astrometric and RV monitoring of wide M dwarfs is essential as parallaxes are obtained over the next few years.

The uncertainty in the individual mass of each star is dominated by the uncertainty in the Doppler semiamplitude. While additional astrometric observations will not significantly improve the measured physical properties of GJ 3305, additional RV observations will be important. RV observations behind AO would be especially beneficial, as the RV from each star could be measured separately, instead of a flux-weighted RV centroid.

Dynamical Effects on 51 Eri b

GJ 3305 AB and 51 Eri Ab exist in a dynamical configuration that may be susceptible to Kozai-Lidov oscillations (Kozai 1962; Lidov 1962), as suggested by Macintosh et al. (2015). In this scenario, the planet-star binary (51 Eri Ab) interacts secularly with GJ 3305 AB, leading to oscillations in inclination and eccentricity of

---

Figure 6.2 *(preceding page)*: (Top) (Left) Combined-light, unresolved and (Right) differential, resolved photometry for GJ 3305 AB (black) compared to predictions (red) of the BHAC15 models as a function of age given the observed masses and parallax. The data are consistent with an age larger than 25 Myr. Plotted bars along the abscissa correspond to the width of each filter and are meant to guide the eye: they do not represent an uncertainty. (Middle left) SED for the system, assuming a 24 ± 3 Myr age and the observed masses. Combined-light photometry is in black and resolved photometry in purple. While the model accurately reproduces the observed flux from GJ 3305 A, it overpredicts the received flux from GJ 3305 B. (Middle right) Joint posterior probability distributions on the masses of the two stars, (black) inferred from the astrometry and RV data and (red) predicted by the BHAC15 models given the observed combined-light and differential photometry assuming an age of 24 ± 3 Myr. Contours correspond to the 1-, 2-, and 3-σ confidence regions. The BHAC15 models predict a mass for GJ 3305 B consistent with the mass inferred from the data, but underpredicts the mass of GJ 3305 A by 20%. (Bottom left) CMD showing the absolute H magnitudes and $H - K$ colors of GJ 3305 AB compared to theoretical models. The models provide a more accurate fit for GJ 3305 A than GJ 3305 B. (Bottom right) Posterior probability distribution on the age of the GJ 3305 system, calculated by marginalizing the joint mass-age posterior over all allowed masses, assuming both stars are the same age. The BHAC15 models predict an age of 37 ± 9 Myr; the dashed line represents the Bell et al. (2015) age of the β Pictoris system.

the planet-star sub-system. The timescale for such an interaction is

$$\tau \approx P_{\rm planet} \frac{M_\star}{M_{\rm pert}} \left(\frac{a_{\rm pert}}{a_{\rm planet}} \right)^3 (1 - e_{\rm pert}^2)^{3/2}, \tag{6.2}$$

where P_{planet} is the orbital period of a planet with a semimajor axis of a_{planet} about a host of mass $M_\star$, $M_{\rm pert}$ is the mass of a distant perturber, and $a_{\rm pert}$ and $e_{\rm pert}$ are the semimajor axis and eccentricity of the perturber/planet-star "binary" orbit (see e.g. Holman et al. 1997).

Although we have limited information about this system, we can estimate the timescale for Kozai-Lidov cycles should the mutual inclination of the 51 Eri Ab system and (51 Eri Ab)-(GJ 3305 AB) system satisfy $140^\circ \lesssim i_m \gtrsim 40^\circ$. Taking the instantaneous sky-projected separations as a proxy for the semimajor axes and inferred masses of $M_\star = 1.75$ $M_\odot$ (Simon & Schaefer 2011) and $M_{\rm pert} = 1.1$ $M_\odot$ yields a timescale of $\tau \sim 2 \times 10^8$ yr $(1 - e_{\rm pert}^2)^{3/2}$. Therefore, unless the eccentricity of GJ 3305 about the 51 Eri subsystem satisfies $e_{\rm pert} \gtrsim 0.9$, the timescale for Kozai-Lidov oscillations is longer than the age of the system, so we do not expect the Kozai-Lidov mechanism to have had time to induce a large eccentricity or spin-orbit misalignment within the 51 Eri sub-system. If future observations indicate non-zero spin-orbit misalignment or a high eccentricity for the orbit of 51 Eri b, a primordial origin unrelated to the distant perturbers would be suggested.

Chapter 7

STELLAR AND PLANETARY PROPERTIES OF *K2* CAMPAIGN 1 CANDIDATES AND VALIDATION OF 17 PLANETS, INCLUDING A PLANET RECEIVING EARTH-LIKE INSOLATION

In the final two science chapters I turn my attention to large surveys. The first of these is *K2* the extended *Kepler* mission. The large systematics inherent to *K2* data make detecting planets more challenging than in *Kepler*; the stellar target list is put together only months before each field as a conglomeration of many other catalogs, making stellar parameters uncertain and potentially systematically biased. Here, we attempt to solve both of these issues. Following a systematic search for transiting planets, we combine RV data, AO imaging, and archival data on the stars to better infer stellar parameters and statistically validate the transiting planets, applying our methods to Campaign 1 of the *K2* mission. We validate 17 planets, including one which receives an Earth-like level of insolation and has an equilibrium temperature of 272 ± 15 K. This chapter was originally published as "Stellar and Planetary Properties of K2 Campaign 1 Candidates and Validation of 17 Planets, Including a Planet Receiving Earth-like Insolation," ApJ, 809, 25 (2015) by BTM, Tim Morton, Dan Foreman-Mackey, John Johnson, David Hogg, Brendan Bowler, Dave Latham, Allyson Bieryla, and Andrew Mann.

7.1 Introduction

The *Kepler* telescope (Borucki et al. 2010) has led to a revolution in stellar and planetary astrophysics, with 7305 "objects of interest" and 4173 "planet candidates" discovered to date (Borucki et al. 2011b,a; Batalha et al. 2013; Burke et al. 2014; Rowe et al. 2015; Mullally et al. 2015). The fidelity of this sample is high: most of these candidates are truly planets (Morton & Johnson 2011; Fressin et al. 2013; Désert et al. 2015). The mechanical failure of two reaction wheels on the spacecraft led to a repurposing of the spacecraft into the *K2* mission, in which the telescope points at fields near the ecliptic plane for $\sim$ 75 days at a time (Howell et al. 2014). In this observing strategy, two axes of motion of the spacecraft are controlled by the two remaining reaction wheels, while the roll of the spacecraft is balanced with solar radiation pressure and quasi-periodic thruster firing. As a result, the detector

drifts relative to the sky at the rate of $\sim$ 1 arcsec hr^{-1}, with rapid corrections due to thruster fires approximately once every six hours. Over the full duration of each campaign, the targets remain near the same location on the detector but both the slow drift and the corrections are observable by eye (Barentsen 2015).

K2 light curves produced with aperture photometry contain substantial pointing-induced photometric variations caused by the star's apparent motion over a poorly-defined flat field. Worse yet, these variations occur on timescales similar to transit signals, potentially masking the observational signature of a planet passing between *Kepler* and its host star.

There has been considerable effort to recover these planetary signals, and to date six planets have been confirmed orbiting three stars in the *K2* data (Armstrong et al. 2015; Crossfield et al. 2015; Vanderburg et al. 2015). What is common to all of these methods are that removal of systematics is considered a step to be undertaken before the search for planets. Under this strategy, it is implicitly assumed that the systematics are removed perfectly, while retaining all of the astrophysical signal. Of course, it is impossible to perfectly separate the astrophysical and instrumental signal, and such a technique is prone to either over-fitting, in which some of the astrophysical signal is also removed, or under-fitting, in which some of the instrumental systematics remain. A better strategy is to simultaneously fit both the signal and the systematics, as is common practice in cosmology and, increasingly, in radial velocity searches for planetary systems (e.g. Ferreira & Jaffe 2000; Boisse et al. 2011; Haywood et al. 2014; Grunblatt et al. 2015).

Foreman-Mackey et al. (2015) simultaneously fit both the systematics and potential planetary transit signals in a search for transiting planets. They assume that the dominant trends in the observed stellar light curves are caused by spacecraft motion and are shared by many stars. They then run PCA on all stars to measure the dominant modes, modeling each star as a linear combination of 150 of these "eigen light curves" and a transit signal. This method enables fitting without over-fitting, and also permits marginalization over uncertainties induced by the systematic model. Therefore, any uncertainties in the systematics can be propagated into uncertainties in detected planet parameters, instead of assuming the systematics are understood perfectly. Using this technique, Foreman-Mackey et al. (2015) detect 36 planet candidates orbiting 31 stars in *K2* Campaign 1 data.

In Foreman-Mackey et al. (2015), only transit properties are provided, not absolute parameters about the planet or the star. Additionally, the authors follow the con-

vention of the *Kepler* team to include any transit event as a candidate system rather than a false positive if a secondary eclipse is not detected: there is no enforced upper limit on the allowed planet radius. The authors intentionally make no effort to separate true transiting planets from astrophysical events that mimic the appearance of transits, such as an eclipsing binary with a high mass ratio, similar to the *Kepler* team's list of "objects of interest."

In this paper, we present stellar and planetary parameters for each system. We also analyze the false positive probability of each system using `vespa`, a new publicly available, general-purpose implementation of the Morton (2012) procedure to calculate false positive probabilities (FPPs) for transiting planets. Through this analysis, as well as archival imaging, ground-based seeing-limited survey data, and adaptive optics imaging, we are able to confirm 21 of these systems as transiting planets at the 99% confidence level. Additionally, we identify six systems as false positives.

This paper is organized as follows. In Section 7.2, we develop stellar properties through photometric and spectroscopic data. In Section 7.3, we combine the derived stellar properties with *K2* data to infer planet candidate properties. In Section 7.4, we combine adaptive optics and radial velocity observations with both archival and modern ground-based, seeing limited survey data and an analysis of the transit parameters to calculate false positive probabilities. In Section 7.5, we discuss potentially interesting systems, including a mini-Neptune orbiting an M dwarf which receives a similar insolation to the Earth. In Section 7.6, we summarize and discuss our results.

7.2 Stellar Properties

Photometry

With the exception of one star in our sample (K2-18), we do not have spectroscopic data with which to characterize the stellar properties. Additionally, there are no measured parallaxes for any of these stars. Instead, we rely on photometry. For each system, we query the VizieR database of astronomical catalogues (Ochsenbein et al. 2000). We record the B, V, g', r', and i' magnitudes and their uncertainties from the AAVSO Photometric All-Sky Survey (APASS) DR6 (Henden & Munari 2014), as reported in the UCAC4 Catalogue (Zacharias et al. 2012). We also record the J, H, and K magnitudes and their uncertainties as found in the 2MASS All-Sky Catalog of Point Sources (Cutri et al. 2003) and the $W1-W3$ WISE magnitudes and

uncertainties from the ALLWise Data Release (Cutri & et al. 2013). For all except two of our targets, the $W4$ band is only an upper limit, and in the remaining two cases, the photometric uncertainty in $W4$ is at least an order of magnitude larger than those in $W1 - W3$, so we do not use $W4$ for any system. These data are reported in Table 7.1, and a color-color diagram showing the $r - J, J - K$ colors of our candidates is included as Figure 7.1.

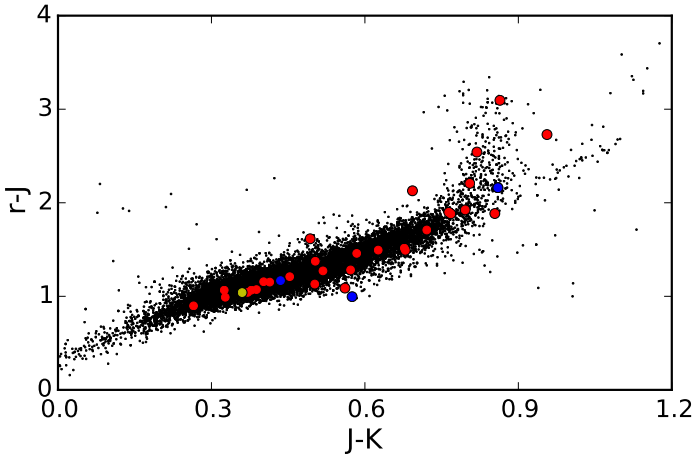

Figure 7.1: Color-color diagram displaying $r - J, J - K$ photometry for targets observed by *Kepler* during the original mission (black), with our *K2* Campaign 1 planet candidates overlaid (red). Also included is the location of the Sun (yellow) and host stars of previously confirmed *K2* planets (blue). 90% of our candidates have photometry consistent with later spectral types than the Sun.

Stellar Models

To convert the observed photometric data into physical properties for each star, we used the new publicly available `isochrones` Python module[1], a general-purpose interpolation tool for the fitting of stellar models to photometric or spectroscopic parameters (Morton 2015a). This software does trilinear interpolation in mass–age–[Fe/H] space for any given set of model grids, and is thus able to predict the value for any physical or photometric property provided by the models at any values of mass, age, and [Fe/H] within the boundaries of the grid.

This enables a set of observed properties ($\{x_i, \sigma_i\}$), either spectroscopic, photometric, or both, to define a likelihood function to be sampled:

$$\ln \mathcal{L}(\boldsymbol{\theta}) \propto -\frac{1}{2} \sum_i \frac{(x_i - I_i(\boldsymbol{\theta}))^2}{\sigma_i^2}, \tag{7.1}$$

[1] `http://github.com/timothydmorton/isochrones`

where $I_i(\boldsymbol{\theta})$ is the isochrone model prediction of property i at the given parameters $\boldsymbol{\theta}$. If the observed properties include any apparent magnitudes, then $\boldsymbol{\theta}$ includes distance and extinction in addition to mass, age, and [Fe/H] .

In this work, we use grids from the Dartmouth Stellar Evolution Database (Dotter et al. 2008) at solar values of [α/Fe] =0.0 and helium abundance $Y = 0.2741$, which come packaged with the `isochrones` module. We then infer the stellar parameters using `MULTINEST` (Feroz et al. 2009), an implementation of a multimodal nested sampling algorithm, for each host star conditioned on the observed photometric properties as presented in Table 7.1. `MULTINEST` is designed to sample multimodal posteriors, where other samplers such as MCMC algorithms often struggle. Given the multimodal nature of our posteriors, this scheme is optimal for capturing parameter space on the subgiant branch where these stars could reside. We include a prior on stellar metallicity representative of the observed metallicities of stars within 1 kpc of the Sun, following the results of Hayden et al. (2015), and a Salpeter-slope prior on mass up to the maximum mass available in the model grids of 3.7 $M_{\odot}$.

During the sampling process, we fit for galactic extinction as one of our physical parameters. We include the WISE bandpasses by applying the relative extinction values between SDSS, 2MASS, and WISE calculated by Davenport et al. (2014). In each step of our fitting process, we draw a value for A_V, calculate the expected extinction in all bandpasses A_X assuming the $R_V = 3.1$ reddening law of (Fitzpatrick 1999), and then measure the likelihood of our model stellar fit to the observed apparent magnitudes. We apply a uniform prior ranging from zero to a maximum extinction value of 0.2 and marginalize over extinction in our final determination of stellar parameters. The NASA/IPAC Extragalactic Database (NED), which reports the Schlafly & Finkbeiner (2011) recalibration of the Schlegel et al. (1998) extinction map as measured by COBE/DIRBE and IRAS/ISSA, suggests that typical A_V extinction values to the edge of the galaxy at this high galactic latitude are $\sim$0.1 magnitudes, so our upper limit appears to be justified.

Such a scheme enables us to infer the statistical uncertainties on the mass, radius, and effective temperature. However, we are subject to biases induced by systematics in the models themselves. There is some evidence that the Dartmouth models may under-predict radii of M dwarfs by $\sim$ 15% when compared to other methods (Montet et al. 2015a; Newton et al. 2015). Such an effect may be the result of the Dartmouth model reliance on BT-Settl atmospheres, which are based on incomplete molecular line lists and have been shown to predict near-IR colors that are too blue

(Thompson et al. 2014).

As our stellar results are model-dependent, we caution users who intend to use these parameters for other works, such as exoplanet population studies. When available, stellar parameters inferred through other techniques such as asteroseismology or spectroscopy should supersede these values. We note the observed photometric parameters are consistent with spectroscopically-derived parameters for stars with published spectra, and consistent with typical model-dependent uncertainties from photometric data (e.g. Huber et al. 2014). We provide full samples of our posteriors on the physical parameters for each star[2].

Bastien et al. (2014) use the "granulation flicker" in the *Kepler* light curves to suggest that approximately 50 percent of planet host stars have evolved off the main sequence onto the subgiant branch, so that both the host stars and their planets are larger than previously reported. Similarly, in *K2* Campaign 1 we may expect to find evolved stars in a sample of planet candidates, although we may expect the effect to be lessened due to the high galactic latitude of Campaign 1. Indeed, we find this to be the case. Two stars, EPIC 201257461 and 201649426 are definitively evolved stars, with inferred masses less than 2 $M_\odot$but radii above 8 $R_\odot$. For approximately one third of the others, we find the stellar radius posterior distribution to be bimodal, with both main sequence and subgiant models of the stars being consistent with the photometric data. This number is consistent with our expectations of the number of subgiant contaminants in the Campaign 1 field (K. Stassun, private communication). Future observations to measure the parallaxes of these stars, such as with Gaia, will be helpful in differentiating between these two models to determine more precisely the stellar, and thus the planetary, radii.

SNIFS and SpeX Spectroscopy

A near-infrared spectrum of K2-18 was obtained using the upgraded SpeX (uSpeX) spectrograph (Rayner et al. 2003) on the NASA Infrared Telescope Facility (IRTF) on January 29 2015 (UT). SpeX observations were taking using the short cross-dispersed mode and the 0.3×15 arcsec slit, which provides simultaneous coverage from 0.7 to 2.5μm at $R \simeq 2000$. The target was observed at two positions along the slit to subsequently subtract the sky background. Eight spectra were taking following this pattern, which provided a final S/N of > 150 per resolving element. The spectrum was flat fielded, extracted, wavelength calibrated, and stacked using

[2] `http://www.astro.princeton.edu/~tdm/k2/`

the *Spextool* package (Cushing et al. 2004). An A0V-type star was observed immediately after the target, which was used to create a telluric correction using the *xtellcor* package (Vacca et al. 2003).

An optical spectrum was obtained using the SuperNova Integral Field Spectrograph (SNIFS, Aldering et al. 2002; Lantz et al. 2004) on the University of Hawai'i 2.2m telescope on the night of January 30 2015. SNIFS provides simultaneous coverage from 3200Å–9700Å at a resolution of $\simeq$ 1000. Final S/N of the spectrum was $>$ 100 per resolving element in the red ($\sim$ 6000Å). Details of the SNIFS reduction, including dark, bias, and flat-field corrections, cleaning the data of bad pixels and cosmic rays, and extraction of the one-dimensional spectrum are described in Bacon et al. (2001) and Aldering et al. (2006). Flux calibration was performed using a separate pipeline described in Mann et al. (2015).

T_{eff} was calculated by comparing our optical spectra with the CFIST suite[3] of the BT-SETTL version of the PHOENIX atmosphere models (Allard et al. 2013), which gave a temperature of 3503 ± 60 K. More details of this procedure are given in Mann et al. (2013b) and Gaidos et al. (2014). This method was used because it is known to accurately reproduce empirical T_{eff} values from long-baseline optical interferometry Boyajian et al. (2012).

Metallicity was determined using the procedures from Mann et al. (2013a), in which the authors provide empirical relations between atomic features and M dwarf metallicity, calibrated using wide binaries. We adopted the weighted mean of the $H-$ and $K-$band calibrations, which yielded a metallicity of 0.09±0.09.

We combined the derived T_{eff} and [Fe/H] values with the empirical T_{eff}-[Fe/H]-R_* relation from Mann et al. (2015) to compute a radius. Accounting for measurement and calibration errors in [Fe/H] and T_{eff} we calculated a radius $0.394\pm0.038 R_\odot$. We use these parameters instead of the derived photometric properties for this target, although we note the two are consistent at the 1σ level.

The full list of stellar parameters adopted in this paper is included in Table 7.2.

7.3 Planet Properties

In Foreman-Mackey et al. (2015), only parameters directly observable from the *K2* light curve itself were reported: the period, time of transit center, and transit depth. With stellar properties now in hand, we can convert these observational results into

[3] `http://phoenix.ens-lyon.fr/Grids/BT-Settl/CIFIST2011/`

fundamental parameters of each planet candidate. For each candidate, we fit the light curve using a physical transit model (Mandel & Agol 2002; Kipping 2010b) simultaneously with a systematics model similar to the one described by Foreman-Mackey et al. (2015). We use `emcee` (Foreman-Mackey et al. 2013), an implementation of the affine-invariant ensemble sampler of Goodman & Weare (2010) to sample from the posterior probability distribution for the stellar—limb darkening coefficients, mass, radius, and effective temperature—and planetary—radius, period, phase, impact parameter, eccentricity, and argument of periapsis—parameters, conditioned on the light curve and the measured stellar properties.

Following Foreman-Mackey et al. (2015), the likelihood function that we use is marginalized over the weights of the "eigen light curves" in the linear systematics model. Unlike Foreman-Mackey et al. (2015), we include an empirical Gaussian prior on the weights determined by robustly computing the distribution of weights across the full set of Campaign 1 light curves. This prior mitigates the incorrect detection of false signals induced by stellar variability—as discussed below in Section 7.5—so we exclude these candidates (EPIC 201929294 and EPIC 201555883) from the tables of results.

In this analysis, we assume the dilution caused by additional stars contributing flux into the aperture is negligible for nearly all systems. Given the location of the Campaign 1 field at a high galactic latitude, we expect low contamination by background giants. Nevertheless, this assumption may not be valid for all systems. Any contamination unaccounted for, as may happen if any of these stars are actually unresolved binaries, would cause us to underestimate the radii of any planets we detect. Therefore, high-contrast adaptive optics imaging of any systems should be obtained before these planets are used in population inference studies. The planet parameters measured by this analysis are listed in Table 7.3.

7.4 False Positive Analysis

There are many scenarios which can cause an astrophysical false positive, where an eclipsing binary star masquerades as a transiting planet. The most common scenarios are if (a) it is a highly grazing eclipse, or (b) the binary system shares a photometric aperture with a significantly brighter star, resulting in a diluted eclipse depth. When possible, such astrophysical false positive scenarios are traditionally ruled out by detailed follow-up observations, often a combination of high-resolution imaging and radial-velocity measurements. However, the *Kepler* mission, with its

thousands of planet candidates around mostly faint stars, necessitated a paradigm shift—a move toward probabilistic interpretation of transit signals, rather than comprehensive follow-up of each individual candidate (Morton & Johnson 2011).

Morton (2012) presented an automated method to calculate the probability that a planet candidate might be caused by an astrophysical false positive. This method uses galactic population simulations to determine the distributions of possible false positive scenarios, comparing the typical light curve shape of each to the data. It then combines this information with observationally motivated prior assumptions about the populations of field stars, the properties of multiple star systems, and the occurrence rate of planets as determined from *Kepler* (Fressin et al. 2013), in order to determine the probability that the observed signal may be a false positive. Similar in spirit to other published methods of probabilistic validation, such as BLENDER (Torres et al. 2011) and PASTIS (Díaz et al. 2014b), it has the advantage of being computationally less demanding and fully automated, and thus easily applied in batch to a large number of candidates.

In this work, we use `vespa`[4] (Morton 2015b), a new publicly available, general-purpose implementation of the Morton (2012) procedure, to calculate false positive probabilities (FPPs) for each of these *K2* candidates. The following constraints on false positive scenarios are imposed:

- A chance-aligned eclipsing binary system may reside anywhere inside or within one pixel of the photometric aperture of the target star. In creating a light curve for each star, we define photometric apertures ranging from 10 to 20 arcseconds for each star, as defined in Table 7.4. Given the 6-arcsecond PSF of the *Kepler* telescope, we allow for the possibility that companions falling just outside of our aperture (within one pixel) may contribute to the light curve, possibly causing a false positive event. The search for such companions is discussed in Section 7.4.

- The maximum allowed depth of a potential secondary eclipse event is the most significantly detected signal at the same period of the planet candidate, once the primary transit is masked out (discussed in Section 7.4). `vespa` does not allow for the possibility of secondary eclipses larger than those observed in the *K2* light curve for each star.

[4] `http://github.com/timothydmorton/vespa`

- Blended stars must be allowed by the available adaptive optics and archival imaging data (discussed in detail in Section 7.4 and 7.4). `vespa` only considers stars below the detection threshold for the AO imaging, which is a position-dependent value following a calculated contrast curve for each star.

Each of these scenarios is an astrophysical eclipse, caused by one object passing in front of another, blocking some fraction of the total light. The calculations here do not include the possibility that each signal is caused by an instrumental artifact in the data or some other astrophysical event, such as stellar activity, masquerading as planet transits.

Table 7.5 summarizes the results of these calculations, presenting the relative probability for each candidate to be caused by any of three false positive scenarios: an undiluted eclipsing binary (EB), a hierarchical triple eclipsing binary (HEB), and a chance-aligned background(/foreground) eclipsing binary (BEB).

Six of the presented candidates have FPP >90%; these are considered to be likely false positives. On the other hand, 24 candidates have FPP < 1%. Three of the transit signals might plausibly be caused by contamination by detected stellar companions within the photometric apertures (see §7.4), so we keep these as candidates.

This leaves 21 candidates that we statistically validate as planets, including four that have been previously identified in the literature (Armstrong et al. 2015; Crossfield et al. 2015). So in total, of the 36 candidates, 21 are secure planets, 17 of which we validate here for the first time.

We emphasize that the majority of these validations rely solely on the transit photometry and SDSS data, with follow-up imaging only obtained for seven of the 31 targets. This demonstrates the utility of the `vespa` tool, which will be crucial to interpreting future candidates detected by *K2*, TESS, and PLATO and prioritizing follow-up observing efforts. We show the transit signals in Figure 7.2.

Secondary Eclipse Observations

One of the definitive signatures of a false positive binary star system masquerading as a transiting planet is the presence of a secondary eclipse. While a nondetection of a secondary does not exclude the possibility of a binary system (the orbit may be eccentric, or the companion too faint for a secondary eclipse to be detectable in the noise), such a nondectection reduces the probability of each of the eclipsing binary false positive scenarios.

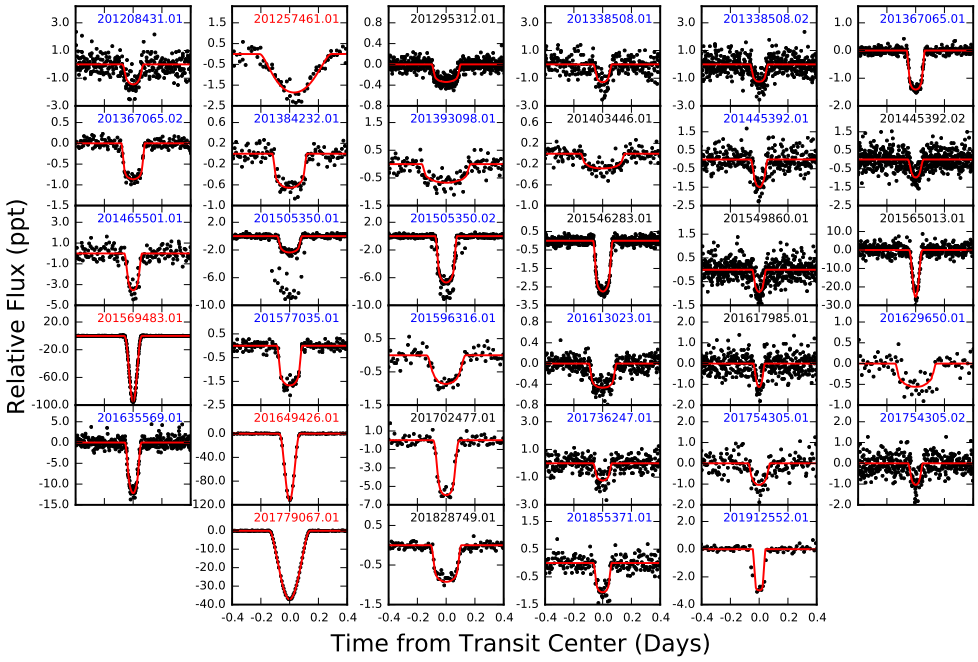

Figure 7.2: Phase-folded *K2* photometry for all planet candidates analyzed in this chapter. Each is the product of a fiducial noise model, in which the median systematic has been removed for illustrative purposes. The systems which we validate as transiting planets are labeled in blue. The systems which we confirm as false positive events are labeled in red. The systems which we leave as candidates are labeled in black. Red curves outline the median transit model for each candidate system.

To attempt to eliminate each eclipsing binary scenario, we first search each *K2* light curve to determine which secondary eclipse signals are not allowed by the data. We mask the transit signal of the planet in question and search for the most significant signal at the same period. Such a scheme does not assume circular orbits: we return the most significant signal at any phase, not only at the midpoint between consecutive transits.

We report these maximum allowable secondary eclipse depths in Table 7.5. These values are used by `vespa` as limits on the allowable secondary eclipse. Any models that cause a larger event, such as a background eclipsing binary consisting of two equal-mass stars in a circular orbit, can be excluded by the data. We note that with the exception of K2-19c, all systems with a maximum eclipse depth of at least one part per thousand have FPPs of 0.866 or larger. The exception, K2-19, is a two-planet system with the two planets near a 3:2 period commensurability, so in this case the "secondary" is actually the transits of the other planet.

Adaptive Optics Imaging

We obtained high resolution images of seven stars with the Palomar High Angular Resolution Observer (PHARO) infrared detector (Hayward et al. 2001) behind the PALM3000 adaptive optics system (Dekany et al. 2013) at the Palomar 5.1-meter Hale telescope on the nights of 2015 February 3 and 4 UT. Sky conditions were mostly clear with light cirrus and ≈1.0–1.3 arcsecond seeing on both nights. We used the smallest plate scale of 25 mas pix^{-1} which resulted in a field of view of 25.6×25.6 arcsec across the 1024^2 pix^2 array. All observations were obtained with the 32x pupil sampling mode, resulting in Strehl ratios of ≈20–30% in K_S for our V=11–13 mag targets as measured by the Strehl monitor at the telescope in real time. We obtained unsaturated dithered frames of each target in K_S-band with typical integration times of 2–10 s. Except for EPIC 201828749 and EPIC 201546283, which had nearby candidate binary companions, we also acquired deep saturated images (5–10 frames at 60 sec each) to search for fainter companions.

Images were registered and contrast curves were generated following Bowler et al. (2015). For the saturated data, the star's position in each image was found by masking the saturated region and fitting a 2D bivariate Gaussian to the PSF wings. Contrast curves for the median-combined image are calibrated using the unsaturated frames. The typical sensitivity is 6.5–7.5 mag at 1″. The images were astrometrically calibrated using dithered observations of the Trapezium cluster centered on θ^1 Ori C taken on 2015 Feb 3 UT. Based on the reference astrometry for pairs of stars in the field from McCaughrean & Stauffer (1994), we measure a plate scale of 25.2 ± 0.4 mas pix^{-1} and north orientation of –0.2 ± 0.3°. Since this latter value is consistent with being aligned with the detector columns, we adopt a value of 0.0 ± 0.3° for this work. Relative photometry of nearby stars is carried out using aperture photometry with an aperture radius of 12 pix (0.3 arcsec). For EPIC 201828749, we also acquired J- and H-band images. Astrometry and photometry is derived separately for each image, and the mean and standard deviation of these measurements is adopted for our final values listed in Table 7.4.

Images for all systems AO data was obtained for is shown in Figure 7.3, while contrast curves showing the 5σ limits for detection as a function of orbital separation are given in Figure 7.4.

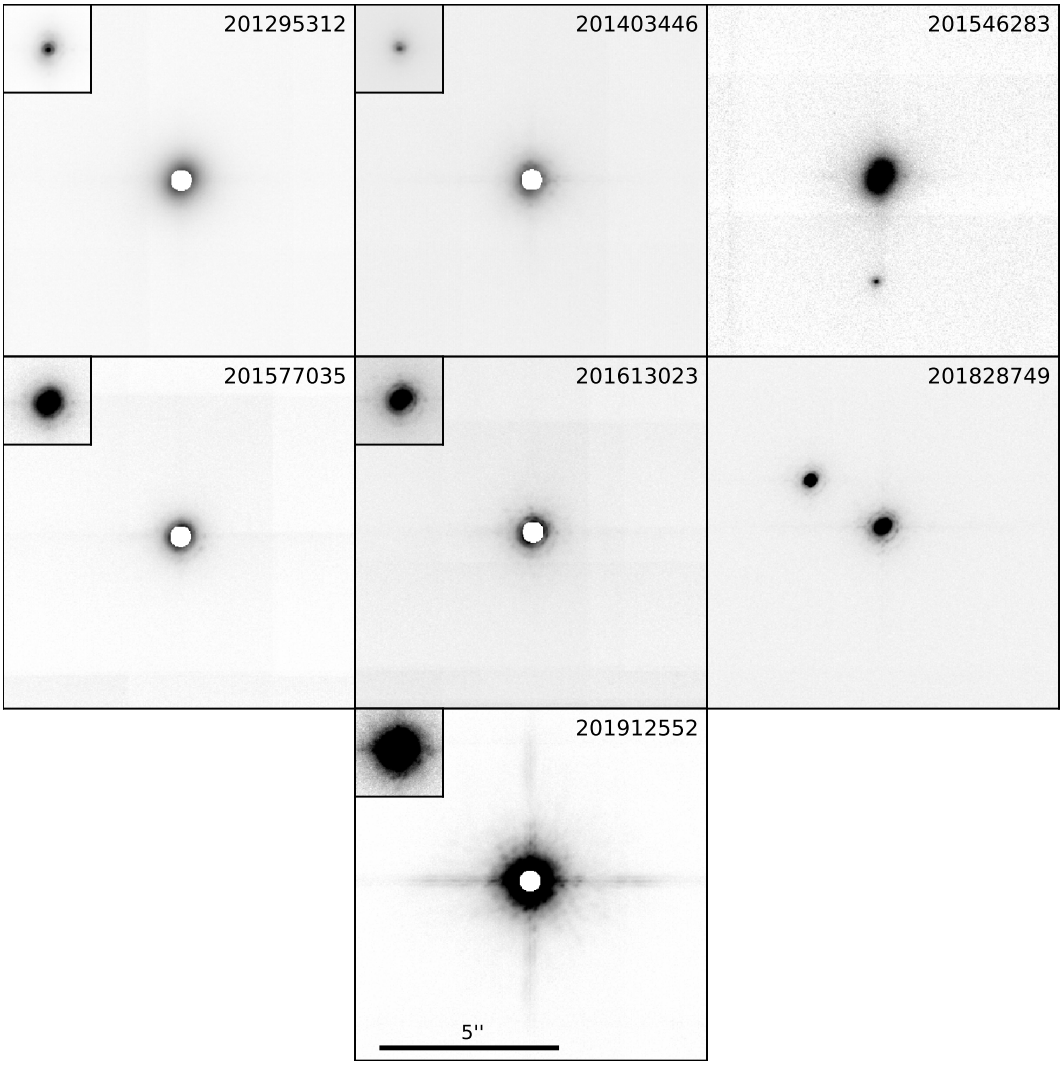

Figure 7.3: Adaptive optics images for the seven stars observed with high-contrast imaging. The main frame for each single system shows the deep, saturated image. The inset for each single system shows a shallower, unsaturated image to better identify companions at close projected orbital separations. For the two systems with imaged companions, EPIC 201546283 and EPIC 201828749, only unsaturated frames are collected. The pixel scale is 0.0252 arcsec per pixel. Each subplot is a square 400 pixels on a side and each inset is a square 100 pixels on a side. All subplots, including insets, are plotted on the same scale.

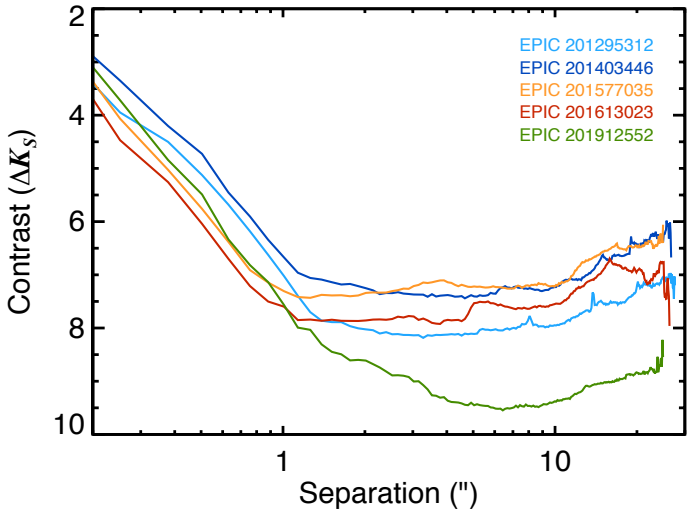

Figure 7.4: 5σ contrast curves for all systems with AO nondetections. For all systems, we can exclude the possibility that a companion at a given ΔK_S exists. From our known transit depths, we can then rule out significant parameter space in which an eclipsing binary could reside and mimic a transit signal.

Known Background Stars

The PHARO AO system has a field of view of 25 arcseconds. Each *K2* pixel is a square, 3.98 arcsec on a side. A background eclipsing binary within a few *K2* pixels of our target stars could mimic a transit signal inside our aperture while evading detection by PHARO. Such wide eclipsing binaries should appear in seeing-limited ground-based surveys.

To investigate the possibility that such wide companions exist, we query the ninth data release of the Sloan Digital Sky Survey (SDSS DR9, Ahn et al. 2012). For each target, from the depth of the observed transit we determine how bright a background object must be to cause the event if the background object were an equal mass totally-eclipsing binary. We then search for all stars within 25 arcsec that are within this brightness limit relative to the candidate host star. All apertures we use in our *K2* analysis are smaller than 20 arcsec so this search should encompass the region where possible background contaminants could reside. Of the 31 stars in our sample, eleven have such a companion, plus one detected in AO imaging.

Unlike the original *Kepler* field, the field for *K2* Campaign 1 is well out of the galactic plane, so the rate of giant, distant background stars is significantly lower. We include all potential contaminants in Table 7.4. We validate or eliminate each of

these as a possibility based on the transit shape. For example, the events near EPIC 201546283 could only be caused by a background binary if the background object was a completely-eclipsing system (so that the eclipse depth was 50%). In this case, the transit would be V-shaped. Since it is not, the background object likely does not cause the transit event.

In Table 7.4, the "maximum depth" column represents the maximum observed "transit" depth if the transit were actually caused by a total eclipse of the hypothetical background binary system, inducing a 50% flux decrement in the background star's apparent brightness.

The photometric apertures used to detect these candidates range in radius from 10.0 to 19.9 arcsec. In order to be a plausible contaminant, any companion star must be either within this aperture or just outside but bright enough for significant flux to leak in. Evaluating each of the systems listed in Table 7.4, we judge that we cannot yet rule out contamination as a potential source of the transit signal for four candidates: 201295312.01, 201403446.01, 201546283.01, and 201828749.01. Despite receiving low FPP scores from `vespa`, we list these systems as candidates in Table 7.5, rather than planets. Further updates to the `vespa` code will allow consideration of "specific" false positive scenarios; that is, scenarios that correspond to actually detected stars such as these, rather than hypothetical background or bound companions.

The candidates with identified companions that we judge to not be plausible sources of potential contamination are the following:

- K2-13b (201629650.01)— The companion to this star is 17.3 arcsec from the EPIC target. As this is outside the aperture (radius 15.9 arcsec) and the background star is not particularly bright, we rule out contamination for this system.
- 201702477.01— The companion to this star is 12.15 arcsec from the EPIC target, and the aperture size is 10.0 arcsec. In addition, the maximum depth in this system is almost identical to the transit depth. For these two reasons we rule out contamination in this case.

SDSS is 95% complete at $r = 22.2$ mag and the telescope has a point spread function of 1.4 arcsec. For the purposes of the `vespa` calculation, we thus treat nonde-

tection in SDSS data as providing a contrast curve at wide separations down to a limiting magnitude of $r = 22.2$ mag.

Archival Imaging

For the stars with AO nondetections, there is still the possibility that a background binary could be positioned directly behind the target star, evading detection. The probability is small, given the 0.1 arcsec diffraction limit of the Hale Telescope at 2 μm, but nonzero. While the `vespa` calculations quantify this probability for this to occur, we can also rule out the possibility of such chance alignments, down to a certain contrast, with archival imaging data.

Five of the stars in our sample have proper motions larger than 50 mas yr^{-1}, so they have moved across the sky by $\gtrsim 2.5$ arcsec since they were imaged during the first Palomar Observatory Sky Survey (POSS) in the 1950s. To rule out background companions, we download data from the POSS I and II surveys, which imaged these targets in 1952-1955 and 1989-1998, respectively. We also download data from the Sloan Digital Sky Survey, which imaged these fields between 2000 and 2009. As shown in Figure 7.5, we do not detect any background targets at the present-day location of any of these stars in any of these images.

For this target, we can extend our contrast curves to zero present-day orbital separation and rule out the possibility that these transit events are caused by a background eclipsing binary. By combining present-day seeing-limited photometric survey data, adaptive optics imaging, and archival photometry, the only stellar companions we would not detect would be those that are gravitationally bound to the target star and positioned in their orbits so that their projected separation is smaller than the diffraction limit of the Hale Telescope. Such an alignment would require the orbital inclination of the binary to be nearly 90° and the phase $\varpi + \theta \approx \pi/2$ or $3\pi/2$. While we cannot fully rule out this possibility, the `vespa` calculations confirm that its probability is negligibly small.

TRES Radial Velocities

We observed K2-18 on 2015 February 04 and 25 UT with the Tillinghast Reflector Echelle Spectrograph (TRES) on the 1.5 m Tillinghast Reflector at the Fred L. Whipple Observatory. These dates were chosen to be near the times of largest RV variations, corresponding to phases of 0.72 and 0.32 relative to the time of transit. The spectra were taken with a resolving power of $R = 44,000$ and integration times ranging from 2800 to 3600 seconds, resulting in signal-to-noise ratios between 17

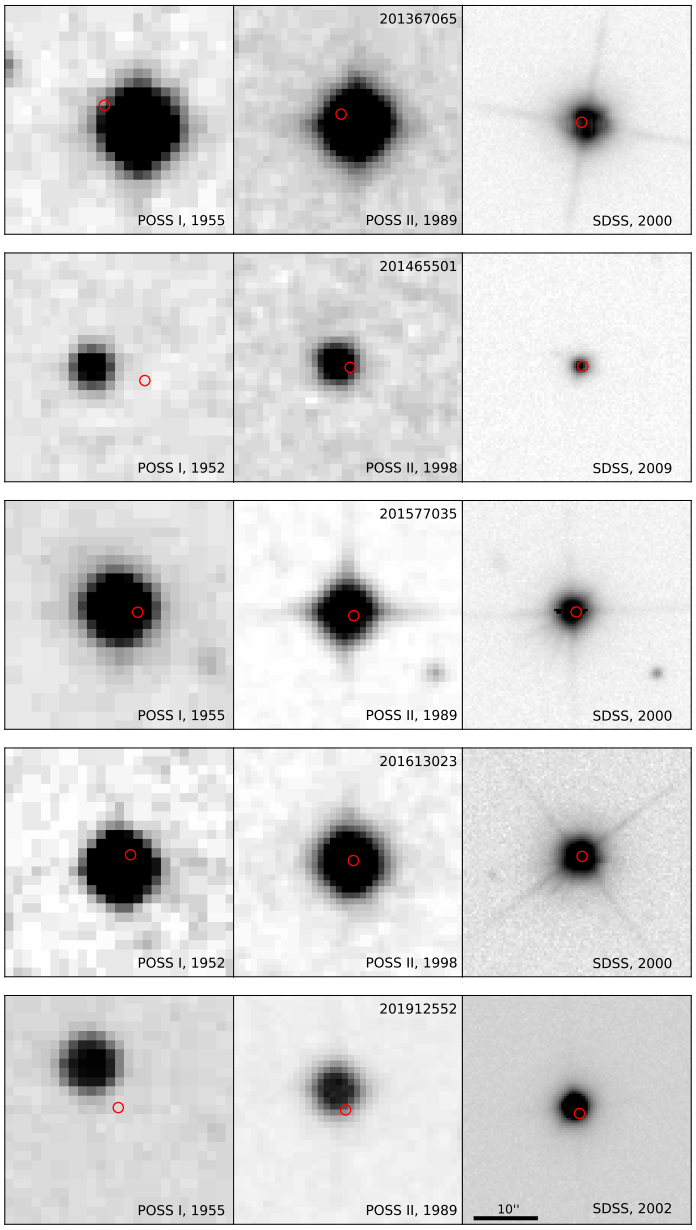

Figure 7.5: Archival imaging for the five highest proper motion targets in our sample. In all cases, there are no background objects directly behind the present day location of the target (red circle) that could be missed by the AO observations. Modern SDSS imaging can also rule out wide companions that may have been missed at wide separations, beyond the AO field of view, such as the companion which can be seen in the images of K2-10. All figures are aligned such that north is up and east to the left. All subplots are on the same scale.

and 29 per resolution element.

The spectra were extracted as described in Buchhave et al. (2010). The relative RVs were derived by cross-correlating the spectra against the strongest observed spectrum (in this case, the first) over the wavelength range 4700 - 6800 Angstroms. We selected 19 echelle orders in the analysis, being careful to reject orders with telluric absorption lines, fringing in the far red and those with very low SNR in the blue.

The two observed spectra have RVs that differ by 47 ± 42 m s^{-1}. If the RVs were caused by a stellar companion, the RV shift between these observations would be on the order of km s^{-1}. Therefore, we can rule out any stellar-mass companions that would be able to create this transit signal.

7.5 Potentially Interesting Systems

A Mini-Neptune with Earthlike Insolation

The planet orbiting K2-18 may be an interesting target for atmospheric studies of transiting exoplanets.

By combining archival and modern seeing-limited data with adaptive optics imaging, we can exclude the possibility these transit events are caused by a background eclipsing binary. The apparent transits must be caused by an object co-moving with K2-18; radial velocities eliminate the possibility the companion is nonplanetary. Therefore, we confirm the planetary nature of this system.

This star is an M2.8 dwarf at a distance of 34 ± 4 pc. Of our planet candidate hosts, only K2-3 (originally discovered by Crossfield et al. 2015) is brighter in K-band. This star is only 0.1 magnitudes fainter in K than GJ 1214 (Charbonneau et al. 2009). Due to the relative brightness of the host star, this target is likely to become a prime target for atmospheric characterization studies and is ideal as a target for future space-based missions such as *JWST*.

The planet is slightly smaller than GJ 1214b, but unlike that planet, K2-18b is not highly irradiated. Instead, it is at a reduced semimajor axis $a/R_\star = 83.8 \pm 9.0$. Its equilibrium temperature is then, assuming zero albedo, $T_{eq} = 272 \pm 15$ K, meaning its bulk insolation is 128 ± 28 percent that of the Earth's. Although the planet is likely too large to be rocky (Rogers 2015), its atmosphere is likely to be the focus of many future observations, providing a cool analogue to the highly irradiated planets of a similar size found by *Kepler*.

Other Sources of False Positives

The method of Foreman-Mackey et al. (2015) assumes that all variability in the light curves are caused by either the motion of *K2*, in which case the variability is shared by all stars, or transits of planets, in which case the variability is intrinsic to only one star. This assumption breaks down for extremely spotted stars where the astrophysical variability is larger than the instrumental magnitude. In that regime, the starspot modulations can be incorrectly fit by the systematic model, causing spurious transits to appear. This appears to be the case with EPIC 201929294, which has coherent starspots that appear to have the same rotation period as the transit period reported previously. Because the starspots are so periodic and coherent, these spurious transits were falsely identified as a planet candidate; we consider that system a false positive in this work.

The candidate object possibly orbiting EPIC 201555883 has a period, time of transit, and transit duration consistent with EPIC 201569483. Such effects are not uncommon in *Kepler* data. Coughlin et al. (2014) identify 685 KOIs as false positives and outline four physical reasons why these anomalies may occur. EPIC 201555883 is a unique case in that it does not appear to fall under any of these cases. It falls on module 23, while EPIC 201569483 is on module 8, neither 180 degrees away from nor on the same column as this candidate. Moreover, there is not any evidence of a mechanism that could cause a third star to induce both the appearance of a 7% eclipse on one module and an additional anomalous transit event on a different module. Instead, this candidate could be a false positive caused by a different systematic mechanism.

Foreman-Mackey et al. (2015) modeled the systematic effects in the *K2* light curves using a linear combination of "eigen light curves" generated empirically by running a principle component analysis on the light curves of every star. This means that the training set includes the light curves for variable stars, eclipsing binaries, and even transiting planets. Again, this star has significant variability caused by starspots. In this case, the fitting procedure tries to account for stellar variability using the eigen light curves. This overfit gives undue weight to eigen light curves that include the transits of EPIC 201569483, causing this spurious transit to occur. Again, we consider this system to be a false positive. As stated in Section 6.3, by including an empirical Gaussian prior on the weights for the eigen light curves in the linear systematics model, the signals observed on EPIC 201555883 and 201929294 are mitigated, suggesting such a scheme should be employed in searching for planet

candidates in future campaigns.

The problem of over-fitting stellar variability using eigen light curves can also be solved by adding a stellar activity model to our fitting procedure. In this case, the spacecraft motion could be fit simultaneously with a model of starspot modulation, asteroseismic oscillations, and planet transits. Such a model is currently under development (Angus et al. *in prep*).

Multiple Planet Systems

Five of the systems reported by Foreman-Mackey et al. (2015) have more than one transiting candidate. One of these is K2-3, a three-planet system originally announced by Crossfield et al. (2015). Another of these is K2-19 (Armstrong et al. 2015), a two-planet system with the orbital periods of the two planets near a 3:2 period commensurability. The remaining three are all representative of the multiple-planet systems observed by *Kepler* (Lissauer et al. 2011b; Fabrycky et al. 2014). Two of the systems are near a period commensurability and all three consist of mini-Neptune sized planets.

We do not detect any significant transit timing variations (TTVs) in any of these systems from the *K2* data alone. K2-5 would be expected to have a TTV period of 117 days, but is likely too far from commensurability to have an observable TTV signal. K2-8 is expected to have a TTV period of 234 days, so this system may be a candidate for additional follow-up to constrain the system masses dynamically. The transiting planets orbiting K2-16 are near a 5:2 period commensurability. There is no evidence from *Kepler* of an abundance of planets near this period ratio, and so this may be coincidence. Follow-up observations may be warranted to search for an additional planet in this system forming a resonant chain, similar to those observed around other stars (e.g. Swift et al. 2013; Campante et al. 2015).

Systems Orbiting Bright Stars

One of the primary goals of *K2* is the detection of transiting planets around bright stars that can be followed up from the ground or with future space-based observatories such as JWST (Howell et al. 2014). Of our sample, two systems orbit stars with $K < 9$ mag: K2-3 (Crossfield et al. 2015) and K2-18. An additional planet candidate may orbit EPIC 201828749, a star with $K = 9.93 \pm 0.03$ mag. These targets are ideal for ground-based followup and may be useful targets for Spitzer and JWST to probe planetary atmospheres.

7.6 Results and Discussion

We have presented stellar parameters for all planet candidates systems identified by Foreman-Mackey et al. (2015). We statistically validate 21 of the 36 candidates as bona fide planets, and we identify 6 as false positives, including two systematic false alarms. Of the planets, 4 have been previously validated in other works, while 17 are validated here for the first time. The systems not validated as planets or false positives remain as planet candidates.

Enabling much of this analysis are two new publicly available Python packages: `isochrones`[5], which we use to infer posteriors on physical stellar properties based on fitting theoretical stellar models to observed data; and `vespa`[6], a new implementation of the Morton (2012) transit false positive analysis scheme. Both of these packages will continue to be useful in future analysis of transit candidates where comprehensive follow-up observations may be unavailable.

The `isochrones` package uses the nested sampling scheme `MULTINEST` to capture the true multimodal nature of the posteriors. Using an MCMC algorithm instead can cause only one peak in the posterior distribution to be sampled. If the photometry is consistent with both a star on the main sequence and the subgiant branch, an MCMC technique could cause one of these peaks (likely the subgiant possibility) to be missed, leading to an underestimation in the likelihood of subgiant stars and and underestimation of the uncertainties of both the stellar and planetary parameters.

With the exception of one object, all of the stellar parameters are derived from comparing photometric observations to the Dartmouth stellar evolution models. As a result, both the stellar and planet parameters are subject to systematic biases induced by discrepancies between the models and reality.

The planets we confirm in this paper, like the planets found in the original *Kepler* mission, span a wide range of parameter space. They are at distances ranging from 34 to 700 pc, have radii ranging from 1.3 to 5.3 $R_\oplus$, and orbit with periods ranging from 5.0 to 50.3 days. Like the original mission, we find significantly more small planets than large planets, as expected from the radius distributions measured from *Kepler* (Howard et al. 2012; Fressin et al. 2013; Morton & Swift 2014).

Unlike the original mission, however, we find that nearly all of our confirmed planets are around stars less massive than the Sun. This difference is a result of both the

[5] `http://github.com/timothydmorton/isochrones`

[6] `http://github.com/timothydmorton/vespa`

Campaign 1 field and the target selection process. Campaign 1 is at a significantly higher galactic latitude than the original *Kepler* mission, meaning there is a much lower number density of targets at large distances. As massive stars at kiloparsec distances are relatively less likely to exist in Campaign 1 than near the galactic plane, the pool of targets that could be selected for Campaign 1 contains a larger fraction of subsolar stars.

Low-mass stars, particularly M dwarfs, are also a specific focus of the *K2* mission. One of the primary goals of the *Kepler* mission was to "determine the abundance of terrestrial and larger planets in or near the habitable zone of a wide variety of spectral types of stars" (Batalha et al. 2013) However, $\sim$ 70% of Kepler's target stars had masses within 20% of the Sun's, while 70% of the stars in the Galaxy have less than 50% the mass of the Sun (Brown et al. 2011). *K2* will fulfill the promise of *Kepler*, with the goal of providing a yield of small planets around bright, small stars to facilitate follow-up measurements (Howell et al. 2014). This is clear from the *K2* target selection process, with thousands of K and M dwarfs being selected in each campaign. Based on these plans, we expect that *K2* will detect hundreds of planets during its lifetime, with the majority being mini-Neptunes and super-Earths around stars less massive than the Sun.

EPIC	B^1	V^1	g^1	r^1	i^1	J^2	H^2	K^2	W1[3]	W2[3]	W3[3]
201208431	16.23(05)	14.91(03)	15.56(04)	14.29(07)	13.89(12)	12.37(02)	11.75(02)	11.57(02)	11.51(02)	11.55(02)	11.58(20)
201257461	12.82(03)	11.77(01)	12.24(04)	11.49(01)	11.19(02)	9.99(02)	9.48(02)	9.37(02)	9.28(02)	9.37(02)	9.30(04)
201295312	12.78(04)	12.19(12)	12.41(03)	12.08(09)	12.01(21)	11.02(03)	10.70(02)	10.69(02)	10.63(02)	10.69(02)	10.75(12)
201338508	16.30(07)	14.91(03)	15.62(05)	14.33(02)	13.79(05)	12.45(03)	11.76(02)	11.60(02)	11.49(03)	11.49(02)	11.16(13)
201367065	13.52(06)	12.17(01)	12.87(03)	11.58(02)	10.98(17)	9.42(03)	8.80(04)	8.56(02)	8.44(02)	8.42(02)	8.32(02)
201384232	13.30(05)	12.65(04)	12.91(05)	12.48(06)	12.34(07)	11.44(02)	11.09(02)	11.07(02)	11.00(02)	11.05(02)	11.21(16)
201393098	13.90(04)	13.21(03)	13.54(06)	13.02(04)	12.85(05)	11.95(02)	11.63(02)	11.56(02)	11.52(02)	11.57(02)	11.61(21)
201403446	12.48(02)	12.03(02)	12.18(01)	11.94(05)	11.86(04)	11.05(03)	10.76(02)	10.78(02)	10.67(03)	10.71(02)	10.36(07)
201445392	15.73(02)	14.61(03)	15.19(04)	14.29(02)	14.03(07)	12.83(03)	12.32(03)	12.24(03)	12.16(02)	12.21(02)	—
201465501	—	—	16.73(02)	15.18(03)	14.35(15	12.45(02)	11.71(02)	11.49(02)	11.35(02)	11.21(02)	11.35(19)
201505350	13.80(02)	13.00(01)	13.36(02)	12.76(01)	12.57(02)	11.60(02)	11.21(02)	11.16(03)	11.10(02)	11.13(02)	10.95(12)
201546283	13.51(07)	12.64(02)	13.03(02)	12.37(02)	12.17(05)	11.16(02)	10.79(03)	10.70(02)	10.61(02)	10.66(02)	10.53(09)
201549860	15.56(06)	14.37(05)	14.95(07)	13.85(03)	13.45(05)	12.14(02)	11.56(02)	11.42(02)	11.38(02)	11.46(02)	11.60(25)
201555883	16.48(01)	15.43(01)	16.19(10)	15.09(13)	14.55(08)	13.20(02)	12.53(03)	12.43(03)	12.34(02)	12.38(03)	—
201565013	—	—	18.25(01)	16.91(01)	16.34(01)	14.78(04)	14.11(05)	14.08(07)	13.94(03)	13.87(04)	—
201569483	12.90(08)	12.05(07)	12.44(03)	11.76(08)	11.48(08)	10.39(02)	9.97(03)	9.88(02)	9.82(02)	9.87(02)	9.82(05)
201577035	13.14(11)	12.42(02)	12.70(04)	12.21(03)	12.13(20)	11.06(02)	10.75(02)	10.64(02)	10.64(02)	10.69(02)	10.55(10)
201596316	14.21(01)	13.39(09)	13.78(07)	13.14(12)	12.88(10)	11.87(02)	11.46(02)	11.35(02)	11.29(02)	11.35(02)	10.80(11)
201613023	12.99(09)	12.26(01)	12.56(03)	12.05(03)	11.96(08)	10.98(02)	10.71(02)	10.61(02)	10.58(02)	10.63(02)	10.59(10)
201617985	16.34(02)	14.86(05)	15.62(06)	14.26(08)	13.42(09)	11.72(02)	11.09(04)	10.90(02)	10.73(02)	10.70(02)	10.86(11)
201629650	13.61(03)	12.90(04)	13.20(03)	12.73(01)	12.53(06)	11.57(03)	11.26(02)	11.17(03)	11.14(02)	11.18(02)	10.93(12)
201635569	17.74(16)	16.31(01)	17.02(01)	15.62(01)	14.87(01)	13.42(03)	12.77(02)	12.61(03)	12.52(03)	12.55(03)	—
201649426	14.57(03)	13.53(01)	14.04(01)	13.18(02)	12.86(06)	11.57(02)	11.07(02)	11.07(02)	10.88(02)	10.91(02)	10.86(12)
201702477	15.27(05)	14.57(04)	14.89(04)	14.40(06)	14.24(03)	13.27(03)	12.88(03)	12.77(03)	12.81(02)	12.84(03)	—
201736247	15.49(06)	14.66(05)	15.01(04)	14.35(04)	14.14(02)	13.07(02)	12.55(02)	12.49(03)	12.46(02)	12.50(02)	—
201754305	15.65(04)	14.65(01)	15.13(04)	14.28(01)	13.93(05)	12.76(03)	12.21(03)	12.09(02)	12.06(02)	12.10(02)	12.34(46)
201779067	11.81(01)	11.27(01)	11.53(07)	11.12(01)	10.95(01)	10.13(02)	9.87(02)	9.80(02)	9.74(02)	9.77(02)	9.74(04)
201828749	12.48(04)	11.76(01)	12.13(05)	11.58(04)	11.32(04)	10.49(03)	10.23(04)	9.93(03)	9.82(02)	9.87(02)	9.98(06)
201855371	14.82(06)	13.52(04)	14.20(06)	12.96(03)	12.45(01)	11.08(02)	10.44(02)	10.31(02)	10.22(02)	10.26(02)	10.12(07)
201912552	15.01(06)	13.50(05)	14.22(05)	12.86(04)	11.66(08)	9.76(03)	9.13(03)	8.90(02)	8.77(02)	8.67(02)	8.55(03)
201929294	14.32(04)	13.31(03)	13.78(05)	12.97(07)	12.61(09)	11.48(03)	10.98(02)	10.80(02)	10.73(02)	10.78(02)	10.67(10)

Table 7.1: Photometry for all Objects of Interest.
(1) Magnitude from the AAVSO Photometric All-Sky Survey (APASS) DR6 (Henden & Munari 2014) as reported in the UCAC4 Catalogue (Zacharias et al. 2012).
(2) Magnitude from the 2MASS All-Sky Catalog of Point Sources (Cutri et al. 2003).
(3) Magnitude from the ALLWise Data Release (Cutri & et al. 2013).

EPIC	Alternate Name	RA (J2000) (Degrees)	Dec (J2000) (Degrees)	Mass ($M_\odot$)	Radius ($R_\odot$)	T_{eff} (K)	[Fe/H] (dex)	Distance (pc)
201208431	K2-4	174.745639	−3.905585	$0.63^{+0.03}_{-0.03}$	$0.60^{+0.02}_{-0.02}$	4197^{+45}_{-43}	$-0.12^{+0.10}_{-0.12}$	218^{+11}_{-10}
201257461	—	178.161110	−3.094936	$1.50^{+0.04}_{-0.02}$	$10.96^{+0.82}_{-0.93}$	5141^{+38}_{-42}	$-0.21^{+0.01}_{-0.01}$	1651^{+121}_{-134}
201295312	—	174.011629	−2.520881	$1.07^{+0.07}_{-0.07}$	$1.09^{+0.20}_{-0.11}$	5989^{+100}_{-81}	$-0.02^{+0.15}_{-0.18}$	331^{+61}_{-35}
201338508	K2-5	169.303502	−1.877976	$0.53^{+0.01}_{-0.01}$	$0.52^{+0.01}_{-0.01}$	4102^{+45}_{-41}	$-0.51^{+0.04}_{-0.06}$	181^{+7}_{-7}
201367065	K2-3	172.334949	−1.454787	$0.53^{+0.02}_{-0.02}$	$0.52^{+0.02}_{-0.02}$	3951^{+33}_{-38}	$-0.30^{+0.07}_{-0.06}$	42^{+2}_{-2}
201384232	K2-6	178.192260	−1.198477	$0.97^{+0.07}_{-0.07}$	$0.96^{+0.14}_{-0.09}$	5850^{+79}_{-98}	$-0.14^{+0.17}_{-0.20}$	343^{+52}_{-33}
201393098	K2-7	167.093771	−1.065755	$0.97^{+0.06}_{-0.06}$	$0.96^{+0.17}_{-0.08}$	5772^{+72}_{-91}	$-0.07^{+0.16}_{-0.16}$	433^{+75}_{-38}
201403446	—	174.266345	−0.907261	$1.01^{+0.08}_{-0.06}$	$1.12^{+0.26}_{-0.14}$	6445^{+81}_{-111}	$-0.50^{+0.15}_{-0.13}$	362^{+86}_{-48}
201445392	K2-8	169.793666	−0.284375	$0.79^{+0.03}_{-0.04}$	$0.74^{+0.02}_{-0.03}$	4890^{+38}_{-58}	$-0.01^{+0.11}_{-0.13}$	405^{+14}_{-16}
201465501	K2-9	176.264467	0.005301	$0.24^{+0.05}_{-0.03}$	$0.25^{+0.04}_{-0.03}$	3468^{+20}_{-19}	$-0.46^{+0.12}_{-0.10}$	66^{+11}_{-7}
201505350	K2-19	174.960319	0.603575	$0.84^{+0.04}_{-0.04}$	$0.81^{+0.09}_{-0.05}$	5519^{+49}_{-82}	$-0.27^{+0.10}_{-0.10}$	291^{+33}_{-20}
201546283	—	171.515164	1.230738	$0.89^{+1.15}_{-0.07}$	$0.88^{+7.37}_{-0.10}$	5422^{+194}_{-93}	$-0.09^{+0.31}_{-0.15}$	251^{+2138}_{-29}
201549860	—	170.103081	1.285956	$0.73^{+0.03}_{-0.03}$	$0.69^{+0.02}_{-0.02}$	4523^{+43}_{-47}	$0.05^{+0.15}_{-0.14}$	249^{+9}_{-9}
201555883	—	176.075940	1.375947	$0.54^{+0.07}_{-0.01}$	$0.52^{+0.08}_{-0.01}$	4419^{+29}_{-33}	$-0.98^{+0.62}_{-0.11}$	289^{+46}_{-9}
201565013	—	176.992193	1.510249	$0.51^{+0.13}_{-0.03}$	$0.50^{+0.12}_{-0.03}$	3987^{+142}_{-68}	$-0.44^{+0.47}_{-0.08}$	506^{+154}_{-38}
201569483	—	167.171300	1.577513	$0.83^{+0.05}_{-0.05}$	$0.79^{+0.06}_{-0.05}$	5192^{+55}_{-70}	$-0.09^{+0.17}_{-0.15}$	152^{+12}_{-10}
201577035	K2-10	172.121957	1.690636	$0.94^{+0.04}_{-0.06}$	$0.93^{+0.16}_{-0.07}$	5647^{+60}_{-89}	$-0.04^{+0.14}_{-0.17}$	271^{+48}_{-21}
201596316	K2-11	169.042002	1.986840	$1.35^{+0.04}_{-0.56}$	$5.15^{+0.20}_{-4.39}$	5433^{+49}_{-144}	$-0.12^{+0.01}_{-0.17}$	2019^{+71}_{-1728}
201613023	K2-12	173.192036	2.244884	$1.01^{+0.05}_{-0.06}$	$1.01^{+0.27}_{-0.09}$	5800^{+53}_{-90}	$0.03^{+0.13}_{-0.17}$	294^{+78}_{-27}
201617985	—	179.491659	2.321476	$0.52^{+0.03}_{-0.03}$	$0.49^{+0.03}_{-0.03}$	3742^{+31}_{-36}	$-0.08^{+0.10}_{-0.11}$	111^{+8}_{-9}
201629650	K2-13	170.155529	2.502696	$0.80^{+0.04}_{-0.04}$	$0.78^{+0.09}_{-0.05}$	5698^{+45}_{-82}	$-0.54^{+0.12}_{-0.14}$	290^{+34}_{-18}
201635569	K2-14	178.057026	2.594245	$0.47^{+0.01}_{-0.01}$	$0.45^{+0.01}_{-0.01}$	3789^{+17}_{-16}	$-0.37^{+0.03}_{-0.04}$	219^{+8}_{-8}
201649426	—	177.234262	2.807619	$1.29^{+0.02}_{-0.02}$	$8.15^{+0.32}_{-0.23}$	5086^{+24}_{-26}	$-0.17^{+0.01}_{-0.01}$	2537^{+92}_{-68}
201702477	—	175.240794	3.681584	$0.87^{+0.06}_{-0.06}$	$0.85^{+0.11}_{-0.08}$	5618^{+86}_{-85}	$-0.26^{+0.17}_{-0.18}$	673^{+87}_{-63}
201736247	K2-15	178.110796	4.254747	$0.72^{+0.06}_{-0.03}$	$0.68^{+0.06}_{-0.03}$	5131^{+69}_{-65}	$-0.46^{+0.20}_{-0.14}$	437^{+43}_{-22}
201754305	K2-16	175.097258	4.557340	$0.67^{+0.04}_{-0.03}$	$0.64^{+0.03}_{-0.03}$	4761^{+50}_{-57}	$-0.40^{+0.12}_{-0.17}$	324^{+16}_{-16}
201779067	—	168.542699	4.988131	$0.91^{+0.03}_{-0.04}$	$0.92^{+0.20}_{-0.07}$	6166^{+30}_{-51}	$-0.54^{+0.07}_{-0.12}$	188^{+39}_{-15}
201828749	—	175.654343	5.894323	$0.74^{+1.06}_{-0.04}$	$0.71^{+9.64}_{-0.06}$	5552^{+87}_{-97}	$-0.69^{+0.34}_{-0.23}$	146^{+1996}_{-12}
201855371	K2-17	178.329776	6.412261	$0.71^{+0.02}_{-0.05}$	$0.66^{+0.02}_{-0.03}$	4320^{+56}_{-47}	$0.15^{+0.09}_{-0.22}$	134^{+5}_{-6}
201912552[1]	K2-18	172.560461	7.588391	$0.413^{+0.043}_{-0.043}$	$0.394^{+0.038}_{-0.038}$	3503^{+60}_{-60}	$0.09^{+0.09}_{-0.09}$	34^{+4}_{-4}
201929294	—	174.656968	7.959611	$0.73^{+0.06}_{-0.09}$	$0.70^{+0.04}_{-0.08}$	4786^{+48}_{-53}	$-0.16^{+0.22}_{-0.34}$	197^{+13}_{-24}

Table 7.2: Stellar Properties for all Objects of Interest. These values and uncertainties are derived from `MULTINEST` analysis and the numbers are computed as the 0.158, 0.500, and 0.842 posterior sample quantiles. The coordinates are retrieved directly from the EPIC. (1) Parameters inferred from spectroscopic observations.

Candidate	Period (days)	Epoch (BJD-2456808)	Radius ($R_\oplus$)	$a/R_\star$	a (AU)	$T_{\rm eq}$ (K)	Disposition
201208431.01/K2-4b	10.00329 ± 0.00159	7.5212 ± 0.0080	2.37 ± 0.40	27.79 ± 0.72	0.0777 ± 0.0012	563 ± 11	Planet
201257461.01	50.27762 ± 0.00785	20.3735 ± 0.0397	209.52 ± 99.23	6.19 ± 0.52	0.3049 ± 0.0030	1466 ± 52	FP
201295312.01	5.65706 ± 0.00079	3.7187 ± 0.0082	2.16 ± 0.57	12.94 ± 4.07	0.0633 ± 0.0019	1211 ± 154	Candidate
201338508.01/K2-5c	10.93406 ± 0.00205	6.5947 ± 0.0080	1.92 ± 0.20	32.27 ± 0.71	0.0783 ± 0.0007	511 ± 9	Planet
201338508.02/K2-5b	5.73491 ± 0.00061	0.8640 ± 0.0063	1.92 ± 0.23	20.99 ± 0.46	0.0509 ± 0.0004	634 ± 12	Planet
201367065.01/K2-3b	10.05448 ± 0.00033	5.4177 ± 0.0015	1.98 ± 0.10	30.72 ± 0.75	0.0740 ± 0.0009	504 ± 9	Planet
201367065.02/K2-3c	24.64745 ± 0.00152	4.2759 ± 0.0030	1.56 ± 0.10	55.85 ± 1.36	0.1345 ± 0.0016	374 ± 7	Planet
201384232.01/K2-6b	30.94191 ± 0.00467	19.5014 ± 0.0090	2.50 ± 0.88	50.27 ± 24.56	0.1898 ± 0.0056	615 ± 105	Planet
201393098.01/K2-7b	28.67992 ± 0.00947	16.6155 ± 0.0149	2.67 ± 0.56	40.29 ± 8.19	0.1814 ± 0.0043	651 ± 61	Planet
201403446.01	19.15344 ± 0.00607	7.3412 ± 0.0152	2.04 ± 0.46	27.05 ± 5.87	0.1408 ± 0.0040	889 ± 88	Candidate
201445392.01/K2-8b	10.35176 ± 0.00133	5.6119 ± 0.0053	2.97 ± 0.51	24.94 ± 0.79	0.0856 ± 0.0012	691 ± 14	Planet
201445392.02	5.06468 ± 0.00063	5.0663 ± 0.0071	2.31 ± 0.33	15.49 ± 0.49	0.0531 ± 0.0008	877 ± 17	Candidate
201465501.01/K2-9b	18.44883 ± 0.00137	14.6723 ± 0.0030	1.60 ± 0.42	74.76 ± 6.66	0.0848 ± 0.0050	284 ± 14	Planet
201505350.01/K2-19c	11.90691 ± 0.00037	9.2764 ± 0.0018	4.31 ± 0.49	24.09 ± 2.48	0.0965 ± 0.0017	797 ± 42	Planet
201505350.02/K2-19b	7.91943 ± 0.00007	5.3836 ± 0.0005	7.11 ± 0.81	18.35 ± 1.89	0.0735 ± 0.0013	913 ± 48	Planet
201546283.01	6.77131 ± 0.00012	4.8440 ± 0.0022	5.77 ± 3.24	17.56 ± 9.24	0.0668 ± 0.0029	991 ± 239	Candidate
201549860.01	5.60840 ± 0.00055	4.1181 ± 0.0047	2.20 ± 0.40	17.42 ± 0.46	0.0555 ± 0.0008	766 ± 14	Candidate
201555883.01	—	—	—	—	—	—	FP[2]
201565013.01	8.63810 ± 0.00024	3.4284 ± 0.0016	15.99 ± 9.19	28.07 ± 2.68	0.0669 ± 0.0031	536 ± 37	Candidate
201569483.01	5.79687 ± 0.00000	5.3135 ± 0.0004	27.81 ± 3.56	15.68 ± 1.91	0.0589 ± 0.0015	930 ± 51	FP
201577035.01/K2-10b	19.30691 ± 0.00127	11.5768 ± 0.0033	3.92 ± 0.69	32.74 ± 5.15	0.1374 ± 0.0025	703 ± 55	Planet
201596316.01/K2-11b	39.93767 ± 0.23229	21.8290 ± 0.1156	7.55 ± 9.33	45.08 ± 58.53	0.2257 ± 0.0143	734 ± 253	Planet
201613023.01/K2-12b	8.28212 ± 0.00060	7.3734 ± 0.0054	2.33 ± 0.58	17.47 ± 5.05	0.0802 ± 0.0021	1003 ± 121	Planet
201617985.01	7.28161 ± 0.00078	4.6366 ± 0.0047	1.78 ± 0.43	26.04 ± 1.16	0.0586 ± 0.0012	518 ± 16	Candidate
201629650.01/K2-13b	39.91488 ± 0.32477	4.5250 ± 0.0146	1.89 ± 0.95	79.69 ± 63.37	0.2114 ± 0.0061	511 ± 126	Planet
201635569.01/K2-14b	8.36802 ± 0.00019	3.4513 ± 0.0013	4.81 ± 0.42	30.16 ± 0.69	0.0627 ± 0.0006	488 ± 8	Planet
201649426.01	27.77045 ± 0.00008	13.3482 ± 0.0012	32.79 ± 9.01	59.26 ± 13.58	0.1517 ± 0.0097	441 ± 42	FP
201702477.01	40.73620 ± 0.00266	3.5455 ± 0.0025	7.28 ± 1.10	56.98 ± 7.61	0.2205 ± 0.0053	529 ± 36	Candidate
201736247.01/K2-15b	11.81040 ± 0.00204	3.8509 ± 0.0076	2.48 ± 0.30	28.84 ± 1.98	0.0910 ± 0.0018	676 ± 26	Planet
201754305.01/K2-16c	19.07536 ± 0.00490	1.4854 ± 0.0119	2.14 ± 0.41	41.43 ± 1.34	0.1220 ± 0.0021	523 ± 12	Planet
201754305.02/K2-16b	7.62067 ± 0.00095	3.6802 ± 0.0054	2.13 ± 0.37	22.47 ± 0.73	0.0662 ± 0.0011	710 ± 16	Planet
201779067.01	27.24273 ± 0.00012	12.2601 ± 0.0003	31.73 ± 5.25	38.25 ± 3.72	0.1718 ± 0.0022	707 ± 34	FP
201828749.01	33.51569 ± 0.00232	5.1504 ± 0.0034	3.83 ± 3.25	67.09 ± 67.64	0.1875 ± 0.0090	613 ± 239	Candidate
201855371.01/K2-17b	17.96753 ± 0.00152	9.9462 ± 0.0035	2.23 ± 0.20	39.38 ± 0.85	0.1190 ± 0.0020	487 ± 10	Planet
201912552.01/K2-18b[1]	32.94488 ± 0.00281	28.1849 ± 0.0027	2.24 ± 0.23	83.83 ± 9.03	0.1491 ± 0.0055	272 ± 15	Planet
201929294.01	—	—	—	—	—	—	FP[2]

Table 7.3: Planet Properties for all Objects of Interest.
(1) Parameters inferred from spectroscopic observations.
(2) Declared a false positive due to noise modeling systematics (see Section 7.5.2)

Primary	Aperture (arcsec)	RA (J2000)	Dec (J2000)	Detection	Separation (arcsec)	Δr (mag)	Max Depth[1] (ppt)	Obs. Depth[2] (ppt)
201208431	15.9	174.748988	-3.902146	SDSS	17.25 ± 0.15^b	5.90 ± 0.12	5.6	1.20
201257461	19.9	178.164376	-3.093431	SDSS	12.91 ± 0.18^b	5.04 ± 0.03	4.8	30.54
201295312	11.9	174.010158	-2.522528	SDSS/AO	8.12 ± 0.09^b	7.10 ± 0.10	0.8	0.30
201338508	15.9	169.308176	-1.873647	SDSS	22.92 ± 0.07^b	4.35 ± 0.03	9.1	1.07
201367065	19.9							1.26
201384232	13.9	178.195303	-1.192501	SDSS	24.14 ± 0.06^b	5.93 ± 0.03	2.1	0.68
201393098	15.9							0.53
201403446	15.9	174.267663	-0.909645	SDSS	9.78 ± 0.14^b	4.56 ± 0.08	7.5	0.23
201445392	13.9							0.78
201465501	11.9							2.83
201505350	19.9							2.64
201546283	17.9	171.515265	1.229950	SDSS/AO	2.98 ± 0.05^a	5.87 ± 0.06	2.3	2.33
201549860	13.9	170.097556	1.288007	SDSS	21.21 ± 0.05^b	2.26 ± 0.03	62.3	0.80
201555883	10.0							3.50
201565013	10.0							45.8
201569483	19.9							160
201577035	19.9	172.118116	1.687798	SDSS	17.19 ± 0.12^b	5.40 ± 0.03	3.5	1.44
201596316	15.9							0.70
201613023	19.9							0.42
201617985	15.9							1.10
201629650	15.9	170.158905	2.502107	SDSS	12.30 ± 0.14^b	5.98 ± 0.06	2.0	0.58
201635569	11.9							9.43
201649426	19.9							216
201702477	10.0	175.238916	3.678764	SDSS	12.15 ± 0.12^b	4.65 ± 0.09	6.9	6.70
201736247	13.9							1.21
201754305	11.9							0.80
201779067	19.9							84.9
201828749	11.9	175.645724	5.894714	AO	2.46 ± 0.04^a	2.0 ± 0.1^c	137	0.76
201855371	19.9							0.99
201912552	13.9							2.85
201929294	19.9							13.56

Table 7.4: Detected companions to candidate host stars. (1) Observed "transit" depth if the imaged companion's flux were fully contained in the aperture and if it were an equal-mass eclipsing binary, leading to an eclipse depth of 50%. (2) Observed transit depth in the *K2* dataset. If larger than the "max depth," this transit event cannot be caused by eclipses of the background star. (a) Separation from AO imaging (b) Separation from SDSS photometry (c) Δr inferred from JHK relative photometry.

Candidate	$\delta_{sec,max}$ [ppt][1]	AO?[2]	Pr_{EB}	Pr_{BEB}	Pr_{HEB}	f_p^3	FPP	Disposition
201208431.01/K2-4b	0.51	-	$< 10^{-4}$	8.1×10^{-4}	$< 10^{-4}$	0.21	8.1×10^{-4}	Planet
201257461.01	0.59	-	0.998	1.7×10^{-3}	$< 10^{-4}$	0.00	1.000	FP
201295312.01	0.04	Y	1.4×10^{-4}	$< 10^{-4}$	$< 10^{-4}$	0.17	1.4×10^{-4}	Candidate[a]
201338508.01/K2-5c	0.63	-	$< 10^{-4}$	2.9×10^{-3}	$< 10^{-4}$	0.22	2.9×10^{-3}	Planet
201338508.02/K2-5b	0.33	-	$< 10^{-4}$	1.7×10^{-4}	$< 10^{-4}$	0.22	1.7×10^{-4}	Planet
201367065.01/K2-3b	0.15	-	$< 10^{-4}$	1.1×10^{-4}	$< 10^{-4}$	0.22	1.1×10^{-4}	Planet[c]
201367065.02/K2-3c	0.67	-	$< 10^{-4}$	$< 10^{-4}$	$< 10^{-4}$	0.16	$< 10^{-4}$	Planet[c]
201384232.01/K2-6b	0.44	-	8.4×10^{-3}	$< 10^{-4}$	$< 10^{-4}$	0.07	8.5×10^{-3}	Planet
201393098.01/K2-7b	0.52	-	$< 10^{-4}$	1.1×10^{-3}	$< 10^{-4}$	0.05	1.1×10^{-3}	Planet
201403446.01	0.18	Y	4.8×10^{-4}	$< 10^{-4}$	$< 10^{-4}$	0.19	4.9×10^{-4}	Candidate[a]
201445392.01/K2-8b	0.26	-	$< 10^{-4}$	2.1×10^{-3}	$< 10^{-4}$	0.18	2.1×10^{-3}	Planet
201445392.02	0.18	-	$< 10^{-4}$	0.019	$< 10^{-4}$	0.21	0.019	Candidate
201465501.01/K2-9b	0.68	-	$< 10^{-4}$	5.8×10^{-3}	$< 10^{-4}$	0.21	5.8×10^{-3}	Planet
201505350.01/K2-19c	2.69	-	$< 10^{-4}$	5.6×10^{-3}	$< 10^{-4}$	0.04	5.6×10^{-3}	Planet[d]
201505350.02/K2-19b	0.70	-	$< 10^{-4}$	1.6×10^{-4}	$< 10^{-4}$	0.07	1.7×10^{-4}	Planet[d]
201546283.01	0.15	-	7.0×10^{-4}	2.6×10^{-4}	$< 10^{-4}$	0.00	9.6×10^{-4}	Candidate[a]
201549860.01	0.18	-	$< 10^{-4}$	0.026	$< 10^{-4}$	0.04	0.026	Candidate
201555883.01	0.94	-	–	–	–	–	–	FP[b]
201565013.01	1.69	-	0.783	7.3×10^{-3}	0.063	0.07	0.853	Candidate
201569483.01	2.06	-	0.822	$< 10^{-4}$	0.174	0.00	0.996	FP
201577035.01/K2-10b	0.14	Y	4.4×10^{-4}	$< 10^{-4}$	$< 10^{-4}$	0.07	4.4×10^{-4}	Planet
201596316.01/K2-11b	0.45	-	$< 10^{-4}$	1.2×10^{-3}	$< 10^{-4}$	0.06	1.2×10^{-3}	Planet
201613023.01/K2-12b	0.08	Y	$< 10^{-4}$	$< 10^{-4}$	$< 10^{-4}$	0.18	$< 10^{-4}$	Planet
201617985.01	0.27	-	$< 10^{-4}$	0.012	$< 10^{-4}$	0.18	0.012	Candidate
201629650.01/K2-13b	0.43	-	5.9×10^{-4}	2.0×10^{-4}	$< 10^{-4}$	0.13	7.8×10^{-4}	Planet
201635569.01/K2-14b	0.79	-	$< 10^{-4}$	4.9×10^{-3}	$< 10^{-4}$	0.05	4.9×10^{-3}	Planet
201649426.01	3.10	-	0.896	$< 10^{-4}$	0.104	0.00	1.000	FP
201702477.01	0.70	-	0.137	1.2×10^{-3}	6.6×10^{-3}	0.05	0.145	Candidate
201736247.01/K2-15b	0.42	-	4.8×10^{-4}	2.1×10^{-4}	$< 10^{-4}$	0.19	6.9×10^{-4}	Planet
201754305.01/K2-16c	0.65	-	1.0×10^{-4}	1.4×10^{-3}	$< 10^{-4}$	0.21	1.5×10^{-3}	Planet

201754305.02/K2-16b	0.38	-	2.3×10^{-4}	9.9×10^{-4}	$< 10^{-4}$	0.19	1.2×10^{-3}	Planet
201779067.01	1.97	-	0.968	1.3×10^{-3}	7.2×10^{-3}	0.00	0.976	FP
201828749.01	0.39	Y	0.644	3.8×10^{-4}	$< 10^{-4}$	0.01	0.645	Candidate
201855371.01/K2-17b	0.62	-	$< 10^{-4}$	8.7×10^{-3}	$< 10^{-4}$	0.01	8.7×10^{-3}	Planet
201912552.01/K2-18b	0.47	Y	$< 10^{-4}$	$< 10^{-4}$	$< 10^{-4}$	0.21	$< 10^{-4}$	Planet
201929294.01	3.12	-	–	–	–	–	–	FP[b]

Table 7.5: Results of the `vespa` astrophysical false positive probability calculations for all candidates. Likely false positives (FPP > 0.9, or otherwise designated) are marked in red. Candidates are declared to be validated planets if FPP < 0.01. EB, BEB, and HEB refer to the three considered astrophysical false positive scenarios, and the relative probability of each is listed in the appropriate column. Planets previously identified in the literature are marked.

(1) Maximum depth of potential secondary eclipse signal.

(2) Whether adaptive optics observation is presented in this paper.

(3) Integrated planet occurrence rate assumed between 0.7× and 1.3× the candidate radius.

(a) Despite low FPP, returned to candidate status out of abundance of caution due to secondary star detection within or near photometric aperture.

(b) Declared a false positive due to noise modeling systematics (see §7.5).

(c) Identified as planets by Crossfield et al. (2015).

(d) Identified as planets by Armstrong et al. (2015).

Chapter 8

MEASURING THE GALACTIC DISTRIBUTION OF TRANSITING SYSTEMS WITH *WFIRST*

Finally, I consider the possibility of *WFIRST* to act as a transit search mission. Designed to search for signals of planets gravitationally microlensing more distant stars, the survey requires high precision observations of millions of stars at a 15-minute cadence, ideal to detect transiting planets. I explore what kinds of planets we would hope to detect from this mission, finding that it could discover more than 30,000 transiting planets, largely hot Jupiters. I then consider what observations would be required to confirm or validate these planets, finding that the small planets will be most easily detectable when they are in dynamically interacting multiple-planet systems through the detection of TTVs. Giant planets, on the other hand, will be able to be confirmed through direct detection of their secondary eclipses. This chapter will be submitted to the Astrophysical Journal as "Measuring the Galactic Distribution of Planets with *WFIRST*" by BTM, Jennifer Yee, and Matthew Penny.

8.1 Introduction

The *Kepler* mission (Borucki et al. 2010) ushered in a revolution in our understanding of exoplanetary systems in the Milky Way. *Kepler* observed a 100 $\deg^2$ region of the sky in Cygnus and Lyra for four years, detecting thousands of transiting planet candidates (Batalha et al. 2013; Burke et al. 2014; Mullally et al. 2015; Rowe et al. 2015). These planets include populations largely undetectable by any other mission. For example, with its high photometric precision, *Kepler* has uncovered a population of systems of tightly-packed inner planets (STIPs), with multiple 1-4 $R_\oplus$ planets all transiting the same star with periods shorter than $\sim$ 20 days. These planets are largely too small to be detected by other transit missions and too lightweight to be detected by RV surveys.

In further contrast to radial velocity surveys (e.g. Udry et al. 2007; Ford 2014), which primarily targeted bright, nearby ($\lesssim$ 100 pc) FGK stars (Valenti & Fischer 2005; Ammons et al. 2006), *Kepler* probes stars as faint as $r = 16$. Therefore, most *Kepler* planet candidates are beyond 300 pc from the Earth, with some as far as a kiloparsec away (Lillo-Box et al. 2014; Barclay et al. 2015; Quinn et al. 2015). The mission has found some surprising differences between the local neighborhood

and more distant regions of the galaxy. In particular, the number of hot Jupiter systems discovered by *Kepler* suggests an occurrence rate approximately 50% of that suggested by RV detections of hot Jupiters in the solar neighborhood. RV surveys estimate an occurrence rate for hot Jupiters on the order of 1% (Cumming et al. 2008; Mayor et al. 2011), while data from the *Kepler* mission suggest an occurrence rate of $0.4\% \pm 0.1\%$ (Howard et al. 2012). While the difference between the two fields is known, the explanation is unclear. Studies have invoked stellar metallicity (Howard et al. 2012; Wright et al. 2012; Dawson & Murray-Clay 2013), stellar age (Schlaufman & Winn 2013), and stellar multiplicity (Wang et al. 2014, 2015a). Regardless, this result suggests that planet occurrence rate may be affected by the local galactic environment.

Aside from this result, so far, comparative studies of exoplanet demographics as a function of galactic environment have been limited. One of the first comparisons in planet occurrence across the galaxy was afforded by microlensing surveys, which is biased toward low-mass host stars at ~kpc distances. Clanton & Gaudi (2014) combined microlensing results (e.g. Gould et al. 2010; Sumi et al. 2010; Cassan et al. 2012) with those from RV and adaptive optics imaging surveys (Montet et al. 2014) to show that the occurrence rate of giant planets around M dwarfs is consistent as measured by the two techniques. However, the microlensing signal from a planet is a much less steep function of mass than the RV signal ($\propto \sqrt{m_p}$ and $\propto m_p$, respectively). At the same time, the radius function around M dwarfs is strongly biased toward smaller mass planets (Swift et al. 2013; Morton & Swift 2014). Both Clanton & Gaudi (2014) and Montet et al. (2014) concluded that M dwarf planets are explained by a steep mass function and most RV surveys miss the ~Saturn-mass, long period planets that likely make up the bulk of the microlensing detections.

The *K2* mission is providing a first opportunity to understand the differences in planet populations across the galaxy for larger planets and higher mass stars. Due to the failure of two reaction wheels on the *Kepler* telescope, the instrument is no longer able to point at its original field. Instead, it relies on solar radiation pressure and its remaining two reaction wheels to point at a series of fields in the ecliptic plane for $\sim$ 70 days at a time. This new mission has led to catalogs of transiting planet candidates (Foreman-Mackey et al. 2015; Vanderburg et al. 2016) as well as statistically validated planets (Montet et al. 2015c) in fields across the ecliptic plane. By the end of the *K2* mission, it will observe $\sim$ 20 fields, largely covering the ecliptic plane, providing an opportunity to probe variations in planet occurrence

as a function of galactic position and stellar age.

The upcoming *TESS* mission (Ricker et al. 2014) will enable additional detections of systems of small transiting planets, especially towards the ecliptic poles where observations will be collected, uninterrupted, for nearly a year. However, *TESS* is designed to target stars brighter than $I = 12$, meaning most planetary detections will be around stars within a few hundred parsec. While ideal for detecting the nearest planets, *TESS* will provide little information about their distribution in the galaxy.

WFIRST (Spergel et al. 2015) offers a unique opportunity to understand the distribution of short-period transiting planets in our galaxy. During the mission, six microlensing campaigns spread over five years will each last 72 days. *WFIRST* will tile 2.8 square degrees of the sky towards the galactic bulge with ten pointings. Each pointing will be observed for 52 seconds every 15 minutes While the photometric precision will not be as good for bright stars as the *Kepler* prime mission, its performance is significantly better for faint stars, of which *WFIRST* will observe millions 8.1. Bennett & Rhie (2002) showed that such a survey should detect large numbers of transiting planets, especially giant planets. In a white paper in Spergel et al. (2015), Tanner & Bennett calculate that *WFIRST*should see 50,000 transiting Jupiters.

WFIRST provides an opportunity to explain the discrepancy between the occurrence rate of hot Jupiters in the *Kepler* field and the solar neighborhood. *WFIRST* will observe stars at large distances along the galactic metallicity gradient (Rolleston et al. 2000; Pedicelli et al. 2009). Observations suggest a change in the metallicity of -0.05 dex/kpc as one moves radially outward from the center of the galaxy. *WFIRST* should be expected to observe stars at preferentially higher metallicities than the solar neighborhood. Indeed, simulations of the *WFIRST* field suggest the median G2V dwarf observable by *WFIRST* with W149 < 19.5 has [Fe/H] = 0.26 8.4. The yield of hot Jupiters detected will provide key insights into the nature of the formation and evolution of these massive planets.

The potential of *WFIRST* to detect large numbers of transiting planets is underappreciated because of the difficulty of confirming and validating those planets. In general, because the host stars of *WFIRST*-detected transiting planets will be so faint, it will not be possible to conduct followup RV observations to confirm their masses. This poses a major challenge for distinguishing transiting Jupiter-radius planets from the multitude of false positives. However, there are several

techniques based on *WFIRST* data alone that can be used to rule-out false positives. For example, McDonald et al. (2014) explore observations of Doppler beaming and secondary eclipses as means to rule-out transiting planet false positives for the proposed *Euclid* microlensing survey.

In this paper, we consider the capability of the upcoming *WFIRST* mission to detect, confirm, and characterize transiting planets. In particular, we focus on the possibility of measuring their transit timing variations (TTVs, Agol et al. 2005; Holman & Murray 2005; Lithwick & Wu 2012). We also discuss various techniques for ruling out false positives. In Section 8.2, we describe the mission photometry and compare it to *Kepler*. In Section 8.3, we study the sensitivity of *WFIRST* to detecting transit events and measuring times of transit. In Section 8.4, we project the yield and demographics of transiting planets *WFIRST* will discover. In Section 8.5, we discuss potential strategies to confirm the transiting planets discovered by *WFIRST*. In Section 8.6 we discuss methods to statistically validate planets which can not be directly confirmed and the potential for ground-based follow-up and strategies to maximize the scientific potential of *WFIRST* for transiting planets. We conclude in Section 8.7.

8.2 Comparison to *Kepler* Photometry

To detect microlensing events, *WFIRST* requires a long time baseline to stare at fields in the bulge, high photometric precision, and a wide field of view in order to observe large numbers of stars. Fundamentally, these are the same requirements as space-based transit surveys such as *Kepler*. We compare the expected performance of *WFIRST* with the actual performance of *Kepler*. Such an analysis enables us to understand the detectability of transiting planets potentially observable by *WFIRST* as the requirements are similar and the statistics of planets discovered by the *Kepler* mission are well-understood.

For unsaturated stars ($H > 15$), we calculate the photometric precision as a function of stellar magnitude, following the standard CCD signal to noise equation. We use the values from the science definition team (SDT) report (Spergel et al. 2015) for the photometric zeropoint of the detector, as well as the bias, read noise, gain, dark current, and sky brightness. This report claims an error floor in the photometry of 1 mmag, which we add in quadrature to the calculations from the SDT. This prescription is shown as the black line in Figure 8.1.

We compare this prescription to that of Gould et al. (2015), who consider *WFIRST*

as a tool for asteroseismology, especially for saturated stars. They perform their own analysis of the expected photometric precision and find that the precision in a single observation will scale such that

$$\sigma = 1.0 \times 10^{(2/15)m_H} \text{mmag}, \tag{8.1}$$

where M_H is the apparent H-band magnitude. Taking W149 as a proxy for H, we also plot this relation on Figure 8.1 (red line).

We show the results of this calculation and compare to *Kepler* photometry in Figure 8.1. To perform a direct comparison to *Kepler*, we must make two corrections. First, *WFIRST* will observe at a faster cadence than *Kepler*. To compare the observations in a uniform way, we follow the *Kepler* convention of considering the average noise of observations binned over six hours, the "combined differential photometric precision" or CDPP (Christiansen et al. 2012). Additionally, the *WFIRST* bandpass is significantly redder than the *Kepler* bandpass. As transit searches focus on FGKM stars, with red colors, these stars appear brighter on the *WFIRST* detector than they would on the *Kepler* detector. To provide a fair comparison, we compare the expected *WFIRST* precision to the H-band magnitude of the stars in the *Kepler* field.

Between 15th and 20th magnitude, the SDT estimates of the precision is very similar to that of Gould et al. (2015). In both cases, the expectation is that *WFIRST* will achieve a relative precision of 1 part per thousand (ppt) in a single observation of a 15th magnitude star in the W149 bandpass (0.93-2.00 μm). This is equivalent to 200 parts per million (ppm) when binned over six hours, comparable to the precision of *Kepler* on a star with $r \approx K_p = 15$. However, since a typical G dwarf has an $R - H$ color of 1.1, the same Sunlike star observed with *Kepler* and *WFIRST* would be observed at a higher precision with *WFIRST*.

In this work, we focus on the detection of planets around stars with W149 < 19.5. The two prescriptions for the photometric noise around such bright stars differ significantly only for stars brighter than 14th magnitude. As these stars make up only a small fraction of the stars in the *WFIRST* field of view, the choice of noise model we apply does not affect our results at an appreciable level. For ease of reproducibility we apply the Gould et al. (2015) model, noting the results change at only the 1-3% level (higher for stars of earlier spectral type) if we apply the Spergel et al. (2015) model instead.

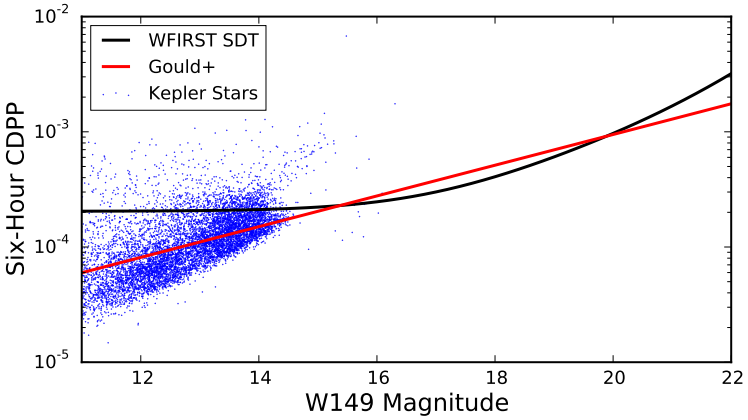

Figure 8.1: Expected noise properties of *WFIRST* observing in the W149 bandpass as a function of stellar magnitude. The black curve represents the estimates of the noise properties from the *WFIRST* SDT report. The red curve represents the estimates of the noise properties from Gould et al. (2015), who focus on saturated stars to detect asteroseismic modes using *WFIRST* data. In blue are actual observations of stars from *Kepler* for comparison. In all cases, we report the six-hour CDPP, or the noise averaged over six hours of observations.

8.3 Detection of Transit Events

To study the detectability of transiting planets with *WFIRST*, we simulate transiting planet light curves with properties based on the anticipated performance of *WFIRST* as described by Gould et al. (2015). We assume a 52-second integration every 5 minutes and 6 evenly-spaced, 72-day campaigns over five years. We assume that all data will be taken in the W149 band (0.927–2.000μm) with the exception of one data point every 12 hours in the Z087 filter (0.760–0.977μm), i.e. one Z087 data point for every 47 obtained in W149.

In this work, we assume the photometric noise is white, so that there are no correlations between observations. Correlated noise can be the result of spacecraft systematics or stellar p-modes (Gilliland et al. 2010; Campante et al. 2011). The timescale for p-modes is inversely proportional with stellar density: for G dwarfs, the granulation timescale is approximately five minutes; for M dwarfs, 30 seconds. Like *Kepler* data, for most stars observations will be spaced widely enough to capture a random phase of p-mode oscillations during each observation. As *WFIRST* has significantly larger levels of photon noise, the correlated stellar signals will be small by comparison, causing the while instrumental noise to dominate over any red astrophysical effects.

Hot Jupiters

The *WFIRST* microlensing mission intends to target more than one million stars with $H < 14$ and 12 million stars with $H < 19$. To better understand the sensitivity of *WFIRST* to giant transiting planets, we simulate transits of a hot Jupiter transiting a Sunlike star.

We simulate individual transits of a hot Jupiter by injecting both realistic noise and a planetary signal into simulated *WFIRST* data. We first create a star with W149 = 15.0 to project a best-case scenario, where the noise expected to be at the milimagnitude noise floor. We then inject a Jupiter-sized planet on a 3.0 day orbit around this star, which transits with impact parameter $b = 0.5$. The transit duration is approximately two hours. Every fifteen minutes, starting at a random phase, we collect an observation of the flux from this system: every twelve hours one observation is taken in Z087, while all other observations are in W149. We model the transit light curve with the transit model of Mandel & Agol (2002). We calculate limb darkening coefficients in each bandpass using the online tool developed and described in Eastman et al. (2013), which interpolates the Claret & Bloemen (2011) quadratic limb darkening tables.

Unlike the *Kepler* mission, each data point will consist of a single 52-second observation, rather than a series of binned observations over 30 minutes. Each observation will then sample one specific point on the transit light curve as opposed to an integrated measure of the observed flux, meaning morphological light curve distortions due to finite integration time will be virtually nonexistent in *WFIRST* data (Kipping 2010a).

The resultant "observed" transits are shown in Figure 8.2. These transits can be seen by eye, even in the case of single transit events. Over the course of the mission, more than 150 transits of such a Hot Jupiter would be observed, leading to approximately 1200 observations during the transit in the W149 bandpass. Moreover, approximately two dozen observations during the transit will be collected in the W089 bandpass, which might be useful for confirmation of the planetary nature of this signal (Section 8.5).

We then attempt to recover the transit signal in the data. By fitting transit models and evaluating their likelihood, we measure a transit depth of $0.998 \pm 0.002\ R_J$, assuming perfect knowledge of the stellar host. This $\sim 500\sigma$ detection of a transit implies transiting hot Jupiters will be easily detected around $H \sim W149 = 15$ stars.

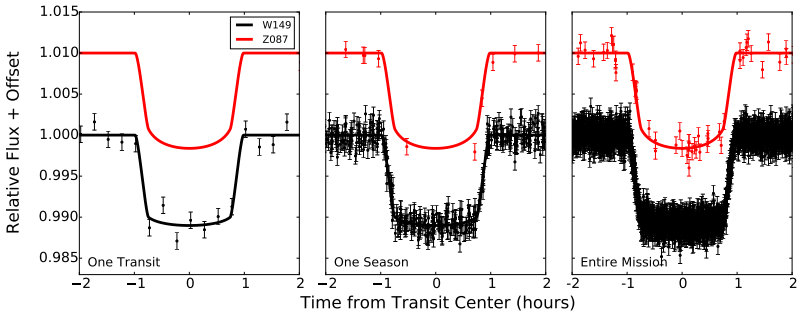

Figure 8.2: Simulated transit photometry for a hot Jupiter in a three-day orbit around a Sunlike star with W149 = 15. In black is photometry from the W149 bandpass; in red, the Z087 bandpass. The left panel corresponds to a single transit. The middle panel corresponds to transits folded together over a 72-day observing season, while the right panel corresponds to six such seasons over the course of the mission.

We can increase the level of the noise to determine the limiting magnitude for which *WFIRST* will be effective at detecting hot Jupiters. In the *Kepler* mission, the threshold for a candidate planet transit was a 7.1σ detection of the transit, a standard we will apply here. By inflating the size of our photometric uncertainties and repeating this exercise we find that, assuming white noise, even when the single-point photometric precision is 8%, we are able to detect hot Jupiters in three-day orbits at 7.1σ over the course of the *WFIRST* mission. The photometric limit is expected to be better than this value even for stars with W149 = 22.0. Typical extinction values in the I-band are 1-2 magnitudes (Nataf et al. 2013) and towards the galactic center $A_H/A_I = 3.2$, so we might expect less than one magnitude of extinction in the W149 bandpass (Nishiyama et al. 2009; Nataf et al. 2016). Even accounting for extinction, this limiting magnitude corresponds to Sunlike stars well beyond $>$ 10 kpc from the Earth, easily allowing us to detect hot Jupiter systems around tens of millions of stars in total, at all galactocentric radii.

For the brightest stars, measuring a transit signal to a precision of 0.2% implies photometric precision of approximately 20 parts per million when binned over two-hour intervals and phase-folded on a two-day period. This is significantly below the precision needed to detect relativistic Doppler beaming in the light curve (Loeb & Gaudi 2003; Faigler & Mazeh 2011), but could be used to detect false positive events such as transiting brown dwarfs and low-mass stars masquerading as hot Jupiters (see Section 8.6).

Sensitivity to Small Planets

Given the high signal to noise expected for hot Jupiters transiting the brightest stars observed with *WFIRST*, we might expect the telescope to be sensitive to planets transiting stars significantly smaller than Jupiter as well. We can determine how small a planet would be detectable by *WFIRST* as a function of planet orbital period and radius. We will repeat this exercise for stars at W149 = 15 and W149 = 19.5; there are expected to be 1 million and 12 million stars brighter than these limiting magnitudes, respectively.

To calculate our sensitivity to planets in general, we first create a planet with a radius and an orbital period drawn from log-flat distributions over the ranges $[1,16]R_{\oplus}$ and $[1,72]$ days, respectively. We then assign an impact parameter for each transiting planet drawn from a uniform distribution over the range $[0,1]$. We assume a circular orbit for the planet and calculate the relative position of the planet and star, applying the transit model of Mandel & Agol (2002). We draw an observation every fifteen minutes. We assume white noise with the photometric precision given by the Gould et al. (2015) curve of Figure 8.1, removing one observation every twelve hours when *WFIRST* is collecting z-band data instead. After all transits have been simulated, we phase-fold on the known period and measure the significance of the observed transit depth. If it is larger than 7.1σ, we declare this transit detected; otherwise, we declare it missed. We also require at least two transits during at least one season to be detected. By repeating this procedure many times with many different planet sizes and periods, we can map the sensitivity of *WFIRST* to small planets. The results are shown in Figure 8.3.

We find that, for the brightest stars observed by *WFIRST*, Neptune-sized planets with orbital periods shorter than one month will be easily detected in a single season of data. The mission will also recover many mini-Neptunes with periods shorter than 20 days, and is likely to recover a small number of planets smaller than 2 $R_{\oplus}$ with periods shorter than two days. Over the entire mission, *WFIRST* will be sensitive to a few Earth-sized planets with orbital periods shorter than two days orbiting the brightest stars. Of the 12 million stars with W149 < 19.5, the prospects for detecting super-Earths or mini-Neptunes are much lower, but the mission will detect the majority of Neptune-sized planets with periods less than a month and all transiting Jupiter-sized planets in that period range as well.

There is a strong decay in the sensitivity of *WFIRST* to transiting planets as a function of planet radius compared to planet period. This is not surprising, and the

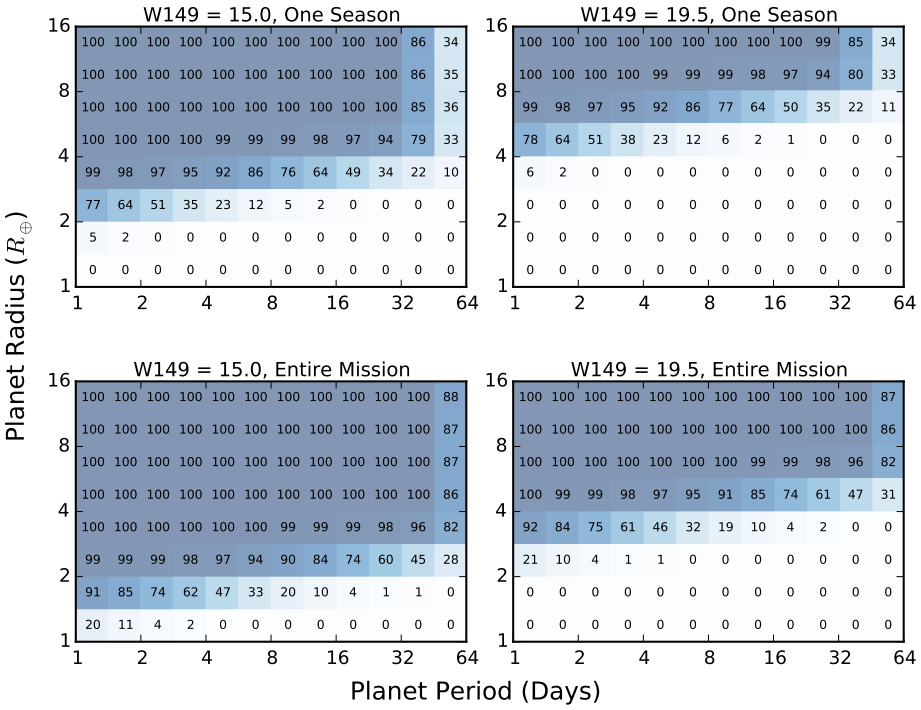

Figure 8.3: Detectability of planets transiting a Sunlike star in simulated *WFIRST* data by analyzing (top) one season of data and (bottom) data from the entire mission. Around very bright stars (W149 = 15.0) nearly all Neptune-sized planets and larger with orbital periods shorter than the seasonal baseline will be detected in a single season of data. To qualify as a detection, we require at least two transits in a single observing season, but not necessarily in all seasons.

same effect is seen in *Kepler* data (Burke et al. 2014; Mullally et al. 2015; Rowe et al. 2015). The transit duration is proportional to $P^{1/3}$ and the observed depth depends on the projected surface area of the planet, so the phase-folded transit signal depends on $R_p^2 P^{-2/3}$ (Seager & Mallén-Ornelas 2003). Therefore a change in the orbital period should have a weaker effect than a change in the size of the planet, as we observe here (see also Carter et al. 2008).

Single Transit Events

WFIRST will, in addition to detecting thousands of planets with short orbital periods, be sensitive to singly transiting events of giant planets in more distant periods. The best measurements of the occurrence rates of these planets is understood from

combining observations of long-term RV accelerations with direct imaging surveys (Montet et al. 2014, Gonzales et al. in prep). There are only a few dozen such planets detected in the *Kepler* data, detected largely through visual inspection (Wang et al. 2015b; Uehara et al. 2016). For a given planet in a long orbital period, the probability of transit is directly proportional to the observing baseline. The *WFIRST* observing baseline is a factor of four shorter than that of *Kepler*, but as the total number of stars observed by *WFIRST* is nearly two orders of magnitude larger than *Kepler*, we expect visual inspection of *WFIRST* data to uncover on the order of one thousand additional giant planets. As even single transit events can provide unique information about transiting planets (Yee & Gaudi 2008; Osborn et al. 2016), these data will improve our understanding of planets at wide separations.

Deriving Transit Times from *WFIRST* data

The sensitivity to short-period planets smaller than Neptune in a single season of *WFIRST* data implies that we may be able to detect variations in the time of transit across the mission. These transit timing variations (TTVs) have been used previously to confirm the planetary nature of transiting signals (Holman et al. 2010; Fabrycky et al. 2012; Ford et al. 2012a; Xie 2013), to detect the presence of non-transiting planets (Ballard et al. 2011; Nesvorný et al. 2012, 2013), and to infer masses and eccentricities of planetary systems (Hadden & Lithwick 2014; Jontof-Hutter et al. 2015, 2016). While TTVs have been observed in *K2* data (Barros et al. 2015), the short time baseline makes these detections the exception rather than the rule. Given that *WFIRST* will observe the same fields over five years, we might expect to detect deviations from a linear transit ephemeris if our sensitivity to transit times is small enough.

To this end, we simulate transit events in order to estimate the precision to which we will be able to measure transit times. We model our benchmark system after Kepler-9b and Kepler-9c, the first planets confirmed via TTVs (Holman et al. 2010). We use orbital periods for the two planets of 19.2 and 38.9 days. Given that less massive planets more often exhibit TTVs than more massive planets (Mazeh et al. 2013), we simulate planets near the bottom of our detectability contours in order to understand the limits for detecting TTVs with *WFIRST*. As such, we assume the two planets are mini-Neptunes with masses of 10 $M_\oplus$ and radii of 3 $R_\oplus$. These are significantly smaller than the real Kepler-9 planets leading to smaller TTVs and larger uncertainty in the measured time of transit center. We simulate transits of these planets orbiting a Sunlike star with W149 = 15.0, so that the photometric

precision on each data point is 1 part per thousand, assigning impact parameters at random.

We focus on TTVs of the inner planet, because more transits will be observed over the course of the *WFIRST* mission. We fit a transit model to the simulated data for the inner planet, fixing the limb darkening to that expected for a Sunlike star in the H-band but allowing all other parameters to vary. The measured transit times are shown in Figure 8.4. Simulating many transits, we find a median uncertainty in the measured transit time for each individual transit of 28 minutes. We then phase-fold all observed transits inside an observing season, finding a median uncertainty on the average time of the folded transit of 15 minutes (Figure 8.4). Given the large number of observed TTV signals in *Kepler* significantly larger than this timing precision, we expect *WFIRST* to be able to efficiently measure TTVs.

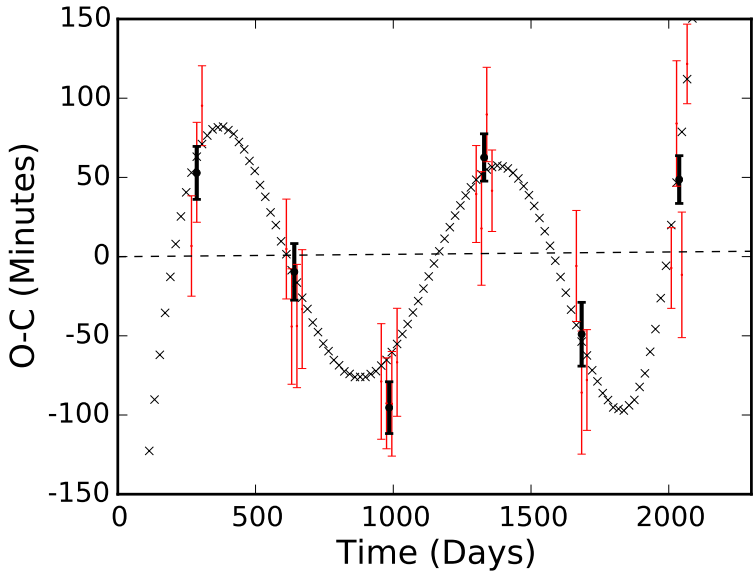

Figure 8.4: Simulated TTV signal from a two-planet system as observed by *WFIRST* (see Section 8.3). Gray X labels correspond to the actual deviation form a linear ephemeris for each individual transit. For those observed during a simulated *WFIRST* season, typical uncertainties are added to the observed time of transit with data shown in red. The black points correspond to binned observations over an entire season. This hypothetical system would be confirmed by TTV observations in *WFIRST* data.

Accurate determinations of transit times is more difficult in the presence of starspots, which induce a correlated signal in the light curve. As a planet transits the stellar disk, if it passes across a relatively dark spot this will cause a distortion in the shape of the light curve. Moreover, spots at other stellar latitudes can cause the

out-of-transit flux baseline to vary, complicating the measurement of the time of transit. *WFIRST* will observe in the near-IR, where the effects of starspots are significantly minimized due to their lower contrast, reducing the possibility of significant starspot-induced timing errors.

8.4 Galactic Exoplanet Demographics

We can simulate realistic populations of both stars in the bulge and their exoplanets to estimate how many transiting planets *WFIRST* will be able to detect over the course of its mission. To simulate a realistic estimate of the stellar population in the bulge, we develop a galactic population generated from the online Besançon models of the galaxy (Robin et al. 2003). To convert the returned apparent magnitudes to near-infrared simulated photometry, we apply the transformations of Bilir et al. (2008). We then apply a correction for interstellar extinction assuming the Cardelli et al. (1989) extinction law with $R_v = 2.5$, following Nataf et al. (2013). From the derived JHK magnitudes, we approximate the W149 magnitude for each star by assuming W149 = (J+H+K)/3.

We then apply a series of corrections to turn the Beasançon models into a realistic simulation of the stars observed by *WFIRST*. The Beasançon model outputs the properties and numbers of stars along a given sightline within a certain solid angle. Because each simulated field is not a perfect match to the *WFIRST* field, we weight each simulated star by the fraction of the simulated field that falls in the *WFIRST* field. We then apply a correction for the mass function in the bulge. The model assumes stars in the bulge follow the Salpeter IMF (Salpeter 1955). We downweight stars of mass $M < 0.5$ $M_\odot$ by a factor of $0.5/M$, which approximates the IMF of Kroupa (2001). We then apply a uniform correction to all stars to match the overall number of bulge main sequence stars near the *WFIRST* fields as measured by Calamida et al. (2015).

We then inject planets around the main-sequence dwarf stars brighter than W149 = 19.5 in our simulation. Since the *WFIRST* sensitivity in the radius-period plane (Figure 8.3) is limited to a region of parameter space well-sampled by the *Kepler* mission in the original *Kepler* field. We assign planets around solar-type FGK stars following the planet occurrence estimates of Howard et al. (2012). We assign planet radii and orbital periods following the "Cutoff Power-Law Model" of Table 5 of that paper, and bulk occurrence rates for each spectral type following the authors' Table 4. For M dwarfs, we follow the relations of Morton & Swift (2014), specifically

their "logflat+exponential" model of the period distribution from their Figure 7 and the radius distribution from their Figure 6. This leads to considerably smaller numbers of giant planets injected around M dwarfs than more massive stars, in line with observations from *Kepler*.

We simulate the transits of these planets following the same prescriptions as in Section 8.3. We assume the noise properties of Gould et al. (2015) and we estimate limb darkening parameters by interpolating our stellar parameters onto the quadratic limb darkening grids of (Claret & Bloemen 2011), taking $H-$band as a proxy for W149. We limit the range of orbital periods to $P < 72$ days. We declare a planet detected if we recover its transit signal at 7.1σ and observe at least two transits in any one season.

The results are shown in Figure 8.5. We expect *WFIRST* to detect approximately 13,000 transiting planets orbiting bright dwarf stars, the majority being giant planets orbiting F and G stars. The mission will also detect more than 100 planets smaller than Neptune, the majority of which will be orbiting M dwarfs. We note that our prescription for the photometric precision does not significantly affect the bulk numbers of planets detected.

The number of transiting planets from this simulation assumes that the occurrence rate is the same in the *WFIRST* field as in *Kepler*. However, radial velocity surveys have unveiled a correlation between giant planet occurrence and stellar metallicity (Fischer & Valenti 2005; Johnson et al. 2010a), while the presence of small transiting planets appear to not be affected by the host star's metallicity (Buchhave & Latham 2015). Given that the median metallicity of dwarfs in the *WFIRST* field is [Fe/H] = 0.25, and most of the planets detected by *WFIRST* will be giants, this correlation could significantly influence the number of giant planets detected.

We account for this metallicity effect by injecting planets according to the radius and period distribution of the *Kepler* field, but increasing the likelihood of a star hosting a planet according to the star's metallicity in our sample. Following Johnson et al. (2010a), who find planet occurrence scales as $10^{1.2[\mathrm{Fe/H}]}$, we modify the likelihood of all planets with radii larger than 5 $R_\oplus$ by this factor. For the median star ([Fe/H] = 0.25), this factor increases giant planet occurrence by a factor of two. We then repeat our simulations with our modified planet occurrence, with the results shown in Figure 8.6. In this case, we detect more than 30,000 transiting planets over the six seasons of the *WFIRST* mission. As expected, the number of small planets is unchanged, with the gains made entirely in the population of planets larger than

Neptune. *WFIRST*, by completing this survey, will provide the best assessment of the effects of high metallicity on the population of giant planets, providing clues to the formation and evolution of these systems.

Finally, we note that our analysis is limited to dwarf stars towards the bulge brighter than W149 = 19.5. While planets have been detected around evolved stars (Lillo-Box et al. 2014; Barclay et al. 2015; Quinn et al. 2015), their occurrence rates are too poorly understood to enable a reliable estimate of their yield in *WFIRST*. However, given the photometric precision (Section 8.2) and scaling from Section 8.3, giant planets will be detectable around evolved stars (i.e. given that $3R_\oplus$ planets are detectable around a $1R_\odot$ star, a $12R_\oplus$ planet should be detectable around a $4R_\odot$ star.). As *WFIRST* will observe large numbers of evolved stars towards the bulge, it will provide the best measurement to date of the occurrence rate of giant planets in short orbits around evolved stars.

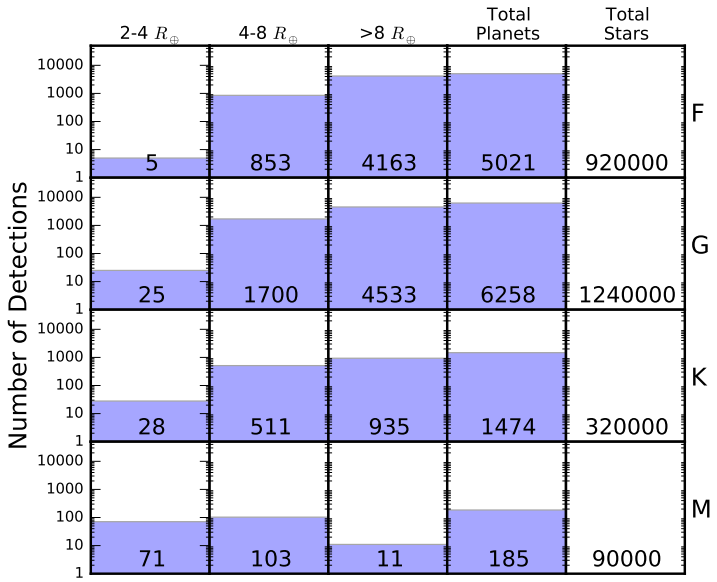

Figure 8.5: Expected yield of transiting planets orbiting dwarf stars brighter than W149 = 19.5 in the *WFIRST* data as a function of planet size and stellar type, assuming the planet occurrence is the same as that in the *Kepler* field. *WFIRST* will detect thousands of Jupiter sized planets, but also more than 100 planets smaller than Neptune, mainly around M dwarfs.

8.5 Confirmation of Transiting Planetary Systems

The major challenge for transiting planet studies is to verify that the observed transiting object is a planet rather than a false positive. Multiple astrophysical events

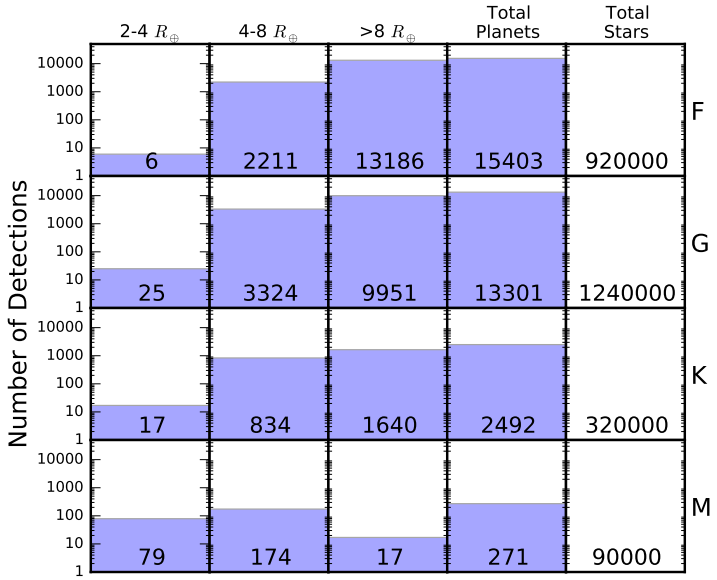

Figure 8.6: The same as Figure 8.5, assuming planet occurrence for planets larger than 5 $R_\oplus$ follows the relation with stellar metallicity as observed in the solar neighborhood, following Johnson & Apps (2009). Under these assumptions *WFIRST* will detect more than 30,000 planets.

can be mistakenly identified as transiting planets. First, because of degeneracy pressure, Jupiters, brown dwarfs, and low-mass M stars all have similar radii (Chabrier & Baraffe 1997): detection of a Jupiter-radius transit depth alone is insufficient to claim a planetary detection. Second, a false positive can occur in the case of blended light, when the star in question in the aperture is actually the combined light of multiple stars. For example, a background unknown eclipsing binary could be blended with the primary target star. Similarly, the primary itself could be an eclipsing binary blended with the chance alignment of a background star or the light of a hierarchical triple third star. These degeneracies are easily resolved with RV observations, but those will not be possible for most *WFIRST* transit candidates. However, previous studies have shown in the case of *Kepler* that it is possible to validate transiting planet candidates by ruling out various false positive scenarios (Morton 2012; Morton et al. 2016). Here and in Section 8.6, we explore various means to confirm, validate, or rule out false positives for *WFIRST* transiting planet candidates.

TTVs

The most straightforward way for *WFIRST* to confirm the planetary nature of transit signals from small planets is through the detection of transit timing variations. In Section 8.3, we showed that TTVs are easily recovered for a scaled-down version of the Kepler-9 system. The exact nature of any TTV curve depends on the architecture of any particular TTV system: two planetary systems with identical planets but different orbital eccentricities, arguments of periapsis, or longitudes of ascending node would exhibit different TTV signals.

A full simulation of this stuff is beyond the scope of this paper. However, we note that the TTV catalog of Holczer et al. (2016) lists 571 *Kepler* planet candidates with TTV signals larger than 30 minutes and 176 with TTV signals larger than 60 minutes. Many of these planets will be too small to be detectable in the relatively noisier *WFIRST* data. Considering these numbers, based on the number of planets we expect *WFIRST* to be able to detect and the timing precision we expect the mission to achieve on individual transits 8.3, we expect more than 100 TTV detections over the observing campaign.

WFIRST will have the added benefit of an observing baseline larger than five years, longer than the original *Kepler* mission. TTVs that manifest themselves on longer timescales, such as those caused by non-resonant planets, Roemer delay from a hierarchical binary star, or orbital evolution of a giant planet in a short orbit (Ragozzine & Wolf 2009; Maciejewski et al. 2016), will be more likely to be detectable with *WFIRST*.

While TTVs will be extremely useful to confirm the planetary nature of small planets, given the observing strategy of *WFIRST* it is unlikely that TTVs will be able to robustly determine masses. To verify this claim we use TTVFast (Deck et al. 2014) to integrate a dynamically interacting planetary system compare the result to the simulated transits from Section 8.3 during six hypothetical *WFIRST* observing seasons. We purposefully schedule the *WFIRST* seasons to coincide with the smallest observed TTV signal to simulate a worst-case scenario. For each observed transit, we add a random offset drawn from a uniform distribution on the range [25 minutes, 40 minutes], similar to the predicted scatter on measurements of the times of individual transits, and assign an uncertainty on the observed time of transit equal to this value.

Fitting only the transits of the inner planet, we find that a dynamically interacting planet model fit the data considerably better than a linear ephemeris ($\Delta\chi^2 = 72$). In

this case, these planets would be easily confirmed via *WFIRST* observations: only very contrived examples of planets with these masses, orbital periods, and eccentricities produce nondetectable TTVs. However, the inferred masses of the transiting planets are a function of the unknown eccentricity: a pair of 10 $M_\oplus$ planets or a pair of 25 $M_\oplus$ planets can both explain the observed TTVs.

In many cases, while confirmation of the planetary nature of systems will be easy, the large gaps between seasons will complicate determination of unique solutions of the masses of individual planets and induce degeneracies between their masses and eccentricities. For the brightest stars, it may be possible to identify particular transits that would be useful for precise determination of planet masses and to follow up these planets with ground-based facilities at these specific times.

Secondary Eclipses

It is unlikely that TTVs will be useful for confirmation of more than a few of the hot Jupiters detected by *WFIRST*. TTVs depend on the existence of a second planet, but giant planets are most often detected in isolation, without a transiting companion (Steffen et al. 2012b). There is only one hot Jupiter system with detected TTVs induced by the presence of an additional planet (Becker et al. 2015). However, it is possible that these planets will be confirmed by observations of their secondary eclipses. The depth of the secondary eclipse yields a measurement of the brightness temperature, and thus the flux in that bandpass (e.g. Charbonneau et al. 2005).

From *Kepler* data alone it is difficult to confirm planets via secondary eclipses. While *Kepler* found thousands of planets, it was only able to confirm planetary systems via detection of their phase curves and secondary eclipses for a handful of these (e.g. Esteves et al. 2013; Quintana et al. 2013; Angerhausen et al. 2015). Because the *Kepler* bandpass spans approximately 0.4 – 0.9 μm, near the peak of a typical stellar spectrum but far bluer than the typical planetary spectrum, only the hottest, largest planets are detectable by their own emission. However, *WFIRST*, with its primary bandpass spanning 0.927-2.000 μm, will be significantly more effective at observing planetary emission directly.

To determine the feasibility of observing secondary eclipses with *WFIRST*, we consider the case of a hot Jupiter transiting a Sunlike star, similar to the case of Section 8.3. We can determine the relative flux of the two objects across the *WFIRST* bandpass to determine the integrated secondary eclipse depth expected. We assume a Jupiter-sized planet with an equilibrium temperature of 1200 K orbiting a

Sunlike star. We obtained a theoretical spectrum for a 1200 K and 5800 K object from the BT-Settl spectral library of Baraffe et al. (2015), using the updated CIFIST2011_2015 models.

We then integrate these spectra across the W149 filter, assuming a planet the size of Jupiter being eclipsed by a star the size of the Sun. We predict, for this system, a secondary eclipse depth of 350 parts per million, approximately equal to the transit depth of a 2 $R_\oplus$ planet. From Figure 8.3, we expect detections of secondary eclipses to be rare around stars with W149 = 19.5, but common around the million stars with W149 brighter than 15.0. For the bright stars, we expect to detect approximately one-third of planets of this size and orbital period in one season of *WFIRST* data, and nearly all planets across the entire mission, so the same will be true for detecting secondary eclipses.

We are likely to recover secondary eclipses of the hottest planets even more effectively. The planetary equilibrium temperature scales as $a^{-1/2}$, and hot planets are often inflated relative to their cooler cousins (Charbonneau et al. 2000; Showman & Guillot 2002), both increasing the depth of the secondary eclipse: WASP-12b's secondary eclipse depth across this bandpass is nearly 2 parts per thousand (Croll et al. 2011; Stevenson et al. 2014a), corresponding to the same depth of a transit of a 4.9 $R_\oplus$ planet. We can then expect observations of secondary eclipses to be useful for confirmation of hot Jupiter systems.

Secondary eclipses will provide additional benefits to our understanding of the population of transiting hot Jupiters beyond simply confirmation. The timing of the secondary eclipse depends on the eccentricity vector $e\cos\omega$, enabling statistical analyses of hot Jupiter eccentricities and detections of non-circular planets, providing clues into the dynamics of hot Jupiter formation.

8.6 Validation of Transiting Planetary Systems

Z087 Photometry

Transits of a dark object across the face of a star should be, to first order, achromatic. False positive events caused by eclipsing binaries, where multiple objects are self-luminous, will have wavelength-dependent depth variations as different portions of the stellar SEDs are sampled at different bandpasses. Multiband photometry can then be used to separate transiting planets from background eclipsing binary events.

In the *WFIRST* mission, one data point will be collected every 12 hours in the Z087 filter, or one data point for every 47 obtained in W149. For the example of Section

8.3, in which a hot Jupiter transits a Sunlike star with a three-day period, only 24 data points will be obtained during the transit event in Z087 over the entire mission, approximately one data point for every six transits. The situation will be even worse for planets with longer orbital periods, or those at higher impact parameters and shorter transit durations.

We can assume that the transit ephemeris and orbital parameters are known from the W149 photometry used to detect planetary transit signals. Therefore, we only need to fit three parameters in the Z087 transit model: two to describe the limb darkening and one to describe the transit depth. For this case, fitting the Z087 photometry we measure a transit depth to a precision of 3.7%. Therefore, an 11% difference in transit depth between Z087 and W149 is the minimum detectable difference at 3σ confidence using data from the entire mission. This is sufficient to rule out many, but not all, stellar false positives.

For example, a false positive M7 dwarf with a temperature of 2900 K and a radius equal to Jupiter's has a flux density smaller than the Sun by a factor of 5.7 in the W149 filter and 11.6 in the Z087 filter, leading to a 9% change in the observed transit depth between the two filters. An increase in the cadence of Z087 observations would be required in order to detect these depth variations to identify false positives. Alternatively, as long as the orbit is aligned such that secondary eclipses are observable from Earth, this star would induce a 2 ppt secondary eclipse, easily detectable with *WFIRST* photometry. While Z087 photometry may be useful at the current cadence in extreme cases, secondary eclipse photometry will be much more significant, as long as the companion's orbit is aligned such that secondary eclipses are visible.

Validation could be complicated by the effects of starspots, both in the case where the planet crosses starspots, affecting the light curve shape, and where starspots are located at different latitudes, affecting the transit depth and out-of-transit flux. Due to the nature of the W149 bandpass, we expect spots to have a minimal effect on the observed light curve. They will be more prevalent in the Z087 photometry, but still diminished relative to the *Kepler* bandpass.

Phase Curves

Although a transit is the most obvious signal in a light curve of a planet orbiting a star, the companion planet affects the observed light curve throughout its orbit. Phase curve variations are the sum of three separate effects: reflected light, rela-

tivistic Doppler beaming, and ellipsoidal variations. These variations have been discussed in previous work as a method to measure planetary masses (Faigler & Mazeh 2011; Mislis et al. 2012), to detect new transiting objects (Faigler et al. 2015), and to understand the atmospheres of transiting planets (Knutson et al. 2007; Faigler & Mazeh 2015). McDonald et al. (2014) analyzed the ability of *Euclid* to use phase curve variations to confirm the planetary nature of transit signals. Here, we consider similar ideas in the context of *WFIRST*.

Doppler Beaming

As a planet and host star orbit their mutual center of mass, changing the velocity of the host star, the flux emitted from the star is beamed towards the direction of travel. A consequence of special relativity, the signal is observable at the non-relativistic speeds at which stars move during their orbits. To first order, the amplitude of the beaming signal is

$$\frac{F_D}{F_0} = (3 - \alpha)\frac{K_s}{c}. \tag{8.2}$$

where F_D is the amplitude of the signal, F_0 the flux from the stationary star, α the shape of the SED at the observed wavelength, K_s the Doppler semiamplitude of the star, and c the speed of light (Loeb & Gaudi 2003). The SED is relevant because, as the star's velocity is modulated, the Doppler shift affects what features of the stellar spectrum fall in our bandpass. For most stars, the W149 filter will fall on the Rayleigh-Jeans tail of the SED, where $\alpha = 2$.

For a typical hot Jupiter ($K \sim 150$ m s^{-1}), this amplitude will be ~ 0.5 parts per million, well below the sensitivity of *WFIRST*. However, this effect will be useful for detecting more massive objects of similar radii masquerading as hot Jupiters, such as brown dwarfs or very low mass stars. A 50 M_{Jup} object with a three-day period would exhibit a 25-ppm signal. From Section 8.3, we determine we can measure a transit depth to a precision of 40 ppm. That transit event has a duration of 1.5 hours, while the beaming signal occurs throughout the planet orbit, providing ample opportunity to detect a 25-ppm signal.

Ellipsoidal Variations

Ellipsoidal variations are an achromatic phenomenon caused by changes in the sky-projected shape of a star as a planet orbits, affecting the star's gravitational potential. The signal has twice the frequency of the planet's orbit. Following Loeb & Gaudi

(2003), to first order the magnitude of the signal is

$$\frac{F_E}{F_0} \sim \beta \frac{M_p}{M_s} \left(\frac{a}{R_s} \right)^{-3}, \tag{8.3}$$

Here, β is a term which depends on the nature of gravity darkening for the host star. For Sunlike stars, this value is approximately 0.45. M_p/M_s is the mass ratio between the planet and star and a/R_s is the reduced orbital semimajor axis.

In general, the signal is of a similar magnitude to the Doppler beaming signal, and only likely to be useful in separating brown dwarfs from planets: transiting planets will only be notable by a nondetection of their ellipsoidal variations.

McDonald et al. (2014) note that in the case of *Euclid*, a color-dependence in observed ellipsoidal variations would be a signature of a background eclipsing binary, as the signal would be achromatic but the relative flux between the foreground and background target would vary between the two bandpasses. The same is true here, although with the cadence of Z087 observations we do not expect this effect to be detectable. In any cases where such an effect would be detectable, variations in the eclipse depth between the bandpasses would also be detectable, likely at a much higher significance.

Thermal Emission

For planets with significant differences in their dayside and nightside surface temperatures, variations in the observed thermal emission from the planet will be detectable. The variation due to thermal emission depends on the difference in temperature between the two sides of the planet, but for some systems can approach the entire depth of the secondary eclipse (Stevenson et al. 2014b), especially in the near-IR where *WFIRST* will observe.

The upcoming *JWST* mission will provide detailed information about the thermal emission for particularly interesting, nearby systems. *WFIRST*, by comparison, will provide much less detailed information about any individual system. The data will be integrated over the entire W149 bandpass and at a considerably lower precision than *JWST*, but will be available for many more systems.

The ability to detect thermal emission in *WFIRST* data depends on the difference in temperature between the day side and the night side of the planet. Those planets that are tidally locked will thus be the most likely to exhibit a visible signal in the phase curve. The same systems will be those for which secondary eclipses will be most

readily visible. Secondary eclipses only provide information about the dayside of the planet, while a phase curve will provide information at all longitudes. Therefore, reflected light observations will likely be useful in concert with detections of secondary eclipses to understand spatial variations in planetary atmospheres.

Ground-based followup

In principle, the transiting planet candidates discovered by *WFIRST* can be followed up by adaptive optics (AO) systems on 30-meter class telescopes. These observations may not provide much leverage over the *WFIRST* data themselves. The diffraction limit of a 30-meter telescope in K-band is $\sim$ 20 milliarcseconds. While considerably smaller than the *WFIRST* pixel scale of 0.11 arcsec pixel^{-1}, this still corresponds to a projected separation of 20 AU for a star with W149 = 14.5 and 200 AU for a star with W149 = 19.5, meaning many bound binary companions will be unresolved even when operating a thirty-meter telescope at the diffraction limit.

8.7 Conclusions

While ostensibly a microlensing mission, *WFIRST* will provide a tremendous opportunity for the study of short-period, transiting planets as well. We have shown in Section 8.4 that if the occurrence rate of planets is the same as for the main *Kepler* field, *WFIRST* will detect over 12,000 transiting planets with sizes as small as $2R_{\oplus}$. If the occurrence rate scales with metallicity as in Johnson et al. (2010a), we expect a factor of $\sim$ 2.4 more (i.e., 30,000 planets) given that the *WFIRST* field is more metal rich than the solar neighborhood.

To maximize the opportunity that *WFIRST* provides, we emphasize a few points to be considered during the design of the instrument. Since more small planets detected by *WFIRST* will be confirmed via observations of TTVs than any other method, the long baselines during which these TTVs can manifest themselves are essential. The current strategy, through which multiple fields are observed in parallel, cycling every fifteen minutes, provides an ideal arrangement to observe TTVs. For this strategy, it is imperative that the time between observations is small relative to the typical transit duration so that individual transits can be well-timed.

Giant planets, meanwhile, will be most efficiently confirmed via analysis of their secondary eclipses. The near-IR bandpass will enable robust determination of the luminosity of the transiting companion, allowing for differentiation between planets and self-luminous low-mass stars. Z-band photometry could also provide useful data for this goal, both during the primary transit and secondary eclipse. As

currently imagined, the 12-hour cadence of z-band photometry does not provide enough data in transit or eclipse to confirm systems as real or as definitive false positives. An increased rate of z-band photometry, perhaps as often as once every three hours, would provide more opportunities to separate transiting hot Jupiters from self-luminous brown dwarfs or giant planets. If an increase in the rate of Z087 photometry at the expense of W149 photometry does not have a significant effect on the expected yield from the primary microlensing mission, and if the time to change filters is small relative to the time to slew from one field to the next, we urge the *WFIRST* team to consider an increased rate of Z087 photometry.

The majority of transiting planet detections will be around faint stars, as these stars will make up the majority of observed stars in the sample. We expect saturated dwarf stars (with W149 $<$ 15) to account for fewer than 100 planet detections. Photometry for these bright stars has been considered for the purposes of asteroseismology (Gould et al. 2015). It will also be important for transiting planets: although these make up only a small fraction of the total planet yield, the low levels of photon noise mean these stars produce the highest sensitivity to the smallest planets observable with *WFIRST*. Additionally, these planets will be nearest transiting planets to Earth discovered by *WFIRST* as well as the ones most easily able to be followed up by other facilities on the ground and in space for detailed characterization. Thus, effort should be made to achieve precision photometry on these saturated stars.

In this work, we assume the noise from *WFIRST* will be purely white, with the correlated noise negligible compared to its uncorrelated counterpart. Given the large levels of white noise expected (1 mmag for the brightest stars) this is not an unreasonable expectation. Observations of TTVs, a time-sensitive phenomenon, require a proper understanding of the noise (Pont et al. 2006). We hope the *WFIRST* team will make every effort to understand the noise properties of the detector before launch.

Chapter 9

SUMMARY AND FUTURE DIRECTIONS

In this thesis, I have focused on the study of low-mass stars and their companions, whether these companions are planets, brown dwarfs, or themselves other M dwarfs. While this work has been able to advance the study of all three of these classes of objects, there is more that can be done in the future as new data are collected and new instruments are built at new facilities. Let us consider each of these classes of objects in turn.

In Chapter 3, I developed a method to measure the occurrence rate of giant planets out to 20 AU through a combination of high-contrast direct imaging and detections of long-term RV trends. The planets inferred in this work form a unique region of parameter space as yet inaccessible to searches via other methods: they are too far from their host stars to be detectable through transit searches, but too near and too faint to be detectable through direct imaging campaigns alone. The method developed here is directly applicable to higher-mass host stars, and the process can be extended to directly measure the occurrence rate of planets around K and G stars. With the larger number of G and K dwarfs observed in RV surveys and the longer observational time baseline, it is possible that we will be able to measure the occurrence rate of giant planets around these stars to an even higher precision. Some of this work is ongoing, while the *Gaia* telescope will provide more information about Jupiter-like planets in the solar neighborhood in the second half of this decade. In Chapter 7 I presented a method to understand the stellar and planetary parameters of candidate systems uncovered by *K2*, a process that can also be applied to the systems detected by *WFIRST* (Chapter 8). *K2* will enable us to better understand the population of planets orbiting M dwarfs in the solar neighborhood. By the end of the mission, *K2* will search for transit signals around as many as 50,000 M dwarfs, while the original *Kepler* mission observed 5,000. Moreover, *K2* will observe mid-M dwarfs, where the original *Kepler* mission largely eschewed stars later than M1. Both *K2* and *WFIRST* will target higher mass stars in vastly different galactic environments: *K2* has targeted young clusters, stars in and well out of the galactic plane, and stars at varied galactocentric distances. *WFIRST* will similarly be able to detect transits around solar-type stars more than 2 kiloparsec away in the direction of the galactic bulge. Following the galactic metallicity gradient (Rolleston et al. 2000),

in which the metallicity of stars decreases at 0.07 ± 0.01 dex kpc^{-1}, we might expect these stars to host Jupiter-sized planets 50% more frequently than stars near the Sun. *WFIRST* will enable us to test theories of planet formation and the relation between stellar metallicity and planet formation with unprecedented detail.

Next, we turn our attention to brown dwarfs. In Chapters 4 and 5 I analyzed LHS 6343 C, the brown dwarf with the most precise radius measurement and the only brown dwarf with a direct mass, radius, and luminosity measurement. This brown dwarf can provide a single test of brown dwarf models, but more similar brown dwarfs are required. Fortunately, more similar brown dwarfs are being discovered. In 2016, Bayliss et al. (2016) presented radial velocity data on EPIC 201702477 b, one of the objects of interest characterized in Chapter 7. I was not able to confirm or rule out the planetary nature of this system; with radial velocities, these authors were able to confirm the system as a transiting brown dwarf with a period of 40.74 days. Similarly, other work has discovered a transiting brown dwarf in the 3 Gyr Ruprecht 147 cluster (Curtis et al. *in prep*). As more systems like these are discovered, especially systems with known ages, we will be able to fill the brown dwarf mass-radius diagram and connect the transiting brown dwarf population to the field brown dwarf population, for which direct measurements of masses and radii are impossible.

Finally, we consider M+M binaries. Throughout the M dwarf spectral class, more objects with direct mass measurements are needed. Nearly all mass measurements come from eclipsing binaries in short periods, which may cause inflated radii due to magnetic activity (Chabrier et al. 2007; Jackson et al. 2009). *K2* and *WFIRST* will enable the discovery of more M dwarf eclipsing binaries on longer periods, which are less likely to be inflated. In Chapter 2, I describe a method to measure masses of single stars with transiting planets by combining RV and TTV observations of the planetary system, avoiding the potential complications of binary stars entirely.

Very young stars rotate rapidly and are photometrically very active, complicating both the detection of transiting planets and the precision RVs required to confirm them directly. The problems with stellar models at these ages are even worse, with only a handful of M dwarfs younger than 100 Myr having directly measured masses. In Chapter 6 I presented GJ 3305 AB, a binary M+M system in the β Pictoris young moving group. I measured the mass of both components, comparing them to stellar models. This is only one binary system of the dozens I am monitoring astrometrically and through RV observations with collaborators. There are more than 20 more

stars in more than 10 systems with orbits that have closed or will close in the next few years in the same mass and age range. As these orbits close, we will develop a population of stars with measured masses to compare against models, enabling the development of the next generation of stellar models.

Of course, much of the future work will rely on future instruments and future telescopes both in the ground and in space. In this thesis I discuss the ongoing *K2* and future *WFIRST* missions. beyond these, the study of M dwarfs can look forward to contributions from future transit search missions like *TESS* (Ricker et al. 2014) and *PLATO* (Catala et al. 2010), as well as the development and construction of the next generation of 30-meter class telescopes. Moreover, RV instruments that are optimized for observations in the near-IR, such as *iLocator* (Crepp 2014) and *MAROON-X* (Seifahrt et al. 2016), will enable later, more distant M dwarfs to be more easily targeted in RV surveys. While the equations of stellar structure force M dwarfs to be faint, their future is very bright indeed.

BIBLIOGRAPHY

Abell, G. O. 1959, Leaflet of the Astronomical Society of the Pacific, 8, 121

Adams, W. S. 1913, PASP, 25, 258

Agol, E., Steffen, J., Sari, R., & Clarkson, W. 2005, MNRAS, 359, 567

Agol, E., Cowan, N. B., Knutson, H. A., et al. 2010, ApJ, 721, 1861

Ahn, C. P., Alexandroff, R., Allende Prieto, C., et al. 2012, ApJS, 203, 21

Albrecht, S., Winn, J. N., Torres, G., et al. 2014, ApJ, 785, 83

Aldering, G., Adam, G., Antilogus, P., et al. 2002, in Proc. SPIE, ed. J. A. Tyson & S. Wolff, Vol. 4836, 61

Aldering, G., Antilogus, P., Bailey, S., et al. 2006, ApJ, 650, 510

Allard, F., Hauschildt, P. H., Alexander, D. R., Tamanai, A., & Schweitzer, A. 2001, ApJ, 556, 357

Allard, F., & Freytag, B. 2010, Highlights of Astronomy, 15, 756

Allard, F., Homeier, D., & Freytag, B. 2012, Philosophical Transactions of the Royal Society of London Series A, 370, 2765

Allard, F., Homeier, D., Freytag, B., Schaffenberger, W., & Rajpurohit, A. S. 2013, Memorie della Societa Astronomica Italiana Supplementi, 24, 128

Ambikasaran, S., Foreman-Mackey, D., Greengard, L., Hogg, D. W., & O'Neil, M. 2016, IEEE Transactions on Pattern Analysis and Machine Intelligence, 38, 252

Ammons, S. M., Robinson, S. E., Strader, J., et al. 2006, ApJ, 638, 1004

Andersen, J. 1991, A&A Rev., 3, 91

Andrews, S. M., Rosenfeld, K. A., Kraus, A. L., & Wilner, D. J. 2013, ApJ, 771, 129

Angerhausen, D., DeLarme, E., & Morse, J. A. 2015, PASP, 127, 1113

Anglada-Escudé, G., Arriagada, P., Vogt, S. S., et al. 2012a, ApJL, 751, L16

Anglada-Escudé, G., Boss, A. P., Weinberger, A. J., et al. 2012b, ApJ, 746, 37

Apps, K., Clubb, K. I., Fischer, D. A., et al. 2010, PASP, 122, 156

Armstrong, D. J., Santerne, A., Veras, D., et al. 2015, A&A, 582, A33

Auvergne, M., Bodin, P., Boisnard, L., et al. 2009, A&A, 506, 411

Bacon, R., Copin, Y., Monnet, G., et al. 2001, MNRAS, 326, 23

Bailey III, J. I., White, R. J., Blake, C. H., et al. 2012, ApJ, 749, 16

Bakos, G. Á., Lázár, J., Papp, I., Sári, P., & Green, E. M. 2002, PASP, 114, 974

Ballard, S., Charbonneau, D., Deming, D., et al. 2010, PASP, 122, 1341

Ballard, S., Fabrycky, D., Fressin, F., et al. 2011, ApJ, 743, 200

Ballard, S., & Johnson, J. A. 2016, ApJ, 816, 66

Baraffe, I., Chabrier, G., Allard, F., & Hauschildt, P. H. 2002, A&A, 382, 563

Baraffe, I., Chabrier, G., Barman, T. S., Allard, F., & Hauschildt, P. H. 2003, A&A, 402, 701

Baraffe, I., & Chabrier, G. 2010, A&A, 521, A44

Baraffe, I., Homeier, D., Allard, F., & Chabrier, G. 2015, A&A, 577, A42

Baranec, C., Riddle, R., Law, N. M., et al. 2014, ApJL, 790, L8

Barclay, T., Quintana, E. V., Adams, F. C., et al. 2015, ApJ, 809, 7

Barentsen, G. 2015, K2flix: Kepler pixel data visualizer, Astrophysics Source Code Library, URL: http://dx.doi.org/10.5281/zenodo.15576

Barnes, S. A. 2003, ApJ, 586, 464

Barros, S. C., Almenara, J. M., Demangeon, O., et al. 2015, MNRAS, 454, 4267

Basri, G., Marcy, G. W., & Graham, J. R. 1996, ApJ, 458, 600

Bastien, F. A., Stassun, K. G., Basri, G., & Pepper, J. 2013, Nature, 500, 427

Bastien, F. A., Stassun, K. G., & Pepper, J. 2014, ApJL, 788, L9

Batalha, N. M., Rowe, J. F., Bryson, S. T., et al. 2013, ApJS, 204, 24

Bayliss, D., Hojjatpanah, S., Santerne, A., et al. 2016, ArXiv e-prints

Bean, J. L., Sneden, C., Hauschildt, P. H., Johns-Krull, C. M., & Benedict, G. F. 2006, ApJ, 652, 1604

Bean, J. L., McArthur, B. E., Benedict, G. F., et al. 2007, AJ, 134, 749

Becker, J. C., Vanderburg, A., Adams, F. C., Rappaport, S. A., & Schwengeler, H. M. 2015, ApJL, 812, L18

Becklin, E. E., & Zuckerman, B. 1988, Nature, 336, 656

Bell, C. P., Mamajek, E. E., & Naylor, T. 2015, MNRAS, 454, 593

Bennett, D. P., & Rhie, S. H. 2002, ApJ, 574, 985

Bennett, D. P., Rhie, S. H., Nikolaev, S., et al. 2010, ApJ, 713, 837

Bergfors, C., Brandner, W., Janson, M., et al. 2010, A&A, 520, A54

Beuzit, J.-L., Ségransan, D., Forveille, T., et al. 2004, A&A, 425, 997

Bidelman, W. P. 1954, ApJS, 1, 175

Bilir, S., Ak, S., Karaali, S., et al. 2008, MNRAS, 384, 1178

Binks, A. S., & Jeffries, R. D. 2014, MNRAS, 438, L11

Birkby, J., Nefs, B., Hodgkin, S., et al. 2012, MNRAS, 426, 1507

Bobylev, V. V. 2006, Astronomy Letters, 32, 816

Boisse, I., Bouchy, F., Hébrard, G., et al. 2011, A&A, 528, A4

Bonfils, X., Forveille, T., Delfosse, X., et al. 2005, A&A, 443, L15

Bonfils, X., Delfosse, X., Udry, S., et al. 2013, A&A, 549, A109

Borucki, W. J., & Summers, A. L. 1984, Icarus, 58, 121

Borucki, W. J., Koch, D., Basri, G., et al. 2010, Science, 327, 977

Borucki, W. J., Koch, D. G., Basri, G., et al. 2011a, ApJ, 736, 19

Borucki, W. J., Koch, D. G., Basri, G., et al. 2011b, ApJ, 728, 117

Bouchy, F., Bonomo, A. S., Santerne, A., et al. 2011a, A&A, 533, A83

Bouchy, F., Deleuil, M., Guillot, T., et al. 2011b, A&A, 525, A68

Bowler, B. P., Johnson, J. A., Marcy, G. W., et al. 2010, ApJ, 709, 396

Bowler, B. P., Liu, M. C., Shkolnik, E. L., et al. 2012, ApJ, 753, 142

Bowler, B. P., Liu, M. C., Shkolnik, E. L., & Tamura, M. 2015, ApJS, 216, 7

Boyajian, T. S., von Braun, K., van Belle, G., et al. 2012, ApJ, 757, 112

Brown, T. M., & Latham, D. W. 2008, ArXiv e-prints

Brown, T. M., Latham, D. W., Everett, M. E., & Esquerdo, G. A. 2011, AJ, 142, 112

Buchhave, L. A., Bakos, G. Á., Hartman, J. D., et al. 2010, ApJ, 720, 1118

Buchhave, L. A., & Latham, D. W. 2015, ApJ, 808, 187

Buenzli, E., Apai, D., Morley, C. V., et al. 2012, ApJL, 760, L31

Burgasser, A. J., Marley, M. S., Ackerman, A. S., et al. 2002a, ApJL, 571, L151

Burgasser, A. J., Kirkpatrick, J. D., Brown, M. E., et al. 2002b, ApJ, 564, 421

Burgasser, A. J., Gillon, M., Faherty, J. K., et al. 2014, ApJ, 785, 48

Burke, C. J., Bryson, S. T., Mullally, F., et al. 2014, ApJS, 210, 19

Burningham, B., Cardoso, C. V., Smith, L., et al. 2013, MNRAS, 433, 457

Burrows, A., Marley, M., Hubbard, W. B., et al. 1997, ApJ, 491, 856

Burrows, A., Hubbard, W. B., Lunine, J. I., & Liebert, J. 2001, Reviews of Modern Physics, 73, 719

Burrows, A., Heng, K., & Nampaisarn, T. 2011, ApJ, 736, 47

Butler, R. P., & Marcy, G. W. 1996, ApJL, 464, L153

Butler, R. P., Marcy, G. W., Williams, E., Hauser, H., & Shirts, P. 1997, ApJL, 474, L115

Butler, R. P., Vogt, S. S., Marcy, G. W., et al. 2004, ApJ, 617, 580

Butler, R. P., Johnson, J. A., Marcy, G. W., et al. 2006, PASP, 118, 1685

Caffau, E., Ludwig, H.-G., Bonifacio, P., et al. 2010, A&A, 514, A92

Calamida, A., Sahu, K. C., Casertano, S., et al. 2015, ApJ, 810, 8

Campante, T. L., Handberg, R., Mathur, S., et al. 2011, A&A, 534, A6

Campante, T. L., Barclay, T., Swift, J. J., et al. 2015, ApJ, 799, 170

Campo, C. J., Harrington, J., Hardy, R. A., et al. 2011, ApJ, 727, 125

Cannon, A. J., & Pickering, E. C. 1901, Annals of Harvard College Observatory, 28, 129

Cardelli, J. A., Clayton, G. C., & Mathis, J. S. 1989, ApJ, 345, 245

Carson, J., Thalmann, C., Janson, M., et al. 2013, ApJL, 763, L32

Carter, J. A., Yee, J. C., Eastman, J., Gaudi, B. S., & Winn, J. N. 2008, ApJ, 689, 499

Casagrande, L., Ramírez, I., Meléndez, J., Bessell, M., & Asplund, M. 2010, A&A, 512, A54

Casertano, S., Lattanzi, M. G., Sozzetti, A., et al. 2008, A&A, 482, 699

Cassan, A., Kubas, D., Beaulieu, J.-P., et al. 2012, Nature, 481, 167

Catala, C., Arentoft, T., Fridlund, M., et al. 2010, in Astronomical Society of the Pacific Conference Series, Pathways Towards Habitable Planets, ed. V. Coudé Du Foresto, D. M. Gelino, & I. Ribas, Vol. 430, 260

Chabrier, G. 2003, PASP, 115, 763

Chabrier, G., & Baraffe, I. 1997, A&A, 327, 1039

Chabrier, G., Baraffe, I., Allard, F., & Hauschildt, P. 2000, ApJ, 542, 464

Chabrier, G., Gallardo, J., & Baraffe, I. 2007, A&A, 472, L17

Chabrier, G., Johansen, A., Janson, M., & Rafikov, R. 2014, Protostars and Planets VI, 619

Chang, C.-K., Ko, C.-M., & Peng, T.-H. 2011, ApJ, 740, 34

Charbonneau, D., Brown, T. M., Latham, D. W., & Mayor, M. 2000, ApJL, 529, L45

Charbonneau, D., Allen, L. E., Megeath, S. T., et al. 2005, ApJ, 626, 523

Charbonneau, D., Berta, Z. K., Irwin, J., et al. 2009, Nature, 462, 891

Choi, J., McCarthy, C., Marcy, G. W., et al. 2013, ApJ, 764, 131

Christiansen, J. L., Jenkins, J. M., Caldwell, D. A., et al. 2012, PASP, 124, 1279

Clanton, C., & Gaudi, B. S. 2014, ApJ, 791, 91

Claret, A., & Bloemen, S. 2011, A&A, 529, A75

Close, L. M., Lenzen, R., Guirado, J. C., et al. 2005, Nature, 433, 286

Cochran, W. D., Fabrycky, D. C., Torres, G., et al. 2011, ApJS, 197, 7

Coughlin, J. L., Thompson, S. E., Bryson, S. T., et al. 2014, AJ, 147, 119

Covey, K. R., Lada, C. J., Román-Zúñiga, C., et al. 2010, ApJ, 722, 971

Crepp, J. R. 2014, Science, 346, 809

Crepp, J. R., & Johnson, J. A. 2011, ApJ, 733, 126

Crepp, J. R., Johnson, J. A., Howard, A. W., et al. 2012a, ApJ, 761, 39

Crepp, J. R., Johnson, J. A., Fischer, D. A., et al. 2012b, ApJ, 751, 97

Crepp, J. R., Johnson, J. A., Howard, A. W., et al. 2013a, ApJ, 771, 46

Crepp, J. R., Johnson, J. A., Howard, A. W., et al. 2013b, ApJ, 774, 1

Croll, B., Lafreniere, D., Albert, L., et al. 2011, AJ, 141, 30

Crossfield, I. J., Petigura, E., Schlieder, J. E., et al. 2015, ApJ, 804, 10

Cumming, A., Butler, R. P., Marcy, G. W., et al. 2008, PASP, 120, 531

Currie, T., Debes, J., Rodigas, T. J., et al. 2012, ApJL, 760, L32

Cushing, M. C., Vacca, W. D., & Rayner, J. T. 2004, PASP, 116, 362

Cushing, M. C., Rayner, J. T., & Vacca, W. D. 2005, ApJ, 623, 1115

Cutri, R. M., Skrutskie, M. F., van Dyk, S., et al. 2003, 2MASS All Sky Catalog of point sources.

Cutri, R. M., & et al. 2013, VizieR Online Data Catalog, 2328,

Czekala, I., Andrews, S. M., Jensen, E. L., et al. 2015, ApJ, 806, 154

Czekala, I., Andrews, S. M., Torres, G., et al. 2016, ApJ, 818, 156

Davenport, J. R., Ivezić, Ž., Becker, A. C., et al. 2014, MNRAS, 440, 3430

David, T. J., Hillenbrand, L. A., Cody, A. M., Carpenter, J. M., & Howard, A. W. 2016, ApJ, 816, 21

Dawson, R. I., & Johnson, J. A. 2012, ApJ, 756, 122

Dawson, R. I., Johnson, J. A., Morton, T. D., et al. 2012, ApJ, 761, 163

Dawson, R. I., & Murray-Clay, R. A. 2013, ApJL, 767, L24

Deck, K. M., Agol, E., Holman, M. J., & Nesvorný, D. 2014, ApJ, 787, 132

Dekany, R., Roberts, J., Burruss, R., et al. 2013, ApJ, 776, 130

Deleuil, M., Deeg, H. J., Alonso, R., et al. 2008, A&A, 491, 889

Delfosse, X., Forveille, T., Mayor, M., et al. 1998, A&A, 338, L67

Delfosse, X., Forveille, T., Ségransan, D., et al. 2000, A&A, 364, 217

Delorme, P., Lagrange, A. M., Chauvin, G., et al. 2012, A&A, 539, A72

Deming, D., Knutson, H., Kammer, J., et al. 2015, ApJ, 805, 132

Désert, J.-M., Charbonneau, D., Torres, G., et al. 2015, ApJ, 804, 59

Desidera, S., Gratton, R. G., Scuderi, S., et al. 2004, A&A, 420, 683

Díaz, R. F., Damiani, C., Deleuil, M., et al. 2013, A&A, 551, L9

Díaz, R. F., Montagnier, G., Leconte, J., et al. 2014a, A&A, 572, A109

Díaz, R. F., Almenara, J. M., Santerne, A., et al. 2014b, MNRAS, 441, 983

Dieterich, S. B., Henry, T. J., Golimowski, D. A., Krist, J. E., & Tanner, A. M. 2012, AJ, 144, 64

Dotter, A., Chaboyer, B., Jevremović, D., et al. 2008, ApJS, 178, 89

Doyle, L. R., Carter, J. A., Fabrycky, D. C., et al. 2011, Science, 333, 1602

Dressing, C. D., & Charbonneau, D. 2013, ApJ, 767, 95

Dumusque, X., Pepe, F., Lovis, C., et al. 2012, Nature, 491, 207

Dupuy, T. J., Liu, M. C., & Ireland, M. J. 2009, ApJ, 692, 729

Dupuy, T. J., Liu, M. C., Bowler, B. P., et al. 2010, ApJ, 721, 1725

Dupuy, T. J., & Liu, M. C. 2012, ApJS, 201, 19

Dupuy, T. J., Liu, M. C., & Ireland, M. J. 2014, ApJ, 790, 133

Dupuy, T. J., Liu, M. C., Leggett, S. K., et al. 2015, ApJ, 805, 56

Eastman, J., Gaudi, B. S., & Agol, E. 2013, PASP, 125, 83

Elliott, P., Bayo, A., Melo, C. H., et al. 2014, A&A, 568, A26

Endl, M., Cochran, W. D., Tull, R. G., & MacQueen, P. J. 2003, AJ, 126, 3099

Esteves, L. J., De Mooij, E. J., & Jayawardhana, R. 2013, ApJ, 772, 51

Evans, T. M., Aigrain, S., Gibson, N., et al. 2015, MNRAS, 451, 680

Fabrycky, D. C., Ford, E. B., Steffen, J. H., et al. 2012, ApJ, 750, 114

Fabrycky, D. C., Lissauer, J. J., Ragozzine, D., et al. 2014, ApJ, 790, 146

Faherty, J. K., Burgasser, A. J., Cruz, K. L., et al. 2009, AJ, 137, 1

Faherty, J. K., Rice, E. L., Cruz, K. L., Mamajek, E. E., & Núñez, A. 2013, AJ, 145, 2

Faherty, J. K., Beletsky, Y., Burgasser, A. J., et al. 2014, ApJ, 790, 90

Faigler, S., & Mazeh, T. 2011, MNRAS, 415, 3921

Faigler, S., Kull, I., Mazeh, T., et al. 2015, ApJ, 815, 26

Faigler, S., & Mazeh, T. 2015, ApJ, 800, 73

Fazio, G. G., Hora, J. L., Allen, L. E., et al. 2004, ApJS, 154, 10

Feigelson, E. D., Lawson, W. A., Stark, M., Townsley, L., & Garmire, G. P. 2006, AJ, 131, 1730

Femenía, B., Rebolo, R., Pérez-Prieto, J. A., et al. 2011, MNRAS, 413, 1524

Feroz, F., Hobson, M. P., & Bridges, M. 2009, MNRAS, 398, 1601

Ferreira, P. G., & Jaffe, A. H. 2000, MNRAS, 312, 89

Filippazzo, J. C., Rice, E. L., Faherty, J., et al. 2015, ApJ, 810, 158

Fischer, D. A., & Marcy, G. W. 1992, ApJ, 396, 178

Fischer, D. A., & Valenti, J. 2005, ApJ, 622, 1102

Fischer, D. A., Gaidos, E., Howard, A. W., et al. 2012, ApJ, 745, 21

Fischer, D. A., Anglada-Escude, G., Arriagada, P., et al. 2016, PASP, 128.6, 066001

Fitzpatrick, E. L. 1999, PASP, 111, 63

Ford, E. B. 2014, Proceedings of the National Academy of Science, 111, 12616

Ford, E. B., Ragozzine, D., Rowe, J. F., et al. 2012a, ApJ, 756, 185

Ford, E. B., Ragozzine, D., Rowe, J. F., et al. 2012b, ArXiv e-prints

Foreman-Mackey, D., Hogg, D. W., Lang, D., & Goodman, J. 2013, PASP, 125, 306

Foreman-Mackey, D., Montet, B. T., Hogg, D. W., et al. 2015, ApJ, 806, 215

Fressin, F., Torres, G., Charbonneau, D., et al. 2013, ApJ, 766, 81

Gaidos, E., Mann, A. W., Lépine, S., et al. 2014, MNRAS, 443, 2561

Gaudi, B. S., Albrow, M. D., An, J., et al. 2002, ApJ, 566, 463

Gaudi, B. S., Seager, S., & Mallen-Ornelas, G. 2005, ApJ, 623, 472

Gaudi, B. S., Bennett, D. P., Udalski, A., et al. 2008, Science, 319, 927

Geweke, J. “Bayesian Statistics IV. Oxford: Clarendon Press”, 1992, in, ed. J. M. Bernardo, 169

Gilliland, R. L., Brown, T. M., Christensen-Dalsgaard, J., et al. 2010, PASP, 122, 131

Girardi, L., Bertelli, G., Bressan, A., et al. 2002, A&A, 391, 195

Gliese, W., & Jahreiß, H. 1991, Preliminary Version of the Third Catalogue of Nearby Stars

Goldman, B., Marsat, S., Henning, T., Clemens, C., & Greiner, J. 2010, MNRAS, 405, 1140

Golimowski, D. A., Henry, T. J., Krist, J. E., et al. 2004, AJ, 128, 1733

Gomes da Silva, J., Santos, N. C., Bonfils, X., et al. 2012, A&A, 541, A9

Goodman, J., & Weare, J. 2010, Communications in Applied Mathematics and Computational Science, 5.1, 65

Gould, A., Dong, S., Gaudi, B. S., et al. 2010, ApJ, 720, 1073

Gould, A., Huber, D., Penny, M., & Stello, D. 2015, Journal of Korean Astronomical Society, 48, 93

Gray, D. F. 1988, Lectures on spectral-line analysis: F,G, and K stars

Gray, R. O., Corbally, C. J., Garrison, R. F., et al. 2006, AJ, 132, 161

Grunblatt, S. K., Howard, A. W., & Haywood, R. D. 2015, ApJ, 808, 127

Hadden, S., & Lithwick, Y. 2014, ApJ, 787, 80

Haghighipour, N., Vogt, S. S., Butler, R. P., et al. 2010, ApJ, 715, 271

Hallinan, G., Littlefair, S. P., Cotter, G., et al. 2015, Nature, 523, 568

Harding, L. K., Hallinan, G., Konopacky, Q. M., et al. 2013, A&A, 554, A113

Hayden, M. R., Bovy, J., Holtzman, J. A., et al. 2015, ApJ, 808, 132

Hayward, T. L., Brandl, B., Pirger, B., et al. 2001, PASP, 113, 105

Haywood, R. D., Collier Cameron, A., Queloz, D., et al. 2014, MNRAS, 443, 2517

Helling, C., & Casewell, S. 2014, A&A Rev., 22, 80

Henden, A. A., Levine, S. E., Terrell, D., Smith, T. C., & Welch, D. 2012, Journal of the American Association of Variable Star Observers (JAAVSO), 40, 430

Henden, A., & Munari, U. 2014, Contributions of the Astronomical Observatory Skalnate Pleso, 43, 518

Henry, T. J., Soderblom, D. R., Donahue, R. A., & Baliunas, S. L. 1996, AJ, 111, 439

Henry, G. W., Marcy, G. W., Butler, R. P., & Vogt, S. S. 2000, ApJL, 529, L41

Henry, T. J., Jao, W.-C., Subasavage, J. P., et al. 2006, AJ, 132, 2360

Herbig, G. H. 2007, AJ, 133, 2679

Herrero, E., Lanza, A. F., Ribas, I., Jordi, C., & Morales, J. C. 2013, A&A, 553, A66

Herrero, E., Lanza, A. F., Ribas, I., et al. 2014, A&A, 563, A104

Herter, T. L., Henderson, C. P., Wilson, J. C., et al. 2008, in Society of Photo-Optical Instrumentation Engineers (SPIE) Conference Series, Society of Photo-Optical Instrumentation Engineers (SPIE) Conference Series, Vol. 7014,

Hillenbrand, L. A., & White, R. J. 2004, ApJ, 604, 741

Ho, S., & Turner, E. L. 2011, ApJ, 739, 26

Høg, E., Fabricius, C., Makarov, V. V., et al. 2000, A&A, 355, L27

Holczer, T., Mazeh, T., Nachmani, G., et al. 2016, ArXiv e-prints

Holman, M., Touma, J., & Tremaine, S. 1997, Nature, 386, 254

Holman, M. J., & Wiegert, P. A. 1999, AJ, 117, 621

Holman, M. J., & Murray, N. W. 2005, Science, 307, 1288

Holman, M. J., Fabrycky, D. C., Ragozzine, D., et al. 2010, Science, 330, 51

Hora, J. L., Carey, S., Surace, J., et al. 2008, PASP, 120, 1233

Horch, E. P., Veillette, D. R., Baena Gallé, R., et al. 2009, AJ, 137, 5057

Horch, E. P., van Altena, W. F., Demarque, P., et al. 2015, AJ, 149, 151

Howard, A. W., Marcy, G. W., Johnson, J. A., et al. 2010a, Science, 330, 653

Howard, A. W., Johnson, J. A., Marcy, G. W., et al. 2010b, ApJ, 721, 1467

Howard, A. W., Marcy, G. W., Bryson, S. T., et al. 2012, ApJS, 201, 15

Howell, S. B., Sobeck, C., Haas, M., et al. 2014, PASP, 126, 398

Huber, D., Carter, J. A., Barbieri, M., et al. 2013, Science, 342, 331

Huber, D., Silva Aguirre, V., Matthews, J. M., et al. 2014, ApJS, 211, 2

Irwin, J., Buchhave, L., Berta, Z. K., et al. 2010, ApJ, 718, 1353

Isaacson, H., & Fischer, D. 2010, ApJ, 725, 875

Jackson, R. J., Jeffries, R. D., & Maxted, P. F. 2009, MNRAS, 399, L89

Jackson, B. K., Lewis, N. K., Barnes, J. W., et al. 2012, ApJ, 751, 112

Janson, M., Hormuth, F., Bergfors, C., et al. 2012, ApJ, 754, 44

Janson, M., Bergfors, C., Brandner, W., et al. 2014, ApJS, 214, 17

Jenkins, J. S., Ramsey, L. W., Jones, H. R., et al. 2009, ApJ, 704, 975

Jenkins, J. M., Caldwell, D. A., Chandrasekaran, H., et al. 2010, ApJL, 713, L87

Jha, S., Charbonneau, D., Garnavich, P. M., et al. 2000, ApJL, 540, L45

Johnson, J. A., Fischer, D. A., Marcy, G. W., et al. 2007a, ApJ, 665, 785

Johnson, J. A., Butler, R. P., Marcy, G. W., et al. 2007b, ApJ, 670, 833

Johnson, J. A., & Apps, K. 2009, ApJ, 699, 933

Johnson, J. A., Aller, K. M., Howard, A. W., & Crepp, J. R. 2010a, PASP, 122, 905

Johnson, J. A., Howard, A. W., Marcy, G. W., et al. 2010b, PASP, 122, 149

Johnson, J. A., Clanton, C., Howard, A. W., et al. 2011a, ApJS, 197, 26

Johnson, J. A., Apps, K., Gazak, J. Z., et al. 2011b, ApJ, 730, 79

Johnson, J. A., Gazak, J. Z., Apps, K., et al. 2012a, AJ, 143, 111

—. 2012b, AJ, 143, 111

Johnson, J. A., Morton, T. D., & Wright, J. T. 2013, ApJ, 763, 53

Jontof-Hutter, D., Rowe, J. F., Lissauer, J. J., Fabrycky, D. C., & Ford, E. B. 2015, Nature, 522, 321

Jontof-Hutter, D., Ford, E. B., Rowe, J. F., et al. 2016, ApJ, 820, 39

Kaib, N. A., Raymond, S. N., & Duncan, M. 2013, Nature, 493, 381

Kalas, P., Graham, J. R., Chiang, E., et al. 2008, Science, 322, 1345

Kasper, M., Apai, D., Janson, M., & Brandner, W. 2007, A&A, 472, 321

Kass, R. E., & Raftery, A. E. 1995, Journal of the American Statistical Association, 90, 773

Kepler, J. 1609, Astronomia nova ..., seu physica coelestis, tradita commentariis de motibus stellae martis

Kharchenko, N. V. 2001, Kinematika i Fizika Nebesnykh Tel, 17, 409

Kipping, D. M. 2010a, MNRAS, 409, L119

—. 2010b, MNRAS, 408, 1758

—. 2013, MNRAS, 434, L51

Kirkpatrick, J. D., Reid, I. N., Liebert, J., et al. 1999, ApJ, 519, 802

Kirkpatrick, J. D., Cushing, M. C., Gelino, C. R., et al. 2011, ApJS, 197, 19

Knutson, H. A., Charbonneau, D., Allen, L. E., et al. 2007, Nature, 447, 183

Knutson, H. A., Charbonneau, D., Allen, L. E., Burrows, A., & Megeath, S. T. 2008, ApJ, 673, 526

Knutson, H. A., Madhusudhan, N., Cowan, N. B., et al. 2011, ApJ, 735, 27

Knutson, H. A., Fulton, B. J., Montet, B. T., et al. 2014, ApJ, 785, 126

Koch, D. G., Borucki, W. J., Basri, G., et al. 2010, ApJL, 713, L79

Koen, C., Kilkenny, D., van Wyk, F., & Marang, F. 2010, MNRAS, 403, 1949

Kozai, Y. 1962, AJ, 67, 591

Kraus, A. L., & Ireland, M. J. 2012, ApJ, 745, 5

Kraus, A. L., Cody, A. M., Covey, K. R., et al. 2015, ApJ, 807, 3

Kroupa, P. 2001, MNRAS, 322, 231

Kuiper, G. P. 1938, ApJ, 88, 472

Kumar, S. S. 1963, ApJ, 137, 1121

Kuzuhara, M., Tamura, M., Kudo, T., et al. 2013, ApJ, 774, 11

Lagrange, A.-M., Gratadour, D., Chauvin, G., et al. 2009, A&A, 493, L21

Landolt, A. U. 1992, AJ, 104, 340

—. 2009, AJ, 137, 4186

Lantz, B., Aldering, G., Antilogus, P., et al. 2004, in Society of Photo-Optical Instrumentation Engineers (SPIE) Conference Series, Society of Photo-Optical Instrumentation Engineers (SPIE) Conference Series, ed. L. Mazuray, P. J. Rogers, & R. Wartmann, Vol. 5249, 146

Latham, D. W., Stefanik, R. P., Mazeh, T., Mayor, M., & Burki, G. 1989, Nature, 339, 38

Law, N. M., Hodgkin, S. T., & Mackay, C. D. 2006, MNRAS, 368, 1917

Law, N. M., Morton, T., Baranec, C., et al. 2014, ApJ, 791, 35

Lidov, M. L. 1962, Planet. Space Sci., 9, 719

Lillo-Box, J., Barrado, D., Moya, A., et al. 2014, A&A, 562, A109

Lissauer, J. J., Fabrycky, D. C., Ford, E. B., et al. 2011a, Nature, 470, 53

Lissauer, J. J., Ragozzine, D., Fabrycky, D. C., et al. 2011b, ApJS, 197, 8

Lissauer, J. J., Marcy, G. W., Rowe, J. F., et al. 2012, ApJ, 750, 112

Lithwick, Y., & Wu, Y. 2012, ApJL, 756, L11

Lithwick, Y., Xie, J., & Wu, Y. 2012, ApJ, 761, 122

Littlefair, S. P., Casewell, S. L., Parsons, S. G., et al. 2014, MNRAS, 445, 2106

Liu, M. C., Fischer, D. A., Graham, J. R., et al. 2002, ApJ, 571, 519

Liu, M. C., Wahhaj, Z., Biller, B. A., et al. 2010, in Society of Photo-Optical Instrumentation Engineers (SPIE) Conference Series, Society of Photo-Optical Instrumentation Engineers (SPIE) Conference Series, Vol. 7736, 1

Lloyd, J. P. 2002, "The detection and characterization of low mass companions to sun-like stars", PhD thesis (University of California, Berkeley)

Loeb, A., & Gaudi, B. S. 2003, ApJL, 588, L117

Luhman, K. L. 2012, ARA&A, 50, 65

—. 2014, ApJL, 786, L18

Mace, G. N., Kirkpatrick, J. D., Cushing, M. C., et al. 2013, ApJS, 205, 6

Maciejewski, G., Dimitrov, D., Fernández, M., et al. 2016, A&A, 588, L6

Macintosh, B., Graham, J. R., Barman, T., et al. 2015, Science, 350, 64

Malo, L., Doyon, R., Lafrenière, D., et al. 2013, ApJ, 762, 88

Mamajek, E. E., & Bell, C. P. 2014, MNRAS, 445, 2169

Mandel, K., & Agol, E. 2002, ApJL, 580, L171

Mann, A. W., Gaidos, E., Lépine, S., & Hilton, E. J. 2012, ApJ, 753, 90

Mann, A. W., Brewer, J. M., Gaidos, E., Lépine, S., & Hilton, E. J. 2013a, AJ, 145, 52

Mann, A. W., Gaidos, E., & Ansdell, M. 2013b, ApJ, 779, 188

Mann, A. W., Feiden, G. A., Gaidos, E., Boyajian, T., & von Braun, K. 2015, ApJ, 804, 64

Marcy, G. W., Butler, R. P., Vogt, S. S., Fischer, D., & Lissauer, J. J. 1998, ApJL, 505, L147

Marcy, G. W., & Butler, R. P. 2000, PASP, 112, 137

Marcy, G. W., Butler, R. P., Fischer, D., et al. 2001, ApJ, 556, 296

Marley, M. S., Gelino, C., Stephens, D., Lunine, J. I., & Freedman, R. 1999, ApJ, 513, 879

Marois, C., Macintosh, B., Barman, T., et al. 2008, Science, 322, 1348

Marois, C., Zuckerman, B., Konopacky, Q. M., Macintosh, B., & Barman, T. 2010, Nature, 468, 1080

Mason, B. D., Wycoff, G. L., Hartkopf, W. I., Douglass, G. G., & Worley, C. E. 2001, AJ, 122, 3466

Mayor, M., & Queloz, D. 1995, Nature, 378, 355

Mayor, M., Bonfils, X., Forveille, T., et al. 2009, A&A, 507, 487

Mayor, M., Marmier, M., Lovis, C., et al. 2011, ArXiv e-prints

Mazeh, T., Nachmani, G., Holczer, T., et al. 2013, ApJS, 208, 16

McCaughrean, M. J., & Stauffer, J. R. 1994, AJ, 108, 1382

McDonald, I., Kerins, E., Penny, M., et al. 2014, MNRAS, 445, 4137

Meschiari, S., Wolf, A. S., Rivera, E., et al. 2009, PASP, 121, 1016

Metchev, S. A., & Hillenbrand, L. A. 2009, ApJS, 181, 62

Metchev, S. A., Heinze, A., Apai, D., et al. 2015, ApJ, 799, 154

Mislis, D., Heller, R., Schmitt, J. H. M., & Hodgkin, S. 2012, A&A, 538, A4

Montes, D., López-Santiago, J., Gálvez, M. C., et al. 2001, MNRAS, 328, 45

Montet, B. T., & Johnson, J. A. 2013, ApJ, 762, 112

Montet, B. T., Crepp, J. R., Johnson, J. A., Howard, A. W., & Marcy, G. W. 2014, ApJ, 781, 28

Montet, B. T., Johnson, J. A., Muirhead, P. S., et al. 2015a, ApJ, 800, 134

Montet, B. T., Bowler, B. P., Shkolnik, E. L., et al. 2015b, ApJL, 813, L11

Montet, B. T., Morton, T. D., Foreman-Mackey, D., et al. 2015c, ApJ, 809, 25

Montet, B. T., Johnson, J. A., Fortney, J. J., & Desert, J.-M. 2016, ApJL, 822, L6

Morgan, W. W. 1938, ApJ, 87, 589

Mortier, A., Santos, N. C., Sousa, S., et al. 2013, A&A, 551, A112

Morton, T. D. 2012, ApJ, 761, 6

—. 2015a, isochrones: Stellar model grid package, Astrophysics Source Code Library

—. 2015b, VESPA: False positive probabilities calculator, Astrophysics Source Code Library

Morton, T. D., & Johnson, J. A. 2011, ApJ, 738, 170

Morton, T. D., & Swift, J. J. 2014, ApJ, 791, 10

Morton, T. D., Bryson, S. T., Coughlin, J. L., et al. 2016, ApJ, 822, 86

Mould, J. R. 1975, A&A, 38, 283

Moulds, V. E., Watson, C. A., Bonfils, X., Littlefair, S. P., & Simpson, E. K. 2013, MNRAS, 430, 1709

Moutou, C., Bonomo, A. S., Bruno, G., et al. 2013, A&A, 558, L6

Muirhead, P. S., Johnson, J. A., Apps, K., et al. 2012a, ApJ, 747, 144

Muirhead, P. S., Hamren, K., Schlawin, E., et al. 2012b, ApJL, 750, L37

Muirhead, P. S., Becker, J., Feiden, G. A., et al. 2014, ApJS, 213, 5

Mullally, F., Coughlin, J. L., Thompson, S. E., et al. 2015, ApJS, 217, 31

Murray, C. D., & Dermott, S. F. 2000, Solar System Dynamics (Cambridge University Press)

Nakajima, T., Oppenheimer, B. R., Kulkarni, S. R., et al. 1995, Nature, 378, 463

Napiwotzki, R. 2009, Journal of Physics Conference Series, 172.1, 012004

Nataf, D. M., Gould, A., Fouqué, P., et al. 2013, ApJ, 769, 88

Nataf, D. M., Gonzalez, O. A., Casagrande, L., et al. 2016, MNRAS, 456, 2692

Nesvorný, D., Kipping, D. M., Buchhave, L. A., et al. 2012, Science, 336, 1133

Nesvorný, D., Kipping, D., Terrell, D., et al. 2013, ApJ, 777, 3

Neves, V., Bonfils, X., Santos, N. C., et al. 2012, A&A, 538, A25

Neves, V., Bonfils, X., Santos, N. C., et al. 2013, A&A, 551, A36

Newton, E. R., Charbonneau, D., Irwin, J., & Mann, A. W. 2015, ApJ, 800, 85

Nielsen, E. L., & Close, L. M. 2010, ApJ, 717, 878

Nishiyama, S., Tamura, M., Hatano, H., et al. 2009, ApJ, 696, 1407

Nutzman, P., & Charbonneau, D. 2008, PASP, 120, 317

Ochsenbein, F., Bauer, P., & Marcout, J. 2000, A&AS, 143, 23

Oja, T. 1985, A&AS, 61, 331

Öpik, E. 1924, Pulications de L'Observatoire Astronomique de l'Université de Tartu, 25, 6

Osborn, H. P., Armstrong, D. J., Brown, D. J., et al. 2016, MNRAS, 457, 2273

Oshagh, M., Boué, G., Haghighipour, N., et al. 2012, A&A, 540, A62

Paddock, G. F. 1913, PASP, 25, 208

Patel, S. G., Vogt, S. S., Marcy, G. W., et al. 2007, ApJ, 665, 744

Pedicelli, S., Bono, G., Lemasle, B., et al. 2009, A&A, 504, 81

Peña-Ramírez, K., Béjar, V. J., Zapatero Osorio, M. R., Petr-Gotzens, M. G., & Martín, E. L. 2012, ApJ, 754, 30

Pickering, E. C. 1890, Annals of Harvard College Observatory, 27, 1

Pineda, J. S., Bottom, M., & Johnson, J. A. 2013, ApJ, 767, 28

Podolak, M., Pollack, J. B., & Reynolds, R. T. 1988, Icarus, 73, 163

Pollack, J. B., Podolak, M., Bodenheimer, P., & Christofferson, B. 1986, Icarus, 67, 409

Pont, F., Zucker, S., & Queloz, D. 2006, MNRAS, 373, 231

Quinn, S. N., White, T. R., Latham, D. W., et al. 2015, ApJ, 803, 49

Quintana, E. V., Rowe, J. F., Barclay, T., et al. 2013, ApJ, 767, 137

Ragozzine, D., & Wolf, A. S. 2009, ApJ, 698, 1778

Rajpaul, V., Aigrain, S., & Roberts, S. 2016, MNRAS, 456, L6

Rameau, J., Chauvin, G., Lagrange, A.-M., et al. 2013, ApJL, 772, L15

Rauscher, E., & Marcy, G. W. 2006, PASP, 118, 617

Rayner, J. T., Toomey, D. W., Onaka, P. M., et al. 2003, PASP, 115, 362

Rayner, J. T., Cushing, M. C., & Vacca, W. D. 2009, ApJS, 185, 289

Rebolo, R., Zapatero Osorio, M. R., & Martín, E. L. 1995, Nature, 377, 129

Reylé, C., Delorme, P., Willott, C. J., et al. 2010, A&A, 522, A112

Rice, E. L., Barman, T., Mclean, I. S., Prato, L., & Kirkpatrick, J. D. 2010, ApJS, 186, 63

Ricker, G. R., Winn, J. N., Vanderspek, R., et al. 2014, in Proc. SPIE, Space Telescopes and Instrumentation 2014: Optical, Infrared, and Millimeter Wave, Vol. 9143, 914320

Rivera, E. J., Lissauer, J. J., Butler, R. P., et al. 2005, ApJ, 634, 625

Rivera, E. J., Laughlin, G., Butler, R. P., et al. 2010, ApJ, 719, 890

Robin, A. C., Reylé, C., Derrière, S., & Picaud, S. 2003, A&A, 409, 523

Robinson, S. E., Laughlin, G., Vogt, S. S., et al. 2007, ApJ, 670, 1391

Rogers, L. A. 2015, ApJ, 801, 41

Rojas-Ayala, B., Covey, K. R., Muirhead, P. S., & Lloyd, J. P. 2010, ApJL, 720, L113

—. 2012, ApJ, 748, 93

Rolleston, W. R., Smartt, S. J., Dufton, P. L., & Ryans, R. S. 2000, A&A, 363, 537

Rowe, J. F., Bryson, S. T., Marcy, G. W., et al. 2014, ApJ, 784, 45

Rowe, J. F., Coughlin, J. L., Antoci, V., et al. 2015, ApJS, 217, 16

Russell, H. N. 1914, Nature, 93, 252

Salpeter, E. E. 1955, ApJ, 121, 161

Saumon, D., & Marley, M. S. 2008, ApJ, 689, 1327

Saumon, D., Marley, M. S., Abel, M., Frommhold, L., & Freedman, R. S. 2012, ApJ, 750, 74

Schaefer, G. H., Prato, L., Simon, M., & Patience, J. 2014, AJ, 147, 157

Schlafly, E. F., & Finkbeiner, D. P. 2011, ApJ, 737, 103

Schlaufman, K. C., & Winn, J. N. 2013, ApJ, 772, 143

Schlegel, D. J., Finkbeiner, D. P., & Davis, M. 1998, ApJ, 500, 525

Schlieder, J. E., Bonnefoy, M., Herbst, T. M., et al. 2014, ApJ, 783, 27

Scholz, R.-D. 2010, A&A, 515, A92

Schwarz, G. 1978, The Annals of Statistics, 6, 461

Seager, S., & Mallén-Ornelas, G. 2003, ApJ, 585, 1038

Seifahrt, A., Bean, J. L., Stürmer, J., et al. 2016, ArXiv e-prints

Shan, Y., Johnson, J. A., & Morton, T. D. 2015, ApJ, 813, 75

Shkolnik, E. L., Anglada-Escudé, G., Liu, M. C., et al. 2012, ApJ, 758, 56

Shkolnik, E. L., & Barman, T. S. 2014, AJ, 148, 64

Showman, A. P., & Guillot, T. 2002, A&A, 385, 166

Shu, F., Najita, J., Ostriker, E., et al. 1994, ApJ, 429, 781

Siegler, N., Close, L. M., Mamajek, E. E., & Freed, M. 2003, ApJ, 598, 1265

Simon, M., & Schaefer, G. H. 2011, ApJ, 743, 158

Siverd, R. J., Beatty, T. G., Pepper, J., et al. 2012, ApJ, 761, 123

Skemer, A. J., Morley, C. V., Zimmerman, N. T., et al. 2016, ApJ, 817, 166

Skrutskie, M. F., Cutri, R. M., Stiening, R., et al. 2006, AJ, 131, 1163

Southworth, J. 2010, MNRAS, 408, 1689

—. 2011, MNRAS, 417, 2166

Sozzetti, A., Torres, G., Charbonneau, D., et al. 2007, ApJ, 664, 1190

Spergel, D., Gehrels, N., Baltay, C., et al. 2015, ArXiv e-prints

Stassun, K. G., Mathieu, R. D., & Valenti, J. A. 2006, Nature, 440, 311

Stassun, K. G., Feiden, G. A., & Torres, G. 2014, New Astronomy Reviews, 60, 1

Steffen, J. H., Ford, E. B., Rowe, J. F., et al. 2012a, ApJ, 756, 186

Steffen, J. H., Ragozzine, D., Fabrycky, D. C., et al. 2012b, Proceedings of the National Academy of Science, 109, 7982

Steffen, J. H., Fabrycky, D. C., Agol, E., et al. 2013, MNRAS, 428, 1077

Stelzer, B., Marino, A., Micela, G., López-Santiago, J., & Liefke, C. 2013, MNRAS, 431, 2063

Stevenson, K. B., Harrington, J., Fortney, J. J., et al. 2012, ApJ, 754, 136

Stevenson, K. B., Bean, J. L., Madhusudhan, N., & Harrington, J. 2014a, ApJ, 791, 36

Stevenson, K. B., Désert, J.-M., Line, M. R., et al. 2014b, Science, 346, 838

Street, R. A., Pollaco, D. L., Fitzsimmons, A., et al. 2003, in Astronomical Society of the Pacific Conference Series, Scientific Frontiers in Research on Extrasolar Planets, ed. D. Deming, & S. Seager, Vol. 294, 405

Sumi, T., Bennett, D. P., Bond, I. A., et al. 2010, ApJ, 710, 1641

Sumi, T., Kamiya, K., Bennett, D. P., et al. 2011, Nature, 473, 349

Swift, J. J., Johnson, J. A., Morton, T. D., et al. 2013, ApJ, 764, 105

Tadeu dos Santos, M., Silva, G. G., Ferraz-Mello, S., & Michtchenko, T. A. 2012, Celestial Mechanics and Dynamical Astronomy, 113, 49

Tarter, J. C. 1975, "The interaction of gas and galaxies within galaxy clusters", PhD thesis (California Univ., Berkeley.)

Thompson, B., Frinchaboy, P., Kinemuchi, K., Sarajedini, A., & Cohen, R. 2014, AJ, 148, 85

Torres, G. 1999, PASP, 111, 169

Torres, C. A., Quast, G. R., Melo, C. H., & Sterzik, M. F. "Young Nearby Loose Associations", 2008, in, Handbook of Star Forming Regions, Volume II, ed. B. Reipurth, 757

Torres, G., Fressin, F., Batalha, N. M., et al. 2011, ApJ, 727, 24

Triaud, A. H. J., Hebb, L., Anderson, D. R., et al. 2013, A&A, 549, A18

Udalski, A., Zebrun, K., Szymanski, M., et al. 2002, Acta Astronomica, 52, 115

Udry, S., Bonfils, X., Delfosse, X., et al. 2007, A&A, 469, L43

Uehara, S., Kawahara, H., Masuda, K., Yamada, S., & Aizawa, M. 2016, ApJ, 822, 2

Vacca, W. D., Cushing, M. C., & Rayner, J. T. 2003, PASP, 115, 389

Valenti, J. A., & Fischer, D. A. 2005, ApJS, 159, 141

van Altena, W. F., Lee, J. T., & Hoffleit, E. D. 1995, The general catalogue of trigonometric parallaxes

van Belle, G. T., & von Braun, K. 2009, ApJ, 694, 1085

van Leeuwen, F. 2007, A&A, 474, 653

Vanderburg, A., Montet, B. T., Johnson, J. A., et al. 2015, ApJ, 800, 59

Vanderburg, A., Latham, D. W., Buchhave, L. A., et al. 2016, ApJS, 222, 14

Veeder, G. J. 1974, AJ, 79, 1056

Vigan, A., Patience, J., Marois, C., et al. 2012, A&A, 544, A9

Vogt, S. S., Allen, S. L., Bigelow, B. C., et al. 1994, in Society of Photo-Optical Instrumentation Engineers (SPIE) Conference Series, Society of Photo-Optical Instrumentation Engineers (SPIE) Conference Series, ed. D. L. Crawford, & E. R. Craine, Vol. 2198, 362

Wang, J., Xie, J.-W., Barclay, T., & Fischer, D. A. 2014, ApJ, 783, 4

Wang, J., Fischer, D. A., Horch, E. P., & Huang, X. 2015a, ApJ, 799, 229

Wang, J., Fischer, D. A., Barclay, T., et al. 2015b, ApJ, 815, 127

Welsh, W. F., Orosz, J. A., Seager, S., et al. 2010, ApJL, 713, L145

Welsh, W. F., Orosz, J. A., Carter, J. A., et al. 2012, Nature, 481, 475

Werner, M. W., Roellig, T. L., Low, F. J., et al. 2004, ApJS, 154, 1

West, A. A., Hawley, S. L., Bochanski, J. J., et al. 2008, AJ, 135, 785

Wheeler, J. C. 2012, ApJ, 758, 123

Wilson, O. C. 1968, ApJ, 153, 221

Wilson, J. C., Henderson, C. P., Herter, T. L., et al. 2004, in Society of Photo-Optical Instrumentation Engineers (SPIE) Conference Series, Ground-based Instrumentation for Astronomy, ed. A. F. Moorwood, & M. Iye, Vol. 5492, 1295

Winget, D. E., Nather, R. E., Clemens, J. C., et al. 1991, ApJ, 378, 326

Winn, J. N. “Exoplanet Transits and Occultations”, 2011, in, Exoplanets, edited by S. Seager. Tucson, AZ: University of Arizona Press, 2011, 526 pp. ISBN 978-0-8165-2945-2., p.55-77, ed. S. Piper, 55

Wizinowich, P., Acton, D. S., Shelton, C., et al. 2000, PASP, 112, 315

Wright, J. T. 2005, PASP, 117, 657

Wright, J. T., Marcy, G. W., Butler, R. P., & Vogt, S. S. 2004, ApJS, 152, 261

Wright, J. T., Marcy, G. W., Fischer, D. A., et al. 2007, ApJ, 657, 533

Wright, J. T., Veras, D., Ford, E. B., et al. 2011, ApJ, 730, 93

Wright, J. T., Marcy, G. W., Howard, A. W., et al. 2012, ApJ, 753, 160

Xie, J.-W. 2013, ApJS, 208, 22

Yee, J. C., & Gaudi, B. S. 2008, ApJ, 688, 616

Yelda, S., Lu, J. R., Ghez, A. M., et al. 2010, ApJ, 725, 331

York, D. G., Adelman, J., Anderson Jr., J. E., et al. 2000, AJ, 120, 1579

Youdin, A. N. 2011, ApJ, 742, 38

Zacharias, N., Finch, C. T., Girard, T. M., et al. 2012, VizieR Online Data Catalog, 1322,

Zakhozhaj, V. A. 2002, Kinematika i Fizika Nebesnykh Tel, 18, 535

Zuckerman, B. 2000, Proceedings of the National Academy of Science, 97, 963

Zuckerman, B., Song, I., & Bessell, M. S. 2004, ApJL, 613, L65